A STABILITY STUDY OF A THREE-DIMENSIONAL PASSIVE-DYNAMIC MODEL OF HUMAN GAIT

A Dissertation
Presented to the Faculty of the Graduate School
of Cornell University
in Partial Fulfillment of the Requirements for the Degree of
Doctor of Philosophy

by
Michael Jon Coleman

February 1998

© Michael Jon Coleman 1998
ALL RIGHTS RESERVED

A STABILITY STUDY OF A THREE-DIMENSIONAL PASSIVE-DYNAMIC MODEL OF HUMAN GAIT

Michael Jon Coleman, Ph.D.
Cornell University 1998

The goal of this research is to examine the possibility of stable gait cycles in simple three-dimensional models of human walking with *no* actuation, other than gravity, and *no* control. We address the passive-dynamic stability of 3D walking using a collection of models of varying complexity – 2D and 3D rimless spoked wheels, a 3D rolling disk with oblique masses attached, and 2D and 3D straight-legged point-foot models of human walking. Analytical and numerical linearized stability studies are carried out to study the behavior of these systems. The mass distribution is varied to study its effect on stability.

The main results are as follows. (1) a fully analytical nonlinear stability study of uphill and downhill motions of the 2D rimless spoked wheel shows that two outcomes exist – coming to rest on two spokes and entering into a limit cycle motion, both of which are always asymptotically stable and have basins of attraction which we describe exactly. (2) A linearized stability analysis of the 3D rolling disk with oblique masses attached, that steer and bank but not roll with the wheel, shows that it can be asymptotically stable given sufficient forward rolling speed, more stable than an axisymmetric disk which is neutrally stable at best. (3) We carry out numerical and analytical stability studies of steady motions of the 3D rimless spoked wheel. At any fixed, large enough slope, the system has a one-parameter family of stable steady rolling motions. We find analytic approximations for the minimum required slope at a given heading for asymptotically stable rolling in three dimensions, for the case of many spokes and small slope. In the limit as the number of spokes approaches infinity, the behavior of the rimless wheel approaches that of a rolling disk in an averaged sense and approaches neutral stability. (4) Numerical stability studies of the 2D straight-legged point walking model have turned up stable periodic motions for a variety of model parameters. Of particular interest is the limiting case of a huge hip mass and tiny point feet that can be stable, a one-parameter model depending only on the downhill slope. (6) Numerical stability studies of a 3D straight-legged point-foot model have only turned up unstable steady walking motions to date. Getting arbitrarily close to neutrally stable steady motions is possible, though, if we allow the model to 'grow' long lateral 'balance bars' from its legs. The resulting motion resembles 'tight-rope' walking, with tiny steps. (7) Experimental studies of a Tinkertoy® model based on the as yet unsuccessful numerical simulations have revealed apparently stable motions. This is the first statically unstable passive-dynamic model in theory, simulation, or experiment to show dynamic balance fore-aft as well as side-to-side, balance.

Biographical Sketch

Mike Coleman was born at Sinai Hospital in Baltimore, Maryland on May 22, 1960 to his proud parents Bernard and Alice. He spent his first three years with his parents and sister Frannie on an idyllic sixty-five acre farm at the intersection of Rinehart Road and Bixler Church Road. The farm (with house, barn, out-buildings, and a log cabin built by a freed slave) was just outside the little town of Westminster, Maryland in the lush rolling hills of Carroll County, foothills to the Blue Ridge Mountains, about twenty miles southeast of Hanover, Pennsylvania, forty miles northeast of Frederick, Maryland, and thirty miles northwest of Baltimore.

When Mike was born, it was discovered that he had two thumbs, like everyone else, but both on his right hand, for a total of three. One was surgically removed at birth but the remaining one was severely deformed. Though it is still deformed, some function was restored through several surgeries done by the famous Dr. Curtis of John's Hopkins University, who always seemed god-like and, thus, very intimidating. Today, there is a special hand center at Hopkins named in his honor. Mike was both ashamed and proud of his small handicap. He always made sure to get on the right when lining up by two's for school trips; he made the mistake on a field trip to the Carroll County Fire Department in the second grade of giving his right hand to Kathy Fringer and still can hear her screech in horror at the sight of the alien creature's appendage for grasping things that was sort of like a human hand. Remember, always on the right.

When Mike was three years old, his family sold the farm for a ridiculously low price of $16,000, including the buildings, land, and house. But, his parents were more concerned that their children would be too isolated on a farm and not have enough friends to play with. They moved to a house at 42 Bishop St. in the town of Westminster. When Mike was eleven, the family moved to 92 West Green St. near Western Maryland College right across from their good friends Helen and Montgomery Schroyer.

Mike's first and forever teachers have been his parents. From gardening to cooking to bicycle riding to football to frisbee throwing to arithmetic to morality to music to art to literature to politics to hand-tools to camping and more, Mike's parents, Bud and Alice, have taught him many, many things with caring patience and humility and and provided him with a multitude of other opportunities to learn and experience. Mike's father continues to teach him things even now; for instance, he recently showed Mike a really cool and new way to draw ellipses. Mike's sister too has taught him many things, such as about singing, swing dance, volleyball, swimming, and what he should know about women.

Mike first went to nursery school when he was three and then back again the next year. After that, he joined Just Five Folks, a Montessori kindergarten, a learn-by-doing school. His teachers were Jackie Finch and Jan Cross, both exquisite individuals. Jan and her husband remain close family friends.

In kindergarten, it was discovered that Mike could draw with perspective, sort of an unusual skill. Ever since, he has been known as an artist, entering contests frequently and giving shows on occasion in school. He remembers drawing his first self-portrait at age nine, posing in his favorite Orioles baseball T-shirt, and looking into the notebook–paper sized mirror with a thin wooden frame painted white that the family used to keep in the bathroom for closer looks at things. His

first organized art class outside of school was at age ten with Mrs. Trump, with whom he learned to draw still lifes with charcoal and pastels. His family and school nurtured him well, especially his first and only private teacher, Stan Gilmore. With Stan, Mike learned the difficult, delicate, art of water color painting. Mike still draws seriously and is most fond of the human figure and the portrait. Most recently, Mike attended figure drawing sessions at the Ithaca Community Arts Center. Mike has saved much of his artwork along the way and many pieces clutter his apartment walls.

Mike started playing piano when he was seven. His first teacher was Mrs. Kennedy on Green St. Then, he switched to Mrs. Giselle on New Windsor road. She was native to Japan and one of the most beautiful women he had ever met. Mike fondly remembers sitting on the piano bench next to her, looking up at her instead of the key board, admiring her beautiful smile, her soft pearly skin, and her lovely eyes. She used to wear very tight dresses which Mike liked very much. After that was Mrs. Adams across the street from his house on Green St. and Mr. Judge down the street who always breathed funny when he played. Finally, Mike learned to see the finer subtleties of playing with his last teacher, the deeply serious, meek and shy Mildred Cole. Mike played recitals starting with Mrs. Giselle at age ten and continued to do so through High School. It was in these recitals that Mike learned he had performance anxiety, a debilitating affliction that stays with him to this day. Nevertheless he is most proud to have played Prelude Op. 28, 1 for pianoforte in C Major (The Minute Prelude) by Chopin and Rhapsody in G Minor, Op.79 No.2 by Brahms at his senior recital. Presently, Mike has an electric piano with synthesized sound and simulated key action at home but would rather have a real one or at least one with digitally sampled sound reproduction.

After kindergarten, Mike attended the East End Elementary School for grades one with Mrs. Westheimer and two with Mrs. Kemper (Mike's grandmother on his father's side attended the East End school in 1899), the Westminster Elementary School for grades three with Mrs. Case and four with Mrs. Reese (who used to read to us from Tom Sawyer and Treasure Island), the William Winchester School for fifth grade with hump-backed Mrs. Rice (with whom he argued once about the commutative law of multiplication and won), the East Middle School for sixth through eighth grade, and, finally, Westminster High School for ninth through twelfth grades. It was in middle and high school that Mike discovered his aptitude for and interest in mathematics and science. He remembers being particularly intrigued with the Human Powered Flight program at MIT that he read about in Popular Science.

Mike went to Princeton University graduating with a Bachelor's of Science and Engineering degree from the Department of Aerospace and Mechanical Engineering in 1982. The most significant academic experience at Princeton for Mike was realizing his writing weakness and then working very hard to improve on it. His best friend and roommate Christopher Barth had a significant impact on Mike's life, especially Chris's zen-like approach to life. His engineering education was mostly not very stimulating, though he did have an interesting summer job at Princeton working for Professor Earl Dowell studying the oscillations of buckled flat plates in an air flow. His favorite engineering course was Engineering Acoustics taught by Donald Bliss, one of the best teachers in the department who was unfortunately denied tenure. Still, no engineering professor in particular had any deep and lasting influence on Mike while at Princeton. His favorite course was Soviet Politics taught by Professor Stephen Cohen (who now appears regularly on television as a commentator). Two studio art courses in drawing and painting taught by Jerry and Sean had a significant impact on his artistic maturity and confidence.

After Princeton, Mike went to work for the IBM Corporation in Endicott, New York in research and development for electronic packaging and stayed for five years. His mentors there were Peter Engel (a T&AM graduate), in structural mechanics, and Bhagat Sammakia, in fluid mechanics and heat transfer. It was at IBM that Mike decided to return to school for a Ph. D. in engineering, strongly encouraged by Bhagat and Cathy Biber, his co-worker, apartment mate and sometimes lover. While at IBM, Mike first came in contact with Don Conway at Cornell. Professor Conway has always been very supportive of Mike while he's been at Cornell.

Much later in life, after college, Mike found new passion in sports. He trained and competed

heavily in bicycle racing and cross-country ski racing. Mike was a member of the Tioga-Velo six-man bicycle racing team in Binghamton and the Cornell Cycling Team. In 1990, he started a x-c ski racing team sponsored by Wildware Outdoors Store and Fischer, Inc. Mike qualified for and raced in the New York State Empire Games in X-C Skiing for a number of years. He participated twice in the U.S. Cross-Country Ski National Championships. Mike was fortunate to win a number of medals now and then. His most cherished result was finishing second overall in the 19 kilometer Tug Hill Try-it race in 1991. He trained very seriously for skiing, working very closely with his training partner, Raj Sundra. Due to Raj's influence, Mike took a a highly studied approach to training, using video taping to improve technique and making periodized training plans. A highlight of Mike's ski experiences was attending the 1995 World Cross-Country Ski Championships in Thunder Bay, Ontario and getting an opportunity to see his skiing idols Bjorn Daehlie, Torgny Mogren, Validimir Smirnov, Michael Alberello, Silvio Fauner, and Vegard Ulvang. In many ways, Mike considered competitive sports a focus of his life while at Cornell, almost on equal footing with his graduate work. Sports kept him alive and able to complete his work. Mike also counts basketball, squash, and weight training among his interests, and now bouldering, due to his new friend, Tomomi Ueda.

After applying to nine graduate schools (Berkeley, Stanford, Wisconsin, Minnesota, Michigan, M.I.T., University of Pennsylvania, Cornell University, and Johns Hopkins), Mike traveled to all except M.I.T before getting any acceptances. He was accepted at eight (who wants to go to M.I.T. anyway?), was offered tuition support from all, and was offered stipend support from all but Stanford and Berkeley. Mike chose Cornell. You see, at the time, among his choices for schools, Mike thought that the best environment, closest to home, for bike training and racing was Ithaca.

In the fall of 1987, Mike joined T&AM as a M.S./Ph.D. student, the beginning of a long journey he thought he might never finish. He passed his Q exam in January 1988. It was the most dreaded experience of his life. He failed the mathematics section but somehow recovered and aced the continuum mechanics and dynamics sections. Mike is credited with coming up with a new concept in mechanics during the exam. In the continuum section, Dick Lance was questioning Mike about the stress vector, the stress tensor, and linear momentum balance. Eventually, the questioning led to how applying angular momentum balance to a small material element yields symmetry of the stress tensor. Trying to lead Mike to the answer, Professor Lance asked Mike what other kind of momentum there is besides linear momentum. Going blank for a moment and desperate, Mike blurted out, "I don't know, nonlinear momentum?", his voice trailing upwards at the end of his response. The answer drew huge laughs from the committee – they thought Mike was just joking. The laughter somehow returned Mike to a state of clarity and he was able to carry on and answer correctly. Memorable also was Jim Jenkins only question of Mike in the dynamics section, "Well, if no one else has any questions, there's just one thing I have to ask: what did you do last semester? Because, you know, it's going to come up in the faculty deliberations after the exam." Mike had only taken one 3-credit course and one 1-credit course in order to leave time to study for the Q-exam. Mike immediately thought, well, that's it, he's outta there. Somehow, he figured, they must know how much Mike had been skiing and biking instead of being at school. Apparently, whatever it was he did that semester, he passed. After that, he took way too many courses.

By far, Mike's most startlingly surprising joy and success at Cornell has been his teaching. Teaching far exceeded his expectations for personal accomplishments and rewards. In 1991, Mike was selected to be Teaching Fellow for the Cornell University Teaching Assistant Development Program. In the next year, Mike was awarded the H. D. Bloch Teaching Prize for best teaching assistant in the department. Most importantly, Mike discovered that he had a talent for something he never thought he could be good at, a vocation that gives him hours to spend helping people understand things, something he loves to do, even for low pay. Particularly satisfying to him was incorporating studio drawing exercises into the engineering drawing and design course he has taught. For one semester, he also offered a free non-credit drawing course to anyone interested but mostly attended by engineering students thirsting for a break from problem sets.

His first try for an advisor was Philip Holmes and for committee member, Paul Steen in Chemical

Engineering. The plan was to study pattern formation in solidifying metals. Paul decided to go on sabbatical which killed that idea. Then, Mike switched to Dick Lance for advisor and Paul Dawson and Leigh Phoenix for committee members. The first idea was to work on the curing of composite materials. They failed Mike on his first A exam attempt because, as Leigh put it, "the department is like a country club and you don't seem to want to be a member". Similar in tone to Leigh's comment, Dick Lance once commented that Mike was using his body too much and not using his head enough, referring to his bicycle racing. They passed him on the second try in 1991 anyway. The new idea was to study the compressive behavior of composites.

In the early stages, when Mike was having trouble focusing and getting motivated, Professor Lance gave him a copy of a commencement speech at Brown University which made wonderful statements about following one's own path in the pursuit of knowledge. This was a nice gesture on Dick's part and the speech had a deep and lasting influence on Mike during his convoluted, unusual, and very long route through Cornell. Indeed, its impact induced drastic changes (eventually benefical) in Mike's travels with his special committee (see below).

After struggling to get going, Mike began work on a project for the Monsanto corporation in collaboration with Herbert Hui, Andy Ruina, and Ed Kramer in Materials Science. The project was to study the fabrication of automobile window shields with a thin layer of sun-sensitive photo-gray material embedded inside the safety-glass polymer. During the curing process, the thin layer was buckling. The project was interesting and provided a fruitful collaboration with Andy Ruina. The analysis involved studying the buckling of thin infinite elastic plates sandwiched symmetrically between two viscoelastic foundations. Happy with a report Mike wrote on the buckling problem, a possibility for research funding from the company seemed imminent and Mike seemed to be headed towards another research topic. But, like many development projects, this one died without further explanation.

Within a year, in a swift, decisive move, Mike "fired" his entire special committee; he was in a down-sizing phase. Mike took up Andy Ruina's offer to work with him on passive-dynamic walking and to join the ranks of Andy's "problem" students (who all turned out to do quite good work in the end). And, thus finally began Mike's dissertation research. In 1992, Mike co-authored a proposal with Jeff Koechling to the Whitaker Foundation for a grant to work on three-dimensional passive-dynamic walking research. To everyone's surprise, the proposal was accepted including three years of graduate student support for Mike. Unfortunately, unbeknownst to everyone except himself, Jeff decided to leave Cornell. Consequently, the money went back to Whitaker and Mike was back at teaching assistantship. From that point on, Mike was not guaranteed any funding to finish his degree and had to scare up what he could each semester and summer. Not knowing where funding was coming from each semester was a very stressful situation; finding new funding at the end of every semester was a time consuming and uncertain process.

For a period of three semesters, starting in fall 1994, Mike assisted Andy Ruina and Rudra Pratap with the writing of their engineering dynamics textbook. He helped with the editing, problem and answer formulation, writing small examples, drawing figures, and typing and formatting text. It was exhausting mentally and physically draining work. All in all, it was a good experience. Mike is extremely grateful to Andy Ruina for paying Mike from his own funds. In the end, Mike wishes that Andy and Rudra had included Mike as a co-author, considering his considerable effort and contribution to the book and his enthusiasm for the project.

Most recently, Mike has been happy to co-author several journal articles on his work and receive international press coverage in The Guardian and The Economist highlighting Andy Ruina's Human Power and Robotics Laboratory and Mike's Tinkertoy ® walking invention. Developing the Tinkertoy ® walking device was one of the most satisfying engineering experiences Mike has ever had. It was the first time that he brought some engineering analysis results together with a creative design and construction process to invent some mechanism that worked, based on some over-reaching vision, from Tad McGeer and his dissertation advisor Andy Ruina, that, though very promising, gave no guarantee of success.

In memory of my mother Alice
and
For my father Bernard and my sister Frances

Acknowledgements

First and foremost to acknowledge is my family. My loving father, mother, and sister have always been supportive of me, in whatever I have chosen to do, without any pressure to be successful, with attentive ears, and with lots of patience. Though my mother died in 1984, I am certain that she continues to watch over me and that she is here with me everyday – in me, in my thoughts, in my flesh and blood. She is in my sister and my father and all of the many people she touched in her life, in our collective memory. I wish she could be here to read this acknowledgment of her; somehow, I am sure she is looking at it, maybe through my eyes. My mother was a great counselor – I hope that I can live up to her standards for listening and facilitating. She had the great opportunity to direct a women's center for which I greatly admire her. I miss sitting with my mother on our green wooden porch swing, talking about my life. I have saved that swing and maybe I will sit on it with my children someday listening to them with the same care.

My mother and father stimulated in me an intellectual curiosity – a general wonderment about why and how things work, from art, science, music, and politics to house repair, crossword puzzles, bicycle riding and love. My mother had a great lust for literature and music, especially the opera. My mother started me on a lifetime love affair with words by doing crossword puzzles together with me. Both my parents had a passion for Broadway musicals and dancing which they passed on to me. My father's self-stimulated inventiveness and enthusiasm for design has been inspirational and his ingenuity continues to astonish me. Every time I see my Dad, he is so excited to tell me about some new ideas for wonderful inventions. I love working together with my Dad fixing things – we are a great team. I have very fond memories of tinkering with things with my Dad, especially our building of a simple electric motor from scratch. I assembled the motor but it didn't work. Combining wisdom, experience, and intuition with playing around, my father got the motor to work. That was a very happy and proud moment for me, for I was able to see at a young age how a creative mind works – my father's.

My parents instilled in me a great concern for the welfare and well-being of others and a strong instinct for being a helper. And, together they were always committed to bettering our world through their tireless commitment to ending wars, promotion of world peace, ending the nuclear arms race, promoting civil rights, improving opportunities for our youth, and many, many other good things too numerous to mention. My parents were different than most in this way, and I am so, so glad for that. I am sad that my father was not elected to Mayor of Westminster for I am sure he would have made a deep and lasting impression on our town for years to come. Because of my parents, I was fortunate to share experiences with a huge variety of people from all walks of life and participate in many unusual activities from protesting U.S. involvement in the Vietnam Conflict to campaigning for George McGovern to attending every cultural festival or fair imaginable.

My parents filled me with a sense of self-confidence and gave me the opportunity to develop myself as far as I could go in many areas. My father and sister have been a continual source of support for me while I finished this dissertation.

My sister Frannie is so sweet and beautiful and loving and encouraging to me. She is my confidant and maybe most importantly, a top-notch coach in my social life. Her pride in me has always been so evident and inspiring. We have been very close, sharing everything that I can imagine. Without

her, I would not have embarked on getting psychological counseling, which she was so courageous to do on her own. Without counseling, I probably would not have finished this dissertation. Her interest and talent in music, singing, and drama have always impressed me and helped stimulate my own interest in those things. Before I came to Cornell, Frannie and I toured western Europe. That trip renewed my lust for life and gave me a fresh mind-set to start school. I cannot imagine anyone better to have taken that trip with.

Frannie's husband Ben has been very encouraging to me in finishing my degree. I am glad to have Ben as my brother-in-law. He and my sister are wonderful parents to my sweet, charming, nephew and Godson Sammy who has brought me much pleasure and inspiration since his birth.

My father's dear friend Miriam Wallace has been so strongly supportive of my efforts to finish my Ph. D., never letting me say that I might quit. I am grateful to her for her lively and sophisticated conversation on an incredibly wide variety of topics, especially while I was home caring for my father after his heart bypass operation. She was a strong reassuring force during that difficult time in my degree program. She continues to be a wonderfully warm and spirited presence in my family.

I am thankful to Jan and David Cross for their friendship and kind, understanding way with me. Jan was one of my kindergarten teachers and has always been one of my biggest fans. I have always valued Dave's advice about academia and industry. They have both been unfailingly supportive of my going on to get my Ph. D.

Raj Sundra has been my constant ally in life. We have spent days on end training and traveling together for cross-country ski racing and now soccer. We have had the most fruitful training partnership that I can imagine, getting into the most refined, subtle aspects of sport. Raj introduced me to more rational, intellectual, methods of serious training. I have learned an immeasurable amount of knowledge from him on how to get better at anything. We have spent many hours discussing what to do in life, especially not following the beaten path. We have had a blast doing it all, too. Raj is one of the few people who laughs at my atrocious jokes and antics and I thank him for putting up with them and making me feel funny. At Cornell, he comes closest to understanding what I am about, why I am doing what I am doing, and what I may do next. Raj is very good at making me feel like a useful human being.

I am grateful to my Special Committee. Andy Ruina is one of the few Professors I have met who seemed to really love thinking about mechanics. He is the first one to make me realize that thinking about and doing science could be fun. It is truly a joy seeing Andy in action thinking about a problem, his eyes widening, then narrowing, then widening again with delight when he has a solution. His knack for elegant simple explanations for complicated phenomena is tremendous. Because of him, I think about science outside the office, not because I have to but because I want to. I have thoroughly enjoyed teaching dynamics with Andy – I started to learn the subject for the first time. Though others may dread Andy's editing process, I treasure his attention to detail and writing about science with great rigor and integrity. I have loved every collaborative writing project with him. I credit him with coming up with the most interesting dissertation topic that I could imagine. I have learned some of the coolest things from him in mechanics and life. He has often been especially sensitive to my needs and incredibly generous and helpful.

Tim Healey and I have had great discussions about some "cute" mechanics problems as well as squash and soccer and he has been generous with his time in answering questions from time to time and especially with loaning me his treasured books. Tim is an excitable, energetic thinker and his upbeat manner is contagious. I was very fortunate to have worked with him on an independent study project concerning symmetry, the principle of equivariance, and bifurcation in buckling of a two member truss. He has been especially supportive of me as a graduate student through some very difficult times in this department, always encouraging me to finish.

I remember the day Al Schatz joined my committee. He overheard me in our main office talking about my research. In his typically exuberant manner he came up and told me that the research sounded so, so interesting and "could I please be on your committee, I'll give you a minor in mathematics?" I was more than happy to oblige him and have his enthusiastic presence on my

committee.

Richard Rand and Steven Strogatz have been very helpful to me with their guidance and suggestions in my work, especially with regard to publications. In particular, Richard edited my paper on the 3D rimless wheel; Steve edited my paper on the Tinkertoy® walker as well as advised Andy Ruina and me in our dealings with *Physical Review Letters*, *The Guardian*, and *The Economist* and the press in general.

Many, many, graduate students have come and gone in my tenure here at Cornell, with varied degrees of impact on my life, more than I can possibly acknowledge here. I apologize to any who aren't mentioned and feel left out.

I greatly admire Pei-Yuen Chen, one of my first office mates, who was known as the "graduate student TA" helping us all out with our homework and research. Rudra Pratap had a huge impact on my first years at Cornell. Having been out of school for five years, I was greatly lacking in confidence. He and wife Kalpana were strongly encouraging to me to hang in there and finish. He was extremely helpful to me in preparing to pass my oral exams, giving me many private practice sessions. He is one of the best teachers I know and I learned so much about teaching from him just by watching him – so confident, buoyant, and inspirational in front of the class.

Guillermo Gabrielli, one of my closest, dearest friends shared many wonderful times with me in the old Bike Lab in Thurston Hall. Guillermo and I share the honor of taking eleven years to finish our Ph.D.'s which of course gives us a special, unique bond and understanding of each other. I was very fortunate to have in him a friend who shared many political and spiritual ideas.

Bhaskar Viswanadham was special for his broad well-read intellect and sophisticated Woody-Allen-esque sense of humor, his succinct descriptions of the intricacies and subtleties of life's absurdities. Bhaskar and I shared a keen and unusual understanding of our psychological foibles. We are alike in many ways, especially in our zeal for movies. Palling around the office with him and Yung-Chen Wang made avoiding work easy.

M'hamed Ibnabdeljalil, my cell mate from 237 Thurston Hall, and I were like college roommates – sharing the office with him was more like living in a dorm than working in a drab engineering building, with all our assorted sports equipment and artwork hanging from the walls. M'hamed and I shared many views of life, chief among the need to be diverse in our interests though we were primarily engineering graduate students. I greatly appreciate his support of my outside pursuits in athletics and the arts though they took time from studies and research. His Engineering Art Show was a great opportunity for me and others and I applaud him for arranging it. I can't imagine a better office mate. It was M'hamed's idea to apply for a Whitaker Foundation grant with Jeff Koechling, for which I am grateful. I was fortunate to get to know Irene Beyerlein through M'hamed. It was a pleasure to have her genteel, smiling, cheerful presence next door with her tuneful Southern accent and infectious, boisterous laugh.

Anindya Chatterjee is the most gifted graduate student I have worked with at Cornell. His facility and dexterity with mathematics and mechanics and his ability to communicate his ideas are truly enviably impressive. His nimble approaches to problem solving are a combination of child-like glee with the tenacity of a jungle cat closing in on its prey. I am glad he decided to work for Andy Ruina. His fingerprints are all over this thesis. From the first day I met him, he took a huge delight in my work and walking research. Sometimes, I am sure he is much more interested in my own work than I am. Anindya would often greet me by saying, " I was thinking. About your ..." and I knew we were off to some cool, and probably exhausting, analysis. He is entirely responsible for the conceptual ideas behind the asymptotic analysis in Chapter 4 of this dissertation and many of the ideas and conclusions presented there. Collaborating on that work was one of the best research experiences I've had. We worked so hard together late at night and into the early morning. His subtle, sophisticated sense of humor is priceless. His philosophical approach of life was often a soothing antidote to whatever was bothering me at a given moment.

My new office pal is lab-mate Mariano Garcia. He and I work together so compatibly, kind of the way I envision the ideal brother. It has been a great pleasure working with him on our presentations,

papers, and research, especially our computer simulations of walking. He was especially helpful to me in reducing the running time in my simulations. I think we are on our way to some great collaboration on three-dimensional passive-dynamic walking research and I can't wait to continue on it. Hopefully, now that the dissertation is done, I will be able to join Ano for more therapeutic mutual support lab lunches/crossword sessions and more biking in the spring. Ano has been a great source of support in getting this dissertation done. We have a lot of fun in the lab.

Mani Thothadri has become a great companion in the department. We have shared many late nights in the computer room having a really good time despite struggling to meet our deadlines and fussing with our advisor's and journal editors' demands. We have shared many meaningful discussions including various aspects of the human condition and Indian and American culture and politics. We have had many great squash matches together and played together and against each other in a lot of fun soccer games. He is a great running partner and I hope soon-to-be biking and weight-training partner. Along with Raj, we have become a dazzling well-known trio in College Town. Mani has been very helpful to me in my research too. We have had some nice discussions about the stability of rolling disks in Chapter 3 of this dissertation and I will need his insights again when I write a paper on that chapter in the near future. He was especially helpful to me in implementing the Henon method to detect collisions in my numerical simulations.

Other graduate students who have helped me in some way or made my stay more pleasurable along the way are Kasey Moulton, Jeff Cipolla, Sunil Gulrajani, Howard Susskind, Vicki Francisco, WenJing Ye, Qing Zhang, Brian Feeney, Sue Campbell, Chris Hall, Mark Thurston, Yung-Chen Wang, Anna Vainchten, Dave Shia, Wei Zhou, Xiao Fei, Fan Xi, Ken Bhalla, John Camp, Chioko Takahashi, and Larry Gosse. I am particularly thankful to my bicycle racing training partners Doug Johnson, Ron Ziemian, and Janet Christiansen.

I would like to thank all of the undergraduate students I have come to know well through my teaching and advising. In particular, I was fortunate to advise Saptarsi Haldar for one summer, to help me with modeling and simulation in my research, Jacqui Rodrick, and Ai-ping Hu.

I wish to express my gratitude to Les Schaffer and Jim Papadopoulos for their support and enthusiasm for my research.

I am thankful to the office staff for their help over the years including: Nikki Lumbard, Tammy Martin, Karla Johnson, Maureen Letteer, and Joan Heffernan. Joan was especially helpful in keeping after me and my paperwork. I am grateful to the department staff: Peter Brown has always been supportive of me, somehow managing to find me funding at the last minute; and Jason Cortell was extremely helpful over the years in the teaching laboratories.

Dr. Anna Matusiewicz, my psychiatrist at Gannet, and Carolyn Kenyon, my psychiatric social worker, have helped me immeasurably at Cornell with their kind care and treatment. I recommend them highly to anyone.

I am thankful to the entire bicycle and x-c ski racing community in Ithaca, Binghamton, and Oneonta, since I have been here, especially Deb Wilcox, Gill Sharpe, Audrey Balander, Dennis Higgins, Dave Rosher, Mike Tacci, Bob Bowen, Jim Danvers, Steve Edgar, Ernie Bayles, Bruce Barkely, Glenn Swan, Mitch Collinsworth, Eric Torniainen, Andy Pearce, the Cornell Cycling Team, and the Cornell X-C ski racing team. Deb Wilcox, Dennis Higgins, and Dave Rosher have been especially good friends and supporters. Glenn Swan was responsible for coaching me in some of the finer aspects of bicycle racing and some key aspects of ski skating, epsecially with regards to the pendular aspects of balance on one ski, feeling the base and edges of the ski, and arm thrust – and the need to be graceful and dancelike. I am grateful to the support from the management at Wildware Outdoor Store, especially Laurie, and to Kevin Brew Associates for their support of the Wildware/Fischer Ski Team.

I treasure the time I have spent with Beth Saulnier since I have met her. She is wonderfully literate, bright, funny, talented and articulate. I have enjoyed our dinners, bike rides, talks about our lives, and playing on a real piano at her house. I am very appreciative of the article she wrote about our research lab in the Cornell Engineering magazine.

Last, but not least, I am so thankful for Tomomi Ueda who arrived in my life this past fall. She has brought much joy and fun over the last semester. She is so talented in many different areas, so thoughtful and caring about others feelings and needs. We share so many interests in art, music, engineering, teaching, and now procrastinating together with crossword puzzles and crypto-quotes. She has been a wonderful listener. Happily for me, she re-introduced me to the live theater this year as well as to the joys and benefits of cooking for myself. I am grateful to her for introducing me to the joy of bouldering. It was a great experience working with her at the climbing wall figuring out various climbing routes and learning technique from her. I look forward to her helping me swim better. It was wonderful taking her out for her first time on cross-country skis. Perhaps most importantly, she has been very supportive of me in finishing up this dissertation, especially in the last weeks, offering her solacing words daily by e-mail from her home in Tennessee. She enriches my life. The Monkey and the Black Cat – what a pair.

Contents

List of Tables

List of Figures

Chapter 1

Introduction

Walking on a horizontal surface is usually easy, hardly fatiguing and sometimes pleasant.
G. A. Borelli, *On the Movement of Animals, 1681*

Various creatures — birds, mammals, reptiles — walk on two legs. How is it that the nervous, muscular, and structural systems of these organisms interact with forces from the environment (e. g., gravity and friction) to synthesize two-legged locomotion? Though walking seems a mundane and nearly unconscious process and has been much studied, it is nevertheless still poorly understood.

Human walking is generated, sustained, and guided by the neuro-muscular system. On one hand, then, a legitimate and oft pursued approach to understanding muscle-powered walking is to study powered and controlled mechanical models of walking. But, how much of walking is controlled by the nervous and muscular systems and how much of the coordination of two-legged locomotion is purely mechanical? Human locomotion might be studied as a mostly passive mechanical process; that is, it may be viewed as requiring little control from the brain and nervous system and only small amounts of actuation from the muscles.

Even before Newton spilled ink on his laws of mechanics, some scientists sought to understand walking as a substantially mechanical process obeying the laws of nature. Paul Maquet [5], translator of the current edition of *De Motu Animalium* (On the Movement of Animals) , the main work of Giovanni Alfonso Borelli (1608 – 1679), writes in the translator's preface:

> "Borelli is a mechanist. ...
> In all his work [on walking] Borelli relies on an axiom which he does not question: Nature always acts using the simplest and most economical means. The differences which are observed are due to mechanical necessities. Conversely, when Nature carries out an operation, it must be concluded that this operation is the simplest possible, that it is carried out according to the laws of mechanics and that it is impossible to do otherwise or better. Such was also the opinion of Descartes." [5]

Unfortunately, having preceded Newton's discovery of the classical laws of mechanics, Borelli apparently subscribed to some unusual notions about forces as can be seen in one of his propositions, as stated in the translation:

> " *Proposition XXXII*
> If a weightless rigid rod is compressed from above by a weight or by any force and rests inferiorly on the hard ground, the force with which the rod resists compression is twice the compressive force." [5]

This proposition seems to say that the resisting force is equal to twice the acting force!

In the more recent past, however, a class of purely mechanical theoretical and physical models of walking obeying Newton's Laws of Mechanics, have been studied and constructed. These can walk down a shallow slope with *no* control system and *no* power source, driven only by gravity. Tad Mcgeer [4], who pioneered the study of these fascinating devices, calls this unpowered uncontrolled behavior *passive dynamic walking* and he considers the mechanisms that exhibit it to be useful models for the study of human locomotion. McGeer's outstanding fundamental study in this area is the motivating force behind this research which is an extension of his work. It is important and in need of further development. Unlike Borelli, however, we will be assuming that the mechanisms we study obey the 'state-of-the-art' mechanics principles — the action is equal and opposite to reaction, and so on.

1.1 Motivation

Mcgeer [4] thought that, in the same way that the aviation pioneers learned about aerodynamics from gliders, we can perhaps learn about the stability and control of walking by studying unpowered, uncontrolled models. The Wright brothers only added power to their plane after they had studied and mastered unpowered glider flight. McGeer's central question might be stated as:

> Can a *statically unstable* assemblage of rigid bodies powered only by gravity down a shallow slope with no active control exhibit *dynamically stable* periodic motion resembling human gait?

McGeer successfully analyzed and constructed two-dimensional, two and four link passive dynamic walking models that displayed very graceful, stable, human-like walking on a range of shallow slopes with *no* actuation and *no* control. Quite unlike control based models of walking, where a controller tries to force a system to follow a prescribed trajectory, McGeer's models exhibit gait cycles that are a result of the natural interaction between the systems (with a given set of parameters) and their environment (gravity forces, friction, and collisions).

An instructive model that we have studied is the 2D point-foot walker shown in Figure 1.1. It is a special case of the more general 2D straight-legged walkers analyzed by McGeer [4] . A typical passive walking step is shown in Figure 1.2 for the 2D point-foot model. This device can exhibit stability in the sagittal plane. That is, it neither falls forward nor backward, and it has a stable walking speed to which it returns following a disturbance. The stability is somehow a result of the intermittent contact between the feet and the ground. When one foot is on the ground, the system is, in part approximately, an unstable inverted pendulum. However, the other leg swings forward, colliding with the ground and, given initial conditions and slope angle in the proper regime, catches the system before it has a chance to fall down.

Unfortunately, all previously known passive walking models have no such stability in the lateral plane. They are all two-dimensional or unstable in three dimensions. Evidence for passive stability of various three-dimensional systems exists, supporting our conjectures regarding the existence of gait stability in three dimensions. A linearized stability analysis shows that a disk (a coin or a phonograph record, for example) rolling on a flat surface is neutrally stable with respect to small lateral disturbances [6]. Given sufficient rolling speed, the disk will wobble indefinitely in response to a small initial disturbance. This wobbling response is due to gyroscopic coupling of the various degrees of freedom. An equilateral polygon with many sides rolling down small slopes exhibits behavior similar to that of the rolling disk [7] (in the limit as the number of sides gets large and the slope approaches zero, the polygon's behavior approaches that of a circular disk on flat ground). A bicycle, unstable while standing still, can be stable when moving depending on its geometry and mass distribution [8]. Off diagonal terms in the inertia tensor induce kinematic coupling that keeps the bicycle from falling over as long as it is rolling forward with sufficient speed. A rigid rider on a skate-board is stabilized by coupling between the riders lean and the angle of the wheels[9]. These examples provide insight into finding methods for stabilizing walking mechanisms.

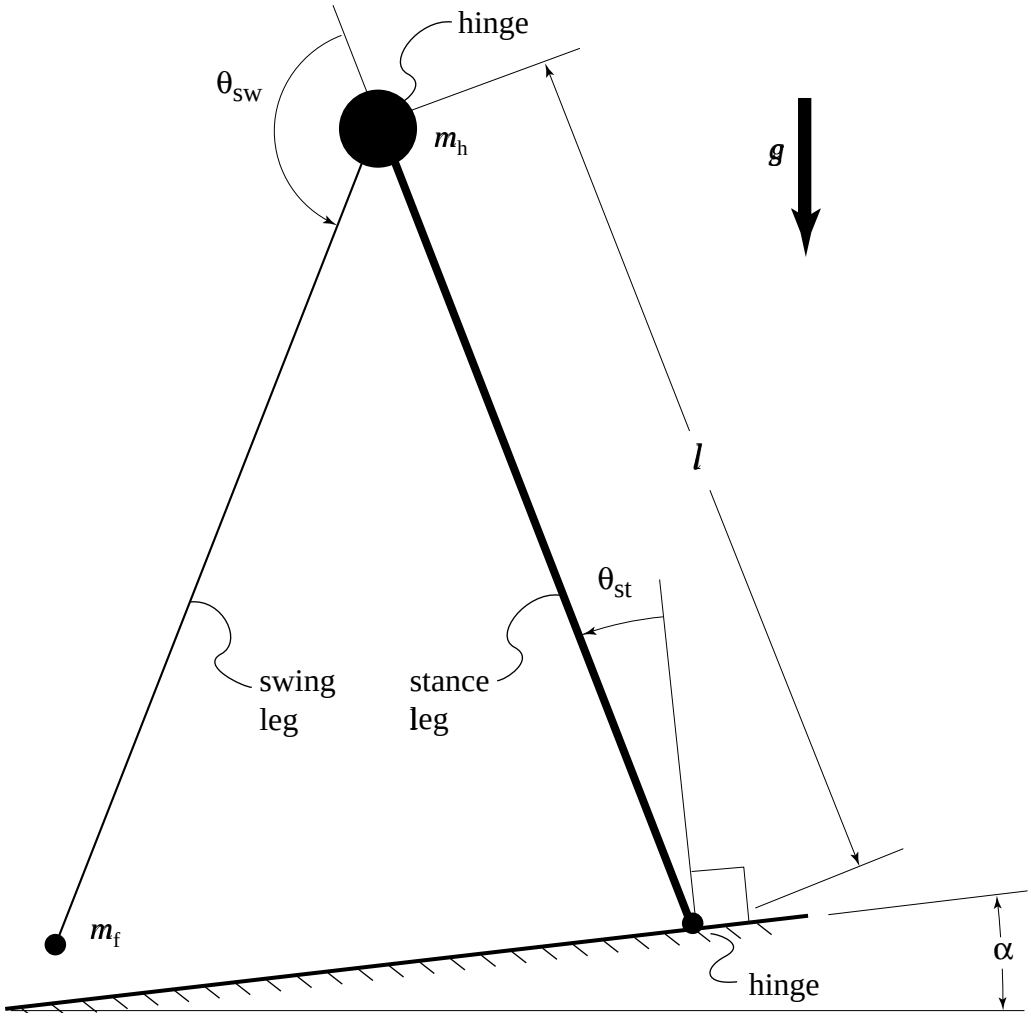

Figure 1.1: The point-foot walking model. Leg lines are drawn with different line weights to correspond to the plot of Figure 1.3. The angle θ_{st} measures the rotation of the *stance leg* with respect to the normal to the slope. The angle θ_{sw} is the rotation of the *swing leg* relative to the stance leg. The hip mass is denoted by m_h, and the foot mass by m_f. The leg length is denoted by ℓ, the slope angle, by α, and the acceleration due to gravity, by g.

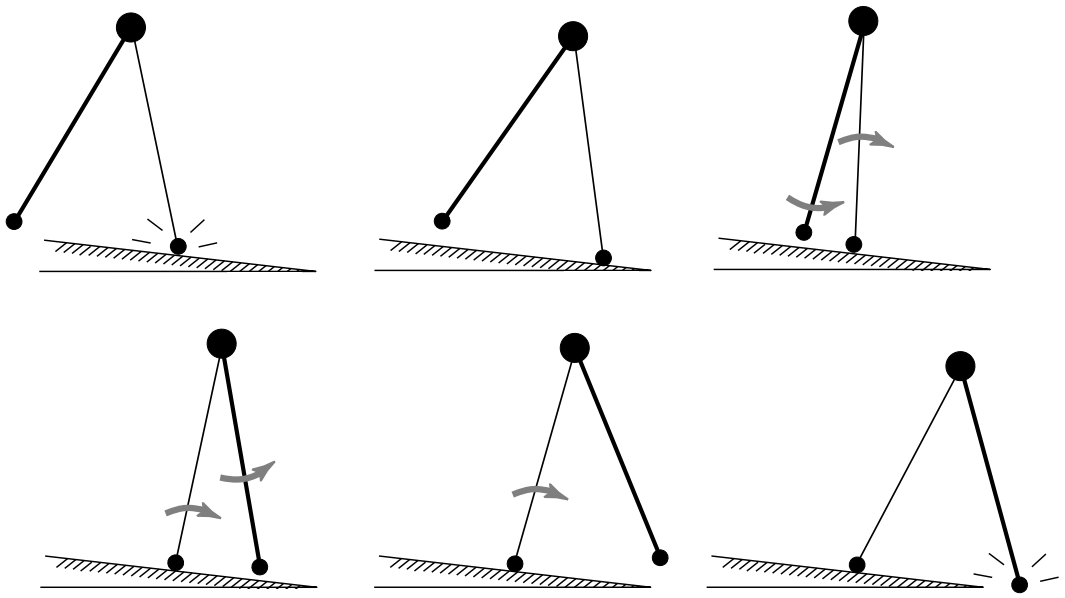

Figure 1.2: A typical passive walking step for the 2D point-foot model.

McGeer began studies of three-dimensional passive walking mechanism finding only unstable periodic motions. Kuo [10] also studied a passive-dynamic 3D model of walking like McGeer's but focussed instead on stabilizing unstable passive steady gaits using simple feedback control laws that govern foot and torso placement. Besides wobbling toys with low mass-centers and broad feet (McGeer [11], Mochon and McMahon [12, 13]), passive-dynamic walking machines that are statically unstable but dynamically stable in three dimensions have not yet been discovered in theory or simulation. Only recently, we have completed experimental studies of a statically unstable walking toy that has apparently stable 3D motions. We report on the device in Chapter 6 (also see Coleman and Ruina [14] and [15]). This thesis extends McGeer's work searching for stable three-dimensional passive-dynamic models of human walking.

McGeer's results with passive dynamic models of human locomotion suggest that human body parameters such as mass distribution or limb lengths may have more influence on the existence and quality of gait than is generally recognized. For instance, inappropriate mass distribution may interfere with the passive stability of gait thereby requiring the neuro-muscular system to expend unnecessary effort to maintain stability. Given a more complete understanding of how mass distribution affects three-dimensional gait stability, we may be able to guide gait clinicians and engineers in devising surgical procedures and prostheses better 'tuned' for a particular individual.

1.2 Objectives

Existing mechanical models for human walking generally treat gait as a planar activity. Recent studies using these models have established the existence of steady, stable walking motions that occur without motor activation or control. These passively generated motions have been termed *stable passive-dynamic Gait cycles.* A passive gait cycle (from Garcia, Chatterjee, Ruina) [16] for the 2D point-foot walker of Figures 1.1 and 1.2 is shown in Figure 1.3. While locomotion occurs almost exclusively in the sagittal plane, the stability of out-of-plane motions is an important issue that has barely been studied. We would like to extend existing planar models to allow out-of-plane motions and search for stable passive gait cycles in these three-dimensional models.

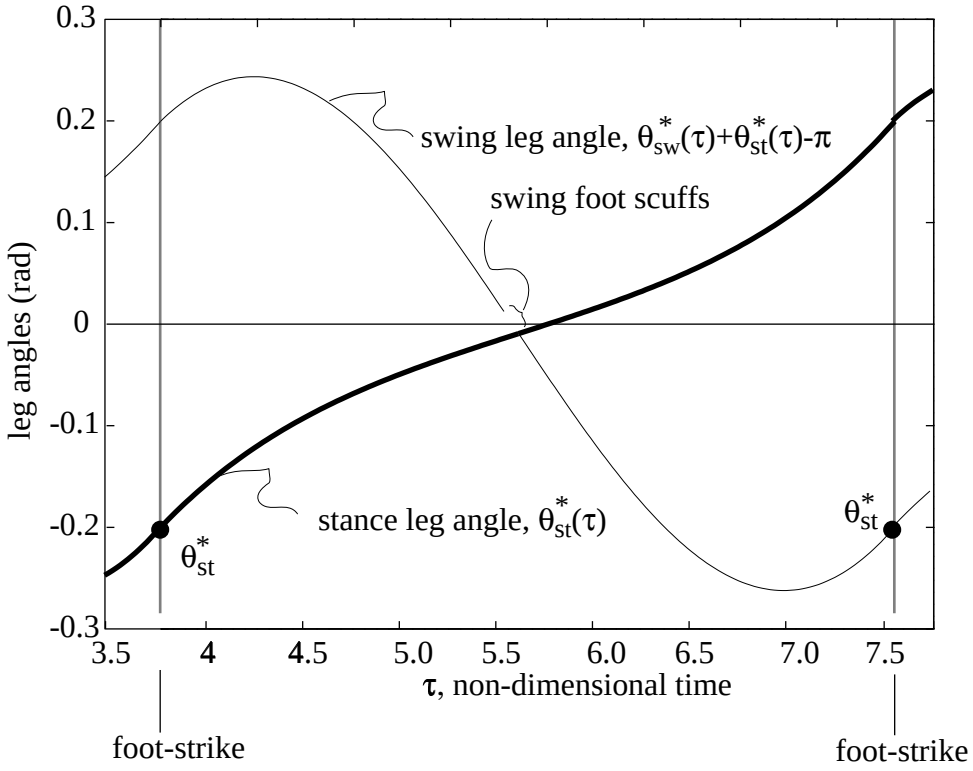

Figure 1.3: The point-foot walker leg angles over one step in a gait cycle. In a gait cycle, heel-strike returns the system to its initial conditions. The line weights correspond to those of Figure 1.1. The asterisks in the superscripts indicate fixed points and the corresponding leg angle trajectories.

1.3 Review of Literature

Here, we give a brief review of work relevant to passive and active gait generation and stability.

1.3.1 What is Walking in a Nutshell?

Human walking is the cyclic movement of the legs to translate the body forward. One-half cycle of gait begins with the pendulum like motion of the 'swing' leg from maximum backward extension to maximum forward extension while the body is supported and balanced on the 'stance' leg. This is followed by the heel strike of the swing leg, a short period of double support, and toe-off of the stance leg to begin the next half-cycle. The cycle involves a complex interaction of a system of flexible linkages, muscular activity, contact with the ground, and neurological control. A comprehensive review of terminology, kinematics, physiological measures, and balance and posture in normal and pathological gait is given by Winter[17, 1].

Disruption of the natural gait cycle can result from disease, aging, or traumatic injury. To restore or partially restore function often requires rehabilitation, corrective surgery, or various devices, braces, or prostheses that must be properly fitted and controlled to be effective.

Understanding how normal and abnormal gait is generated and maintained is important for developing effective design solutions for restoring lost function. Most engineering models for understanding gait stability treat the static human body as a system of linkages. The question commonly addressed is how the body synthesizes stable locomotion.

1.3.2 Actuated and Controlled Gait

Most gait models assume that the natural flow of events in generating stable motion proceeds outward from the nervous system to the musculoskeletal system with sensory feedback to the nervous system.

Zajac and Winters[18] give a comprehensive overview of synthesizing a musculoskeletal dynamical model including body and joint segment kinematics, equations of motion, passive-tissue joint mechanics, geometric joint transformation, musculotendon force generation processes, and neuromotor circuitry of the central nervous system (they do not discuss a specific human gait model). With numerical models, Yamaguchi[19] and Yamaguchi and Zajac [20, 21] studied the feasibility of using functional neuromotor stimulation(FNS) to restore normal function to paraplegics. Using dynamic programming control, they obtained nearly normal gait characteristics (for the single support phase only) using a three-dimensional eight degree-of-freedom model with simplified musculature, low force levels, and minimal control of muscle activation[19]. Hausdorff and Durfee[22], Anderson *et al.* [23], and Kobetic *et al.*[24] have investigated the feasibility of FNS experimentally. Using a knee-jointed model confined to the sagittal plane, Taga, *et al.* [25] achieved stable locomotion (for entire gait cycles, from step to step including foot and joint collisions) as a global limit cycle generated by a global entrainment between the rhythmic activities of a nervous system composed of coupled neural oscillators and the rhythmic movements of a musculo-skeletal system. Pandy and Berme[26, 27] developed two and three dimensional models of the single-support phase of gait including six degrees of freedom, passive tissue elements, applied joint moments, and open-loop control. They predicted joint angles and reaction forces similar to those in normal and abnormal human human gait over one step, between foot collisions.

Some of the approaches involve optimization strategies to yield a particular gait pattern such as minimizing some estimate of energy cost (Becket and Chang [28]), peak muscle force, jerk, ligament or bone stress, etc., as reviewed by Collins [29] and also discussed by Nelson [30].

One of the biggest deficiencies of many models is that they often do not involve a complete walking step (Pandy and Berme [26, 27], Yamaguchi and Zajac [21]). In order to more fruitfully study gait, especially gait stability, we believe that models should include the entire gait cycle. Besides our

work and McGeer's work, other research supports this opinion (Taga, *et al.* [25], Hurmuzlu and Moskowitz [31, 32]).

Various means of active control have been implemented to generate locomotion patterns in bipedal walking mechanisms designed to mimic human walking. Walkers built by Mita *et al.* [33], Yamada *et al.* [34], Takanishi *et al.*[35], Lee and Liao[36], and Zheng *et al.*[37] generate gait using feedback control while the bipeds of Miura and Shimoyama[38] generate motion using feedforward control.

Active control also appears in prosthetic design. Phillips *et al.* [39], Phillips[40], and Durfee and Hausdorff[41] have done experiments to test the feasibility of integrating FNS with prostheses for above-the-knee amputees and orthoses for restoring normal gait to paraplegics.

One can also approach the problems of gait generation and stability in a way that deemphasizes the role of the neural control system. Can stability be achieved solely through the passive interaction of gravity, inertia of the body, and contact with the ground rather than by active neuromuscular control?

1.3.3 Passive Dynamic Locomotion: Some Evidence and Research

Data from studies of human biomechanics and of controlled walking mechanisms hint at the possibility that models of walking which use no motor activation or control are plausible. Electromyographic (EMG) recordings show lower levels of muscular activity in human legs during ordinary walking than other voluntary movements[42]. Muscles of the swing leg are nearly inactive during the whole swing period, except for peaks at the beginning and end[42, 1]. An EMG profile for the soleus muscle, for example, is shown in Figure 1.4. Data is displayed for one stride period: from heel contact (HC) of one foot to HC of the same foot, expressed as 0 to 100% in the profile. The stance period is from 0 to 60% of the stride period, where toe-off (TO) occurs, and the swing period is from 60 to 100%. The profile shows that the muscle is nearly inactive in the swing phase and that most of the activity occurs between 40 to 60% during the explosive push-off (PO) phase [1].

Mochon and McMahon[13] used a coupled-pendulum model, confined to the sagittal plane, to demonstrate that, with proper initial conditions, a passive mechanical walking system could produce swing times, joint angles, and reaction forces similar to those in normal gait (during the swing phase).

McGeer's[43, 44, 4] magnificent work with two-dimensional passive gait models and walking mechanisms proceeded with an evolution of models of increasing complexity coupled with appropriate empirical studies to validate his hypotheses. This evolution is illustrated in a schematic diagram in Figure 1.5. With mathematical gait models and using linearized stability analysis, McGeer was able to find stable limit cycle motions confined to the sagittal plane. McGeer also built several physical models, with and without knees, that exhibited stable passive dynamic walking in two dimensions. Driven only by gravity down a shallow slope, McGeer's walking mechanisms approach a steady gait similar to human walking, without any active control or actuated energy input. McGeer[4] also began to develop a three-dimensional mathematical model but only found unstable passive gait cycles.

More recently, our lab (Garcia, *et. al.*, [16]) and Goswami *et. al.*, [45] have also studied extensively 2D straight-legged point-foot passive-dynamic models of human walking finding stable period-1 gaits as well as stable higher period 'limping' and 'stumbling' gaits. In addition, Garcia and Ruina [2] have duplicated McGeer's [44, 4] 2D kneed walking work including the analytical model and building and demonstrating a copy of McGeer's kneed walking machine and extended his analysis.

1.4 Classification of Dynamical Systems

Here, we categorize the stability models we study, compare and contrast their stability characteristics with other dynamical systems, and, where possible, determine their general characteristics. An

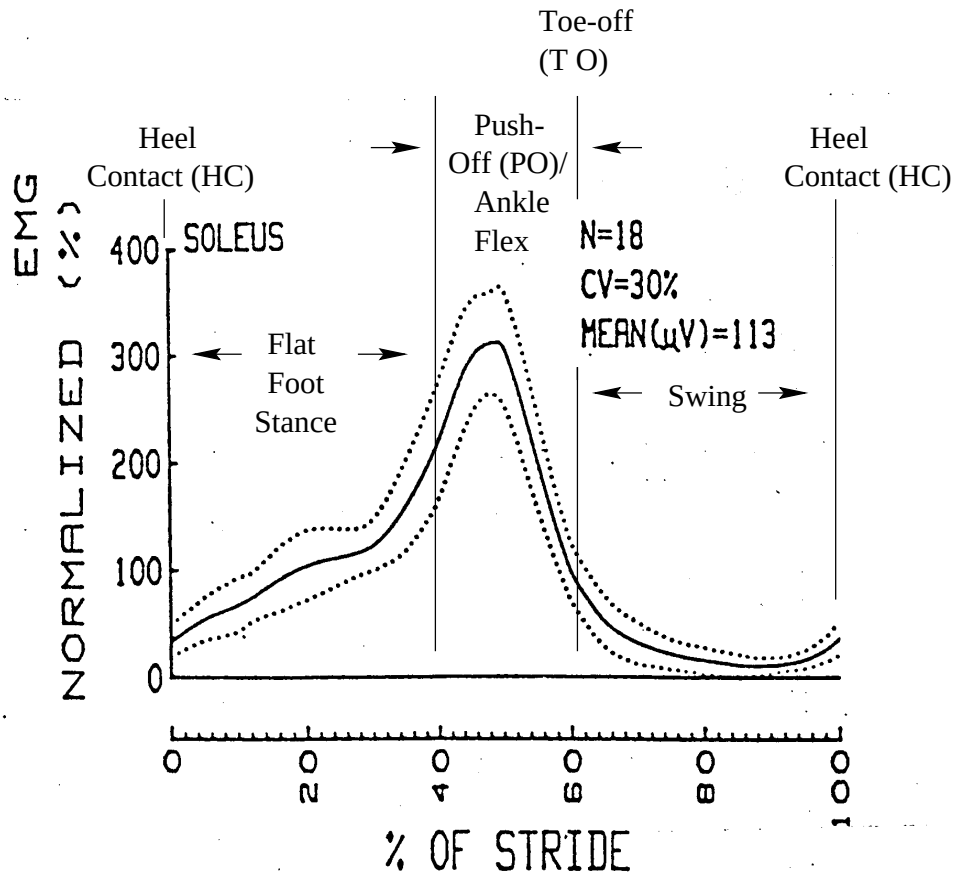

Figure 1.4: A normalized EMG profile of the soleus muscle during one stride period (Reprinted from Winter [1]). N is the number of data sampling intervals over the stride period and the coefficient of variation (CV) is a measure of the mean variability across many repeat trials over the stride period. Each subject's mean EMG was normalized to 100% before averaging.

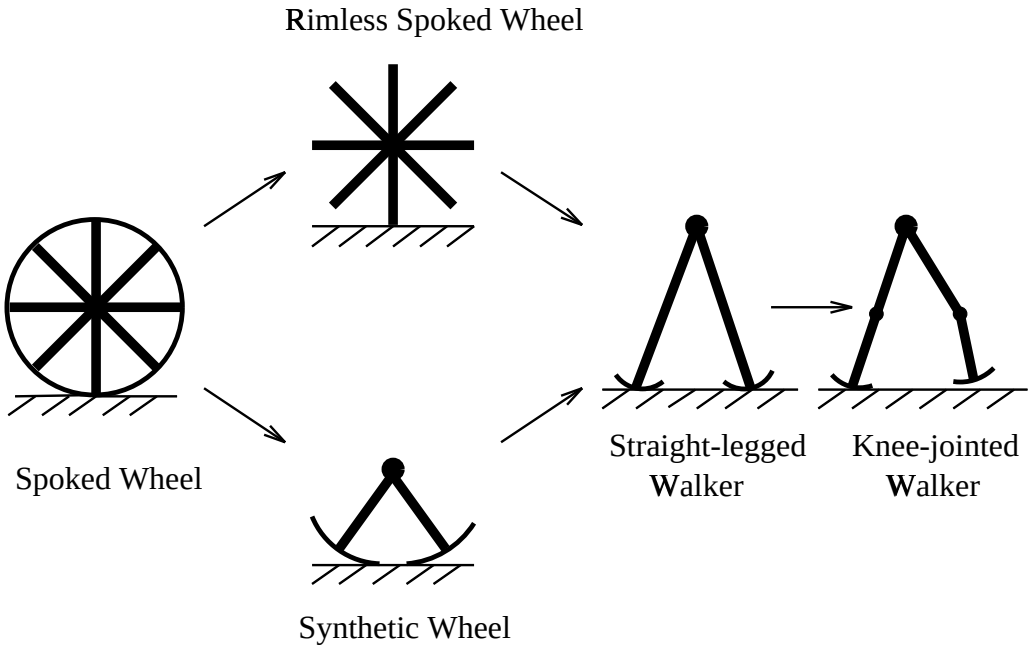

Figure 1.5: Taxonomy of McGeer's Evolution of Passive Dynamic Mechanisms

excellent reference on the dynamics of nonholonomic systems is the book by Neimark and Fufaev [46]. An excellent, if somewhat dated, reference on classifications of systems is by Ziegler [47]

First, we will briefly review the definitions of terms that we will use to characterize our walking systems.

A *geometric or configuration constraint* restricts the geometric position of individual parts of a system. A *rate or velocity constraint* restricts the velocities of the individual parts. Geometric constraints must give rise to a specific constraint on velocities. The converse need not be true, however: a velocity constraint need not lead to specific restrictions on the *possible* positions of the parts of a system. Kinematic constraints are integrable if the differential equations that represent them are integrable with respect to time. If a kinematic constraint is integrable, it is is called *holonomic*; if it is not, it is termed *nonholonomic*. Below, we will give alternative and equally valid definitions of nonholonomic systems.

Equivalently, we can define nonholonomic systems as those where:

1. velocity constraints are non-integrable (cannot be reduced to geometric constraints) or

2. the number of generalized coordinates is greater than the instantaneous degrees of freedom by the number of non-integrable kinematic constraints (the dimension of the configuration space is greater than the number of degrees of freedom) [46] or

3. the number of generalized coordinates is greater than the number of velocity constraints by the number of non-integrable kinematic constraints (the dimension of the configuration space is greater than the dimension of the instantaneously accessible velocity space).

An example of a nonholonomic system is a disk free to roll without slip on a plane. The position of the disk is described by five generalized coordinates: two to mark the position of the contact point of the disk on the plane and three independent orientation coordinates. The no-slip constraint gives rise to two non-integrable velocity constraints.

Though these two kinematic constraints must be satisfied at all times, the five coordinates can take all sets of values on the plane; i.e., the kinematic constraints do not impose any restrictions on the possible configurations. In other words, even though the coordinates that determine the position of the disk relative to the plane must always satisfy two conditions, meeting the conditions does not specify its position; while satisfying the kinematic constraints, the disk can be brought from one position to any other position by a variety of moves.

Equivalently, the system is nonholonomic because the number of generalized coordinates exceeds the dimension of the velocity space by two ($5 > 3$). Only three rates are necessary to specify the velocity of the disk at any time.

Conservative and Non-conservative Systems

A *conservative* system is characterized by work-less constraints and conservative forces (those that are derivable from a potential). In conservative systems, potential energy plus kinetic energy is a constant. In a *nonconservative system*, the time rate of change of the sum of potential plus kinetic energy is less than zero; the sum is not a constant. Systems with friction, inelastic collisions, or inelastic deformations are nonconservative.

Equilibrium States, Steady Motions, and Stability

Equilibrium states of a system are those where its position does not change in time (its velocities are zero). An equilibrium state may also be one where the system has the same position and velocities at regular temporal or spatial intervals, such as steady or periodic motions.

An equilibrium state is said to be *stable* if, when subjected to arbitrarily small perturbations, the resulting motion of the system over time or at regular spatial or temporal intervals remains in a small neighborhood whose extent depends on the size of the initial perturbation. If, in addition, small perturbations to the equilibrium state decay to zero over time or over regular intervals, then the equilibrium state is said to be *asymptotically stable*.

According to Neimark and Fufaev [46], equilibrium states of a nonholonomic system cannot be *isolated* but instead form a surface or *manifold* whose dimension is equal to the number of nonholonomic constraints; the manifold is parameterized by a subset of the state variables whose dimension is equal to the number of nonholonomic constraints. Thus, one may think of the remaining state variables as functions of this parameter subset.

Since isolated equilibrium states do not exist, we can only talk about the stability of the manifold of equilibria. The linearized equations of motion in the neighborhood of a certain point of the manifold of equilibrium states enables one to study the stability of a system in a small neighborhood of the surface. If in some region of the manifold of equilibria states, small deviations from the surface decay over time, then that region of the manifold is asymptotically stable in the following sense. If one disturbs a system from one of the states in this asymptotically stable region of the manifold, then the disturbances will decay over in time and the system will return to an equilibrium state on the manifold that is nearby to but not in general the original equilibrium state.

Steady motions of holonomic and nonholonomic systems may also form manifolds of various dimensions in the phase space and configuration space. Stability of such steady motions may be studied in the same way as for the manifolds of equilibrium states.

It is well known that manifolds of equilibrium states or steady motions of conservative holonomic (Hamiltonian) systems cannot be asymptotically stable. On the other hand, not as well known is that conservative *non*holonomic systems can have asymptotically (exponentially) stable steady motions in some variables while at most mild instability in the others, as recalled in Zenkov, *et al.* [48].

Summary Table of System Stability Behavior

In the table in Figure 1.6, we classify systems as conservative (or non-dissipative) or nonconservative with holonomic, nonholonomic, or piece-wise holonomic constraints. In each case, we list the stability characteristics and, if possible, give the simplest example(s) we know about.

Our models are nonlinear, piecewise conservative and holonomic yet globally nonconservative and possibly globally nonholonomic dynamical systems. For instance, the point-foot, straight-legged walker constrained to two-dimensional motions is simply a double pendulum without dissipation between collisions; it is holonomic between collisions since there are no kinematic constraints on the stance and swing leg rates, only geometric constraints on the position of points of the system relative to each other. The overall motions of the system are dissipative due to the inelastic foot collisions. Globally the system can be said to be nonholonomic in the following sense: describing the position of the walker requires three generalized coordinates but at any instant in time the dimension of the accessible generalized velocity space is only two.

As suggested by the simple example of a discrete Chaplygin sleigh, a rigid body moving on a plane constrained by a single skate, in Ruina [49], this discrete nonholonomicity may account for exponential stability of some systems. Ruina [49] shows that, for the discrete model of the sleigh, its stability eigenvalues approach those of the smooth analog system in the limit as the dissipation due to collisions goes to zero. The walking models we study are all nonholonomic in this intermittent sense (and also in the conventional sense if they have rounded feet). They can, for example, translate forwards by walking although the contact constraint does not allow forward sliding.

General understanding of the stability of such intermittent systems is lacking. Two questions this thesis only indirectly addresses are: (1) Does stability of passive motion depend on dissipation (say, due to inelastic foot and joint collisions)? and (2) Does nonholonomicity enhance stability of passive motion?

	Constraints		
	Holonomic *Integrable kinematic constraints(# of degrees of freedom equal to dimension of the configuration space);	**Nonholonomic** * Non-integrable kinematic constraints (dimension of the instantaneously accesible velocity space less than the dimension of the configuration space)	**Piecewise holonomic**
Conservative * Workless constraints; * Conservative forces; * Potential + Kinetic Energy = constant;	* Hamiltonian; * Cannot be asymptotically stable; * Simple example(s): simple pendulum, spring-mass.	* Non-Hamiltonian; * Can be asymptotically stable; * Simple example(s): bike, skateboard, arrow w/ feathers, skate, rolling coin (not well known).	* Piecewise Hamiltonian * Stability? * Simple example(s): piecewise skate?
Non-conservative * d/dt(Pot. + Kin.) ≤0; * Friction; * Inelastic collisions; * Inelastic deformation;	* Can be asymptotically stable; * Simple example(s): Damped oscillators.	* Can be asymptotically stable (though damping is not always stabilizing); * Simple example(s): Damped coin.	* Can be asymptotically stable (even when statically unstable); * Example(s): 2D, 3D rimless wheel, McGeer's 2D walking machines, Tinkertoy Walker

Figure 1.6: Classification of dynamical systems by type of constraints and by the whether the system is conservative or not. Stability characteristics and examples are given in each case if possible.

1.5 Research Program

Following McGeer, this dissertation follows a an evolution of models of increasing complexity (see Figure 1.5.) In most cases, the bulk of our modeling approaches and analysis procedures are similar in style to that used by McGeer for his successful two-dimensional and unsuccessful three-dimensional walking analyses.

1.5.1 Evolution of Models

A brief summary of McGeer's models are summarized here.

1. McGeer began with a study of a 2D rimless spoked wheel. The rimless wheel mimics the foot collisions and inverted pendulum behavior of walking but not the oscillations of the leg. The main feature of the 2D rimless wheel is that dissipation from the inelastic spoke collisions regulates its speed. In simple mechanical terms, the gravitational energy available per step is speed-independent for a given slope whereas the kinetic energy lost per collision increases with speed (proportional to speed squared). The balance of the energy loss and gain per step determines the steady-state speed. A one-dimensional map can be used to characterize the motion of the 2D rimless wheel from one step to the next and determine the stability of periodic motions (motions in which the state variables are the same after each step). Using the linearized equations of motion for the rimless wheel (small slopes angles and large number of spokes), McGeer constructed an iterative map for the state of the wheel from collision to collision, and showed that asymptotically stable limit cycle motions of the wheel exist.

2. The next model McGeer studied (which we have not) is the 2D synthetic wheel, two straight legs pinned at the hip with curved feet having a radius equal to the leg length. Whether a foot slides freely or rolls is determined by a ratchet-like foot contact condition. The synthetic wheel simulates leg oscillations and inverted pendulum behavior but not foot collisions.

3. McGeer's next model was the 2D two-degree-freedom straight legged walker, with foot radius less than the leg length.

4. Next, McGeer investigated a 2D, four link knee-jointed walker (Figure 1.7) which avoids the foot scuffing problems in the previous walkers. A passive gait cycle for McGeer's 2D kneed walker is shown in Figure 1.8.

5. Finally, McGeer [4] analyzed a two-legged straight-legged walker with curved feet and hip-spacing that was free to move in three dimensions but only found unstable limit cycles.

Our evolution of models and how it fits in with McGeer's is shown in Figure 1.9. Our analysis also proceeds with a rimless spoked wheel, constrained to move in two dimensions (in a vertical plane) down a shallow slope. Our 2D analysis, however, only adds a slight depth to McGeer's results.

We start our study of three-dimensional systems by studying the motions and stability of rolling disks. To investigate our ideas of the how mass distribution affects stability of steady 3D motions, we add rigid bodies which turn and bank with a disk but do not roll with it, thereby adding new couplings between gyroscopic terms.

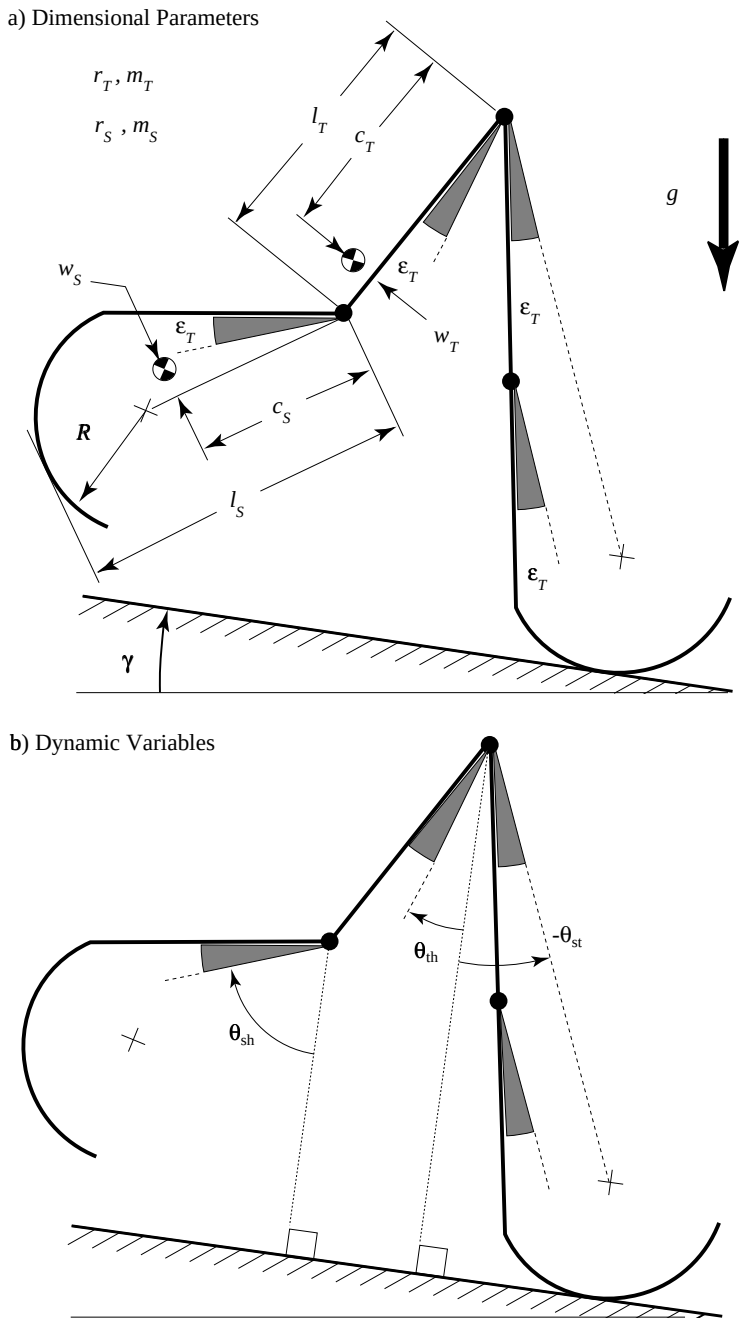

Figure 1.7: Our realization of McGeer's knee-jointed walking model. Shown are the (a) model parameters and (b) dynamic variables (from [2]). Radii of gyration and masses of thigh and shank are denoted by r_t, m_t, r_s, and m_s, respectively. The foot is a circular arc centered at the '+'. The angle between the stance thigh and the line connecting the hip to the foot center is defined to be ϵ_T. The dynamic variables θ_{st}, θ_{th}, and θ_{sh} are measured from a line, normal to the slope, to lines offset by ϵ_T from their respective segments. A stop (not shown) at each knee prevents hyper-extension of either knee. (Drawings courtesy Mariano Garcia [3])

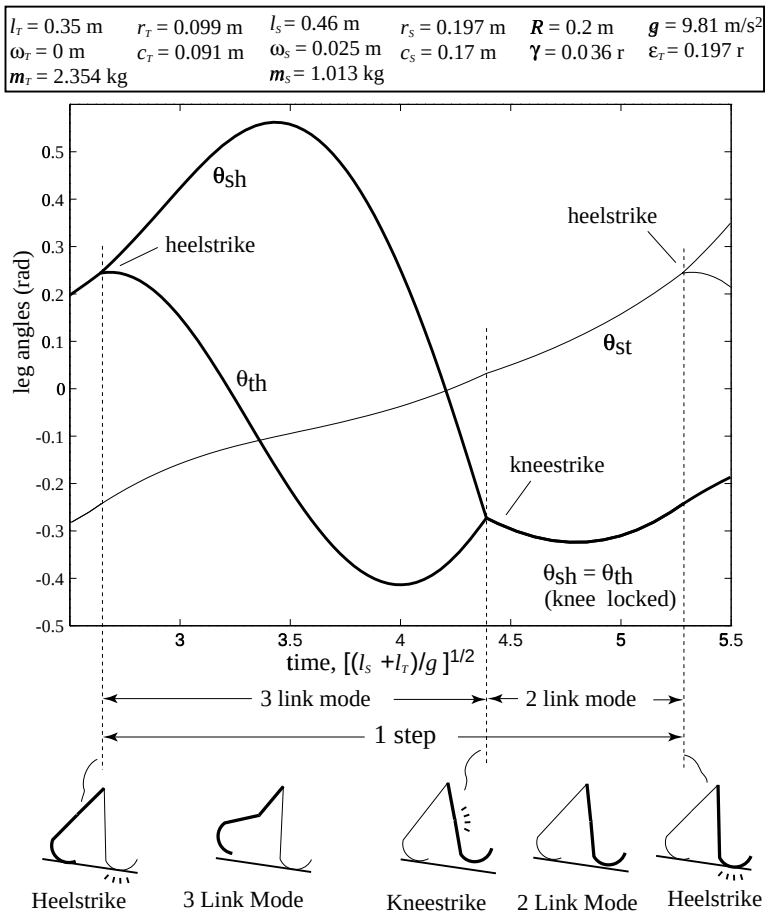

Figure 1.8: A simulated gait cycle of McGeer's 2D kneed walker (from [2]). Angles of leg segments are shown from just before heel-strike to just after the next heel-strike for a stable gait cycle of the walker from Figure 1.7. In this gait simulation, the system returns to its original initial conditions after one step. The parameters shown in the figure correspond to measured values from an experimental walker studied by [2]. The heavy line on the graph corresponds to the motion of the heavy-line leg on the cartoon under the graph. At the start of the step, this is the stance leg, but it becomes the swing leg just after the first heel-strike. After the first heel-strike, the swing leg begins to flex and swing as a double pendulum under the moving hip. At knee-strike, the swing shank collides against a knee-stop. The swing leg then swings as a simple pendulum under the moving hip until it has a heel-strike, when the two legs exchange roles. Heel-strike and the double-support phase are instantaneous in this model. In general, the angular velocities of the joint segments have discontinuities at knee-strike and heel-strike, which would appear as kinks in the plots of angle trajectories. These kinks do not happen to be prominent in this particular simulation. (Figure and caption courtesy Mariano Garcia [3])

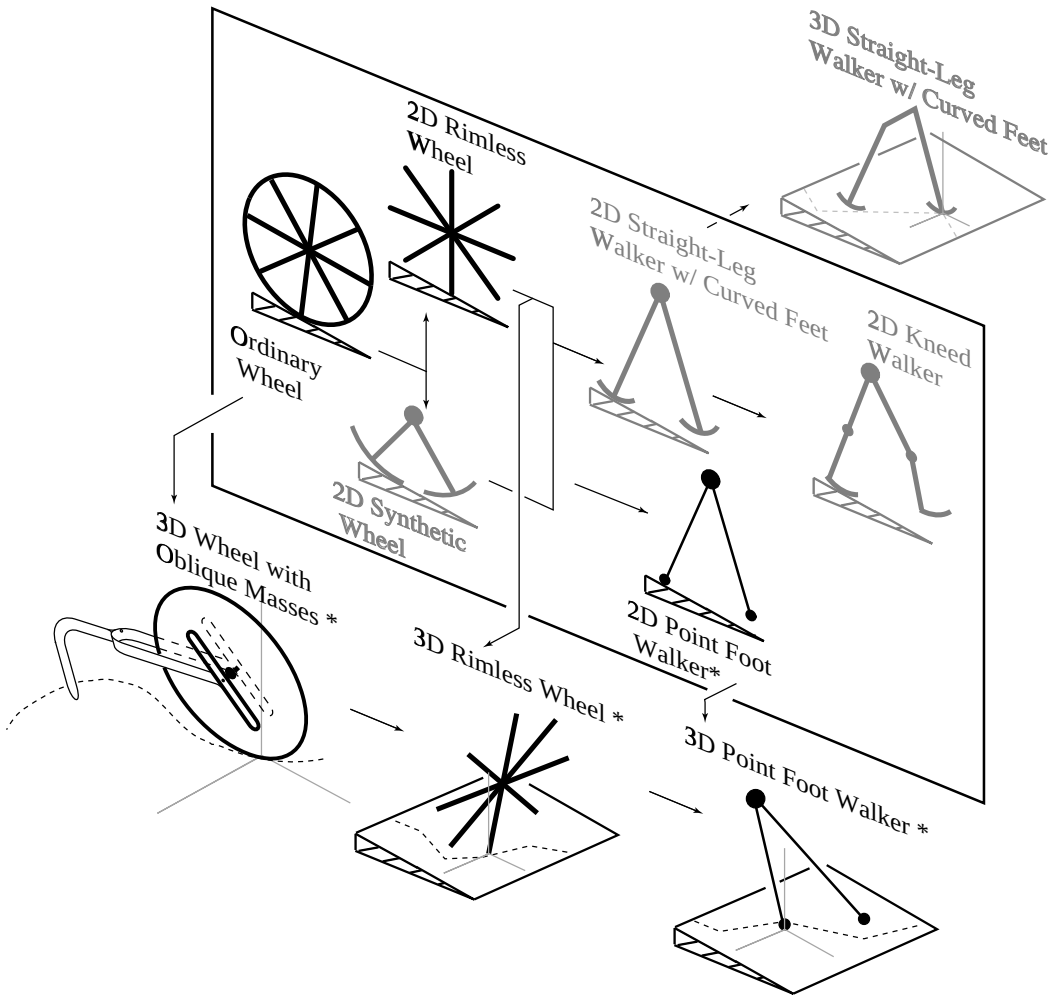

Figure 1.9: The un-invention of the wheel. Taxonomy of our analysis models. Models studied by McGeer but not by the author are shown in gray. Models the author has studied are shown in black. Models not studied by McGeer are indicated by an asterisk.

We adjust the distribution of mass in the additional bodies to upgrade the neutral stability of the uniform disk to asymptotic stability with respect to small lateral disturbances.

Next, an analysis of the 3D rimless wheel captures the essential features of our proposed study of three-dimensional walking mechanisms by allowing us to study out-of-plane stability of a simple mechanical analogue to walking. We use our insights from this spoked wheel to progress to the legged walker.

Finally, then, moving away from 3D wheels, we study a straight-legged point-foot walking model free to move in three-dimensions. We study planar motions of this model as a special case and a starting point.

1.5.2 Modeling Approach and Analysis Procedures

We first begin with a qualitative overview of the procedures of study and then make their description more formal with mathematical notation in Appendices A, B, and E.

Qualitative Overview of Procedures of Study

A *step* of a walking mechanism can be represented by a function which takes as input the measurement of the state of the device at definite points in its motion, usually(and perhaps most logically) just after foot collisions with the ground, and returns as output the values just after the next identically defined event. Thus, the state of the system after a step is a function of the state just after the previous step. McGeer calls the function or *return map* the *stride function.*

This mapping approach has also been used in other work involving discontinuous vector fields such as studies of: hopping robots (Bühler and Koditschek, 1990 [50]); bouncing balls (Guckenheimer and Holmes, 1983 [51]); elasto-plastic oscillators (Pratap, *et. al.*, 1992 [52, 53]); impact oscillators (Shaw and Holmes, 1983 [54], Shaw and Rand, 1989 [55]); balance wheels and pendula in clocks (Andronov, *et al.* [56]); and walking (McGeer, 1991 [4], Hurmuzlu, 1993 [57, 58]). A more general discussion of the dynamics of systems with impacts can be found in Brogliato, 1996 [59].

If nonlinear one-dimensional return maps describing the state of systems at successive collisions fall into a class of well defined functions, then certain conclusions may be made about the stability of periodic points of the maps. Koditschek and Bühler[60] verified one aspect of Raibert's [61] experimental work with hopping and running robots by establishing the existence of globally attracting vertical hopping modes (constrained against falling over) using unimodal maps whose properties are well established. In addition, Bühler and Koditschek [50] determined the existence of globally attracting 1D juggling modes for the one-dimensional juggler using unimodal maps and verified their simulations with careful experiments.

The stride function is found by deriving the differential equations of motion between collisions and collision conditions at end-of-step, subject to the classical laws of mechanics. Appendix B describes the details of deriving the equations of motion and the collision rules for the case of the point-foot straight-legged walker free to move in three-dimensions.

The models we study are systems of rigid-body links with hinge connections at the link joints. In this study, we only consider mechanisms with at most two links.

For two-link devices, in between foot collisions, we assume the stance foot remains on the ground. We treat it as a ball joint if it is modeled as having point feet or as having no-slip rolling constraints if it is modeled as having rolling contact, until the swing foot makes contact. We model the hip joint as a hinge. We assume additionally that there are no resisting torques about the point of contact and about the hinge joint axis. We derive the equations of motion between foot collisions by applying angular momentum balance about: (1) the stance foot contact point for the entire system and (2) the hinge rotation axis at the hip joint for the swing leg.

The swing foot contact point receives an impulse at foot-strike. Due to the swing foot collision, an impulse is also transmitted to the swing leg at the hip joint. We assume that, during collision,

other smaller forces (e.g., gravity) acting on the system are negligible in comparison to the collision impulses. We also assume there are no impulsive ground contact torques. At the instant of collision at the hip, we assume that the former stance leg loses contact with the ground (at the same instant the swing foot makes contact) and that it has no impulsive reaction with the ground as it leaves. Based on these assumptions, angular momentum is conserved for the entire system about the swing foot contact point during the collision process. Angular momentum is also conserved for the new swing leg (formerly the stance leg) about the hip joint hinge axis. These statements of angular momentum conservation during the collision process yield the transition rules for velocities from just before to just after foot-strike.

We derive the governing equations and collision rules by hand or on a computer using symbolic mathematics packages such as Maple® (see Appendix B).

For a given set of initial conditions, we integrate the equations of motion over one step analytically, if possible, but most often, numerically using the 4th-5th order Runge-Kutta method from MATLAB®. End-of-step is detected using a method developed by Henon [62] for the numerical computation of Poincaré Maps. Once a collision is detected, the collision condition is applied. This sequence of integration, collision detection, and application of jump condition constitute one evaluation of a cycle of motion.

A state of the system that returns to itself is called a fixed point of the stride function. Such a fixed point corresponds to a gait cycle (not necessarily stable). In order to find a stable cycle, first we have to find a cycle. We find fixed points of the stride function analytically if possible or by a numerical search. Appendix A describes a multi-dimensional Newton's Method fixed point search algorithm. Fixed points known from analysis of two-dimensional walkers may serve as initial guesses for the iterative numerical searches in three-dimensional models. For models that do not have strict two-dimensional interpretation, we use our knowledge and intuition about walking for initial guesses.

Given that we find gait cycles (fixed points of the return map), we evaluate stability by linearizing the stride function in the neighborhood of each fixed point. The linearization requires an estimate of how perturbations of each state-variable away from the fixed point are propagated to the next step. These estimates come from a series of analytical calculations or numerical simulations in the neighborhood of the fixed point. From these estimates, we can assemble the Jacobian matrix. Close to a fixed point, the Jacobian matrix maps the perturbation to a fixed point just after a collision to the perturbation of the fixed point just after the next collision. Since, in most cases, we do not know the stride function explicitly, we must find the Jacobian of the stride function numerically. Appendix A summarizes how to do this calculation. In some cases, we may obtain analytical approximations to the Jacobian of the the stride function evaluated at a fixed point by using perturbation methods, for example. Appendix A outlines such a procedure.

The eigenvalues of the Jacobian matrix indicate the stability of the system. If all eigenvalues have magnitude less than one, then the fixed point, and the gait cycle, are asymptotically stable. If any eigenvalues are outside the unit circle, then the periodic motion is *unstable*. If the 'biggest' eigenvalue has magnitude of one, then the limit cycle is *neutrally stable*. Appendix A explains how the eigenvalues determine the stability of fixed points.

For a given set of parameters, the search for a gait cycle and the stability check may be automated. If none of the fixed points for a set of parameters are stable, we modify the parameters and check again. An automatic search through all of parameter space is impractical, however. Instead, we guide the search using results from simpler models, our experience and insight about stability mechanisms and natural walking, and if possible numerical optimization procedures such as a multi-dimensional gradient search method or the method of simulated annealing.

Once we find a stable gait cycle, we perturb the parameter values and repeat the stability analysis, in order to evaluate the sensitivity of the stable cycle to changes in parameters.

We summarize the procedure as follows:

1. Define a mechanical model and make assumptions that determine parameters, kinematical description, and constraints.

2. Derive the equations of motion between foot collisions.
3. Describe the foot collision and derive a rule for the change in velocities during a collision.
4. Construct the stride function numerically by integrating the equations of motion between collisions, detecting a collision, and applying the collision rule.
5. Check validity of simulation. If the simulation results are not consistent with the laws of mechanics or the walking mechanisms are otherwise not behaving as should be expected, start at the beginning and refine the simulation.
6. Use root finding to find fixed points of the stride function.
7. Numerically evaluate the Jacobian of the stride function at the fixed points and find its eigenvalues.
8. If there are stable limit cycles for a set of parameters, try to determine the basin of attraction for the fixed points and vary the parameters to achieve the most stable periodic motions. If there are no stable limit cycles for a set of parameters, adjust parameters to find stable walking motions and redo the analysis procedure.

1.6 Dissertation Organization by Chapters

The rest of this dissertation is organized as follows: the motions, behaviors, and stability of the 2D rimless wheel are presented in Chapter 2; the effects of mass distribution on the stability of a rolling disk are presented in Chapter 3; numerical and analytical stability analyses of planar limit cycles of the 3D rimless wheel are presented in Chapter 4; finding walking motions and their stability for the 2D straight-legged point-foot walker is presented in Chapter 5; and, finding walking motions and their stability for the 3D straight-legged point-foot walker is presented in Chapter 6. Appendix A gives a mathematical description of the analytical, numerical, and simulation procedures and includes relevant Maple® and MATLAB® codes. Appendix B describes the methodology for the derivation of the governing equations for the 3D straight-legged passive-dynamic walking mechanism including relevant Maple® codes. Appendix C outlines the derivation of a special sequence of angular rates for the 2D rimless wheel analysis referred to in Chapter 2. Appendix D reviews the special set of 3-1-2 Euler angles used to describe orientations in Chapter 4 of the 3D rimless wheel and Chapter 6 of the 3D walker. Appendix E presents the Maple® code for the perturbation analysis of the stability of the 3D rimless wheel reported on in Chapter 4.

Chapter 2

'Step One': Rimless Spoked Wheel Constrained to Motions in a Vertical Plane

... I envy the spokes of wheels ...
Emily Dickinson, *Poems. Book II. Love. XXI. Longing*

2.1 Introduction

Following McGeer, our analysis of walking mechanisms starts with an investigation of a rimless spoked wheel confined to move in a vertical plane in a fixed direction on a slope. The 2D rimless wheel is shown circled in Figure 2.1 below to remind the reader of where it fits into the evolution of models in the research program. Henceforth, we will repeat the figure at the beginning of each chapter to show the progression of the models.

The configuration of the wheel is shown in Figure 2.2. A rimless wheel free to move in three dimensions is the subject of the Chapter 4. The rimless wheel captures some of the essential features of human walking. It mimics the foot collision, falling-and-catching, and inverted pendulum behavior of walking but not leg oscillations or fore and aft instability. The 2D rimless wheel also, obviously, does not have the lateral instability issues of 3D walking. The 2D wheel is a first 'step' in a progression to walking mechanisms with two swinging legs with and without knees in two and three dimensions. It is amenable to simple analyses yielding results about periodic motion and stability of a particular passive dynamic system without active energy input or control. In this problem, the wheel, statically unstable when balancing on one spoke, is stabilized dynamically in the direction of motion by repeated collisions. McGeer[43, 44, 4], claiming to follow Margaria[63], carried out a stability analysis of the rimless wheel, using linearized equations of motion, accurate when the number of spokes is large and the slope is small; i. e., when $n \to \infty$ and $\alpha \ll 1$. McGeer found stable limit cycles and the asymptotic rate of approach to these cycles. The subject of this chapter is a full nonlinear analysis of the wheel. This analysis adds a slight depth to the discussions of McGeer[43, 44, 4].

The rimless wheel is an example of a mechanical system with intermittent contacts. The spoke impacts give rise to discontinuities in the velocities. One can deduce the trajectories and the phase plane portrait of this simple system. The system is piecewise holonomic and conservative, or Hamiltonian. Like the 2D rolling disk, in its overall motion, it is holonomic. Globally, it is non-conservative due to the instantaneous loss in energy at each inelastic spoke collision.

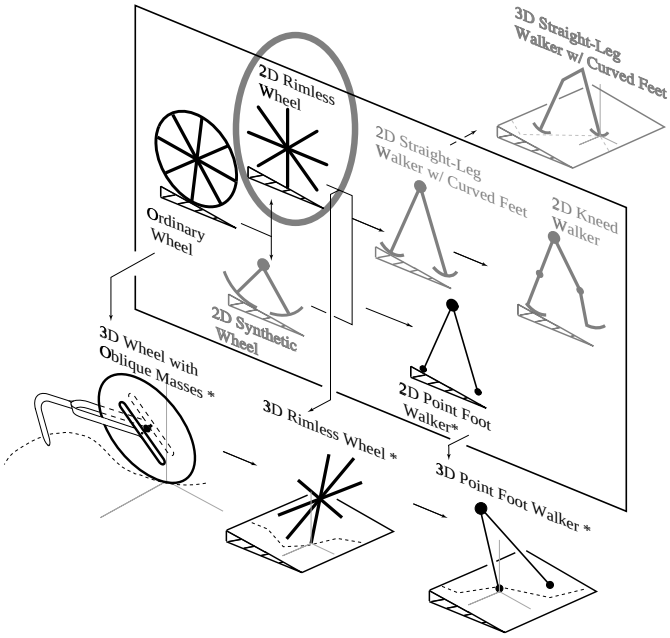

Figure 2.1: The place of the 2D rimless wheel in the passive-dynamic family tree.

Though the 2D rimless wheel is nonlinear in between collisions, it is simply an inverted rigid body pendulum for which a first integral exists - conservation of energy. Thus, the orbits in between collisions are easily generated. They are then pieced together using angular momentum balance at the collisions to obtain a complete phase plane portrait.

From this formulation, an explicit one-dimensional piecewise continuous Poinc-aré map is obtained that takes a measure of the velocity just after a spoke collision to just after the next. The Poincaré map samples the phase space at an angle of rotation fixed by the number of spokes, just after each spoke collision with the ground.

From this map, we obtain results regarding the existence and stability of two possible fixed points corresponding to static equilibrium and limit cycle motion of the wheel. The existence of these points depends on the model parameters. The birth and death of the fixed points cannot be classified according to classical theory of bifurcation of smooth scalar maps due to discontinuity in the Poincaré map.

We also find the asymptotic rate of approach to the fixed points, the non-dimensional energy loss per wheel revolution, steady-state non-dimensional speed and rate of change of speed of the center of mass as functions of slope angle, number of spokes, and moment of inertia about the center of mass. We show that in the limit as the number of spokes goes to infinity the rimless wheel behaves like a rolling disk. Finally, we summarize McGeer's linear analysis of the wheel and compare it to our nonlinear results. Numerical simulations are presented to verify and demonstrate the results.

2.1.1 Chapter Organization

The rest of this chapter is organized as follows: The physical system and model are described in Section 2.2; the governing equations and phase space are presented in Section 2.3; the Poincaré section and return map are defined in Section 2.4; fixed points, their stability, their criteria for existence and the rate of approach to them are described in Sections 2.5 to 2.9; an energy analysis is carried out in Section 2.10; the limit cycle non-dimensional speed and rate of change of speed are calculated in Section 2.11; a review of McGeer's linear analysis is given in Section 2.12, and a

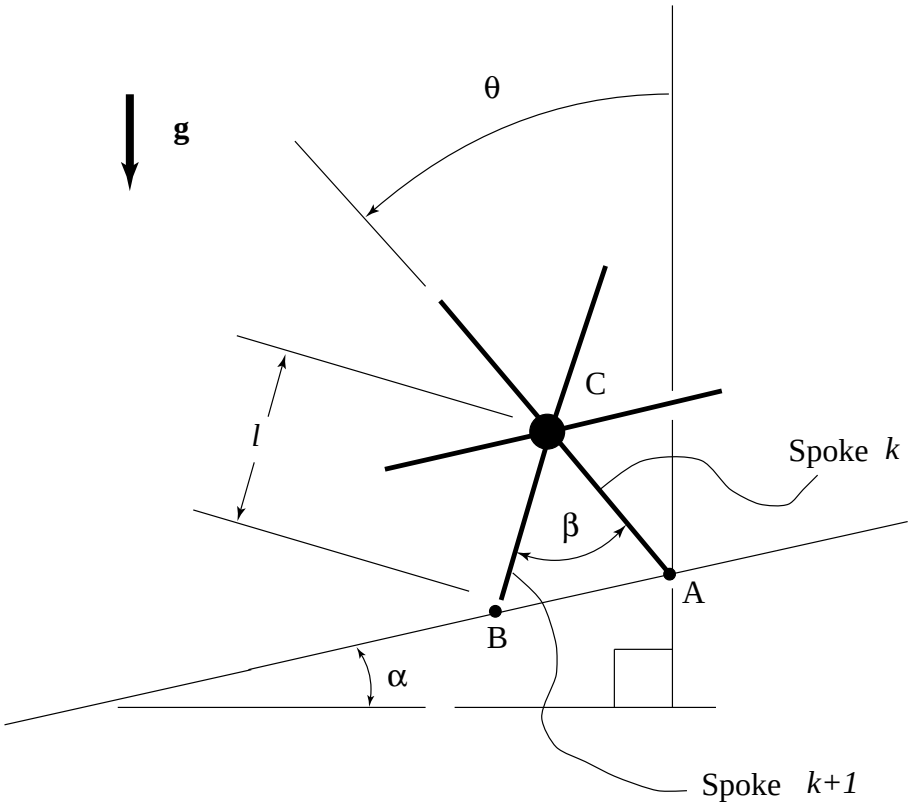

Figure 2.2: Wheel model: A rimless spoked wheel of mass m, moment of inertia about the center of mass I_C, and n evenly spaced spokes of uniform mass and length l rolls down a slope of angle α. The orientation of the wheel is given by angle θ. The angle between the spokes is $\beta = 2\pi/n$.

summary and discussion of this analysis with reference to the study of walking and the goals of this research are presented in Section 2.13.

In addition to introducing the physical system and assumptions, Section 2.2 (Description of the System), is intended as an overview of the concepts and techniques of our analysis and as a prelude to a more formal presentation of the details of the analysis in subsequent sections.

2.2 Description of the System

A wheel of mass m and moment of inertia about the center of mass I_C with the rim removed and n evenly spaced spokes of uniform mass and length l, acting as 'legs', rolls down a slope of angle α. (See Figure 2.2.) Unlike a wheel with a rim, this device cannot roll steadily on a level surface since it loses energy at collisions. We assume the spoke collisions are perfectly inelastic and impulsive, an idealization of foot collisions. Kinetic energy is, thus, lost in each dissipative impact and the wheel's speed is consequently reduced. For completeness, we also allow the wheel to roll backward and forward.

Once a spoke contacts the ground, it maintains hinged contact with the ground until the next spoke collides. In the model here, we explicitly exclude loss of ground contact and do not allow any slip – unrealistic assumptions for some of the motions. (Allowing for slip and/or loss of contact would limit the maximum slope for no-bounce, no-slip limit cycles to exist. Other, more complicated limit cycles could exist, however.)

2.2.1 Configuration

The orientation of the wheel is characterized by θ_k, the angle of spoke k measured from the vertical, positive in the counter clockwise sense. θ_k is zero when spoke k is vertical and in contact with the ground. Since the spoked wheel has n-fold symmetry, the angle with the vertical of the spoke presently on the ground in some sense characterizes the configuration of the system.

Special times of interest are just before and just after collision i. $(-)$ and $(+)$ are used as the superscripts to denote these times. For instance, ${}^i\theta_k^+$ is the angle of any spoke k, just after collision i. $j(i)$ is the spoke touching the ground just after collision i. For downhill rolling, $j(i) = i$ and $j(i+1) = j(i) + 1$. For uphill rolling, $j(i+1) = j(i) - 1$. ${}^i\theta_{j(i)}^+$ is the angle of spoke $j(i)$, the spoke which just collided with the ground at collision i, just after collision i. The overall motion of the wheel is recorded by, say, $\theta_1(t)$.

2.2.2 Cycle of Motion

A schematic of one cycle, for downhill rolling, is shown in Figure 2.3. The wheel rotates over the 'stance' spoke, spoke $j(i)$, as an inverted pendulum with initial angle ${}^i\theta_{j(i)}^+ = \alpha - \pi/n$ and rotation rate $\dot\theta = {}^i\dot\theta_{j(i)}^+$. The non-collisional portion of the stride ends just before the next spoke in sequence, spoke $j(i+1)$, analogous to the swing leg in walking, strikes the ground at ${}^{i+1}\theta_{j(i)}^- = \alpha + \pi/n$ and $\dot\theta = {}^{i+1}\dot\theta_{j(i)}^-$ instantaneously transferring support from the trailing spoke to the leading spoke. After impact, the wheel is now poised for the next start-of-cycle at ${}^{i+1}\theta_{j(i+1)}^+ = {}^i\theta_{j(i)}^+ = \alpha - \pi/n$ and $\dot\theta = {}^{i+1}\dot\theta_{j(i+1)}^+$. Since the angular velocity of all of the spokes is the same, we will drop subscripts on $\dot\theta$ henceforth.

2.2.3 Motions and Limiting States of the Wheel

When the wheel is rolling *up* or *down*, it may or may not have sufficient energy to pass over the vertical position. When the wheel does not have enough energy to pass the vertical in the downhill

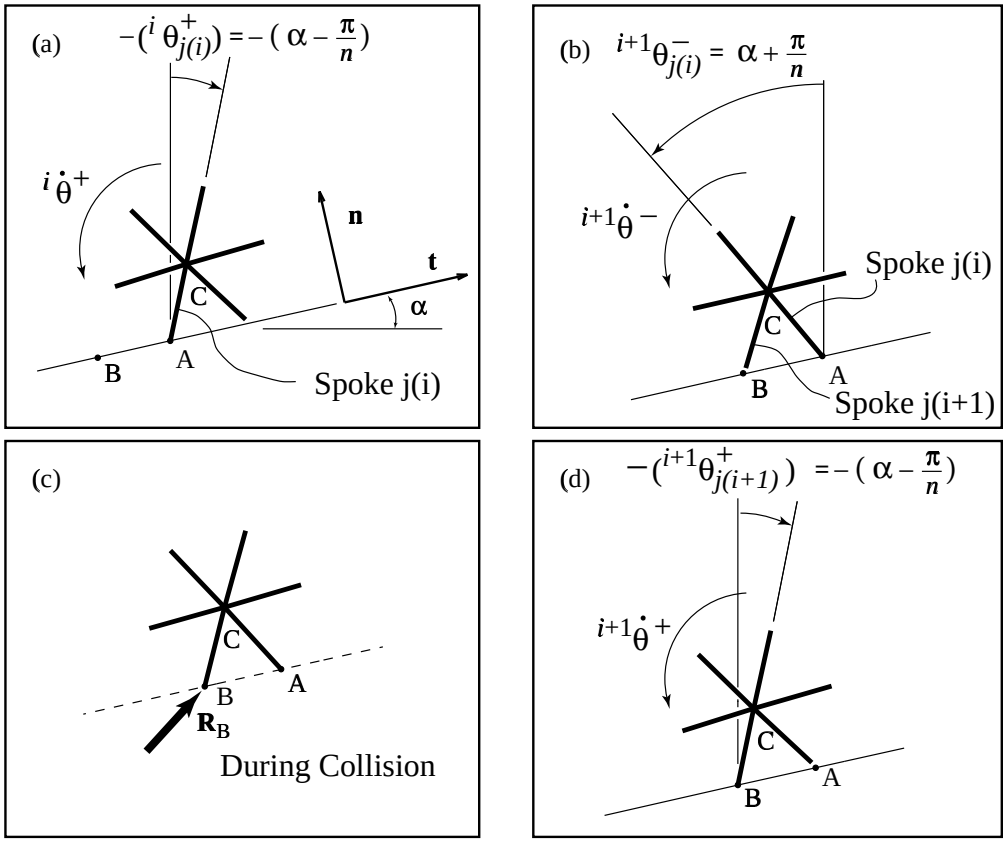

Figure 2.3: Schematic showing: (a) the state of the wheel over one stride just after the collision of spoke $j(i)$ with point A, (b) the state of the wheel just before collision $i+1$ of spoke $j(i+1)$ at point B, (c) the free body diagram of the wheel during the collision of spoke $j(i+1)$ at point B, and (d) the state of the wheel just after the collision of spoke $j(i+1)$ at point B. The unit vector $\mathbf{n}$ is normal to the slope and the unit vector $\mathbf{t}$ is tangent to the slope.

direction, the wheel has one motion: reversing direction and then *rocking* back and forth between two spokes. When the wheel does not have enough energy to pass the vertical in the uphill direction, the wheel can have two motions: reversing direction and rocking back and forth between two spokes, as above, or reversing direction and rolling downhill.

If the wheel completes a downhill cycle, the kinetic energy of the wheel just before collision is greater than the kinetic energy at the start-of-cycle due to the downhill slope ($KE_{i+1}^{-} > KE_{i}^{+}$). The kinetic energy of the wheel drops instantaneously at impact, however. For downhill motions, the following outcomes are possible.

- 1. Periodic motion arises if the the energy lost in collision is exactly balanced by the kinetic energy gained in falling. In this case, the state variables are equal to those at the start of the previous stride. The wheel is in periodic or limit cycle motion that repeats indefinitely.
- 2. If more energy is lost in collision than gained in falling, the wheel slows, either towards a periodic motion or to an eventual stop on two spokes, depending on the slope, inertia, and number of spokes.
- 3. If more energy is gained in falling than lost in collision, we expect the wheel to increase in speed towards the periodic motion.
- 4. For a particular angular velocity after collision and small enough slope, the wheel will approach the unstable vertical equilibrium in infinite time.

For uphill motions, the wheel will eventually reverse direction, roll downhill, and reach one of the outcomes above for downhill rolling.

Thus, the possible limiting states for the wheel are limit cycle motion, the stopped position on two spokes, and the unstable vertical equilibrium. Limit cycles and the stopped position correspond to the condition ${}^{i+1}\dot{\theta}^{+} = {}^{i}\dot{\theta}^{+}$ and ${}^{i+1}\theta^{+} = {}^{i}\theta^{+} = \alpha - \frac{\pi}{n}$; i.e., the state of the wheel is the same just after every collision i.

2.2.4 Behaviors of the Wheel

The behaviors of the wheel are the ways in which the wheel approaches the possible limiting states. The behaviors depend upon the wheel parameters and initial conditions. For example, the wheel can roll down the slope at higher than the angular rate needed to just reach the vertical position in infinite time but less than the limit cycle angular rate, increase in speed and approach a limit cycle from below. Using our notation, we can represent the behavior schematically as Down$\overset{+}{\rightarrow}$ Limit Cycle where the $(+)$ or $(-)$ refers to increasing or decreasing angular velocity after each collision.

In summary, using our shorthand notation, the behaviors of the wheel are as follows:

- 1. Down$\overset{+}{\rightarrow}$ Limit Cycle
- 2. Down$\overset{-}{\rightarrow}$ Limit Cycle
- 3. Down$\rightarrow$ Rock $\rightarrow$ Stop
- 4. Rock$\rightarrow$ Stop
- 5. Up$\rightarrow$ Rock $\rightarrow$ Stop
- 6. Up$\rightarrow$ Down$\overset{+}{\rightarrow}$ Limit Cycle
- 7. Down$\rightarrow$ Vertical
- 8. Up$\rightarrow$ Vertical

- 9. Up→ Down → Vertical
- 10. Up→ Stop
- 11. Down→ Stop

These behaviors are more compactly summarized in a diagram in Figure 2.4.

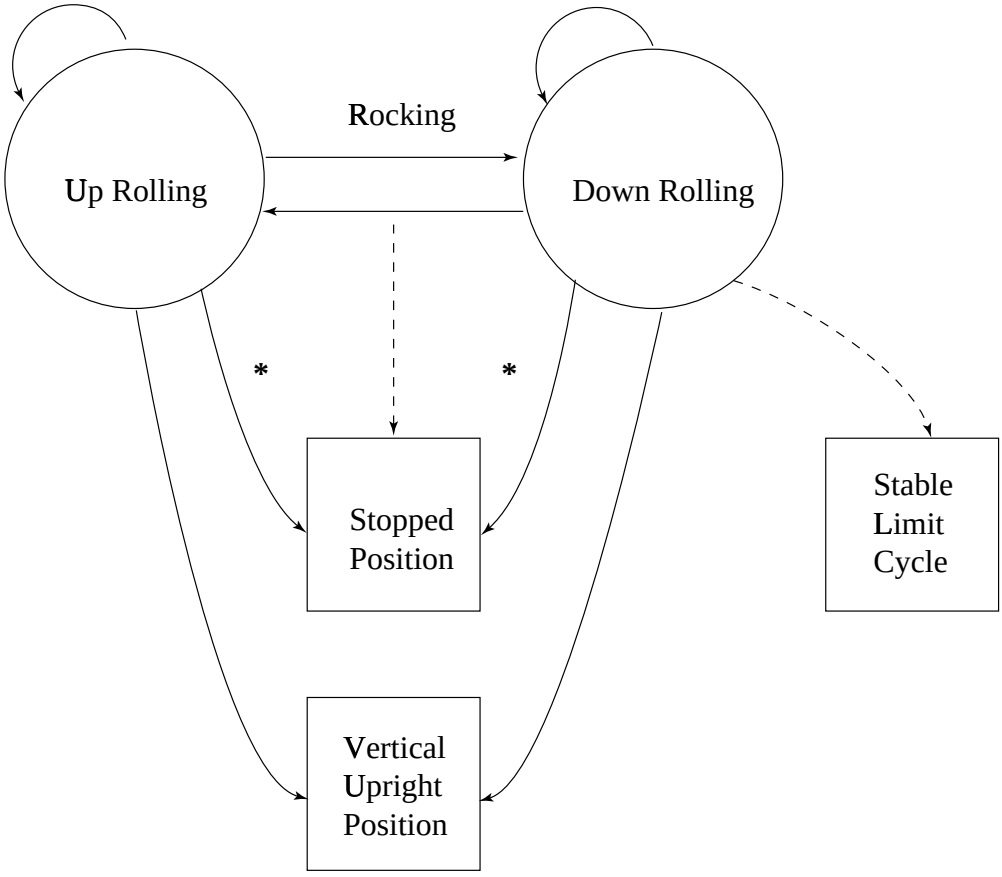

Figure 2.4: Diagram showing the possible motions, the condition of rocking, and the possible limiting states, stopped on two spokes, the limit cycle, and the vertical position. Solid arrows indicate that a motion or limiting state can be reached in finite time after one collision or in infinite time before the next collision can occur. Dotted arrows indicate that a limiting state is reached asymptotically after infinite collisions in finite time. The asterisks next to a solid arrow indicate that the stopped position can be reached in one collision; e.g., cases 10 and 11 in the text. The arrows turning back on themselves and attached to the motions indicate that the motion can occur over one or more iterations.

In cases 3, 4, 5, the wheel rocks back and forth on two spokes until coming to rest on two spokes after an *infinite* number of collisions in *finite* time. Since, as we will see, support transfer produces a simple ratio (less than one) between adjacent terms in the sequence of angular rates, the rocking cannot stop in a finite number of collisions. But, it can stop in finite time since the total time of rocking is an infinite geometric series that has a finite sum. McGeer [64] finds the finite sum of this

infinite series, obtained from a linear analysis of rocking, with arbitrary accuracy for the case where the angular rate has gotten very small after some large but finite number of collisions.

Cases 10 and 11 can only happen with three and four spoked wheels and sufficiently small radius of gyration. In these special cases, the wheel comes to a stop after the first spoke collision, for any initial conditions.

We now move on to the details of the full nonlinear analysis of the 2D rimless wheel by starting with the equation of motion, collision transition conditions, and the associated phase space.

2.3 Governing Equations and the Phase Space

Since the rimless wheel has n-fold symmetry, the wheel looks the same for a given angle of any spoke that is currently in contact with the ground between collisions. The angle with the vertical of the spoke presently on the ground in between collisions, then, can be used to characterize the configuration of the system, as noted in Section 2.2.1. As the center of rotation of the rimless wheel is instantaneously moved with each collision from the tip of one spoke to the next, we thus consider the orientation of the wheel between collisions restricted to the closed interval $I = [\alpha - \pi/n, \alpha + \pi/n]$ over many collisions by resetting the angle at each collision. The boundaries of the interval are determined by the number of spokes, n, and the slope angle, α. The rule for updating the orientation was introduced in Equation (2.4).

We use angular momentum balance about the point of spoke contact to find the equation of motion between collisions, the configuration scheme described above to find the collision transition rule for the orientation angle of the wheel, and conservation of angular momentum about the incipient point of spoke contact to find the collision transition condition for the angular velocity of wheel.

2.3.1 Equation of Motion between Collisions

Referring to Figure 2.3, the equation of motion is derived from angular momentum balance about point A,

$$\Sigma \mathbf{M} = \dot{\mathbf{H}}_A. \tag{2.1}$$

The non-dimensionalized equation of motion between collisions is:

$$\ddot{\theta} - \lambda^2 \sin\theta = 0, \qquad |\theta - \alpha| < \pi/n. \tag{2.2}$$

where

$$\begin{aligned} \lambda^2 &= \frac{1}{2J+1} \\ 2J &= \frac{I_C}{ml^2} \\ 3 &\leq n < \infty, \quad \text{and} \\ 0 &\leq \alpha \leq \pi/2. \end{aligned} \tag{2.3}$$

An overdot indicates differentiation with respect to non-dimensional time $\tau = t\sqrt{g/l}$. This equation is simply that of an inverted rigid body pendulum.

2.3.2 Collision Transition Conditions

The angle is reset at each collision $i+1$ as support is transferred from spoke $j(i)$ to $j(i+1)$ according to the following mapping:

$$(\theta - \alpha) \mapsto -(\theta - \alpha), \qquad |\theta - \alpha| = \pi/n. \tag{2.4}$$

This relation is obtained by noting that the orientation of the wheel is rotated by $-\frac{2\pi}{n}$ after a downhill collision and by $\frac{2\pi}{n}$ after an uphill collision.

Ignoring the impulse due to gravity during collision, the condition relating the angular velocity of the wheel before and after collision is derived from the conservation of angular momentum during collision about the incipient point of spoke contact. Referring to Figure 2.3, we can write this as

$$\mathbf{H}_B^- = \mathbf{H}_B^+ \tag{2.5}$$

where $\mathbf{H}$ is angular momentum and

$$\begin{aligned} \mathbf{H}_B^- &= \mathbf{H}_C^- + \mathbf{r}_{C/B} \times m\mathbf{v}_C^- \\ \mathbf{H}_C^- &= I_C \left({}^{i+1}\dot{\theta}^- \right) \mathbf{k} \\ \mathbf{v}_C^- &= \left({}^{i+1}\dot{\theta}^- \right) \mathbf{k} \times \mathbf{r}_{C/A}, \\ \mathbf{H}_B^+ &= I_B \left({}^{i+1}\dot{\theta}^+ \right) \mathbf{k}, \quad \text{and} \\ I_B &= I_C + ml^2. \end{aligned} \tag{2.6}$$

The conservation of angular momentum stated in Equation (2.5) yields the following transition function relating angular velocity before and after collision:

$$\dot{\theta} \mapsto \mu\dot{\theta}, \qquad |\theta - \alpha| = \pi/n \tag{2.7}$$

where

$$\mu = \frac{2J + \cos(\frac{2\pi}{n})}{2J+1} = 1 + \lambda^2(\cos(\frac{2\pi}{n}) - 1), \qquad 0 \le \mu < 1. \tag{2.8}$$

The collision parameter μ in Equation (2.7) represents energy lost during impact since it is always less than one, except when the number of spokes is infinity so that μ is equal to one. Before we can define the Poincaré section and return map for the 2D rimless wheel, we must first describe the phase space and trajectories for the system.

2.3.3 The Phase Space and Trajectories

The Phase Space

Rewriting Equation (2.2) in first order form, the $(\theta, \dot{\theta})$ phase flow is governed by

$$\dot{\theta} = y, \qquad |\theta - \alpha| < \pi/n \tag{2.9}$$

$$\dot{y} = \lambda^2 \sin\theta$$

$$(\theta - \alpha, y) \mapsto (-(\theta - \alpha), \mu y), \qquad |\theta - \alpha| = \pi/n \tag{2.10}$$

The flow in phase space between collisions is easily generated using the first integral of motion(conservation of energy)

$$\dot{\theta} = \sqrt{\dot{\theta}_0^2 + 2\lambda^2(\cos(\theta_0) - \cos(\theta))}. \tag{2.11}$$

The simple rigid body pendulum without collisions has the usual phase space with coordinates $(\theta, \dot{\theta}) \in \mathbb{R}^2$. The evolution of the trajectories for the rimless wheel, however, is contained in a closed subset of phase space

$$U = \{(\theta, \dot{\theta}) | \quad |\theta - \alpha| \le \pi/n\} = I \times \mathbb{R} \subset \mathbb{R}^2. \tag{2.12}$$

All trajectories start in U and terminate in U. Figure 2.5 shows the subtended phase space U for the rimless wheel superimposed on the phase space for the simple rigid body pendulum.

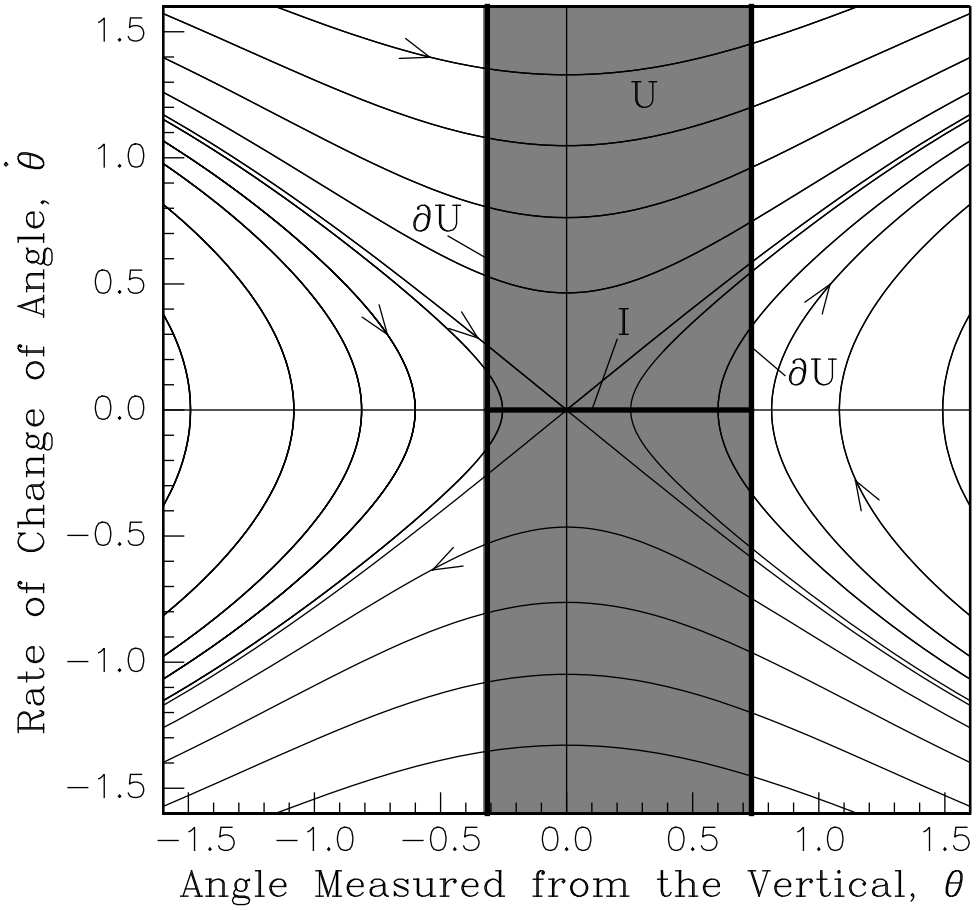

Figure 2.5: The phase space U and its boundaries ∂U with slope angle $\alpha = \frac{\pi}{15}$, number of spokes $n = 6$, and $2J = 0.5$ for the rimless wheel is shown superimposed on the phase portrait for the nonlinear simple rigid body pendulum. The interval I is $I = [\alpha - \pi/n, \alpha + \pi/n] = [-0.3142, 0.733]$. The trajectories of the motion of the rimless wheel are contained in this subset of the phase space for the simple rigid body pendulum also with non-dimensional inertia $2J = 0.5$. Note the asymmetry of U about the vertical axis due to the slope angle: the greater the slope angle the greater the asymmetry.

Phase Flow in U

We can re-write Equation (2.9) as

$$\dot{\mathbf{q}} = \mathbf{f}(\mathbf{q}, \mathbf{p}) \tag{2.13}$$

where $\mathbf{q} = (\theta, \dot{\theta})$ and $\mathbf{f} : U \to U$ is a time-independent vector field depending upon a vector of parameters, $\boldsymbol{p} = \{\lambda^2, n, \alpha\}$. Back, et. al [65] have elucidated a concise framework for describing dynamical systems such as the rimless wheel which require a mixture of discrete and continuously evolving events, what they call *hybrid systems*. Conceptually, they view the evolution of the system as a sequence of trajectory segments where the endpoint of one segment is connected to the initial point of the next by a transformation. They divide time into contiguous periods, called *epochs*, separated by instantaneous *events* where *transition functions* are applied. We will borrow this terminology to describe our system.

The epochs here are the time periods between spoke collisions which are the events. The transition function here is a map $\mathbf{T} : \partial U \to \partial U$, where $\partial U = \{(\theta, \dot{\theta}) | \quad |\theta - \alpha| = \pi/n\}$ and $\mathbf{T}$ is defined by Equation (2.10). Within this framework, an orbit in the flow of this system which begins at a time t_0 and terminates at time t_f may be completely described. Back, et. al [65] define a trajectory for Equation (2.13) to be a curve $\gamma : [t_0, t_f] \to U$ together with an increasing sequence of real numbers $t_0 < t_1 < \cdots < t_f$ that satisfies three properties:

- Each time interval corresponds to an epoch and $\gamma(t)$ lies entirely in U for all $t \in (t_i, t_{i+1})$.
- For $t \in [t_i, t_{i+1})$, $t \to \gamma(t)$ is an integral curve of the vector field $\mathbf{f}$.
- $\lim_{t \to t_{i+1}^-} \gamma(t) = \mathbf{v}$ exists, $\mathbf{v} \in \partial U$, and $\mathbf{T}(\mathbf{v}) = \lim_{t \to t_{i+1}^+} \gamma(t)$, $\mathbf{T}(\mathbf{v}) \in \partial U$.

It is possible for $\gamma(t_f) \in U$; i.e., $\gamma(t)$ terminates in U.

A representative phase plane portrait, generated using modified MATLAB® integration routines is shown in Figure 2.6 for several initial conditions. Some remarks regarding the phase plane portrait:

- The nature of the phase plane portrait and, hence, the physical behavior of the wheel depend on the wheel parameters.
- Trajectories for a simple pendulum cannot cross the separatrices but the collisions allow this for the rimless spoked wheel.
- Every trajectory terminates on ∂U except for those on the separatrices which initiate at

$$^{dn}\dot{\theta} = \sqrt{2\lambda^2(1 - \cos(\alpha - \pi/n))} \tag{2.14}$$

or

$$^{up}\dot{\theta} = -\sqrt{2\lambda^2(1 - \cos(\alpha + \pi/n))} \tag{2.15}$$

and terminate at the unstable equilibrium $(\theta, \dot{\theta}) = (0, 0)$. If $\alpha > \frac{\pi}{n}$, the unstable equilibrium is not in U.

In Figure 2.7, θ and $\dot{\theta}$ are plotted versus non-dimensional time, τ, corresponding to trajectory $\gamma_1(t)$ in Figure 2.6. The plots show the discontinuities in the state variables at the collisions and shows how θ is bounded by $\theta = \alpha - \frac{\pi}{n}$ and $\theta = \alpha + \frac{\pi}{n}$.

For illustrative purposes, the trajectories and phase space for the rimless wheel shown in Figure 2.6 are shown superimposed on the corresponding trajectories of the simple rigid body pendulum in Figure 2.8.

Now that we have described the phase space and trajectories, we can define the Poincarè section and return map.

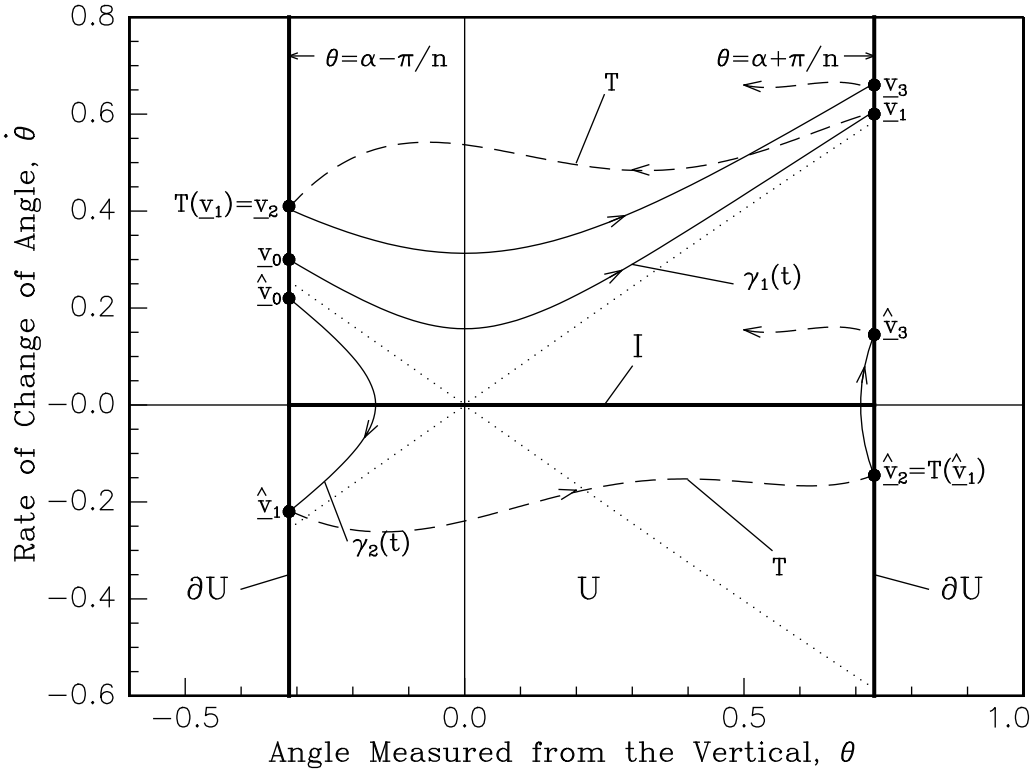

Figure 2.6: Two phase plane trajectories in U and between the boundaries of U. The trajectories are labeled $\gamma_1(t)$ and $\gamma_2(t)$ and both use $2J = 0.5$, $n = 6$, and $\alpha = \frac{\pi}{15}$. The initial condition for the first trajectory is $\gamma_1(t_0) = \mathbf{v}_0 = (-0.314, 0.30)$ and subsequent points of the trajectory on the boundary of U are denoted by $\mathbf{v}_i$, $i = 1, 2, 3, \ldots$. The initial condition for the second trajectory is $\gamma_2(t_0) = \hat{\mathbf{v}}_0 = (-0.314, 0.22)$ and subsequent points of the trajectory on the boundary of U are $\hat{\mathbf{v}}_i$, $i = 1, 2, 3, \ldots$. The *solid* lines are integral curves of the vector field $\mathbf{f}$ representing the motion between collisions and the *dashed* lines are fictitious 'curves' that piece together the integral curves at collisions to make a complete trajectory. The dashed lines represent the instantaneous application of the transition function $\mathbf{T}$ at each collision that manifests itself as a decrease in angular velocity. The *dotted* lines are trajectories that correspond to the separatrices for the simple pendulum. If the wheel starts at initial conditions that are on these trajectories the wheel either reaches the vertical unstable equilibrium $\theta = 0$ in infinite time or leaves the vertical position and makes a collision in finite time. The arrows on the trajectories indicate the forward direction in time.

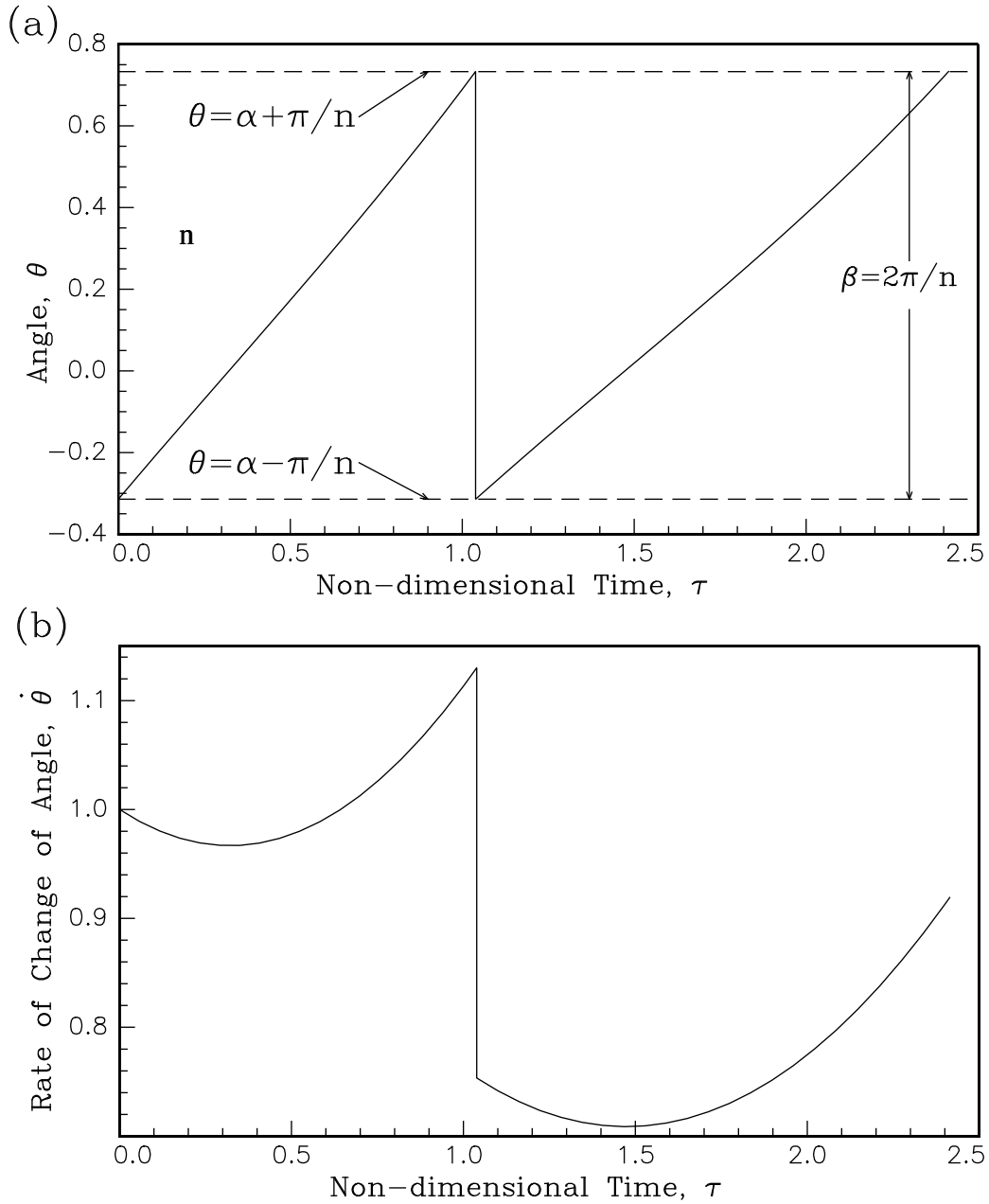

Figure 2.7: In figures (a) and (b), θ and $\dot{\theta}$ are plotted, respectively, versus non-dimensional time, τ, corresponding to trajectory $\gamma_1(t)$ in Figure 2.6. In the time interval shown, the wheel makes two collisions. The plots show the discontinuities in the state variables at the collisions. The first plot shows how θ is bounded by $\theta = \alpha - \frac{\pi}{n}$ and $\theta = \alpha + \frac{\pi}{n}$ and how the angle is reset after each collision according to the collision transition rule Equation (2.4). The size of the interval is equal to the angle between the spokes, $\beta = \frac{2\pi}{n}$.

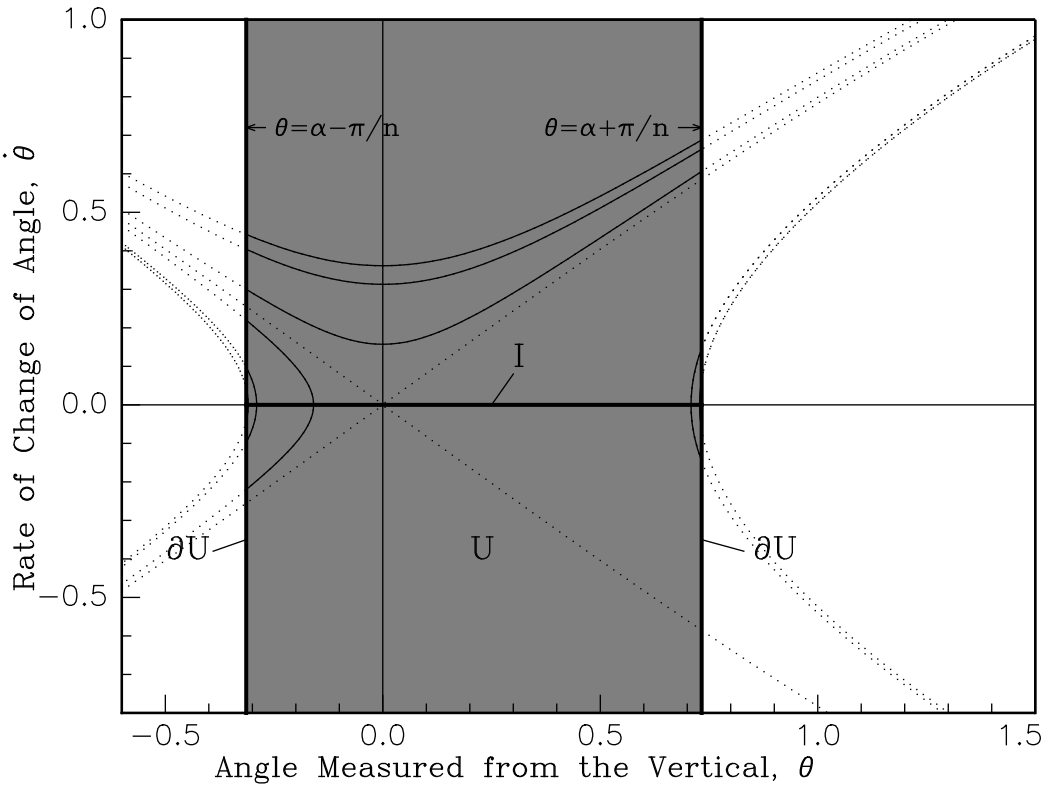

Figure 2.8: The trajectories and the phase space for the rimless wheel shown in Figure 2.6 are shown superimposed on the corresponding trajectories of the simple rigid body pendulum that pass through the angular velocities after collision on the boundaries of U where the trajectories of the rimless wheel start. The bold lines are the trajectories of the rimless wheel and the dotted lines are the trajectories of the simple rigid body pendulum.

2.4 Poincaré Section and Return Map

To study this system, we shall use the method of a Poincaré section. The one degree of freedom rimless wheel has a two dimensional phase space with coordinates $(\theta, \dot{\theta}) \in U$. A natural place to sample this space is at the points of discontinuity, the collisions, where we know the orientation of the wheel. We then will define a scalar map P that takes an angular velocity after a collision that is in the section to the angular velocity after the next collision that is also in the section.

2.4.1 The Poincaré Section

We define the sampling location in the phase space, the Poincaré section Σ, as:

$$\Sigma = \left\{ (\theta, \dot{\theta}) \;\middle|\; \begin{array}{lll} \theta = (\alpha - \frac{\pi}{n}), & \dot{\theta} \geq 0, & \text{and } \dot{\theta} \neq {}^{dn}\dot{\theta} \\ \theta = (\alpha + \frac{\pi}{n}), & \dot{\theta} < 0, & \text{and } \dot{\theta} \neq {}^{up}\dot{\theta} \end{array} \right\} \tag{2.16}$$

where

$${}^{dn}\dot{\theta} = \sqrt{2\lambda^2(1 - \cos(\alpha - \frac{\pi}{n}))} \tag{2.17}$$

and

$${}^{up}\dot{\theta} = -\sqrt{2\lambda^2(1 - \cos(\alpha + \frac{\pi}{n}))}. \tag{2.18}$$

${}^{dn}\dot{\theta}$ is the angular velocity just after collision in the forward direction such that the wheel reaches the vertical position $\theta = 0$ in infinite time. ${}^{up}\dot{\theta}$ is the angular velocity just after collision in the backward direction such that the wheel reaches $\theta = 0$ in infinite time. These critical values are obtained using conservation of energy; all of the kinetic energy of the wheel following a spoke collision is converted to potential energy at $\theta = 0$.

The critical values of angular velocity after collision, ${}^{dn}\dot{\theta}$ and ${}^{up}\dot{\theta}$, defined above, are excluded from the Poincaré section because once the wheel attains either of the critical values after a collision, the wheel will not have any more collisions since the wheel reaches the vertical in infinite time. Thus, we cannot sample the space after collisions since the wheel has stopped in the vertical position.

The flow of the differential equation is everywhere transverse to Σ; i.e. the phase plane trajectories pass through the Poincaré section. This is easily seen by considering the vector field in $(\theta, \dot{\theta})$ space on Σ given by Equation (2.9). The flow is transverse to Σ since $\left.\frac{d\dot{\theta}}{d\theta}\right|_{\theta=\alpha\pm\frac{\pi}{n}}$ is defined.

Orbits in the phase space will be studied by considering the mapping

$$P : \Sigma \to \Sigma \tag{2.19}$$

induced by the solutions of Equation (2.2). Figure 2.9 shows the phase space and the section Σ. Positive orbits are sequences of the angular velocity of wheel after each collision. The sequences are obtained by iterating forward from an initial condition in Σ using the Poincaré map P. The orbits can be visualized by marking the sequences of angular velocities on the Poincaré section. Consider orbits with initial angular velocities just after collision, $\dot{\theta}_0 \in \Sigma$, in Figure 2.9. Positive orbits from initial conditions with $\dot{\theta} > {}^{dn}\dot{\theta} > 0$ and ${}^{up}\dot{\theta} < \dot{\theta} < {}^{dn}\dot{\theta}$ are shown for several iterates with $\alpha \leq \frac{\pi}{n}$. The section we have defined is used since the first integral of motion, the conservation of energy, exists for motion between collisions and since the transition function for the angular velocity at each collision is simple. Thus, the map P can be obtained in closed form. Discontinuities in the map can exist, however, and we must locate them and determine their dependence on the wheel parameters before constructing the map.

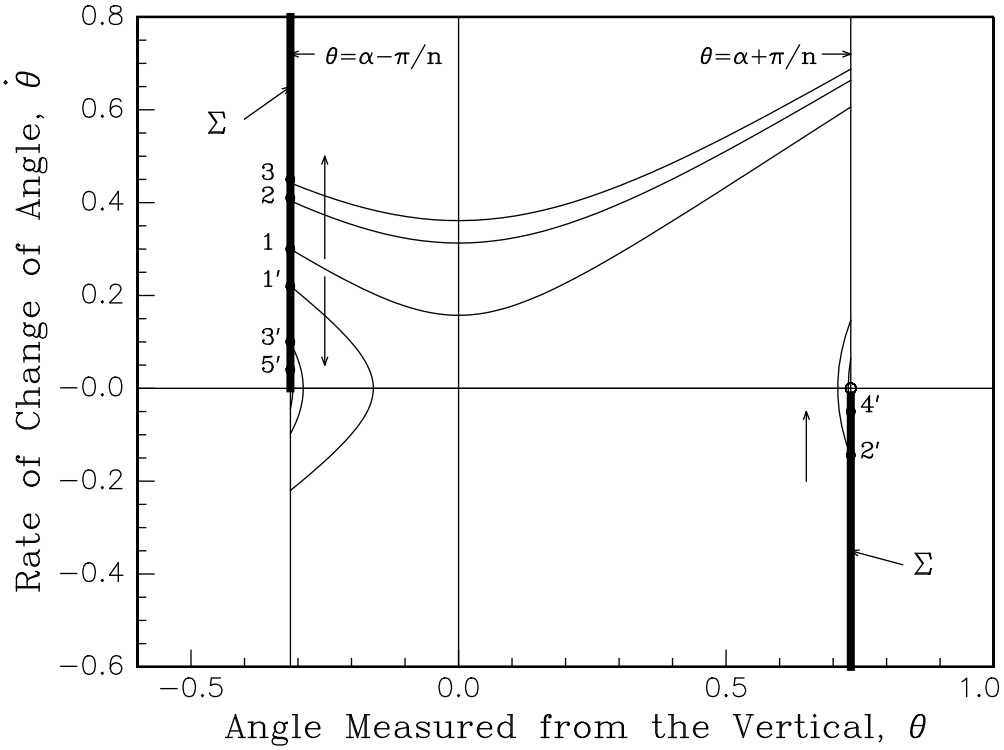

Figure 2.9: The phase space $(\theta, \dot{\theta}) \in U$ showing the Poincaré section Σ. Positive orbits from initial conditions $\dot{\theta}_0 > {}^{dn}\dot{\theta} > 0$ and ${}^{up}\dot{\theta} < \dot{\theta}_0 < {}^{dn}\dot{\theta}$ are shown for several iterates with $\alpha = \frac{\pi}{15}$, $2J = 0.5$, and $n = 6$. In this case, ${}^{dn}\dot{\theta} = 0.255$ and ${}^{up}\dot{\theta} = -0.585$. The orbits in Σ starting with with $\dot{\theta}_0 = 0.30$ and $\dot{\theta}_0 = 0.22$ are marked by the sequences, $1, 2, 3, \ldots$ and $1', 2', 3', \ldots$, respectively. The orbit starting with $\dot{\theta}_0 = 0.30 > {}^{dn}\dot{\theta}$ corresponds to the wheel starting off downhill and approaching a limit cycle. The orbit starting at $\dot{\theta}_0 = 0.22 < {}^{dn}\dot{\theta}$ corresponds to starting off downhill with too little energy to make it past the vertical position and rocking back and forth between two spokes, eventually coming to rest.

Piecewise Continuity of the Return Map

The Poincarè map can be discontinuous. Discontinuities can arise in the return map at the critical values of angular velocity after collision for stopping at the vertical position in infinite time, ${}^{up}\dot{\theta}$ and ${}^{dn}\dot{\theta}$. The critical values depend upon the number of spokes, the slope angle, and the non-dimensional inertia. The critical angular velocities exist for shallow and intermediate slopes, $\alpha \leq \frac{\pi}{n}$. The map will have one functional dependence on the angular velocities after collision in the interval between the critical velocities, ${}^{up}\dot{\theta} < \dot{\theta} < {}^{dn}\dot{\theta}$, and another outside the interval. In the interval, the map P must represent the wheel having too little energy to reach the vertical and then reversing its direction. Outside the interval, the map must represent the wheel having enough energy to pass the vertical. The critical angular velocities do not exist for very steep slopes, $\alpha > \frac{\pi}{n}$, and, hence, no discontinuities exist in that case. For steep slopes, the map is continuous for all angular velocities after collision.

Now, using conservation of energy between collisions, the collision transition condition for angular velocity, and the slope dependence of the discontinuities, we can construct the map P.

Constructing the Return Map, P

To simplify the definition of the map and its interpretation, it is desirable to first make a change of variables which gives a new measure of the angular velocity just after a collision. The new variable, the *measure of angular velocity after collision*, z, is taken to be the square of the angular rate times its sign

$$z(\dot{\theta}) = \dot{\theta}^2 sgn(\dot{\theta}) \tag{2.20}$$

such that

$${}^{dn}z = z({}^{dn}\dot{\theta}) = ({}^{dn}\dot{\theta})^2 \quad \text{and} \quad {}^{up}z = z({}^{up}\dot{\theta}) = -({}^{up}\dot{\theta})^2. \tag{2.21}$$

With this change in variables, P will be at least piecewise linear in z. We will refer to z as the *measure of angular velocity*, henceforward.

The first order equations, Equation (2.9), and collision transition functions, Equation (2.10), rewritten in terms of z, are

$$\begin{aligned} \dot{\theta} &= sgn(z)\sqrt{|z|}, & |\theta - \alpha| < \pi/n & \qquad (2.22) \\ \dot{y} &= \lambda^2 \sqrt{|z|}\sin\theta & & \\ (\theta - \alpha, z) &\mapsto (-(\theta - \alpha), \mu^2 z), & |\theta - \alpha| = \pi/n & \qquad (2.23) \end{aligned}$$

We are looking for the map P in a form given schematically as the difference equation

$$[z(\dot{\theta})]_{i+1} = P([z(\dot{\theta})]_i), \quad \dot{\theta} \in \Sigma. \tag{2.24}$$

Due to the two possible discontinuities, the map P can be composed of two linear functions. The first function applies in two cases. It applies if the slope is small enough, $\alpha \leq \frac{\pi}{n}$, and if the wheel has enough energy after a collision to make it past the vertical in the uphill or downhill direction, $z > {}^{up}z > 0$ or $z < {}^{dn}z < 0$, respectively. It is also the only part of P that applies when the slope is so large, $\alpha > \frac{\pi}{n}$, that the center of mass is always past the vertical in the downhill direction, for any measure of angular velocity, $-\infty < z < \infty$. To construct this part of the map, conservation of energy takes the measure of angular velocity of the wheel just after collision i to just before collision $i+1$ and, then, the collision transition condition, $z \to \mu^2 z$, takes the measure of angular velocity just before collision $i+1$ to just after collision $i+1$.

The second function applies if the slope is small enough, $\alpha \leq \frac{\pi}{n}$, and if the wheel does not have enough energy after a collision to make it past the vertical in the uphill or downhill direction, ${}^{up}z < z < {}^{dn}z$, and consequently reverses direction in between collisions. This part does not apply to very steep slopes. To construct this part of the map, conservation of energy between collisions

gives us that the measure of angular velocity just after collision i is equal in magnitude but opposite in sign to the measure of angular velocity just before collision $i+1$ and, again, the collision transition condition, $z \to \mu^2 z$, takes the angular velocity just before collision $i+1$ to just after collision $i+1$.

In functional form, then, the map P can be summarized as:

$$P(z(\dot{\theta})) = \begin{cases} (1) \quad \mu^2(z + 4\lambda^2 \sin\alpha \sin\frac{\pi}{n}) & \text{if } z > {}^{dn}z > 0 \text{ and } \alpha \leq \frac{\pi}{n}, \text{ or} \\ & z < {}^{up}z < 0 \text{ and } \alpha \leq \frac{\pi}{n}, \text{ or} \\ & -\infty < z < \infty \text{ and } \alpha > \frac{\pi}{n}. \\ (2) \quad -\mu^2 z & \text{if } {}^{up}z < z < {}^{dn}z \text{ and } \alpha \leq \frac{\pi}{n}. \end{cases} \tag{2.25}$$

The different regimes of slope and the measure of angular velocity for which each part of the map applies are summarized by the inequalities listed on separate lines after the definition of each part of the map.

The piecewise linearity of the map makes its graphical construction and interpretation easier. Three typical graphs of the Poincarè map, $P(z)$ versus z, are shown for $\alpha < \frac{\pi}{n}$, $\alpha = \frac{\pi}{n}$, and $\alpha > \frac{\pi}{n}$ in Figure 2.10.

Next, reconsider the first graph of the Poincaré map from the previous figure in more detail, with the parameter values, non-dimensional inertia, $2J = 0.5$, number of spokes, $n = 6$, and slope angle, $\alpha = \frac{\pi}{15} < \frac{\pi}{6}$ in Figure 2.11. Three intervals of the measure of angular velocity, z, are shown on the graph:

- 1. In the first interval, $z < {}^{up}z$, the wheel has enough energy to make it past the vertical in the uphill direction and $P(z) = \mu^2(z + 4\lambda^2 \sin\alpha \sin\frac{\pi}{n})$.
- 2. In the second interval, ${}^{up}z < z < {}^{dn}z$, the wheel does not have enough energy to make it past the vertical position in the uphill or downhill direction and $P(z) = -\mu^2 z$.
- 3. In the third interval, $z > {}^{dn}z$, the wheel has enough energy to make it past the vertical in the downhill direction and $P(z) = \mu^2(z + 4\lambda^2 \sin\alpha \sin\frac{\pi}{n})$.

The graph shows a stair-step diagram, with initial condition z_1. The progress of the wheel can be traced by following the arrows on the diagram:

- 1. The wheel starts off uphill with initial measure of angular velocity z_1 in the first interval.
- 2. The wheel makes it past the vertical and has a collision with the slope and emerges with a new measure of angular velocity $z_2 = P(z_1)$ in the second interval.
- 3. The energy lost to the collision does not leave the wheel with enough energy to make it past the vertical. It reverses direction and makes another collision with the slope leaving the wheel with the next measure of velocity $z_3 = P(z_2)$ in the third interval. The wheel now has enough energy to make it past the vertical in the downhill direction.
- 4. The wheel rolls downhill and makes repeated collisions with the slope and so on until the wheel eventually approaches a steady-state measure of angular velocity after an infinite number of collisions in finite time. The fixed point is marked by the intersection of the graph of P with the identity line $P(z) = z$.

In short, the wheel rolls uphill, collides with the slope, reverses direction, rolls downhill and approaches the limit cycle motion in infinite time, from below. Previously, we denoted this motion in Section 2.2.4 as Up$\to$ Down$\overset{+}{\to}$ Limit Cycle.

Next, we show how the character of the return map P varies with the slope angle for fixed inertia J and number of spokes n. In Figure 2.12, the return map is shown for a variety of slope angles.

We define and find the fixed points of P and determine their stability exactly in the next section.

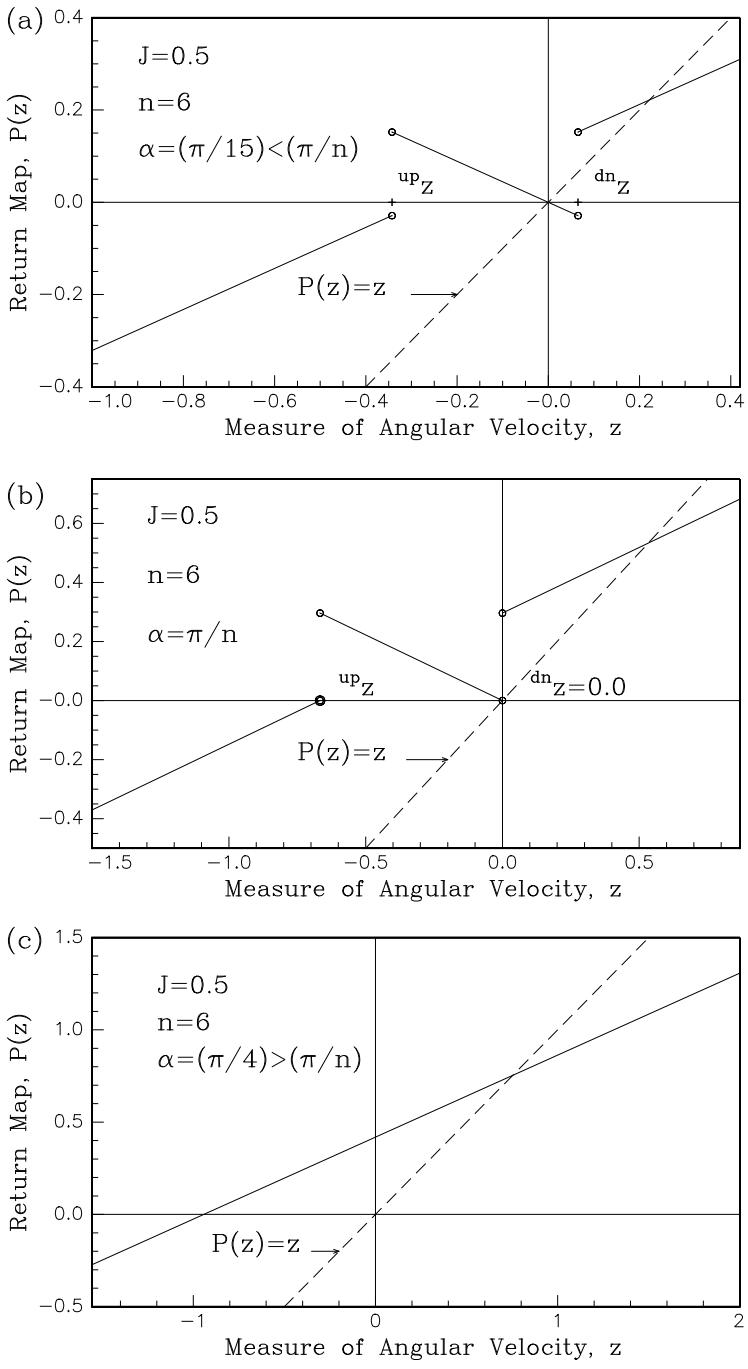

Figure 2.10: Three typical graphs of the Poincarè map, $P(z)$ versus z, with $2J = 0.5$ and $n = 6$:(a) $\alpha = \frac{\pi}{15} < \frac{\pi}{n}$, showing the piecewise linearity and two discontinuities at $z = {}^{up}z$ and $z = {}^{dn}z$; (b) $\alpha = \frac{\pi}{6} = \frac{\pi}{n}$, showing the piecewise linearity and the two discontinuities of the map at ${}^{dn}z = 0$ and ${}^{up}z = -\sqrt{4\lambda^2 \sin^2 \frac{\pi}{n}}$; and (c) $\alpha = \frac{\pi}{4} > \frac{\pi}{n}$, showing the linearity of the map for all z. The open circles in (a) and (b) indicate that the maps are not defined at these locations.

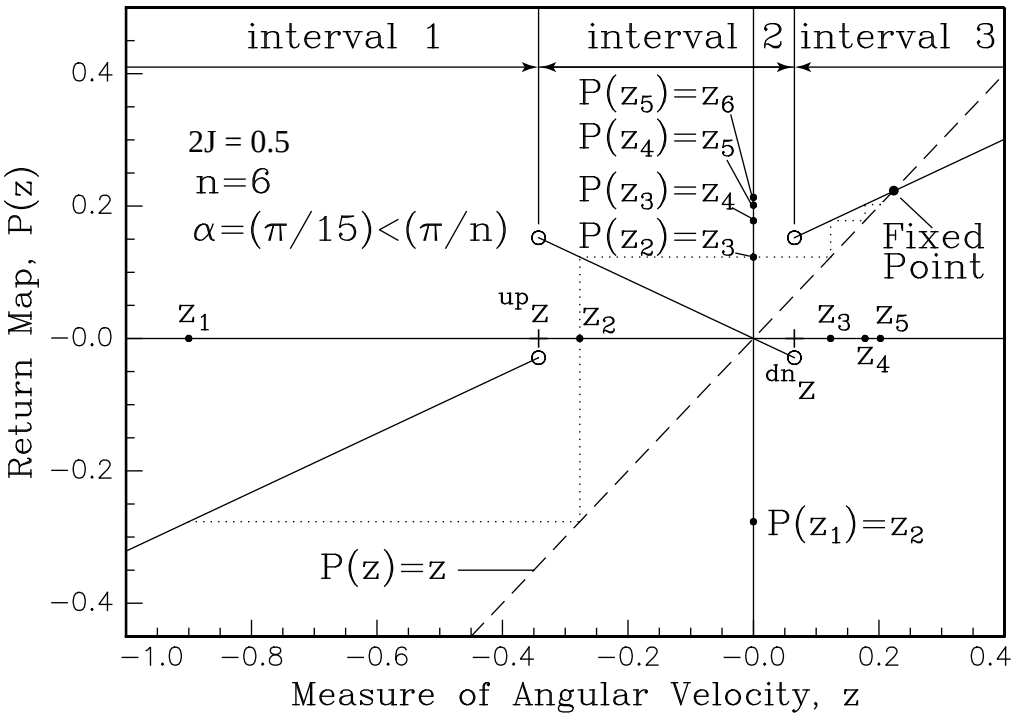

Figure 2.11: The graph of the Poincarè map with $2J = 0.5$, $n = 6$, and $\alpha = \frac{\pi}{15} < \frac{\pi}{6}$. Three intervals of the measure of velocity after each collision, z, are shown: (1) $z <^{up} z < 0$, (2) $^{up}z < z < ^{dn}z$, and (3) $z > ^{dn}z$. A stair-step diagram is shown with initial condition z_1 for several iterations. The wheel starts off uphill at initial value z_1, makes it past the vertical, collides with the slope, and emerges with $P(z_1) = z_2$. The wheel does not make past the vertical now, reverses direction, collides with the slope, and emerges with $P(z_2) = z_3$. Thereafter, it continues to make it past the vertical position after each collision increasing its angular velocity as it goes until it eventually converges in infinite time to the fixed point shown on the diagram. The fixed point is at the intersection of the graph with the identity line, $P(z) = z$.

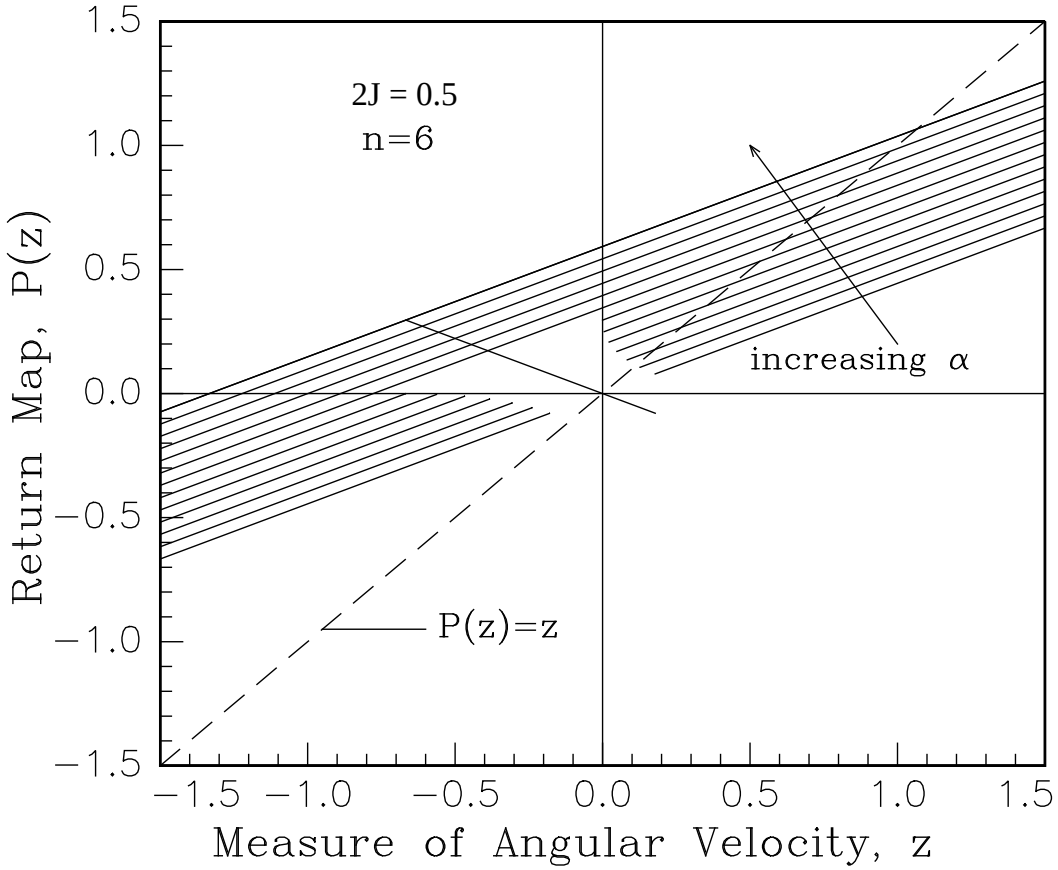

Figure 2.12: The return map is shown for a variety of slope angles, $0 \leq \alpha \leq \frac{\pi}{2}$ and $2J = 0.5$ and $n = 6$. Note that the the part of the map $P(z) = -\mu^2 z$ cannot be represented properly as α varies since for each α the slope of the map is the same but the values of ${}^{up}z$ and ${}^{dn}z$ are different; i.e., the part of the map $P(z) = -\mu^2 z$ overlaps for each α.

2.5 Fixed Points and Stability

The limiting states, limit cycle motion and the eventual stopping of the wheel, are fixed points of the map P, since, for each of these limiting states, the state of the wheel is the same after every collision. The vertical unstable vertical equilibrium is not a fixed point of P, however, since the wheel does not complete a cycle in that case. The vertical position is, however, an unstable equilibrium of the system describing the motion *in between* collisions.

Here, we find the analytical expressions for the measure of angular velocity associated with the limit cycle and show that the fixed points are asymptotically stable by showing that the absolute value of the slope of the map evaluated at the fixed points is less than one.

2.5.1 Fixed Points of P

A point z^* is a fixed point of P if $P(z^*) = z^*$. The possible fixed points of P are:

$$z^* = \begin{cases} (1) & {}^{lc}z^* \equiv \frac{4\mu^2\lambda^2 \sin\frac{\pi}{n}\sin\alpha}{1-\mu^2} > 0 \\ (2) & {}^{stp}z^* \equiv 0, \end{cases} \quad . \tag{2.26}$$

The non-zero fixed point ${}^{lc}z^*$ is the measure of angular velocity after each collision that corresponds to the limit cycle motion. The limit cycle is approached monotonically from above or below as the wheel rolls down the slope. The zero fixed point ${}^{stp}z^*$ is the measure of angular velocity that corresponds to the stopped position of the wheel at rest on two spokes. The stopped position is approached monotonically as the wheel rocks back and forth between two spokes. The angular velocities corresponding to the fixed points are ${}^{lc}\dot{\theta}^* = \sqrt{{}^{lc}z^*} > 0$ and ${}^{stp}\dot{\theta}^* = {}^{stp}z^* = 0$.

The ranges of slope angles for which the limit cycle and stopped condition fixed points exist and the initial conditions which are attracted to the fixed points are specified in a subsequent section.

2.5.2 Stability of the Fixed Points

The stability of a fixed point of a scalar map is determined by the first derivative of the map evaluated at that point. A fixed point z^* of P is asymptotically stable if the absolute value of the first derivative of the map evaluated at the fixed points is less than one, $|DP(z^*)| < 1$. The first derivative of the map P at the fixed points ${}^{lc}z^*$ and ${}^{stp}z^*$ is

$$DP(z^*) = \begin{cases} \left.\frac{dP}{dz}\right|_{z={}^{lc}z^*} = \mu^2 \\ \left.\frac{dP}{dz}\right|_{z={}^{stp}z^*} = -\mu^2 \end{cases} \quad . \tag{2.27}$$

Since the collision parameter μ is always less than one, $0 \leq \mu < 1$, the first derivative of the map at the fixed points is always less than one, $|DP(z^*)| < 1$. Both fixed points of P, ${}^{lc}z^*$ and ${}^{stp}z^*$ are, thus, asymptotically stable.

In the next section, we present the conditions on the wheel parameters for the existence of the fixed points, and for given wheel parameters, which initial conditions are attracted to the fixed points.

2.6 Existence of Fixed Points and Their Basins of Attraction of Initial Angular Velocities after Collision

A sufficient condition on the slope angle for the existence of the the limit cycle associated with the fixed point ${}^{lc}z^*$ is $\alpha > \frac{\pi}{n}$. The condition is sufficient since, for steep slopes and any measure of angular velocity, only the limit cycle exists. In other words, the map is linear and continuous with positive slope less than one, for all z, and, hence, intersects the identity line $P(z) = z$ only once

at some positive measure of angular velocity, the limit cycle fixed point. The graph of the map in Figure 2.10(c) shows how only the limit cycle exists for $\alpha > \frac{\pi}{n}$.

A necessary condition for the existence of the stopped position associated with the fixed point ${}^{stp}z^*$ is $\alpha \leq \frac{\pi}{n}$. This condition is necessary since the second part of the map does not exist for $\alpha > \frac{\pi}{n}$ and, thus, the wheel can never approach the stopped position; i.e., the part of the map that intersects the identity line at $z = 0$ is not defined. The graphs of the map in Figure 2.10(a) and Figure 2.10(c) illustrate how the stopped condition does not exist for $\alpha > \frac{\pi}{n}$.

We have not presented the complete conditions on slope angle that guarantee the existence of the fixed points. There are additional restrictions, however, on the slope angle that, together with those above, completely specify the existence of the fixed points. Below, we derive the additional conditions for the existence of the fixed points.

2.6.1 Slope Angle and Existence of the Fixed Points

The necessary condition for the existence of the limit cycle corresponding to the fixed point ${}^{lc}z^* > 0$ can be derived as follows. For a limit cycle to exist, the wheel must be able to make it past the vertical position in the downhill direction repeatedly after each collision; i.e., the angular velocity of the limit cycle must be greater than the angular velocity just after a collision required to reach the vertical in infinite time, ${}^{dn}\dot{\theta}$. Written in terms of the measure of angular velocity after collision, this requirement is

$$ {}^{lc}z^* > {}^{dn}z. \tag{2.28}$$

Referring to the definitions of ${}^{lc}z^*$ in Equation (2.26) and ${}^{dn}z$ in Equation (2.21) this inequality can be rewritten as a criterion relating slope angle α, nondimensional inertia λ^2, and number of spokes n,

$$ g(\alpha, \lambda^2, n) \equiv 1 - \cos\frac{\pi}{n}\cos\alpha - \frac{1+\mu^2}{1-\mu^2}\sin\frac{\pi}{n}\sin\alpha < 0. \tag{2.29}$$

Taking α as a function of λ^2 and n, this inequality requires that

$$ \alpha > \alpha_c \tag{2.30}$$

where α_c is a solution to $g(\alpha, \lambda^2, n) = 0$. A graph of $g(\alpha, \lambda^2, n)$ versus α for fixed λ^2 and n verifies that $\alpha > \alpha_c$ satisfies the inequality in Equation 2.29(See Figure 2.13).

A necessary condition, then, for the existence of the limit cycle corresponding to the fixed point ${}^{lc}z^* > 0$ and the stopped position corresponding to the fixed point ${}^{stp}z^* = 0$ are $\alpha > \alpha_c$ and $\alpha \leq \frac{\pi}{n}$, respectively.

We can now summarize the necessary and sufficient conditions on slope angle for the existence of the fixed points of P:

- $0 \leq \alpha < \alpha_c$, only ${}^{stp}z^*$ exists,
- $\alpha_c \leq \alpha \leq \frac{\pi}{n}$, both ${}^{lc}z^*$ and ${}^{stp}z^*$ exist, and
- $\alpha > \frac{\pi}{n}$, only ${}^{lc}z^*$ exists.

As α is varied, then, the number and type of fixed points changes. The appearance and disappearance of the fixed points as the slope angle α is varied cannot be classified according to the classical theory of bifurcation of scalar maps due to the discontinuity in the Poincaré map. The fixed points are shown as a function of α in Figure 2.14.

In the next section we quantify the domains of attraction for the fixed points within each of the three slope intervals.

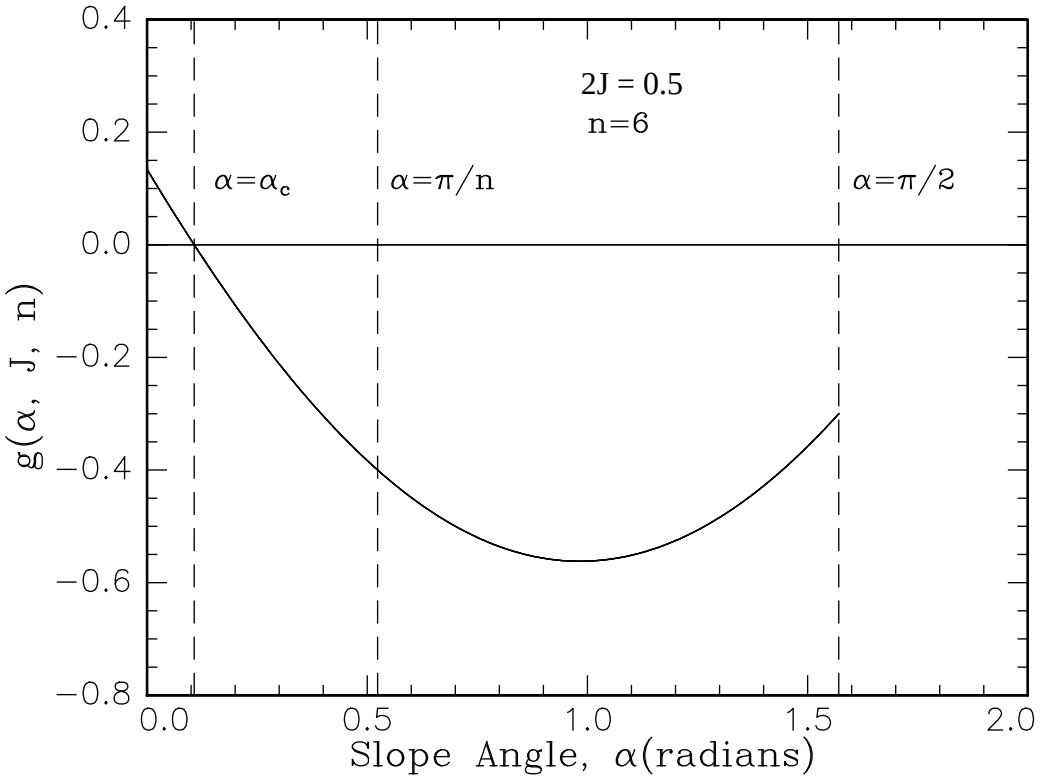

Figure 2.13: A graph of $g(\alpha, \lambda^2, n)$ versus α for $2J = 0.5$ and $n = 6$. The function g is less than zero for $\alpha > \alpha_c$. If $g < 0$, then limit cycles can exist.

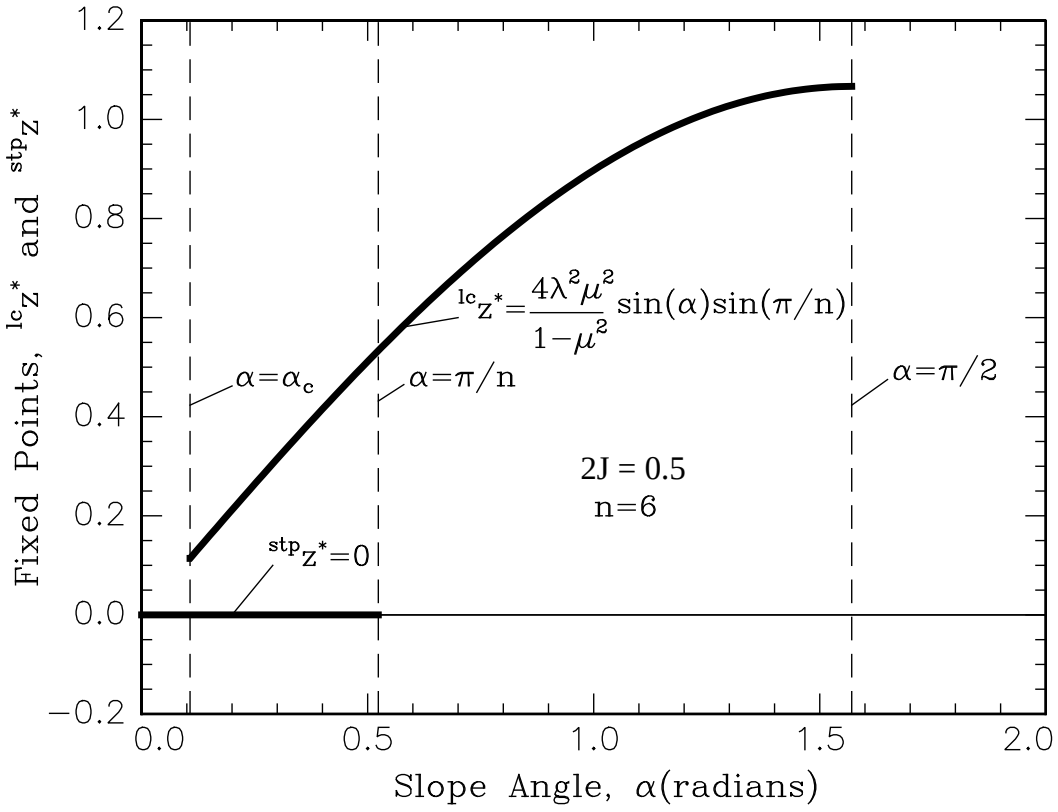

Figure 2.14: The fixed points of P are graphed as a function of slope angle α for $2J = 0.5$ and $n = 6$. The graph shows that only the stopped position is available as a limiting state for $\alpha < \alpha_c$, both the stopped position and the limit cycle are available as limiting states for $\alpha_c \leq \alpha \leq \frac{\pi}{n}$, and only the limit cycle is available as a limiting state for $\alpha > \frac{\pi}{n}$.

2.6.2 Basins of Attraction for the Fixed Points

So far, we have determined within each slope interval which fixed points exist. We also know that, for all initial conditions, the wheel always enters into a limit cycle for steep slopes, $\alpha > \frac{\pi}{n}$. Any initial condition is attracted to limit cycle motion for this slope range since the map P is linear, with slope less than one, continuous for all z, and thus intersects the identity line only once at some non-zero measure of angular velocity. The domains of attraction for the fixed points within the remaining two slope intervals remains to be prescribed because of the piecewise linearity of the map and the possibility of the wheel eventually stopping in the vertical position after one or more collisions.

The values of initial measure of angular velocity attracted to the fixed points for shallow and intermediate slopes can be completely specified by considering two situations regarding the measure of angular velocity. We describe the two situations first and then follow with a detailed analysis of each.

First, for rolling uphill or downhill on shallow or intermediate slopes, it is possible that the wheel starts with a velocity just after collision that eventually leaves the wheel, after one or more collisions, with the critical velocities after collision for reaching the vertical position in infinite time, ${}^{up}\dot{\theta}$ or ${}^{dn}\dot{\theta}$. For such initial conditions, limit cycles and the stopped position cannot exist. The initial conditions that eventually leave the wheel in the vertical position can be found as three different monotonic infinite sequences of angular velocities after collision where each term in the sequence depends on the wheel parameters.

Second, for intermediate slopes only, the wheel can do one of three things: reach the vertical position, come to rest on two spokes, or approach the limit cycle. Initial angular velocities which are attracted to the limit cycle and those which are attracted to the stopped position are organized into alternating 'patches' of initial angular velocity after collisions; i.e., alternating subsets of the domain of the map P that we call *basins of attraction*. The 'patches' can be visualized as alternating line segments along the horizontal axis of the graph of $P(z)$. The boundaries of the the 'patches' are the defined by the critical angular velocities after collision for reaching the vertical in infinite time and the terms in the infinite sequences described above that eventually get mapped to the vertical position.

Infinite Sequences of Angular Velocity After Collision

We first describe qualitatively the three very special and improbable infinite sequences of the after-collision angular rate that leave the wheel eventually in the vertical position. Then, we will define them and the criteria for their existence precisely in Appendix C.

- 1. The first sequence of points is defined for initially rolling downhill with greater angular velocity after collision than that required to eventually stop in the vertical position. For any point in the sequence, the wheel will eventually reach the vertical in the downhill direction. The sequence is written as ${}^{dn}z_m > {}^{dn}z$ for $m = 1, 2, 3, \ldots$ and exists only for nearly flat slopes, $\alpha < \alpha_c$.

- 2. The second sequence of points is defined for initially rolling uphill with angular velocity after collision greater in magnitude than that required to eventually stop in the vertical in the uphill direction. For any point in the sequence, the wheel will eventually reach the vertical in the uphill direction. The sequence is written as ${}^{up}z_m <^{up} z$ for $m = 1, 2, 3, \ldots$ and exists for nearly flat and intermediate slopes, $0 \leq \alpha \leq \frac{\pi}{n}$.

- 3. The third sequence of points is defined for initially rolling uphill with angular velocity after collision greater in magnitude than that required to eventually stop in the vertical position. The wheel, however, eventually reverses direction after one or more uphill collisions and then makes one downhill collision before stopping in the vertical position in the downhill direction

in infinite time. This sequence is written as ${}^{up}\bar{z}_m <^{up} z$, $m = 1, 2, 3, \ldots$ and exists only for intermediate slopes, $\alpha_c < \alpha < \frac{\pi}{n}$.

The existence of these sequences and critical angular velocities, as we have shown in Appendix C, depends upon slope angle and is summarized in Table 2.1. In the next section, we define the alter-

Table 2.1: The existence of the critical angular velocities and sequences of angular velocities for $0 \leq \alpha \leq \frac{\pi}{2}$. The existence of the points and sequences in each slope regime are noted by an asterisk in each column of the table.

	Measures of Angular Velocity					
Slope Angle α	${}^{up}z$	${}^{up}z_m$	${}^{dn}z$	${}^{dn}z_m$	${}^{up}\bar{z}$	${}^{up}\bar{z}_m$
$0 \leq \alpha < \alpha_c$	*	*	*	*		
$\alpha = \alpha_c$	*		*			
$\alpha_c < \alpha < \frac{\pi}{n}$	*	*	*		*	*
$\alpha = \frac{\pi}{n}$	*	*				
$\frac{\pi}{n} < \alpha \leq \frac{\pi}{2}$						

nating basins of attraction of initial angular velocity after collision that exist only for intermediate slopes.

Alternating Basins of Attraction of Angular Velocity After Collision for Intermediate Slopes

The alternating basins of attraction exist only for intermediate slope angles, $\alpha_c < \alpha \leq \frac{\pi}{n}$. For this slope range, if the wheel starts off downhill, it has one of three initial energies: (1) the critical energy for reaching the vertical in infinite time (denoted by Down$\rightarrow$ Vertical), (2) less than the energy needed to pass the vertical in the downhill direction so that it approaches the stopped position by rocking back and forth on two spokes (denoted by Down$\rightarrow$ Rock $\rightarrow$ Stop), or (3) more than the energy needed to pass the vertical so that it approaches the limit cycle from above or below (denoted by Down$\stackrel{-}{\rightarrow}$ Limit Cycle or Down$\stackrel{+}{\rightarrow}$ Limit Cycle, respectively).

If the wheel starts uphill, it has one of three initial energies: (1) critical energy for reaching the vertical in infinite time(denoted by Up$\rightarrow$ Vertical), (2) energy such that the initial angular velocity is in one of the critical sequences and it eventually stops in the vertical position, or (3) enough energy to pass the vertical in the uphill direction but, after one or more collisions, loses so much energy in the collision(s) that, eventually, it cannot make it past the vertical, reverses direction and starts downhill. The subsequent behavior after the wheel reverses direction is determined by the the energy of the wheel after the last collision before reversing direction. If the wheel has too little energy after the last collision before reversing direction, it makes one downhill collision, cannot make it past the vertical in the downhill direction, rocks back and forth between two spokes, and approaches the stopped position (Stop) (denoted by Up$\rightarrow$ Rock $\rightarrow$ Stop). If the wheel has sufficient energy after the last collision before reversing direction, it has enough energy to pass the vertical in the downhill direction, increases in angular velocity and approaches the limit cycle (Limit Cycle) from below (denoted by Up$\rightarrow$ Down $\stackrel{+}{\rightarrow}$ Limit Cycle).

For intermediate slopes, whether starting off downhill or uphill, the initial energy of the wheel, then, predetermines if the wheel will reach the vertical position, the limit cycle, or the stopped position. If the wheel starts with the measure of angular velocity ${}^{dn}z$ and ${}^{up}z$ or one of the measures of angular velocity in the sequences ${}^{up}z_m$ or ${}^{up}\bar{z}_m$, the wheel will eventually stop in the vertical position, as we have shown.

Now, we show that similarly well defined sets of initial measure of angular velocity eventually approach either the limit cycle or the stopped condition, exclusively. As we noted, the initial

angular velocities that are attracted to the limit cycle and those which are attracted to the stopped position are organized into alternating 'patches' or basins of attraction. If the angular velocities in a given basin of attraction get mapped to the limit cycle, the adjacent basin of initial conditions gets mapped to the stopped condition, and so on, for each succeeding 'patch', alternating in this way. The boundaries of the basins are formed by the critical measures of angular velocity, ${}^{dn}z$ and ${}^{up}z$, and the terms of the second and third sequences we have just defined, ${}^{up}z_m$ and ${}^{up}\bar{z}_m$.

In order to define the basins of attraction, we need first to order the critical points and the terms of the second and third sequences. The critical points and the terms of the sequences are ordered as follows:

$$ {}^{up}z_m < {}^{up}\bar{z}_m < {}^{up}z < {}^{up}\bar{z} < 0 \tag{2.31} $$

and

$$ {}^{up}z_{m+1} < {}^{up}\bar{z}_{m+1} < {}^{up}z_m. \tag{2.32} $$

It is trivial to prove that these inequalities hold for $\alpha_c < \alpha < \frac{\pi}{n}$.

Now that the important points are ordered, which basins are attracted to the limit cycle and which are attracted to the stopped position can be determined visually by examining graphs of the Poincaré map. For example, reconsider the map of Figure 2.11 in Figure 2.15 with restrictions on the measure of angular velocity added for determining which fixed points exist.

Thus, generalizing from the special case illustrated in Figure 2.15 for $\alpha_c < \alpha < \frac{\pi}{n}$, we state without proof: the basins of attraction for the limit cycle are

$$ z > {}^{dn}z, {}^{up}z < z < {}^{up}\bar{z}, \quad \text{and} \quad {}^{up}z_m < z < {}^{up}\bar{z}_m, \tag{2.33} $$

and the basins of attraction for the stopped position are

$$ {}^{up}\bar{z} < z < {}^{dn}z, {}^{up}\bar{z}_1 < z < {}^{up}z, \quad \text{and} \quad {}^{up}\bar{z}_{m+1} < z < {}^{up}z_m. \tag{2.34} $$

The basins of attraction for the fixed fixed points given intermediate slope angles, $\alpha_c < \alpha < \frac{\pi}{n}$, are summarized in Table 2.2.

Table 2.2: The basins of attraction for the fixed points corresponding to the limit cycle and the stopped position with intermediate slope angle, $\alpha_c < \alpha < \frac{\pi}{n}$, are noted by an asterisk in each row of the table.

	Fixed Points	
Measure of Angular Velocity	${}^{lc}z^*$	${}^{stp}z^*$
${}^{up}\bar{z}_{m+1} < z < {}^{up}z_m$		*
${}^{up}z_m < z < {}^{up}\bar{z}_m$	*	
${}^{up}\bar{z}_1 < z < {}^{up}z$		*
${}^{up}z < z < {}^{up}\bar{z}$	*	
${}^{up}\bar{z} < z < {}^{dn}z$		*
$z > {}^{dn}z$	*	

In the next section, we consider the behavior of the wheel for some special values of the wheel parameters.

2.6.3 Special Cases

If $\alpha = \alpha_c$, the limit cycle can only be approached from above and the limit cycle angular velocity is equal to the angular velocity after collision in the downhill direction for stopping in the vertical position in infinite time; i.e., ${}^{dn}z = {}^{lc}z^*$.

If $\alpha = \frac{\pi}{n}$,

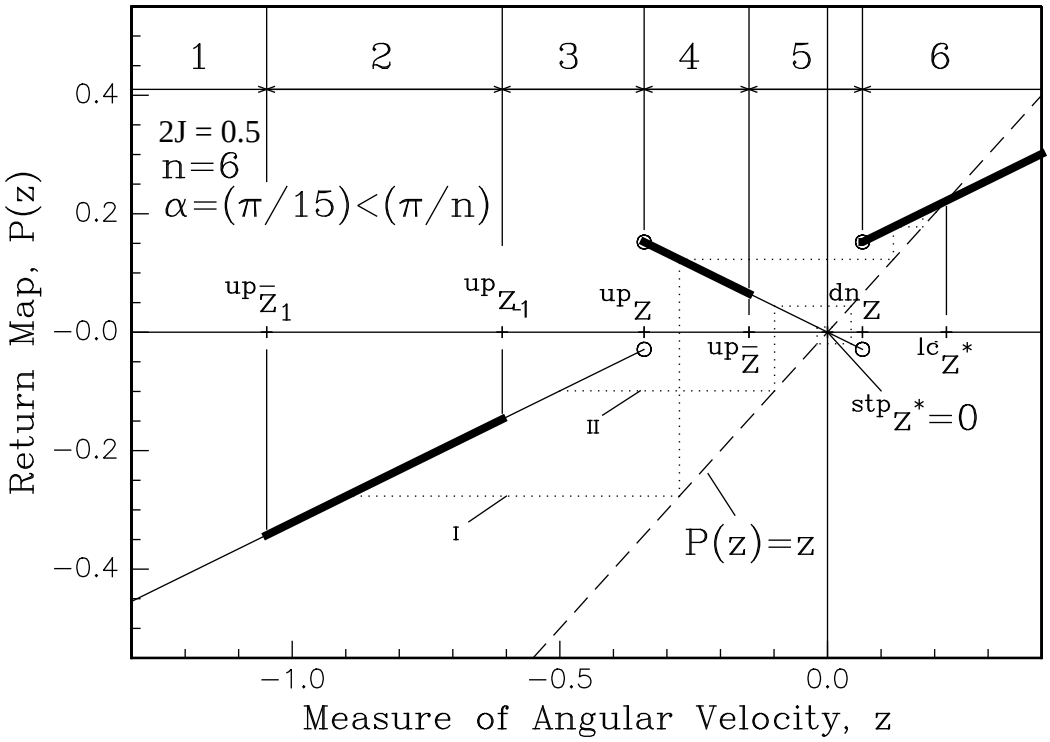

Figure 2.15: Again, the graph of the Poincarè map with $2J = 0.5$, $n = 6$, and $\alpha = \frac{\pi}{15} < \frac{\pi}{6}$. The critical measures of angular velocity, the fixed points, and the sequences ${}^{up}z_m$ and ${}^{up}\bar{z}_m$ are marked on the graph up to $m = 1$ for the given wheel parameters. The basins of initial measure of angular velocity attracted to the limit cycle are marked on the graph with bold line segments to differentiate them from those attracted to the stopped position. Six representative basins of attraction are labelled on the graph. Initial conditions in the intervals (1), ${}^{up}\bar{z}_2 < z < {}^{up}z_1$, (3), ${}^{up}\bar{z}_1 < z < {}^{up}z$, and (5), ${}^{up}\bar{z} < z < {}^{dn}z$ get mapped to the stopped condition corresponding to the fixed point ${}^{stp}z^*$. Initial conditions in the intervals (2), ${}^{up}z_1 < z < {}^{up}\bar{z}_1$, (4), ${}^{up}z < z < {}^{up}\bar{z}$, and (6), ${}^{dn}z < z < \infty$ get mapped to the limit cycle corresponding to the fixed point ${}^{lc}z^*$. The orbit labelled I starts in interval(2) and goes to the limit cycle fixed point. The orbit labelled II starts in interval (3) and goes to the zero fixed point.

- 1. The wheel is oriented at the vertical position $\theta = 0$ at each collision. The critical measures of angular velocity are ${}^{dn}z = 0$ and ${}^{up}z = -4\lambda^2 \sin^2 \frac{\pi}{n}$.
- 2. If the measure of angular velocity is $z > 0$, the wheel will roll down the slope. If $z = 0$, a small positive disturbance will cause the wheel to fall downhill.
- 3. If the measure of angular velocity is ${}^{up}z < z < 0$, the wheel makes a collision instantaneously with the slope in the uphill direction but loses so much energy in collision that it cannot reach the next vertical position and falls back down the slope eventually entering into a limit cycle.
- 4. If the angular velocity just after collision is $z < {}^{up}z < 0$, the wheel makes a collision instantaneously with the slope in the uphill direction and makes one or more collisions in the uphill direction before reversing direction and approaching a limit cycle..

In this case, ${}^{dn}z = {}^{stp}z^* = 0$. Thus, the vertical position, balanced at rest unstably on one spoke, and the stopped position, at rest stably on two spokes, are indistinguishable for $\alpha = \frac{\pi}{n}$. The only way, then, in which the stopped condition, corresponding to the fixed point ${}^{stp}z = {}^{dn}z^* = 0$, can exist is if the wheel stays at rest, $z = 0$.

Next, for $0 \leq 2J \leq 1$ and $3 \leq n < \infty$, it can be shown that $\alpha_c \leq \frac{\pi}{n}$. The case $\alpha_c = \frac{\pi}{n}$ occurs when $\mu = 0$ or $2J = -\cos(\frac{2\pi}{n}) \geq 0$; i.e., when $2J = 0.5$ and $n = 3$ or $J = 0$ and $n = 4$.

If $\mu = 0$, the angular rate after collision equals zero, according to the collision condition, Equation (2.10), and, thus, for any initial conditions, only the stopped position exists. The wheel either rotates past the vertical or does not and then comes to a complete stop after one collision in finite time, (not by rocking back and forth on two spokes and coming to a stop after infinite collisions in finite time). We denoted this behavior previously by Up$\rightarrow$ Stop or Down$\rightarrow$ Stop. These behaviors only exist, then, for $\alpha \leq \frac{\pi}{n}$.

If $n = 3$ and $0 \leq 2J < -\cos\frac{2\pi}{n} = 0.5$, then $-0.5 \leq \mu < 0$. For this parameter combination where $\mu < 0$, the wheel would instantaneously reverse direction after a collision AND slow down, leading to an infinite sequence of collisions in *zero* time with *no* motion. That, is, the entire wheel stops dead, not just the tip of the colliding spoke.

To summarize:

1. if $n = 4$ and $J = 0$, then $\mu = 0$ and
2. if $n = 3$ and $0 \leq 2J \leq -\cos\frac{2\pi}{n} = 0.5$ then $-0.5 \leq \mu \leq 0$.

In both cases (a) and (b) above, the wheel comes to a dead stop.

The dependence of the critical angles on the number of spokes, n, and inertia parameter, J, are shown in Figure 2.16.

2.6.4 Summary of the Existence Criteria and Basins of Attraction for Fixed Points

In Table 2.3, we summarize the necessary and sufficient conditions on slope angle, α, and measure of angular velocity, z, that specify which of the fixed points will arise. We display the information tabulated in Table 2.3 in a diagram in Figure 2.17. If similar information shown in Figure 2.17, were plotted in the phase plane, or on a phase cyclinder, we would notice that the 2D rimless wheel dynamics is nearly completely analogous in qualitative behavior to the forced, damped simple pendulum (see, for example, the excellent discussion in Andronov, *et al* [56], pp. 422–436). The main difference bewteen the systems, of course, is the discontinous decrease in velocities for the wheel due to spoke collisions. For certain combinations of torques and damping constants, three cases arise for the pendulum, depending on the initial conditions: (1) only stable limit cycles exist; (2) both stable limit cycles and tending to a state of rest exist; and (3) no limit cycles exist and no coming to rest. Case (2) is similar to the case for the rimless wheel shown in Figure 2.17. Given

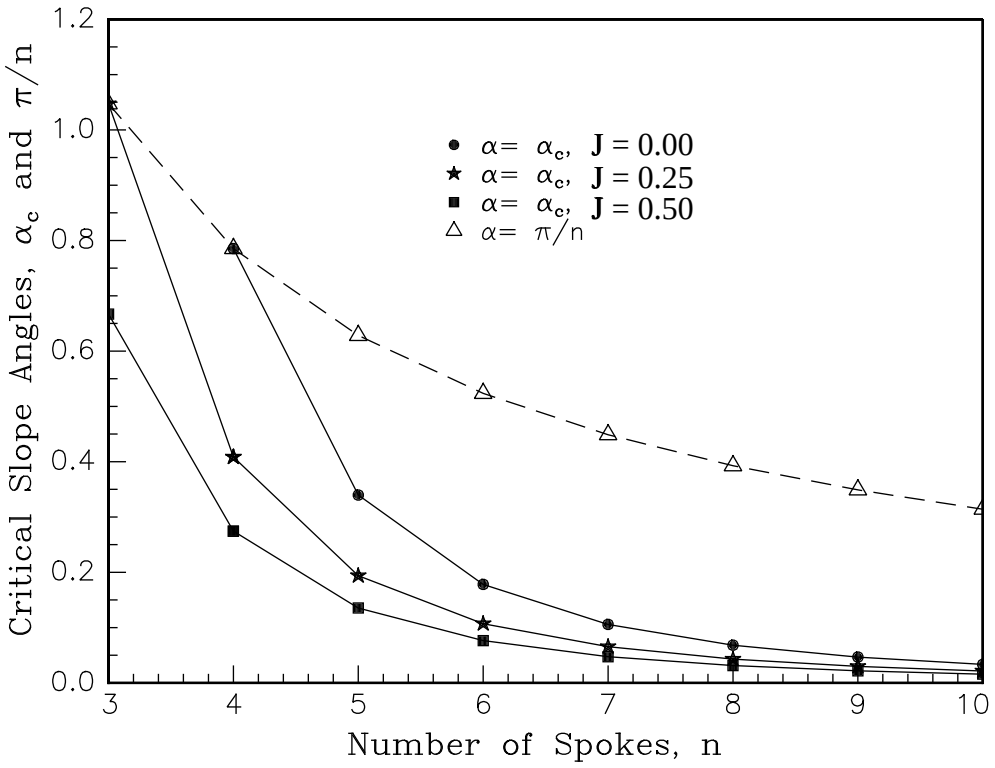

Figure 2.16: The critical angles, α_c and $\frac{\pi}{n}$, are shown as functions of n for several values of J. The critical angles α_c and $\frac{\pi}{n}$ are discrete functions of n but the function values are connected with lines for illustrative purposes.

Table 2.3: The dependence of the fixed points on the wheel parameters and the basins of attraction for the fixed points are summarized in the table. The critical angles, α_c and $\frac{\pi}{n}$, are functions of the non-dimensional inertia, J and the number of spokes, n. The critical measures of the angular velocity are functions of α, J, and n. For each slope range and all possible initial conditions, which fixed points arise is denoted by an asterisk in the appropriate column.

		Fixed Points	
Slope Angle α	Measure of Angular Velocity	${}^{lc}z^*$	${}^{stp}z^*$
$0 \le \alpha < \alpha_c$	$z \neq {}^{dn}z, {}^{dn}z_m, {}^{up}z, {}^{up}z_m$		*
$\alpha_c \le \alpha \le \frac{\pi}{n}$	${}^{up}\bar{z}_{m+1} < z < {}^{up}z_m$		*
	${}^{up}z_m < z < {}^{up}\bar{z}_m$	*	
	${}^{up}\bar{z}_1 < z < {}^{up}z$		*
	${}^{up}z < z < {}^{up}\bar{z}$	*	
	${}^{up}\bar{z} < z < {}^{dn}z$		*
	$z > {}^{dn}z$	*	
$\frac{\pi}{n} < \alpha \le \frac{\pi}{2}$	all z	*	

a damping constant and torque within certain ranges, initial conditions are attracted to either (1) a stable focus or node (a rest position) or (2) a stable limit cycle. The regions of attraction can be displayed on a phase cyclinder. For the wheel, too, there are three regimes depending on slope angle. Coming to rest, however, is an option in the third regime for the wheel.

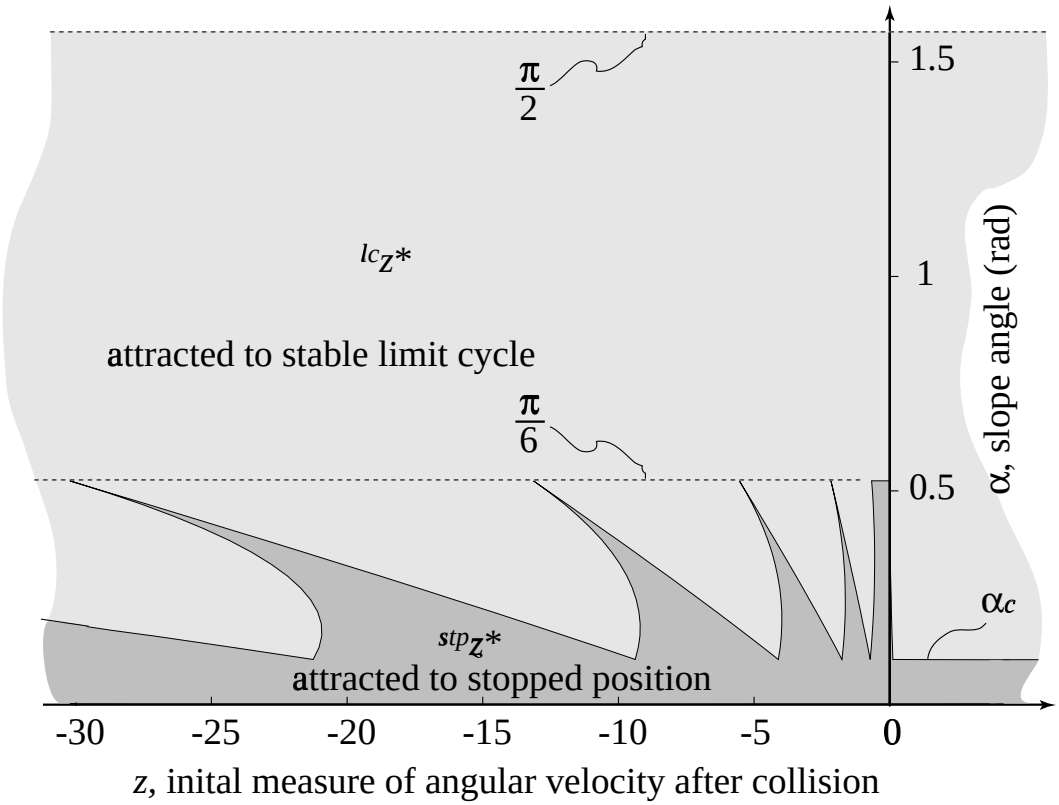

Figure 2.17: A plot displaying the information summarized in Table 2.3. The basins of attraction for the two fixed points are plotted for $n = 6$ and $2J = 0.5$. Initial speeds z falling in the dark gray region for a given slope angle α are attracted to ${}^{stp}z^*$ and those falling in the light gray region are attracted to a limit cycle, ${}^{lc}z^*$.

Finally, using another representation to display the existence criteria for the fixed points and their dependence on initial conditions, we code the maps previously shown in Figure 2.12 to show which initial conditions are attracted to the limit cycle and those which are attracted to the stopped position. (See Figures 2.18 and 2.19.)

In Figures 2.18, 2.19, and 2.17 there are analytical expressions for the curves bounding the regions that mark the basins of attraction for each slope angle.

Two of the bounding curves are formed by the set of critical angular velocities for reaching the vertical in infinite time, ${}^{dn}z(\alpha)$ and ${}^{up}z(\alpha)$ for slope angle $0 \leq \alpha < \frac{\pi}{n}$. The curves can be found as functions of z.

In terms of the map P, we define the first curve as

$$\begin{aligned} f({}^{dn}z(\alpha)) &\equiv P({}^{dn}z(\alpha)) \\ &= \mu^2({}^{dn}z(\alpha) + 2\lambda^2(\cos(\alpha - \frac{\pi}{n}) - \cos(\alpha + \frac{\pi}{n})) \\ &= 2\lambda^2\mu^2(1 - \cos(\alpha + \frac{\pi}{n})) \end{aligned} \tag{2.35}$$

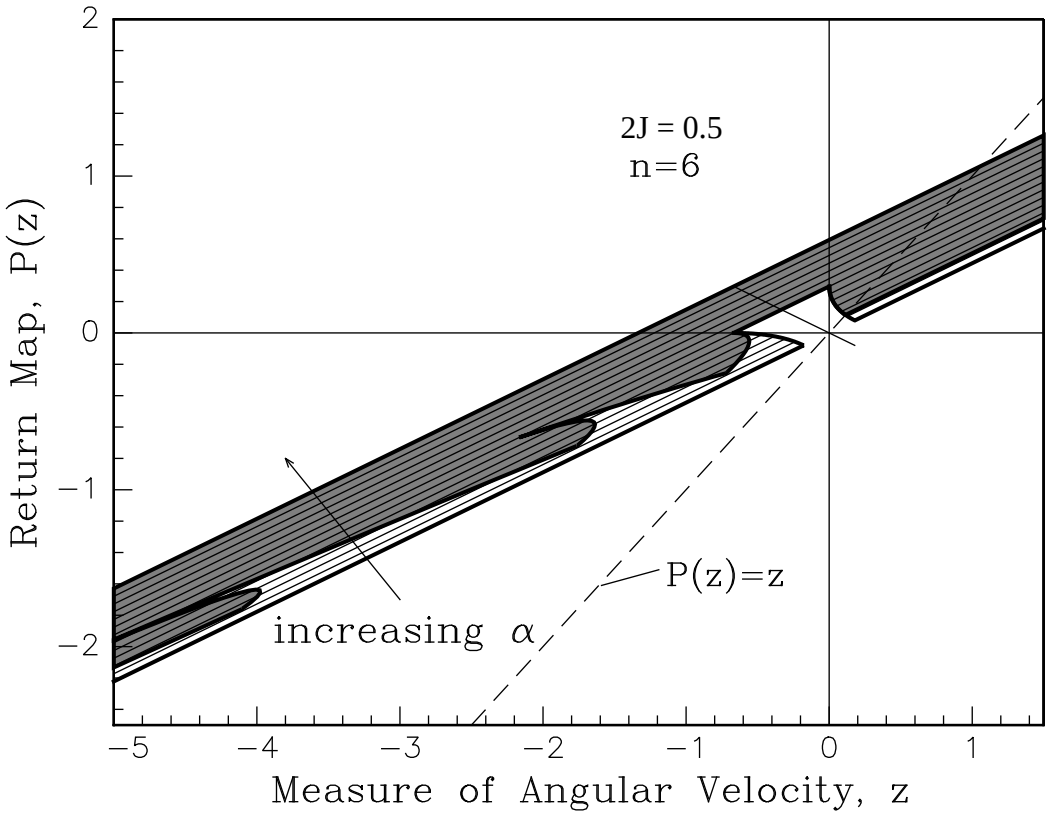

Figure 2.18: The return map is shown for a variety of slope angles, $0 \leq \alpha \leq \frac{\pi}{2}$ and $2J = 0.5$ and $n = 6$. The initial values on the horizontal axis corresponding to the shaded region get mapped eventually to the limit cycle fixed point, ${}^{lc}z^*$. All other initial conditions get mapped to the stopped position fixed point, ${}^{stp}z^*$. Note that the maps are not coded for ${}^{up}z < z^{dn}z$ are not coded because for each α the map information is overlapping in this interval of measure of angular velocity.

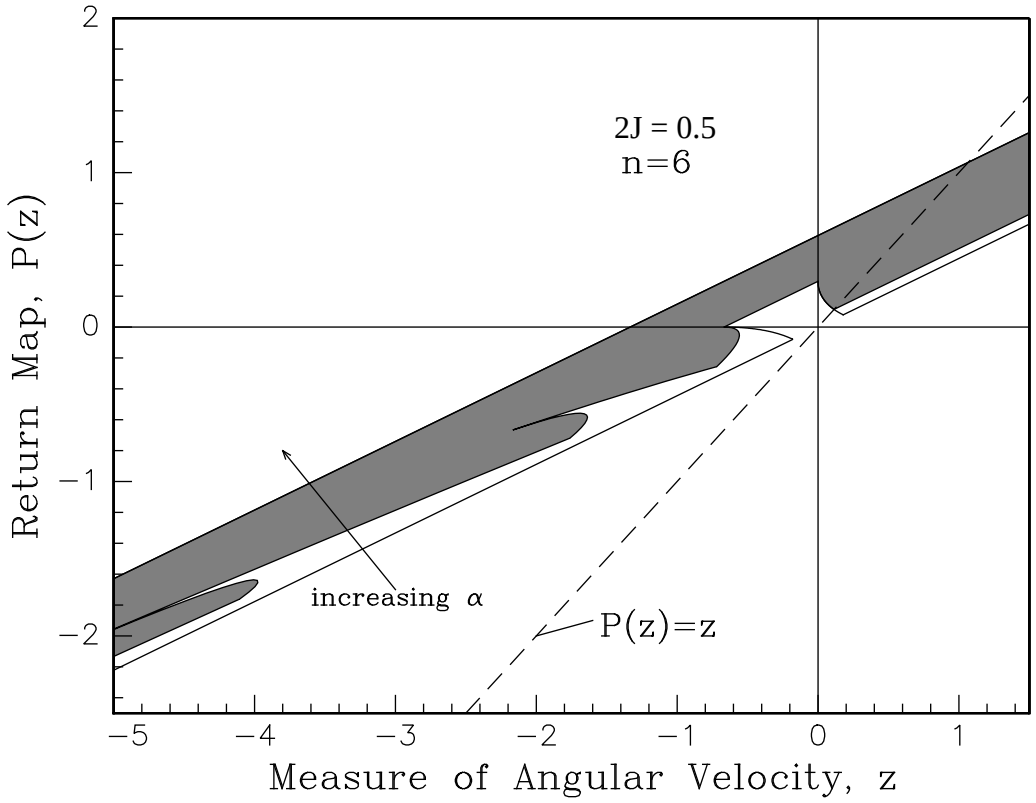

Figure 2.19: In this plot, only the bounding curves on the regions and the shaded region that get mapped to each fixed point are shown to help clarify the previous figure.

$$= \quad 2\lambda^2\mu^2[1-\cos(\frac{2\pi}{n}-\arccos(1-\frac{{}^{dn}z}{2\lambda^2}))]$$

where, referring to Equation (2.21),

$$\alpha = \frac{\pi}{n} - \arccos(1-\frac{{}^{dn}z}{2\lambda^2}). \tag{2.36}$$

So, we have

$$f(z) = 2\lambda^2\mu^2[1-\cos(\frac{2\pi}{n}-\arccos(1-\frac{z}{2\lambda^2}))], \tag{2.37}$$

$$\text{for} \quad 0 < z < 2\lambda^2(1-\cos(\frac{\pi}{n})). \tag{2.38}$$

Similarly, we define the second curve to be

$$h(z) = 2\lambda^2\mu^2[\cos(\arccos(1+\frac{z}{2\lambda^2})-\frac{2\pi}{n})-1], \tag{2.39}$$

$$\text{for} \quad -2\lambda^2(1-\cos(\frac{2\pi}{n})) < z < -2\lambda^2(1-\cos(\frac{\pi}{n})). \tag{2.40}$$

The remaining bounding curves are formed by sets of terms from the infinite sequences of angular velocities for intermediate slopes, ${}^{up}z_m < {}^{up}z$ and ${}^{up}\bar{z}_m < {}^{up}z$. For each m, the bounding curves can be found as functions of slope angle α.

The first of the pair of curves for each m is

$$f_m(\alpha) = \frac{2\lambda^2}{(\mu^2-1)\mu^{2(m-1)}}\left[(\mu^2-1)\left(1-\cos\alpha\cos\frac{\pi}{n}\right)-\ldots\right. \tag{2.41}$$

$$\left.(3\mu^2-2\mu^{2m}-1)\left(\sin\alpha\sin\frac{\pi}{n}\right)\right]. \tag{2.42}$$

The second of the pair of curves for each m is

$$h_m(\alpha) = \frac{2\lambda^2}{(\mu^2-1)\mu^{2m}}\left[(\mu^2-1)\left(\cos\alpha\cos\frac{\pi}{n}-1\right)-\ldots\right. \tag{2.43}$$

$$\left.\left(2\mu^4+\mu^2-2\mu^{2(m+1)}-1\right)\left(\sin\alpha\sin\frac{\pi}{n}\right)\right]. \tag{2.44}$$

In each case, the slope angle is $\alpha_c < \alpha < \frac{\pi}{n}$. The bounding curves are noted in Figures 2.18 and 2.19.

Now, having summarized the analysis of the fixed points, we summarize in the next section how the wheel behavior, that is, how the wheel reaches a final state, depends on the wheel parameters and initial conditions.

2.7 Existence of Possible Wheel Behaviors and their Dependence on Initial Conditions

Different behaviors occur depending on whether the slope is very steep, intermediately steep, or nearly flat. Which behaviors arise in each of these slope intervals depends upon the initial conditions.

The occurrence of each of the eleven behaviors, described above in Section 2.2.4, in the three slope intervals and for the two critical angles, α_c and $\alpha = \frac{\pi}{n}$, is indicated in Table 2.4.

The initial conditions for the angular velocity after collision can be greater than, less than, or equal to the critical angular velocities for reaching the vertical position in infinite time, ${}^{dn}z$ or

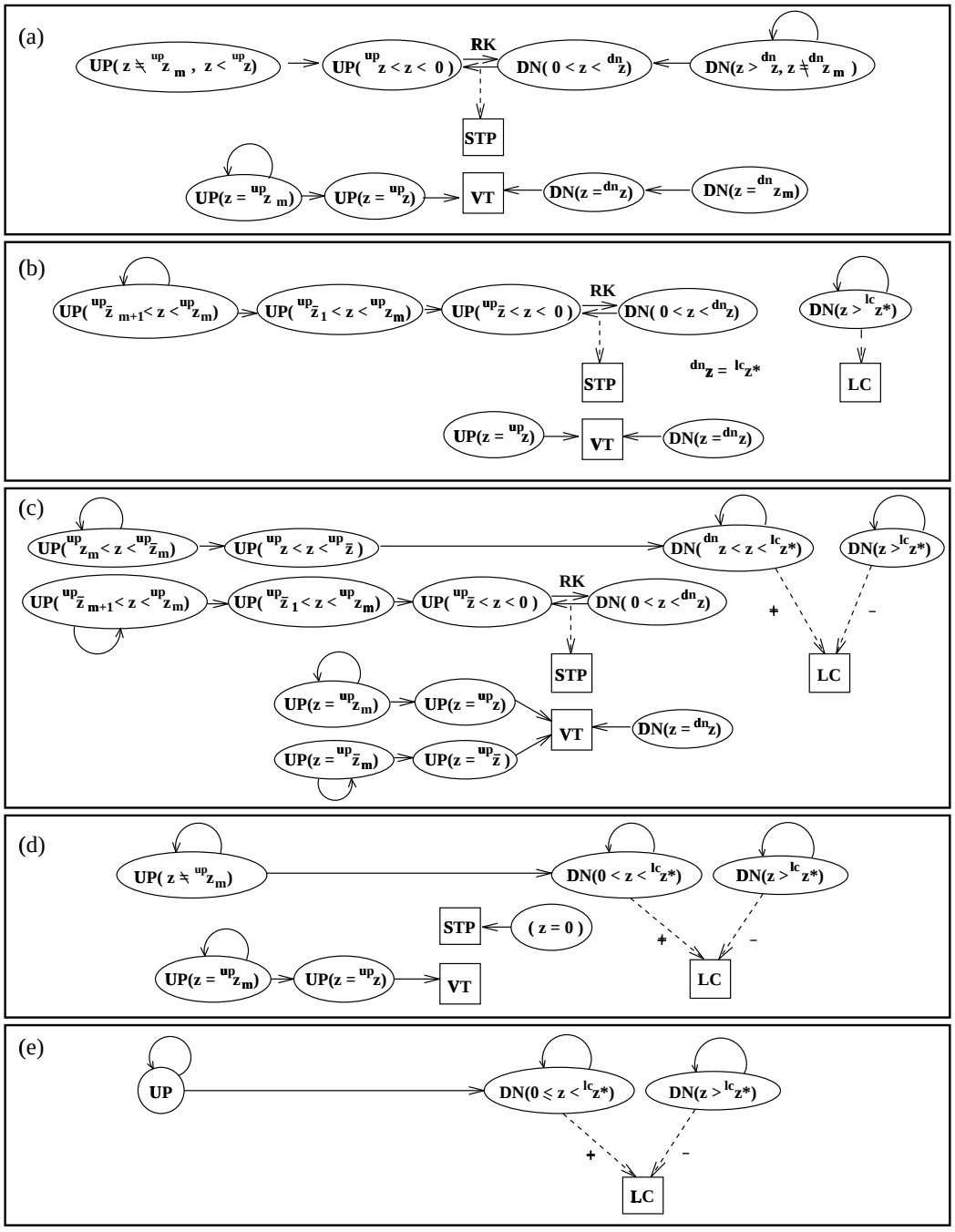

Figure 2.20: Five diagrams encapsulating the possible behaviors and their dependence on initial conditions for (a) $0 \leq \alpha < \alpha_c$, (b) $\alpha = \alpha_c$, (c) $\alpha_c < \alpha < \frac{\pi}{n}$, (d) $\alpha = \frac{\pi}{n}$, and (e) $\frac{\pi}{n} < \alpha \leq \frac{\pi}{2}$. The conventions used here are the same as in Figure 2.4 except that the plus(+) and minus(−) signs have been added to indicate increasing and decreasing speed, respectively, in reaching a limit cycle. Note that limit cycle motion does not exist for nearly flat slopes and neither the vertical position nor coming to rest on two spokes exists for very steep slopes.

Table 2.4: The dependence of the eleven possible behaviors on slope angle is indicated by an asterisk in each column.

		Slope Angle α				
Behavior		$0 \le \alpha < \alpha_c$	$\alpha = \alpha_c$	$\alpha_c < \alpha < \frac{\pi}{n}$	$\alpha = \frac{\pi}{n}$	$\frac{\pi}{n} < \alpha \le \frac{\pi}{2}$
1	Down$\stackrel{+}{\rightarrow}$ Limit Cycle			*	*	*
2	Down$\stackrel{-}{\rightarrow}$ Limit Cycle		*	*	*	*
3	Down$\rightarrow$ Rock $\rightarrow$ Stop	*				
4	Rock$\rightarrow$ Stop	*	*	*		
5	Up$\rightarrow$ Rock $\rightarrow$ Stop	*	*	*		
6	Up$\rightarrow$ Down $\stackrel{+}{\rightarrow}$ Limit Cycle			*	*	*
7	Down$\rightarrow$ Vertical	*	*	*		
8	Up$\rightarrow$ Vertical	*	*	*	*	
9	Up$\rightarrow$ Down $\rightarrow$ Vertical		*	*		
10	Up$\rightarrow$ Stop	*	*	*		
11	Down$\rightarrow$ Stop	*	*	*		

${}^{up}z$, or the fixed point angular velocities, ${}^{lc}z^* > 0$ or ${}^{stp}z^* = 0$. The possible behaviors for each slope interval and their dependence on initial conditions is summarized in five flowchart diagrams in Figure 2.20. The critical angular velocities ${}^{up}z$ and ${}^{dn}z$, the vertical position, and the stopped position do not exist for very steep slopes and limit cycles do not exist for nearly flat slopes.

In the next section, we present a few other results.

2.8 Other Results

For shallow, intermediate, and steep slopes, we display some of the more interesting possible behaviors, out of a possible total of eleven behaviors, in the following plots:

- (i). Poincaré map showing fixed points and characteristic stair-step diagrams.
- (ii). Phase portrait showing the trajectories as the wheel approaches the fixed points.

The two plots are displayed on one page for each behavior that exists for each slope range. Each plot displays the shorthand notation for the behavior displayed, the critical measures of angular velocity and sequences for reaching the vertical position in infinite time, the fixed points, the slope angle, the wheel parameters, and the initial conditions. For all cases, the non-dimensional inertia is $2J = 0.5$ ($\lambda^2 = 2/3$) and the number of spokes is $n = 6$. For these given wheel parameters, the critical slope angle is $\alpha_c = 0.107$.

The fixed points found using the exact solution given by Equation (2.26) agree well with those found numerically. These graphs show how the existence of the fixed points depends on slope angle α and the initial angular velocity, $\dot{\theta}_0 \in \Sigma$. They also show how the wheel approaches the fixed points. The behaviors where the wheel reaches the vertical in infinite time or comes to a stop in one collision are not displayed; i.e., behaviors 7-11, Down$\rightarrow$ Vertical, Up$\rightarrow$ Vertical, Up$\rightarrow$ Down$\rightarrow$ Vertical, Up$\rightarrow$ Stop, and Down$\rightarrow$ Stop. In addition, behavior 4 is the final part of behaviors 3 and 5 and, thus, is not displayed separately.

Figure 2.21 and Figure 2.22 shows behaviors 3 and 5, Down$\rightarrow$ Rock $\rightarrow$ Stop and Up$\rightarrow$ Rock $\rightarrow$ Stop, respectively, for $0 \le \alpha < \alpha_c$. Here, $\alpha = \frac{\pi}{50}$.

Figure 2.23 shows behavior 6, Up$\rightarrow$ Down $\stackrel{+}{\rightarrow}$ Limit Cycle , for $\alpha_c \le \alpha \le \frac{\pi}{n}$. Here, $\alpha = \frac{\pi}{15}$.

Figure 2.24 and Figure 2.25 show behaviors 1 and 2, Down$\stackrel{+}{\rightarrow}$ Limit Cycle and Down$\stackrel{-}{\rightarrow}$ Limit Cycle, respectively, for $\frac{\pi}{n} < \alpha \leq \frac{\pi}{2}$. Here, $\alpha = \frac{\pi}{4}$.

2.9 Rate of Approach to Fixed Points

The Poincaré map may be written schematically as

$$z_{k+1} = P(z_k). \tag{2.45}$$

Consider the evolution of small perturbations from the fixed point z^*. The linearization of P near z^* is given by

$$\begin{aligned} z_{k+1} = z^* + \Delta z_{k+1} = P(z_k) &= P(z^* + \Delta z_k) \\ &= P(z^*) + \left.\frac{dP}{dz}\right|_{z=z_*} \Delta z_k \end{aligned} \tag{2.46}$$

Canceling the cyclic term $P(z^*)$ yields

$$\begin{aligned} \Delta z_{k+1} &= \left.\frac{dP}{dz}\right|_{z=z^*} \Delta z_k \\ &= \mu^2 \Delta z_k \end{aligned} \tag{2.47}$$

Thus, a perturbation from the fixed point, Δz^*, iterates according to

$$\Delta z_k = \mu^{2k} \Delta z^*. \tag{2.48}$$

In the next section, we consider the energy of the rolling wheel.

2.10 Energy Analysis

2.10.1 Approach to Fixed Points

How limit cycles or the stopped position are approached can be seen by considering the energy of the wheel. Below, we will consider this discussion more formally. In between spoke collisions, the kinetic energy gained by the wheel is proportional to the distance the center of mass falls and is a constant. The energy lost per collision is variable, however, and proportional to the wheel speed squared.

If the wheel starts off very slowly on a large enough slope, the energy lost per collision is much less than the energy gained between collisions so that the speed of the wheel increases with each collision. The loss in energy per collision, proportional to the speed squared, eventually catches up with, but cannot exceed, the constant gain in energy and the wheel approaches a steady speed.

If the same wheel starts off very fast on a large enough slope, the energy lost per collision is much more than the energy gained between collisions so that the wheel speed decreases with each collision. But the energy lost per collision in this case eventually diminishes to, but not below, the constant gain in energy, and the wheel approaches the same steady speed.

If the slope is not high enough, the energy loss per collision is greater than the energy gained between collisions so that the wheel speed decreases. In this case, however, the wheel eventually reaches a condition where its speed after collision is too low to carry it past the vertical and the wheel falls backward, eventually coming to rest. Once the wheel falls backward, there is no gain in energy, only losses, as the wheel rocks back and forth between two spokes.

The approach to a limit cycle or static equilibrium is monotonic; i.e., the wheel does not alternate between slowing down and speeding up. In addition, the only case in which the wheel speed can increase without bound is when the number of spokes is infinity, which is the case of the rolling disc.

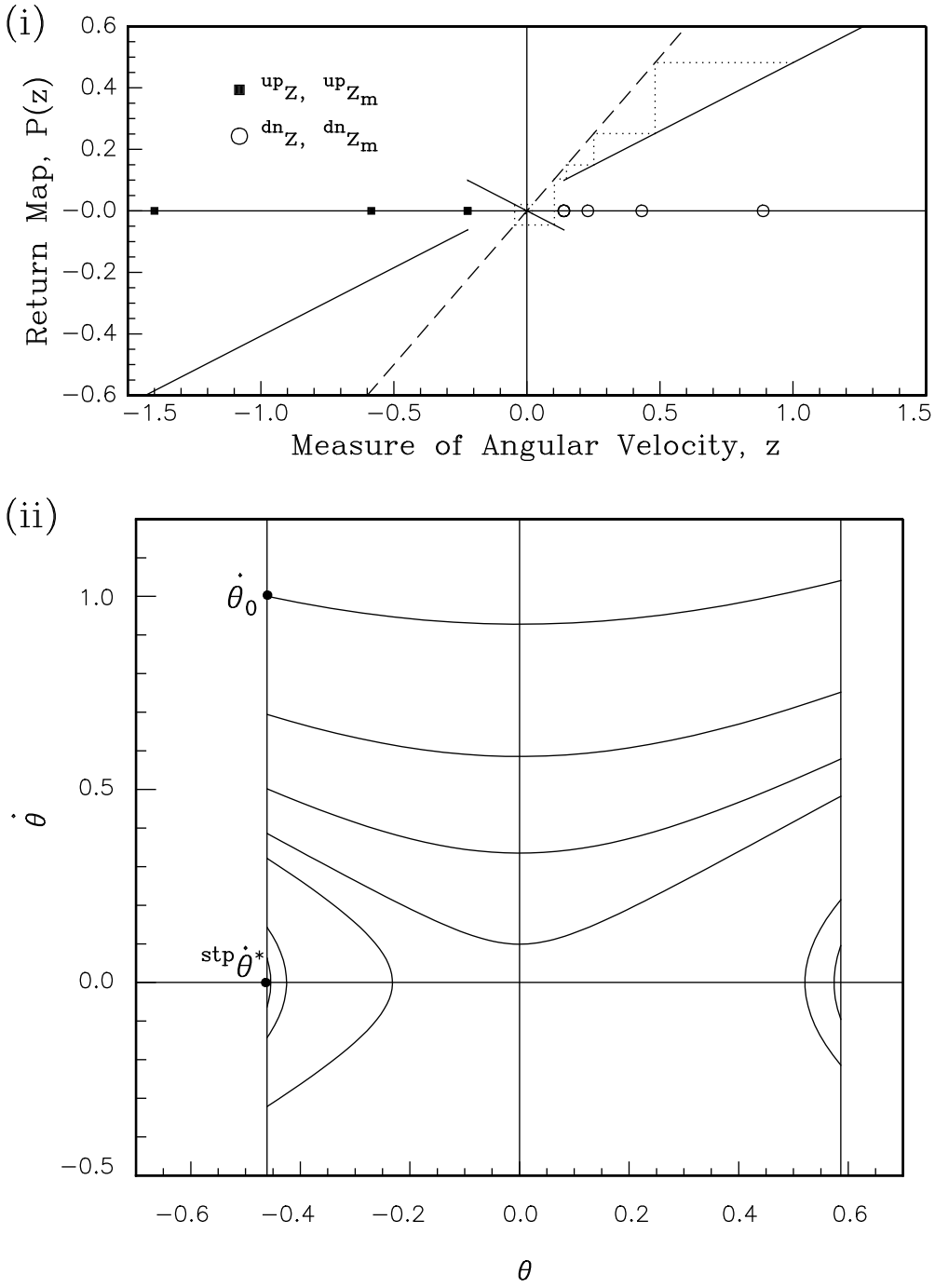

Figure 2.21: The plots shown here characterize behavior 3, Down→ Rock → Stop. The wheel parameters are $2J = 0.5$, $n = 6$, and $\alpha = \frac{\pi}{50}$. The initial condition is $z_0 = 1.0$. The fixed point is ${}^{stp}z^* = 0$.

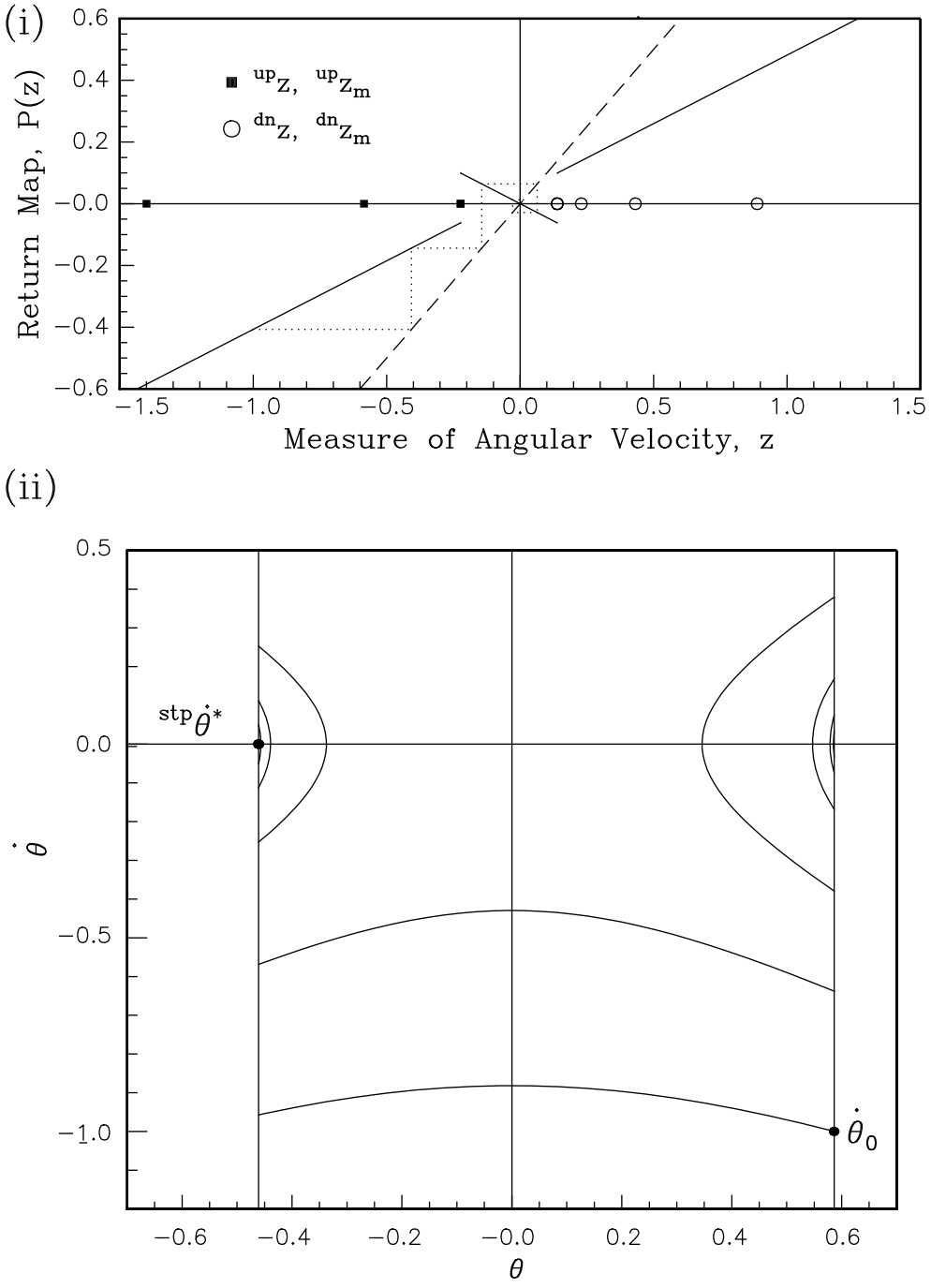

Figure 2.22: The plots shown here characterize behavior 5, Up→ Rock → Stop. The wheel parameters are $2J = 0.5$, $n = 6$, and $\alpha = \frac{\pi}{50}$. The initial condition is $= z_0 = -0.1$. The fixed point is ${}^{stp}z^* = 0$.

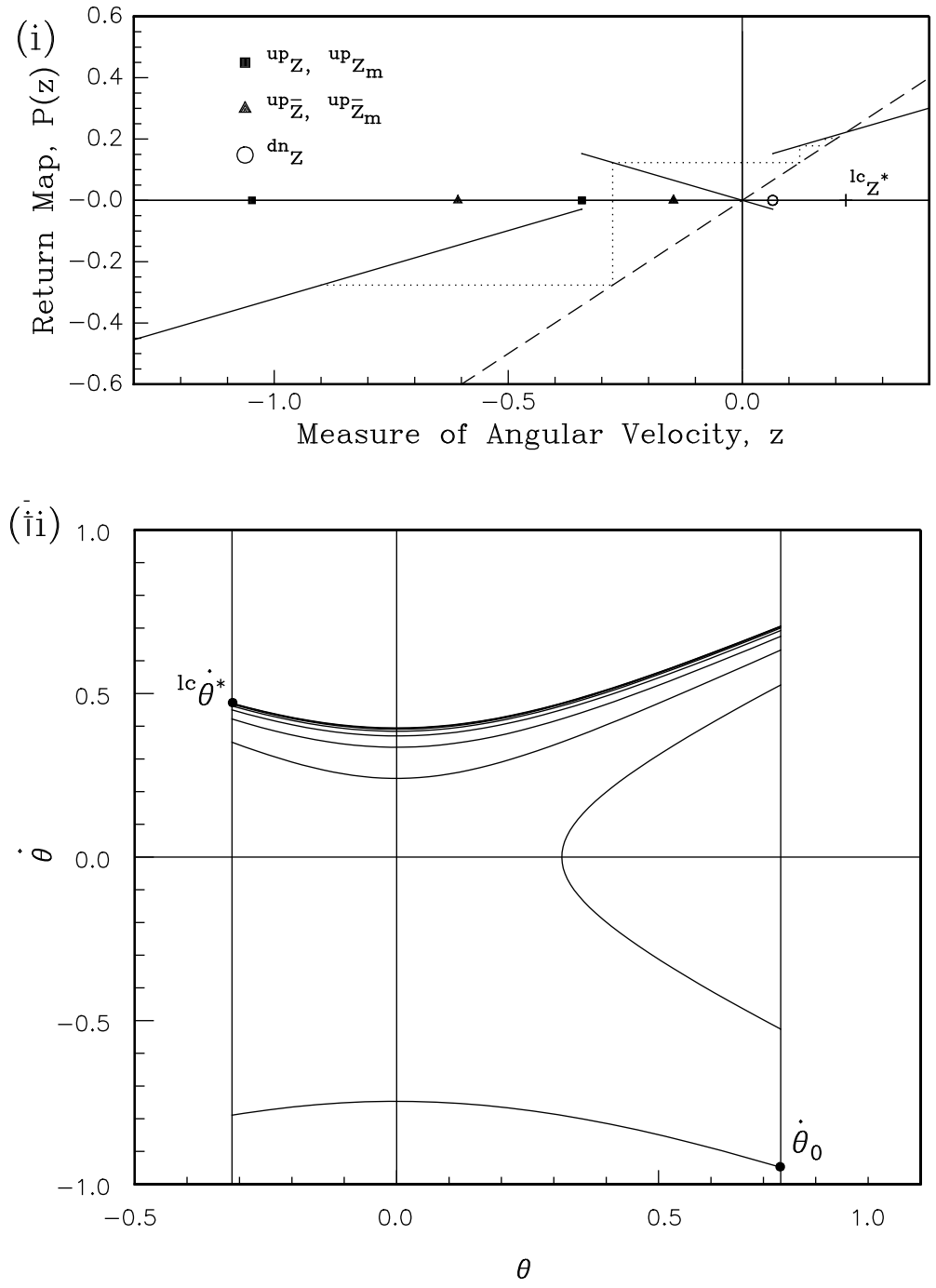

Figure 2.23: The plots shown here characterize behavior 6, Up$\rightarrow$ Down$\stackrel{+}{\rightarrow}$ Limit Cycle. The wheel parameters are $2J = 0.5$, $n = 6$, and $\alpha = \frac{\pi}{15}$. The initial condition is $z_0 = -0.9$. For the given initial condition, the fixed point is ${}^{lc}z^* = 0.2218$.

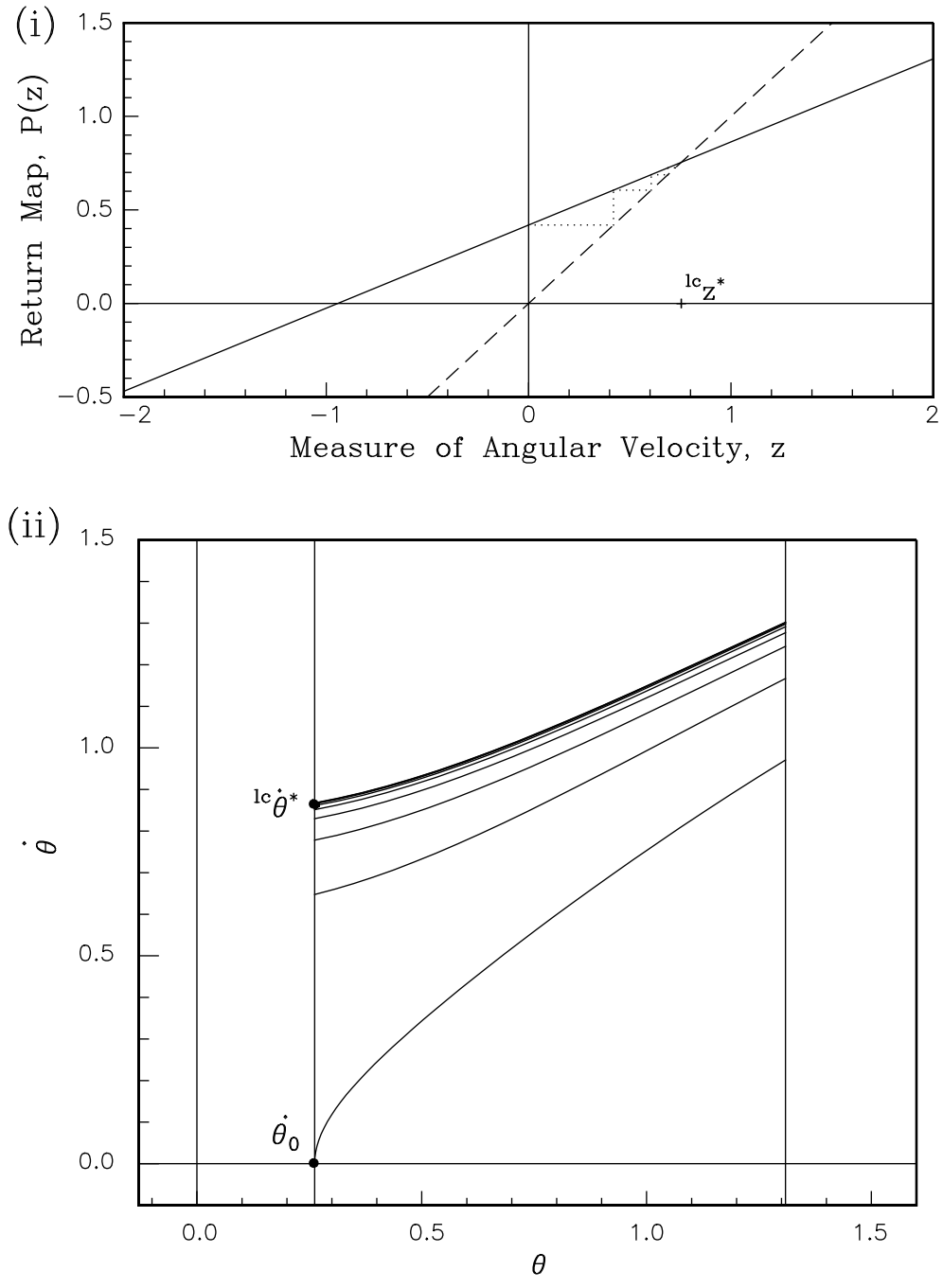

Figure 2.24: The plots shown here characterize behavior 1, Down$\stackrel{+}{\rightarrow}$ Limit Cycle. The wheel parameters are $2J = 0.5$, $n = 6$, and $\alpha = \frac{\pi}{4}$. The initial condition is $z_0 = 0.0$. The fixed point is ${}^{lc}z^* = 0.7542$.

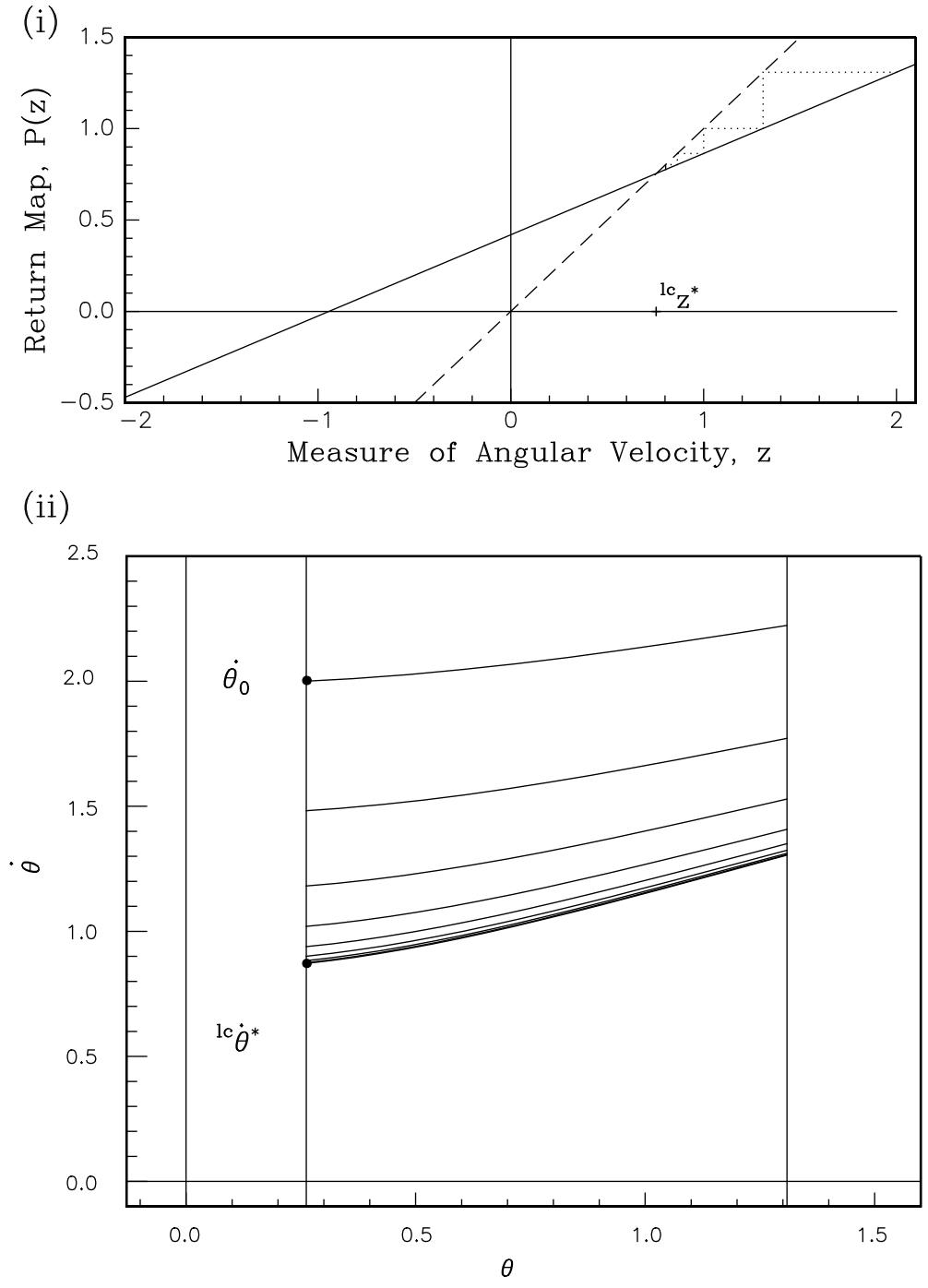

Figure 2.25: The plots shown here characterize behavior 2, Down$\bar{\rightarrow}$ Limit Cycle. The wheel parameters are $2J = 0.5$, $n = 6$, and $\alpha = \frac{\pi}{4}$. The initial condition is $z_0 = 2.0$. The fixed point is ${}^{lc}z^* = 0.7542$.

2.10.2 Energy Loss per Spoke Collision with the Ground

The energy loss during each spoke collision is equal to the change in kinetic energy during the collision since there is no change in potential energy; i e., no change in elevation of the center of mass occurs at collisions. The non-dimensional energy loss during collision i is

$$\Delta KE_i = KE_i^+ - KE_i^- = \frac{1-\mu^2}{2\lambda^2\mu^2}|[z(\dot{\theta})]|_i \tag{2.49}$$

where $\dot{\theta}$ is the angular velocity after the i_{th} collision or $\dot{\theta} \in \Sigma$. ΔKE_i is independent of slope angle.

The energy gained by the wheel in falling downhill between the collisions is the loss in potential energy and is a constant for a given slope, inertia, and number of spokes. The non-dimensional gain in potential energy between collisions is

$$\Delta PE = PE_i^- - PE_{i-1}^+ = KE_i^- = 2\sin\alpha\sin\frac{\pi}{n}. \tag{2.50}$$

The wheel enters into a limit cycle motion when the energy lost in each collision is balanced by the energy gained in falling between collisions when the wheel makes it past the vertical in the downhill direction; i.e., when

$$\frac{1-\mu^2}{2\lambda^2\mu^2}z^* = 2\sin\alpha\sin\frac{\pi}{n}. \tag{2.51}$$

Solving this equation for the limit cycle measure of angular velocity, we get the fixed point

$${}^{lc}z^* \equiv \frac{4\mu^2\lambda^2\sin\frac{\pi}{n}\sin\alpha}{1-\mu^2} > 0 \tag{2.52}$$

which agrees, of course, with the previous result in Equation (2.26). This result is illustrated in Figure 2.26.

In Figure 2.27, we show how the existence of the limit cycle fixed point depends on the slope angle and the measure of angular velocity. In order for the limit cycle to exist, the fixed point measure of angular velocity must be greater than the measure of angular velocity needed for the wheel to stop in the vertical position in infinite time.

The fractional change in energy loss per collision is given by

$$\frac{\Delta KE_i}{KE_i^-} = 1-\mu^2 \tag{2.53}$$

which is independent of slope and the angular velocity of the wheel after collision. So, when $\mu = 0$ all of the wheel energy is lost in collision and when $\mu = 1$, which only happens if the number of spokes equals infinity, no energy is lost in collision.

Next, we are interested in the energy lost per revolution of the wheel in the limit as the number of spokes n goes to infinity, for two cases: when the wheel is and is not in a limit cycle but has enough energy to make it past the vertical in the downhill direction for both cases.

2.10.3 Energy Loss per Revolution of the Wheel

Non-steady State Energy Accounting

At any given speed not at steady-state but where the measure of angular velocity after each collision i is great enough for the wheel to pass the vertical position, $z_i > {}^{dn}z$, the non-dimensional energy loss per revolution of an n-spoked wheel is

$$\begin{aligned} \xi &= \frac{1-\mu^2}{4\lambda^2\mu^2 n\sin\frac{\pi}{n}}\sum_{i=1}^{n}|z_i| \\ &= \frac{1-\mu^2}{4\lambda^2\mu^2 n\sin\frac{\pi}{n}}\sum_{i=1}^{n}P^i(z_0), \end{aligned} \tag{2.54}$$

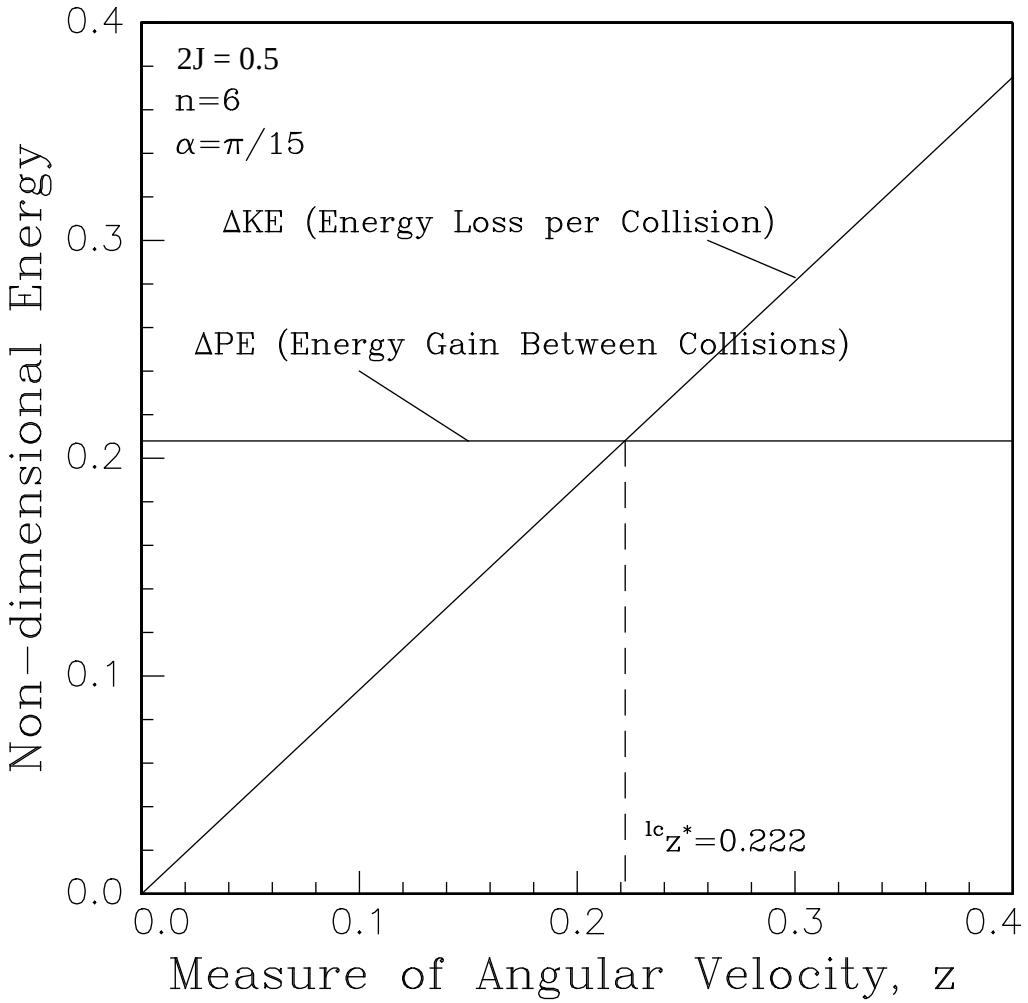

Figure 2.26: A plot of ΔKE, directly proportional to the measure of angular velocity and independent of slope angle, and ΔPE, a constant for fixed J and n, versus measure of angular velocity after collision with $\alpha = \frac{\pi}{15}$, $2J = 0.5$, and $n = 6$. The slope of the line representing the energy loss per collision is $\frac{1-\mu^2}{2\lambda^2\mu^2} = 0.9375$. The point of intersection of this line with the horizontal line representing the energy loss per collision, $\Delta PE = 2\sin\alpha\sin\frac{\pi}{n} = 0.2079$, is the limit cycle fixed point, ${}^{lc}z^* = \frac{16}{15}\sin\frac{\pi}{15} = 0.222$, marked by the vertical dashed line. The vertical dotted line represents the measure of angular velocity needed to reach the vertical in infinite time in the downhill direction, ${}^{dn}z = 0.0653$.

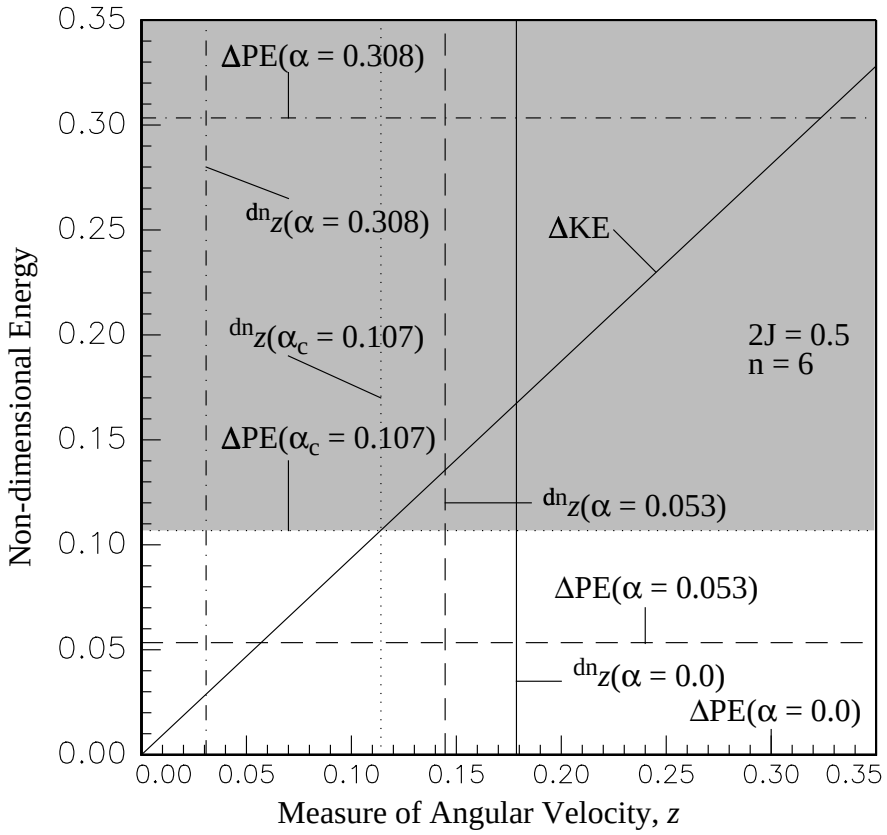

Figure 2.27: A plot of ΔKE and ΔPE versus angular velocity after collision with $0 \leq \alpha \leq \frac{\pi}{n}$, $2J = 0.5$, and $n = 6$. Four horizontal lines represent the constant gain in energy between collisions for slope angles $\alpha = 0.0, 0, 053, 0.107,$ and 0.3083. The horizontal line corresponding to zero slope angle is the z axis. The vertical lines represent the critical measures of angular velocity for the wheel to reach the vertical position in infinite time in the downhill direction, ${}^{dn}z$. Each vertical line corresponds to the slope angle associated with each horizontal line. The vertical and horizontal lines corresponding to the same slope angle are plotted in the same linestyle. The horizontal dash-dot line $\Delta PE(\alpha = 0.3083)$, intersects the solid sloping line, representing the energy loss per collision, at $z > {}^{dn}z(\alpha = 0.3083)$ indicated by the vertical dash-dot line. In this case, a limit cycle exists. In contrast, the horizontal dashed line, $\Delta PE(\alpha = 0.053)$ intersects the energy loss line at $z < {}^{dn}z(\alpha = 0.053)$ indicated by the vertical dashed line. In this case, no limit cycle exits. For fixed wheel parameters, J and n, the minimum slope angle for which limit cycles exist corresponds to the point where the loss in energy per collision, constant gain in energy between collisions, and the associated critical measure of angular velocity intersect. The minimum slope angle is the critical angle α_c found previously. The shaded region, $\Delta PE > \Delta PE(\alpha_c)$, indicates where only limit cycles exist.

where $z_0 \neq {}^{lc}z^*$ is the angular velocity of the wheel just after the the first collision in a particular revolution of the wheel, collision $i = 0$. The energy has been non-dimensionalized with respect to time, mass, the moment of inertia, and the perimeter Q_n of the rimless wheel, an equilateral polygon,

$$Q_n = 2n \sin \frac{\pi}{n}. \tag{2.55}$$

The map P has been defined previously.

Iterating P under the summation in Equation (2.54), we obtain

$$\xi = \frac{1-\mu^2}{4\lambda^2\mu^2 n \sin\frac{\pi}{n}} \sum_{i=1}^{n} \left[\mu^{2i} z_0 + 4\lambda^2 \sin\alpha \sin\frac{\pi}{n} \sum_{r=1}^{i} \mu^{2r} \right] \tag{2.56}$$

Summing the two series and simplifying yields

$$\xi = \frac{1}{2\lambda^2} \left[\frac{z_0(1-\mu^{2n})}{2n\sin\frac{\pi}{n}} + \frac{2\lambda^2 \sin\alpha}{n} \left(n - \frac{(1-\mu^{2n})\mu^2}{1-\mu^2} \right) \right] \tag{2.57}$$

As n gets large, we have

$$\begin{aligned} \mu &\rightarrow 1 - \frac{\lambda^2}{2}\left(\frac{2\pi}{n}\right)^2, \\ \mu^2 &\rightarrow 1 - \lambda^2 \left(\frac{2\pi}{n}\right)^2, \text{and} \\ \mu^{2n} &\rightarrow 1 - \lambda^2 n \left(\frac{2\pi}{n}\right)^2. \end{aligned} \tag{2.58}$$

Substituting the above and after much simplification, we obtain

$$\lim_{n\to\infty} \xi = \lim_{n\to\infty} (\frac{\pi}{n})^2 (\frac{z_0}{\sin\frac{\pi}{n}} + 4\lambda^2 \sin\alpha) = 0. \tag{2.59}$$

That is, $\xi \propto \frac{C_1}{n} + \frac{C_2}{n^2}$ as $n \rightarrow \infty$, where C_1 and C_2 are constants. Thus, as the number of spokes goes to infinity, the energy loss per revolution goes to zero and the speed of the wheel approaches infinity, as for a uniform disk.

Limit Cycle Energy Accounting

When the wheel is in a limit cycle, the measure of angular velocity after each collision in a revolution is $z_i = {}^{lc}z^*$ and the non-dimensional energy lost per revolution is

$$\begin{aligned} \xi^* &= \frac{1-\mu^2}{4\lambda^2\mu^2} n \sin\frac{\pi}{n} \sum_{i=1}^{n} |z_i| \\ &= \frac{1-\mu^2}{4\lambda^2\mu^2 n \sin\frac{\pi}{n}} n ({}^{lc}z^*)^2 \\ &= \sin\alpha \end{aligned} \tag{2.60}$$

At steady state, the non-dimensional energy loss per revolution simply equals the sine of the slope angle α for any number of spokes n.

A graph of the non-dimensional energy loss per revolution ξ is shown as a function of revolution number in Figure 2.28.

In addition, we show in Figure 2.29 a plot of the non-dimensionalized potential energy, kinetic energy, and total energy of the rimless wheel versus time for the case of the wheel approaching a limit cycle from above, the behavior denoted by Down$\bar{\rightarrow}$ Limit Cycle.

In the next section, we consider the speed and rate of change of speed of the center of mass of the rimless wheel.

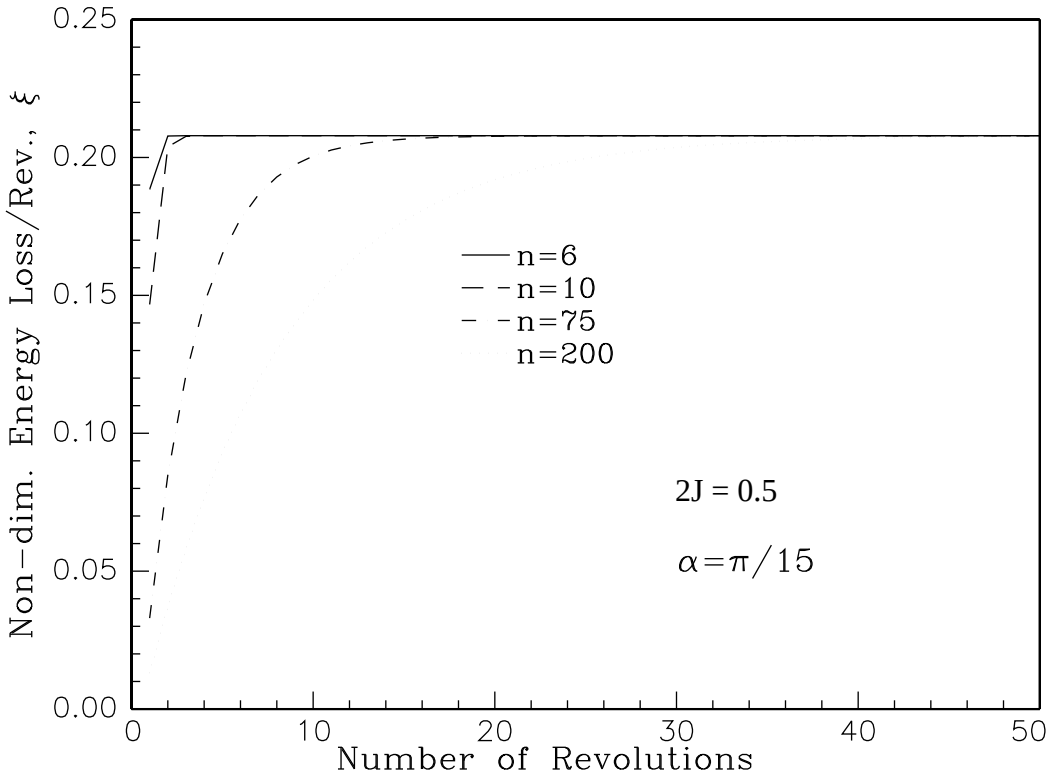

Figure 2.28: Non-dimensionalized energy loss per revolution up to steady state for $2J = 0.5$, $\alpha = \frac{\pi}{15}$, and $n = 6$, 10, 75 and 200 spokes. After many revolutions, and, hence, many spoke collisions , the energy loss per revolution is $\xi^* = \sin\alpha = 0.2079$ as the wheel approaches a limit cycle, for any number of spokes n.

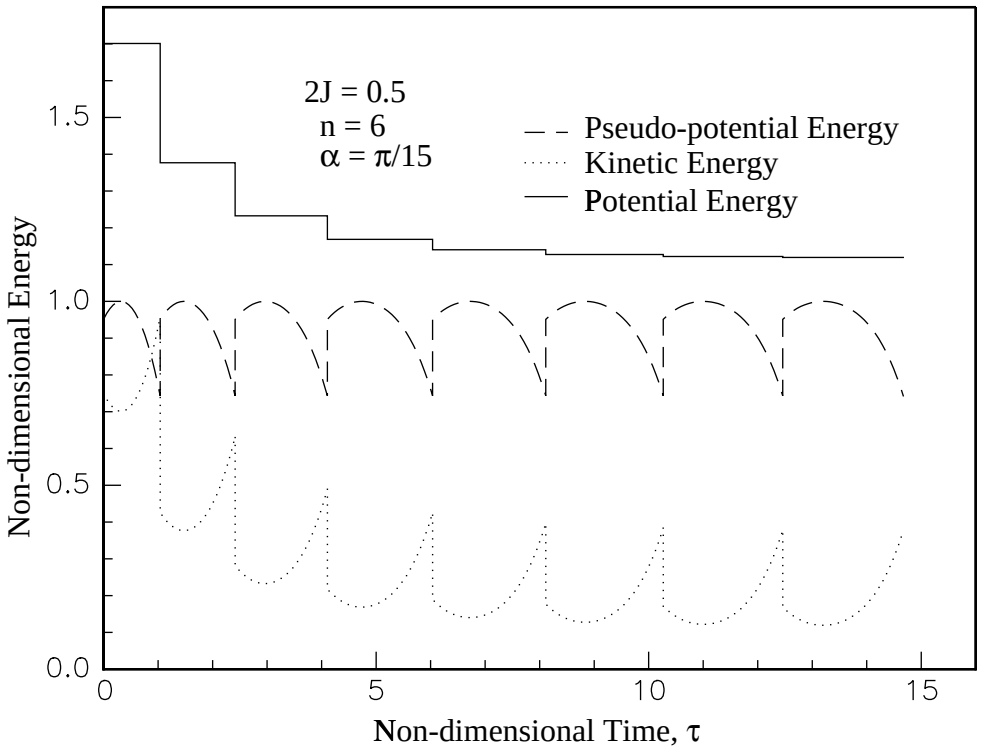

Figure 2.29: The non-dimensionalized potential energy, kinetic energy, and total energy of the rimless wheel are plotted versus time as the wheel approaches a limit cycle from above. The total energy is conserved between collisions but decreases with every collision due to the dissipative impact. The potential energy of the wheel between every collision is always measured with respect to a datum set at the foot of the spoke currently in contact with the ground. We thus term this unusual energy measure *pseudo-potential energy*. The range of the pseudo-potential energy is determined by the wheel parameters. Eventually, the total energy between collisions becomes constant as the wheel approaches a limit cycle motion. The energy lost per collision is represented by the vertical *dotted* lines and the energy gained between collisions, a constant, is represented by the vertical *dashed* lines. The plot shows that the wheel starts off at a velocity greater than the limit cycle velocity. Since the kinetic energy of the wheel is proportional to the wheel speed squared, at first the energy loss per collision is much greater than the energy gain between collisions so that the wheel speed decreases with each collision. The energy lost per collision eventually diminishes to, but not below, the constant gain in energy and the wheel speed after each collision approaches the same value in infinite time after every collision. As the wheel enters into the limit cycle, the vertical lines representing the energy loss at collisions and the energy gain between collisions approach the same length, indicating the eventual balance between energy loss and energy gain.

2.11 Non-dimensional Average Speed and Average Rate of Change of Speed of the Center of Mass of the Wheel in the Limit Cycle

Let $\Delta\tau_{lc}$ be the non-dimensional time between spoke collisions in the limit cycle. From the first integral of motion in Equation (2.11), we obtain

$$\Delta\tau_{lc} = \int_{\alpha-\frac{\pi}{n}}^{\alpha+\frac{\pi}{n}} \frac{d\theta}{\sqrt{({}^{lc}\dot{\theta}^*)^2 + 2\lambda^2(\cos(\alpha-\frac{\pi}{n}) - \cos\theta)}} \tag{2.61}$$

The non-dimensional speed of the center of mass in between collisions is given by

$$v_{cm}(\tau) = \dot{\theta}(\tau) \tag{2.62}$$

where the speed has been non-dimensionalized with respect to the spoke length l. The non-dimensionalized average speed of the center of mass in the limit cycle is

$$\begin{aligned} v_{cm_{avg}} &= \frac{1}{\Delta\tau_{lc}} \int_0^{\Delta\tau_{lc}} |\dot{\theta}(\tau)| d\tau \\ &= \frac{1}{\Delta\tau_{lc}} \int_0^{\Delta\tau_{lc}} \left|\frac{d\theta(\tau)}{d\tau}\right| d\tau \\ &= \frac{1}{\Delta\tau_{lc}} \theta(\tau)|_0^{\Delta\tau_{lc}} \\ &= \frac{1}{\Delta\tau_{lc}} [(\alpha + \frac{\pi}{n}) - (\alpha - \frac{\pi}{n})] \\ &= \frac{1}{\Delta\tau_{lc}} \frac{2\pi}{n}. \end{aligned} \tag{2.63}$$

The non-dimensionalized average speed of the rimless wheel in the limit cycle is plotted as a function of slope angle for a variety of number of spokes in Figure 2.30.

The non-dimensionalized average rate of change of speed of the center of mass in the limit cycle is

$$\begin{aligned} \dot{v}_{cm_{avg}} &= \frac{1}{\Delta\tau_{lc}} \int_0^{\Delta\tau_{lc}} \left|\frac{d\dot{\theta}(\tau)}{d\tau}\right| d\tau \\ &= \frac{1}{\Delta\tau_{lc}} \dot{\theta}(\tau)|_0^{\Delta\tau_{lc}} \\ &= \frac{1}{\Delta\tau_{lc}} [\frac{{}^{lc}\dot{\theta}^*}{\mu} - {}^{lc}\dot{\theta}^*] \\ &= \frac{1}{\Delta\tau_{lc}} \frac{1-\mu}{\mu} ({}^{lc}\dot{\theta}^*), \end{aligned} \tag{2.64}$$

where again the overdot indicates differentiation with respect to non-dimensional time $\tau = t\sqrt{g/l}$.

In the limit as the number of spokes goes to infinity, we expect the rimless wheel to behave like a uniform disk rolling down a slope; i.e., the velocity should become infinite and the acceleration constant. To check this expectation, we first compute the non-dimensional time between collisions for finite slope in the limit as n gets large:

$$\Delta\tau_{lc} = \int_{\alpha-\frac{\pi}{n}}^{\alpha+\frac{\pi}{n}} \frac{d\theta}{\sqrt{({}^{lc}\dot{\theta}^*)^2 + 2\lambda^2(\cos(\alpha-\frac{\pi}{n}) - \cos\theta)}}$$

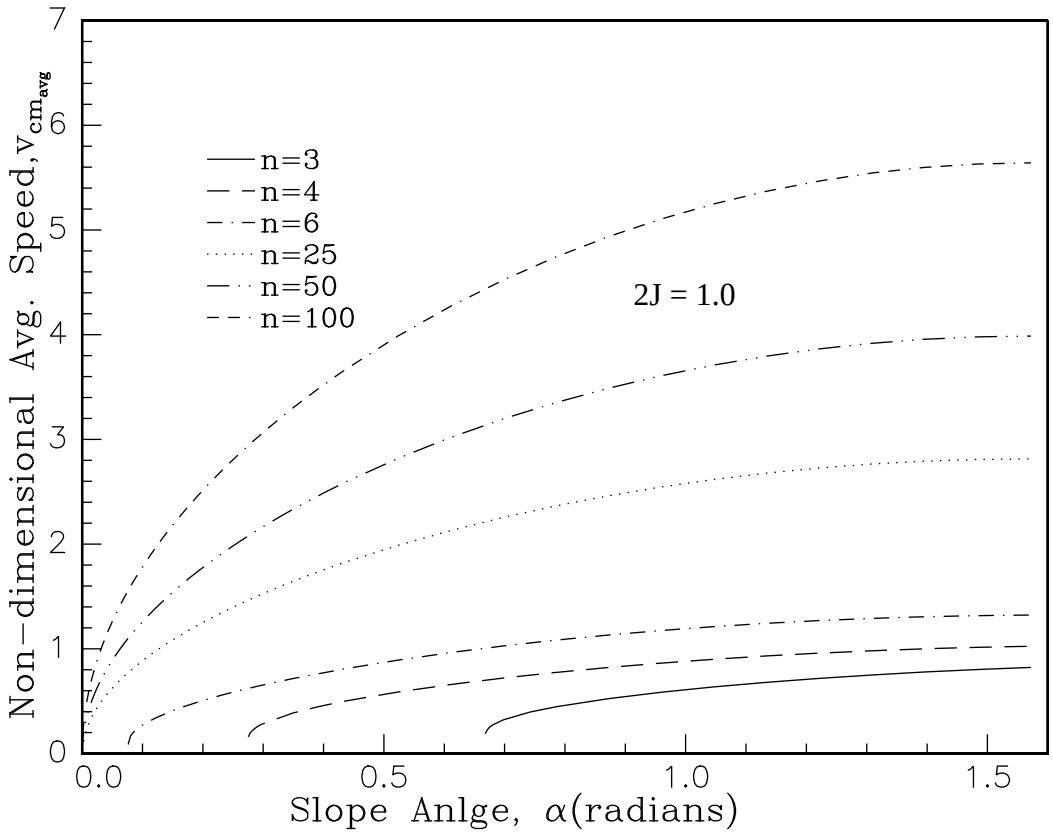

Figure 2.30: Non-dimensionalized average speed at steady state, $v_{cm_{avg}}$, as a function of slope angle and for n =3, 4, 6, 25, 50, and 100 spokes. At each of these spoke numbers, the plots are initialized at an angle above the critical slope angle, α_c. As expected, the steady state speed increases with the number of spokes and slope angle.

$$\begin{aligned} &\approx \frac{1}{\sqrt{({}^{lc}\dot{\theta}^*)^2 + 4\lambda^2 \sin\alpha \sin\frac{\pi}{n}}} \int_{\alpha-\frac{\pi}{n}}^{\alpha+\frac{\pi}{n}} d\theta \\ &\approx \frac{\frac{2\pi}{n}}{\sqrt{\frac{n}{\pi}\sin\alpha}}, \\ &\approx \frac{2(\frac{\pi}{n})^{\frac{3}{2}}}{\sqrt{\sin\alpha}}, \end{aligned} \tag{2.65}$$

where we have assumed that the integrand is constant as the interval $[\alpha - \frac{\pi}{n}, \alpha + \frac{\pi}{n}]$ shrinks to zero. Thus, for finite slope angle α, as n gets large, $\Delta\tau_{lc} \sim O(n^{-\frac{3}{2}})$.

Next, for the non-dimensional average speed in the limit cycle, we have

$$\begin{aligned} \lim_{n\to\infty} v_{cm_{avg}} &= \lim_{n\to\infty} \frac{1}{\Delta\tau_{lc}} \frac{2\pi}{n} \\ &= \lim_{n\to\infty} \sqrt{\frac{n}{\pi}\sin\alpha} = \infty. \end{aligned} \tag{2.66}$$

If, in the limit as the number of spokes goes to infinity, the rimless wheel approaches a thin uniform disk, then the moment of inertia about the center of mass $I_C = \frac{1}{2}ml^2$ or the non-dimensional moment of inertia $2J = \frac{1}{2}$. For the non-dimensional average rate of change of speed in the limit cycle, then, we have

$$\begin{aligned} \lim_{n\to\infty} \dot{v}_{cm_{avg}} &= \lim_{n\to\infty} \frac{1}{\Delta\tau_{lc}} \frac{1-\mu}{\mu} ({}^{lc}\dot{\theta}^*) \\ &= \lambda^2 \sin\alpha \\ &= \frac{2}{3}\sin\alpha, \end{aligned}$$

since $\lambda^2 = \frac{1}{2J+1} \to \frac{2}{3}$ for a uniform disk as $n \to \infty$.

As the number of spokes gets large, then, the speed and acceleration of the center of mass of the rimless wheel in the limit cycle approaches that of a uniform disk rolling down a slope of angle α.

For slope angle $\alpha = \frac{\pi}{7}$ and non-dimensional inertia $2J = 0.5$ corresponding to a uniform disk, Figure 2.31 shows how in the limit cycle as the number of spokes goes to infinity, the speed of the rimless wheel, $v_{cm_{avg}}$, approaches infinity and the rate of change of speed, $\dot{v}_{cm_{avg}}$, approaches a constant.

If we take α to be small as well as letting n go to infinity, say, $\alpha \sim O(\frac{1}{n})$ but bigger than $\alpha_c \simeq O(\frac{1}{n^3})$, then we find from Equation (2.65) that the time between spoke collisions, when the wheel is in a limit cycle, is of the same order,

$$\Delta\tau_{lc} \sim O(\frac{1}{n}). \tag{2.67}$$

2.12 Linear Analysis

Here, we review McGeer's[43, 44, 4] linearized analysis for finding limit cycles and their stability for the rimless wheel. For small angles, the equation of motion between collisions and collision conditions are

$$\begin{aligned} \ddot{\theta} - \lambda^2\theta &= 0, \qquad |\theta - \alpha| < \frac{\pi}{n} \\ (\theta - \alpha) &\mapsto -(\theta - \alpha), \qquad |\theta - \alpha| = \frac{\pi}{n}, \quad \text{and} \\ \dot{\theta} &\mapsto \mu\dot{\theta}, \qquad |\theta - \alpha| = \frac{\pi}{n}. \end{aligned} \tag{2.68}$$

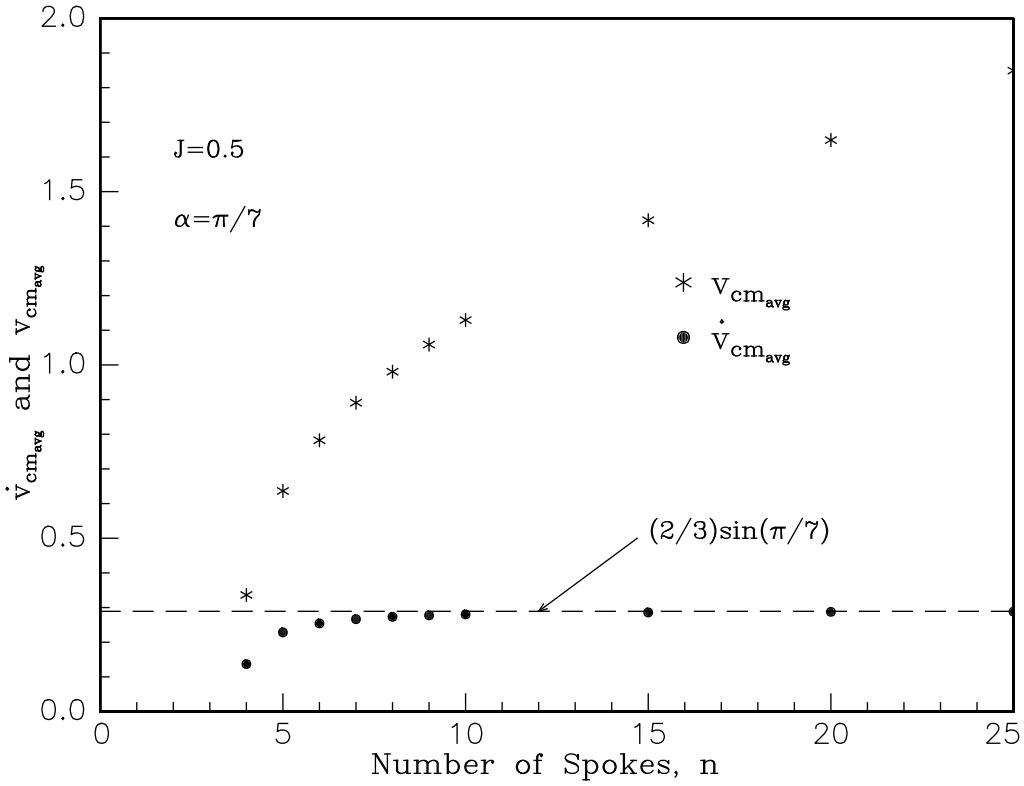

Figure 2.31: Non-dimensionalized average speed, $v_{cm_{avg}}$, and average rate of change of speed, $\dot{v}_{cm_{avg}}$, of the rimless wheel at steady state as a function of slope angle and for $2J = 0.5$, and $n = 4$ to $n = 25$ spokes. As the number of spokes gets large, the speed increases without bound and the rate of change of speed is asymptotic to $\dot{v}_{cm_{avg}} = \frac{2}{3}\sin\alpha = 0.2893$, indicated by the horizontal dashed line which is the acceleration of a uniform disk, with inertia $2J = 0.5$ rolling down a slope of angle α.

Again, an overdot indicates differentiation with respect to non-dimensional time $\tau = t\sqrt{g/l}$.

Considering Equation (2.68) as a linear first order system, the phase space is defined as before in Section 2.3.3 and the trajectories are generated using the first integral of motion

$$\dot{\theta} = \sqrt{\dot{\theta}_0^2 + \lambda^2(\theta^2 - \theta_0^2)}. \tag{2.69}$$

The linear phase plane portrait is locally approximate to the nonlinear one near $\theta = 0$.

The start-of-cycle conditions just after the collision i are

$$\begin{aligned} \theta(0) = \theta_i^+ &= \alpha - \frac{\pi}{n} \\ \dot{\theta}(0) = \dot{\theta}(0) &= \dot{\theta}_i^+ \end{aligned} \tag{2.70}$$

Solving Equation (2.68) satisfying Equation (2.70) gives

$$\begin{aligned} \theta(\tau) &= \frac{1}{2}(\alpha - \frac{\pi}{n} + \frac{\dot{\theta}_i^+}{\lambda})e^{\lambda\tau} + \frac{1}{2}(\alpha - \frac{\pi}{n} - \frac{\dot{\theta}_i^+}{\lambda})e^{-\lambda\tau} \quad \text{and} \\ \dot{\theta}(\tau) &= \frac{\lambda}{2}(\alpha - \frac{\pi}{n} + \frac{\dot{\theta}_i^+}{\lambda})e^{\lambda\tau} - \frac{\lambda}{2}(\alpha - \frac{\pi}{n} - \frac{\dot{\theta}_i^+}{\lambda})e^{-\lambda\tau}. \end{aligned} \tag{2.71}$$

McGeer was only interested in finding limit cycles and, thus, only considered the wheel having enough energy to make it past the vertical after each collision. In this case, a cycle of motion after starting after collision i at time $\tau_i^+ = 0$ ends at time $\tau = \tau_{i+1}^-$ when $\theta(\tau_{i+1}) = \theta_{i+1}^- = \alpha + \frac{\pi}{n}$. Applying this condition to the linear solution, we get the cycle period, $\Delta\tau = \tau_{i+1}^- - \tau_i^+ = \tau_{i+1}^-$, and the end-of-cycle angular velocity, $\dot{\theta}_{i+1}^-$, given by

$$e^{\lambda(\Delta\tau)} = \frac{\alpha + \frac{\pi}{n} + \sqrt{(\frac{\dot{\theta}_i^+}{\lambda})^2 + 4\alpha\frac{\pi}{n}}}{\alpha - \frac{\pi}{n} + \frac{\dot{\theta}_i^+}{\lambda}} \quad \text{and} \tag{2.72}$$

$$\dot{\theta}_{i+1}^- = \sqrt{(\dot{\theta}_i^+)^2 + 4\lambda^2\alpha\frac{\pi}{n}}. \tag{2.73}$$

The collision condition is

$$\dot{\theta}_{i+1}^+ = \mu\dot{\theta}_{i+1}^-. \tag{2.74}$$

Thus, we get a map for small angles

$$\begin{aligned} \dot{\theta}_{i+1}^+ &= \mu\sqrt{(\dot{\theta}_i^+)^2 + 4\lambda^2\alpha\frac{\pi}{n}} \quad \text{or} \\ L(\dot{\theta}) &= \mu\sqrt{\dot{\theta}^2 + 4\lambda^2\alpha\frac{\pi}{n}}. \end{aligned} \tag{2.75}$$

We find the fixed point $\dot{\theta}^*$ of the map L as before by requiring that $\dot{\theta}_{i+1}^+ = \dot{\theta}_i^+ = \dot{\theta}^*$ or $L(\dot{\theta}^*) = \dot{\theta}^*$. This yields the fixed point

$${}^{lc}\dot{\theta}^* = \sqrt{\frac{4\alpha\frac{\pi}{n}\mu^2\lambda^2}{1-\mu^2}} > 0. \tag{2.76}$$

Differentiating L and evaluating at the fixed point gives

$$\left.\frac{dL(\dot{\theta})}{d\dot{\theta}}\right|_{\dot{\theta}={}^{lc}\dot{\theta}^*} = \left.\mu\frac{\dot{\theta}}{\sqrt{\dot{\theta}^2 + 4\alpha\frac{\pi}{n}\lambda^2}}\right|_{\dot{\theta}={}^{lc}\dot{\theta}^*} = \mu^2 < 1 \tag{2.77}$$

as we found before in Equation (2.27) indicating that the limit cycles are stable.

The limit cycle period $\Delta\tau_{lc}$ can be found by substituting the limit cycle angular velocity $\dot{\theta}_i^+ = {}^{lc}\dot{\theta}^*$ into Equation (2.72).

The non-dimensional average speed of the center of mass of the wheel for large numbers of spokes and small slopes is as before in the non-linear case

$$v_{cm_{avg}} = \frac{1}{\Delta\tau_{lc}} \frac{2\pi}{n}. \tag{2.78}$$

The equation of motion, Equation (2.2), first integral of motion, Equation (2.11), map P, Equation (2.25) and the fixed point ${}^{lc}\dot{\theta}^*$, Equation (2.26), from the nonlinear analysis, reduce to the equation of motion, Equation (2.68), the first integral of motion, Equation (2.69), the map L, Equation (2.76), and the fixed point ${}^{lc}\dot{\theta}^*$, Equation (2.76), determined by the linear analysis for large numbers of spokes and small slope angle.

For large n, the limit cycle angular speed is

$${}^{lc}\dot{\theta} \approx \sqrt{\frac{n\alpha}{\pi}}. \tag{2.79}$$

McGeer [66] noted that no cycle exists if the slope is too small. As before, if the slope is too small, the wheel does not start with sufficient speed in a limit cycle to rotate past the vertical. Mathematically, McGeer found the critical slope angle by finding the slope angle corresponding to infinite cycle time; i.e., the angle corresponding to the denominator of Equation (2.72) going to zero or

$$\alpha_c = \frac{\pi}{n} \frac{(1-\mu)^2}{1-\mu^2}. \tag{2.80}$$

If the terms in the transcendental equation from the nonlinear analysis for the critical slope angle, $g(\alpha, J, n) = 0$, are linearized for small slope angle and large numbers of spokes, it can be solved for α and the solution agrees with that above.

For large n, if we take $\alpha \sim O(\frac{1}{n})$, guaranteeing limit cycles, then we find from Equation (2.73) that the limit cycle period is of the same order

$$\Delta\tau_{lc} \sim O(\frac{1}{n}) \tag{2.81}$$

which agrees with the result we found from the nonlinear analysis, Equation (2.67).

2.13 Conclusion

In this complete nonlinear analysis of the 2D rimless wheel, we have defined a cycle of motion of the wheel, derived the equations of motion and collision transition conditions, defined the phase space of the motion, defined a Poincaré section and return map to represent the cyclic motion of the wheel, found fixed points of the map that correspond to limit cycle motion and eventual stopping of the wheel, showed the two fixed points are stable, and defined various behaviors of the wheel. In addition, we showed for what slope angles the fixed points and behaviors exist and how they depend on the initial angular velocity of the wheel. Analyses of the energy and speed of the wheel show that the wheel behaves like a disk rolling down a slope when the number of spokes is infinity. The results are only a small enhancement to the elegant linear analysis of the wheel carried out by McGeer. For small slope angles and large numbers of spokes, all of the results of the nonlinear analysis reduce to the results of McGeer's linear analysis.

Next, in Chapter 3, we begin our study of three-dimensional walking mechanisms by analyzing the motions and stability of a three-dimensional device whose behavior is altered by modifying its

mass distribution; i.e., by adding oblique masses to a disk rolling in a vertical position at constant speed.

In Chapter 4 we return to the rimless wheel. This time, however, we study the stability of planar limit cycle motions of a rimless spoked wheel free to move in three dimensions.

Chapter 3

'Step Two': Stabilizing a Rolling Disk by Adjusting its Mass Distribution

The world is a wheel, and it will all come round right.
Benjamin Disraeli (Earl Beaconsfield) *Endymion. Chap. lxx*

3.1 Introduction

In this chapter, we begin our study of three-dimensional passive-dynamic walking mechanisms by investigating the stability of a disk rolling without slip at constant speed in a vertical plane both with and without a uniform mass distribution. The 3D rolling disk with oblique masses added is shown in Figure 3.1 below to remind the reader of where it fits into the evolution of models in the research program.

The purpose of the analysis in this chapter is to demonstrate that we can alter the stability characteristics of a simple conservative 3D system *passively* (without dissipation), by adjusting its physical parameters, namely its mass distribution, rather than *actively* through some control algorithm. This result has been demonstrated previously in a paper on monocycles and bicycles by Carvallo [67].

Conservative *holonomic* systems cannot have asymptotically stable steady motions. On the other hand, not as widely known is that conservative *non*holonomic systems can have asymptotically (exponentially) stable steady motions in some variables while at most mildly unstable in the others, as recalled in Zenkov, *et al.* [48]. We know of only a few examples of conservative *nonholonomic* systems which can have asymptotically stable steady motions at or near a potential energy maximum without fast-spinning parts: 1) a no-hands bicycle with massless wheels (say skates) and a special mass distribution [8, 68]; (2) a no-hands tricycle (where gyroscopic terms from the spinning wheels are not relevant for balance because of the three point support) with a mildly soft de-centering (negative spring constant) spring on the steering [69, 70]; (3) a rigid rider attached appropriately to a moving skate-board [9]; and (4) rattlebacks (or celts) [71]. (For a general discussion of the dynamics and stability of nonholonomic systems see Neimark and Fufaev [46].)

It is well known from linearized stability analyses that a disk rolling at constant rate, at a constant bank angle, and at a constant heading rate in a circle is stable, thought not asymptotically stable, given sufficient forward rolling speed; i.e., small lateral disturbances cause the disk to 'wobble' indefinitely in simple harmonic motion – the wobbles do not grow or decay in time [6]. This family of steady motions on circular paths forms a surface or manifold of steady motions and it is this

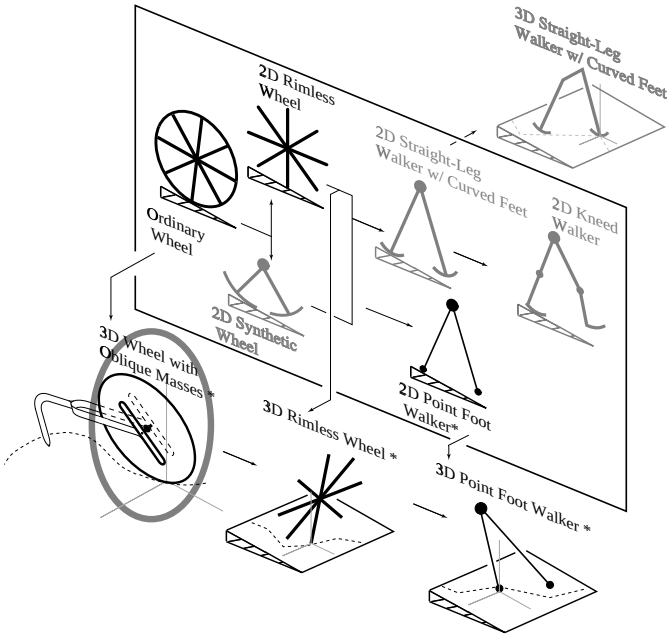

Figure 3.1: The place of the 3D rolling disk with oblique masses in the passive-dynamic family tree.

manifold whose stability we are considering. If one perturbs a member of the family of solutions, it is considered asymptotically stable if you end up on another nearby member of the family. A special member of the family of solutions is rolling straight ahead at constant rate in a vertical plane.

A reasonable question to ask is whether a physically realizable mechanical device or adjustment of parameters can allow the disk to recover from small disturbances and eventually return to the vertical (or near vertical) reference condition, without active control or dissipation. We investigate a suitable device below after first reviewing the thin uniform disk rolling without slip.

3.2 Rolling Disk

We review here the well known analysis of rolling disk (see, e.g., Greenwood [6], Neimark and Fufaev [46]). More recent extensive analyses can be found in O'reilly [72] and Cushman, it et. al. [73].

Consider a thin uniform disk of mass m and radius r that rolls without slipping on a horizontal plane. Its orientation is defined by the 3-1-2 Euler angles: heading angle ϕ, bank angle ψ, and pitch angle θ. (Refer to Appendix D for a description of 3-1-2 Euler angles.) Gravity acts in the negative z direction and the disk rolls forward in the positive x direction. The configuration is shown in Figure 3.2. The moment of inertia matrix for the uniform planar disk with respect to its center of mass and in body coordinates is given by :

$$\begin{pmatrix} I^C_{xx} & 0 & 0 \\ 0 & I^C_{yy} & 0 \\ 0 & 0 & I^C_{zz} \end{pmatrix}$$

For the disk, $I^C_{xx} = I^C_{zz}$ and $I^C_{yy} = I^C_{xx} + I^C_{zz}$. We write our equations of motion in terms of the non-dimensionalized quantities $J = I^C_{xx}/mr^2 = I^C_{zz}/mr^2$ and $2J = I^C_{yy}/mr^2$.

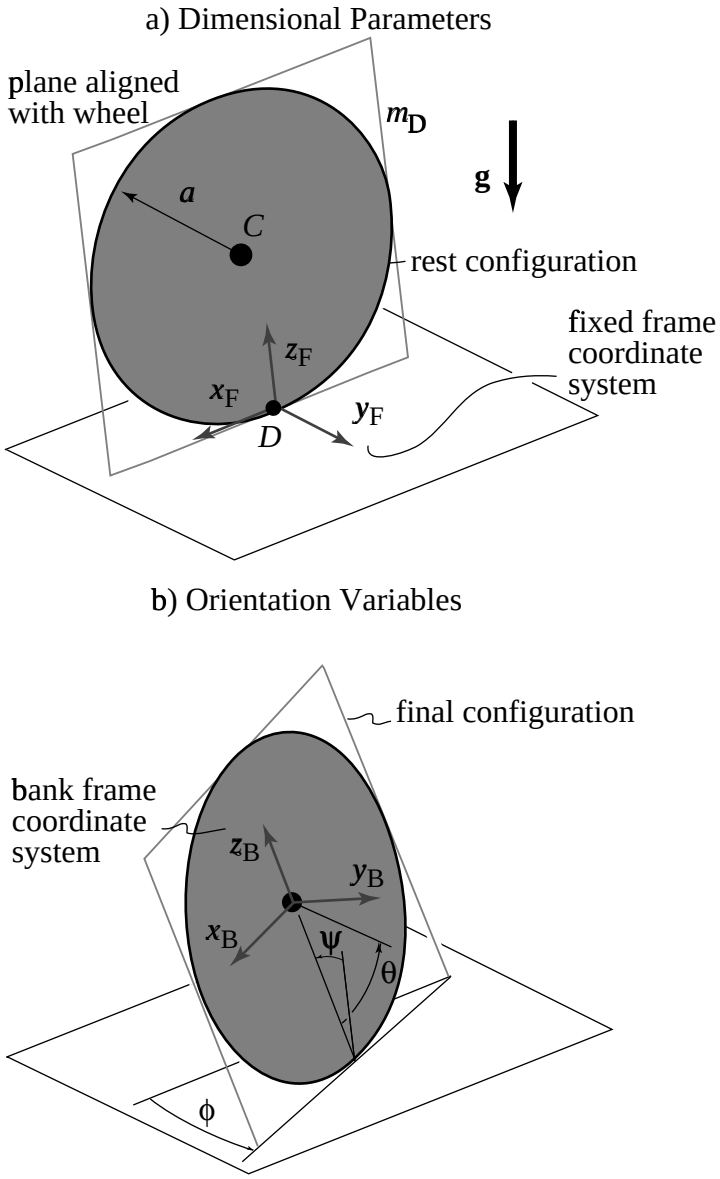

Figure 3.2: The dimensional parameters and orientation variables for the uniform disk.

The system is non-holonomic (see page 9 in Chapter 1) ; the configuration space is five dimensional. The state space is six dimensional and $\mathbf{q}$, the state vector, is

$$\mathbf{q} = \{\phi, \psi, \theta, \dot{\phi}, \dot{\psi}, \dot{\theta}\}^T. \tag{3.1}$$

Taking angular momentum balance about the point of contact, point D, the non-dimensionalized equations of motion are:

$$\begin{aligned} 0 &= (1+\lambda^2)\ddot{\psi} - 2\ c\psi\ \dot{\phi}\dot{\theta} - (1+\lambda^2)s\psi\ c\psi\ \dot{\phi}^2 - 2\lambda^2\ s\psi & (3.2)\\ 0 &= c\psi\ \ddot{\phi} + 2\ \dot{\psi}\dot{\theta} & (3.3)\\ 0 &= \ddot{\theta} + s\psi\ \ddot{\phi} + (1+\lambda^2)c\psi\ \dot{\phi}\dot{\psi}, & (3.4) \end{aligned}$$

where 's'and 'c' are used to denote 'sin' and 'cos' and

$$\lambda^2 = \frac{1}{2J+1}. \tag{3.5}$$

An overdot indicates differentiation with respect to non-dimensional time $\tau = t\sqrt{g/r}$.

Linearization of the non-linear equations about the steady vertical rolling reference condition ($\dot{\theta}_0 \equiv$ constant) or

$$\mathbf{q}_0 = \{\theta_0(\tau) = \dot{\theta}_0\tau, 0, 0, 0, 0, \dot{\theta}_0\}, \tag{3.6}$$

is accomplished by letting $\mathbf{q}(\tau) = \mathbf{q_0} + \epsilon\hat{\mathbf{q}}(\tau)$, substituting it into the equations of motion and truncating the result to first order in ϵ, where ϵ is a small number. A 'hat' ($\hat{}$) denotes perturbed quantities.

The equations of motion linearized about the reference condition are:

$$\begin{aligned} 0 &= (1+\lambda^2)\ddot{\hat{\psi}} - 2\dot{\theta}_0\dot{\hat{\phi}} - 2\lambda^2\hat{\psi} & (3.7)\\ 0 &= \ddot{\hat{\phi}} + 2\dot{\theta}_0\dot{\hat{\psi}} & (3.8)\\ 0 &= \ddot{\hat{\theta}} & (3.9) \end{aligned}$$

Equation (3.9) above indicates that a perturbation in the pitch rate is constant to first order, $\dot{\hat{\theta}} = \dot{\hat{\theta}}_0$, resulting in a small change in the overall speed of the disk. Integrating Equation (3.8) with respect to time yields

$$\dot{\hat{\phi}} = -2\dot{\theta}_0(\hat{\psi} - \hat{\psi}_0) + \dot{\hat{\phi}}_0. \tag{3.10}$$

Substituting Equation (3.10) into Equation (3.7) yields a simple linear inhomogeneous second order ordinary differential equation governing small disturbances in the bank angle

$$\ddot{\hat{\psi}} + \frac{2(2\dot{\theta}_0^2 - \lambda^2)}{1+\lambda^2}\hat{\psi} = \frac{2\dot{\theta}_0}{1+\lambda^2}(2\dot{\theta}_0\hat{\psi}_0 + \hat{\phi}_0). \tag{3.11}$$

Oscillating solutions to the homogeneous version of Equation (3.11) exist when the roots of the characteristic equation are imaginary. That requires $2\dot{\theta}_0^2 - \lambda^2$ or

$$\dot{\theta}_0^2 > \frac{\lambda^2}{2}. \tag{3.12}$$

The non-zero constant on the right hand side of Equation (3.11) gives rise to a constant particular solution. Thus, given initial perturbations in the bank or heading angles, the solution will oscillate about some small non-zero bank angle. In addition, Equation (3.10) shows that the heading rate will oscillate about some small non-zero value that depends on the bank angle. This means that the the disk will shift away from its original zero heading onto a circular path while it is wobbling forever about some mean bank angle at some mean heading rate.

3.3 Disk with Oblique Masses

Two identical planar rigid bodies of total mass m_C are fixed symmetrically about the plane of the disk with centers of mass collinear with the center of mass of the disk, point G, but are not free to roll with the disk. The masses are rigidly attached to a supporting 'fork' of negligible mass constrained to slide frictionlessly on the the ground at point E at a distance L from the contact point D of the disk. The fork has a frictionless axle of negligible length about which the disk rotates. Again, its orientation is defined by the 3-1-2 Euler angles, gravity acts in the negative z direction, and the system moves forward in the positive x direction. The configuration is shown in Figure 3.3. The

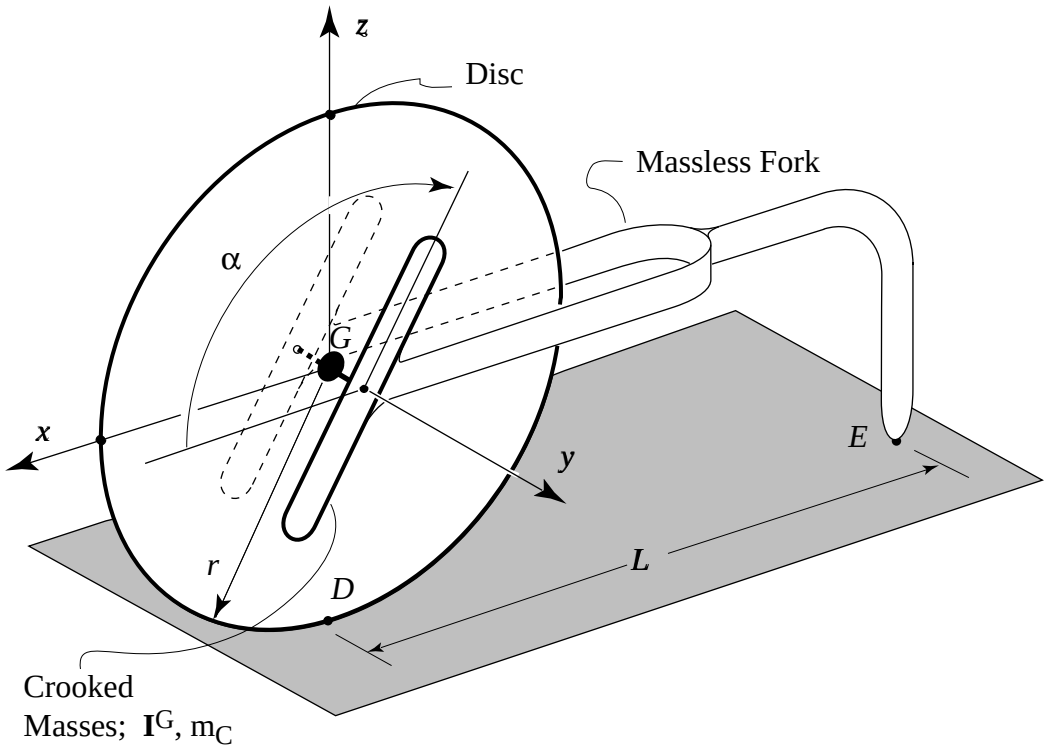

Figure 3.3: The dimensional parameters of the disk plus oblique masses. The angle α is a geometric design parameter that describes the orientation of the masses in the plane of the disk and may be adjusted to stabilize the disk.

masses do not roll with the disk but have the same heading and bank angles as the disk. The inertia matrix for the masses with respect to point G and in body coordinates is given by:

$$\begin{pmatrix} I^G_{xx} & 0 & I^G_{xz} \\ 0 & I^G_{yy} & 0 \\ I^G_{xz} & 0 & I^G_{zz} \end{pmatrix}.$$

For the crooked masses, $I^G_{yy} = I^G_{xx} + I^G_{zz}$. We write the equations of motion in terms of the non-dimensionalized quantities $A = I^G_{xx}/m_T r^2$, $B = I^G_{zz}/m_T r^2$, $A + B = I^G_{yy}/m_T r^2$, and $C = I^G_{xz}/m_T r^2$, where $m_T = m + m_C$ is the total mass of the system of disk and crooked masses. Here, we re-define the non-dimensional transverse moment of inertia to be $J = I^C_{xx}/m_T r^2$.

For the moment of inertia matrix for the crooked masses to be positive definite, its eigenvalues: (1) must be positive and (2) must satisfy the triangle inequality (the sum of any two of the eigenvalues

is greater than or equal to the the third). Since $A > 0$ and $B > 0$, condition(2) determines that $AB > C^2$.

Taking angular momentum balance of (1) the system of disk and crooked masses about point D of and (2) the fork and crooked masses about the axle yields the following non-dimensionalized equations of motion:

$$\begin{aligned} 0 &= (1+\rho^2(1+2A))\ddot{\psi} + 2\rho^2 C\ c\psi\ \ddot{\phi} - (1+\rho^2(1+2A))\ s\psi\ c\psi\dot{\phi}^2 - \\ &\quad 2c\psi\ \dot{\phi}\dot{\theta} - 2\rho^2\ s\psi \qquad (3.13) \\ 0 &= (\rho^2(2(A+2B)-1) + 2(1-\rho^2(1+2A))\ s\psi\ c\psi + 1)\ddot{\phi} \\ &\quad +4C\rho^2(c\psi\ \ddot{\psi} - s\psi\ \dot{\psi}^2) + 8A\rho^2\ c\psi\ s\psi\ \dot{\psi}\dot{\phi} + 4(1-\rho^2)\ c\psi\ \dot{\psi}\dot{\theta} \qquad (3.14) \\ 0 &= \ddot{\theta} + s\psi\ \ddot{\phi} + (1+\rho^2)c\psi\ \dot{\phi}\dot{\psi} \qquad (3.15) \end{aligned}$$

where $\rho^2 = 1/2J + 1$. Following the same procedure as above but for the system of disk and additional masses, the linearization of the equations of motion yields

$$\begin{aligned} 0 &= (1+\rho^2(1+2A))\ddot{\hat{\psi}} + 2C\rho^2\ddot{\hat{\phi}} - 2\dot{\theta}_0\dot{\hat{\phi}} - 2\rho^2\hat{\psi} \qquad (3.16) \\ 0 &= (1+\rho^2(2B-1))\ddot{\hat{\phi}} + 2C\rho^2\ddot{\hat{\psi}} + 2(1-\rho^2)\dot{\theta}_0\dot{\hat{\psi}} \qquad (3.17) \\ 0 &= \ddot{\hat{\theta}} \qquad (3.18) \end{aligned}$$

Integrating Equation (3.17) with respect to time yields

$$\dot{\hat{\phi}} = \frac{1}{1+\rho^2(2B-1)}\left[-2C\rho^2(\dot{\hat{\psi}} - \dot{\hat{\psi}}_0) - 2(1-\rho^2)\dot{\theta}_0(\hat{\psi} - \hat{\psi}_0)\right] + \dot{\hat{\phi}}_0. \qquad (3.19)$$

Substituting Equation (3.19) into Equation (3.16) yields a single simple equation for small disturbances in the bank angle

$$P\ddot{\hat{\psi}} + Q\dot{\hat{\psi}} + R\hat{\psi} = S \qquad (3.20)$$

where

$$\begin{aligned} P &= \left[\frac{4\rho^4(AB-C^2)}{1-\rho^4} + 2\rho^2\left(\frac{B}{1-\rho^2} + \frac{A}{1+\rho^2}\right) + 1\right], \\ Q &= \frac{4C\rho^4\dot{\theta}_0}{1-\rho^4}, \\ R &= 2\left[\frac{(2\dot{\theta}_0^2 - \rho^2)}{1+\rho^2} - \frac{2B\rho^4}{1-\rho^4}\right], \text{ and} \qquad (3.21) \\ S &= \frac{2\dot{\theta}_0}{1+\rho^2}\left[2(\hat{\psi}_0\dot{\theta}_0 + \dot{\hat{\phi}}_0) + \frac{2\rho^2(B\dot{\hat{\phi}}_0 + C\dot{\hat{\psi}}_0)}{1-\rho^2}\right] \qquad (3.22) \end{aligned}$$

Equation (3.20) is similar to Equation (3.11) except for the additional term proportional to the bank rate which resembles a linear damping term. Again, the right hand terms in Equation (3.20) give rise to a small constant steady-state solution. Despite the fact that the system of disk plus masses is has the linear growth in the heading angle, the crooked masses can cause the wobbling to die out. Damping of bank angle disturbances requires negative real roots of the characteristic equation for Equation (3.20). That is, according to Routh's criterion, P, Q, and R must be positive. Thus, we make the following observations:

1. $P > 0$ is automatically satisfied since $\rho^2 = 1/(2J+1) < 1$ and $AB > C^2$ by definition,
2. $Q > 0$ if $C > 0$ since $\rho^2 < 1$, and

3. $R > 0$ if the pitch rate satisfies

$$\dot{\theta}_0^2 > \frac{\rho^2}{2}\left(\frac{1+\rho^2(2B-1)}{1-\rho^2}\right). \tag{3.23}$$

The middle term in Equation (3.20) is a 'damping' term that arises due to a coupling between heading and bank rate. The coupling is induced by the off-diagonal product of inertia term, I_{xz}, introduced by the non-axisymmetric masses. While the diagonal elements of the moment of inertia matrix are always positive, the off diagonal elements, the products of inertia, can be positive or negative. Given sufficient rolling speed and a proper orientation of the masses, the lateral oscillations of the disk can be damped out. For example, if two identical uniform thin bars are fixed in the bank frame of the disk with orientation $\pi/2 < \alpha < \pi$ (giving $C > 0$) such that $C^2 < AB$, then the conditions for asymptotic stability are met.

It is interesting to note that if the moments of inertia of the disk are zero, we get the following equation for stability,

$$(B + AB - C^2)\ddot{\hat{\psi}} + C\dot{\theta}_0\dot{\hat{\psi}} - B\hat{\psi} = \dot{\theta}_0(B\dot{\hat{\phi}}_0 + C\dot{\hat{\psi}}_0). \tag{3.24}$$

In this case, since $B > 0$, the characteristic will not have negative real roots. So, it seems that for wobbling to die out (or continue indefinitely), the gyroscopic effect of the rolling disk is necessary to counteract the effect of gravity tending to make the disk fall over when it is perturbed from vertical rolling.

Finally, taking $A = B = C = 0$ and m_C=0, then $\rho^2 = \lambda^2$ and all of the equations and stability results for the disk with the crooked masses reduce to the results obtained above for the uniform disk.

3.4 Numerical Simulation

We numerically integrate the fully nonlinear equations of motion for the uniform disk and the disk with crooked masses using MATLAB® and compare the results.

3.4.1 Uniform Disk

First, we present the result of a simulation of the uniform disk (A=B=C=0) with $\lambda^2 = 2/3$, $\Delta\psi_0 = 0.001$, and $\dot{\theta}_0^2 = 100\lambda^2/2$ (the steady rolling speed is ten times the minimum speed required for the disk to be neutrally stable). Results of numerical integration are shown in Figure 3.4. Note that ψ and $\dot{\phi}$ oscillate about constant non-zero values as predicted by the linearization. The linearization predicts the particular solution for the bank angle to be

$$\psi^* = \frac{\dot{\theta}_0(2\hat{\psi}_0\dot{\theta}_0 + \dot{\hat{\phi}}_0)}{(2\dot{\theta}_0^2 - \lambda^2)} = \frac{1}{990} \approx 0.00101010, \tag{3.25}$$

The numerical solution gives $\psi^* = 0.00101007$. The linearization predicts the particular solution for the heading rate as given by Equation (3.10)

$$\dot{\phi}^* = -2\dot{\theta}_0(\hat{\psi} - \hat{\psi}_0) + \dot{\hat{\phi}}_0 \approx -0.00011675. \tag{3.26}$$

The numerical solution gives $\dot{\phi}^* = -0.00011673$. Finally, the frequency of oscillation ω of the perturbations is predicted to be

$$\omega = \frac{2(2\dot{\theta}_0^2 - \lambda^2)}{1+\lambda^2} \approx 0.706. \tag{3.27}$$

The numerical simulation gives $\omega \approx 0.704$.

The numerical results are in good agreement with the analytical predictions from the linearization.

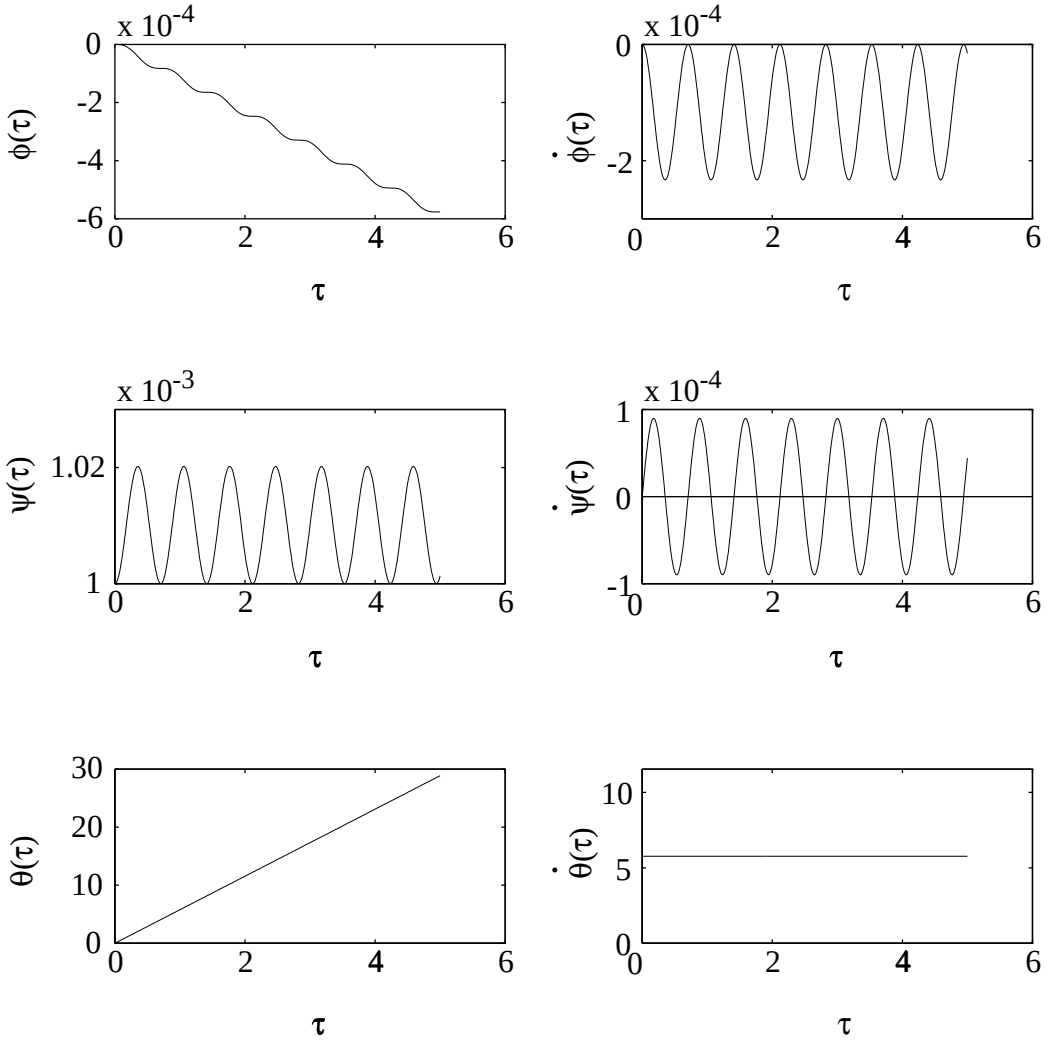

Figure 3.4: State of the uniform disk versus non-dimensional time τ up to $\tau = 5$ after it is perturbed from its steady vertical motion with a disturbance in the bank angle $\Delta\psi_0 = 0.001$. For this simulation, $2J = 0.5$ (or $\lambda^2 = 2/3$).

3.4.2 Disk with Crooked Masses

Next, we present the result of a simulation of the uniform disk plus crooked masses with $A = B = 0.5$, $C = 0.25$, $\rho^2 = 2/3$, and $\Delta\psi_0 = 0.001$. Note that $AB > C^2$, a requirement of the inertia matrix. For the given parameters, we set the steady rolling speed at $\dot{\theta}_0^2 = 100\frac{\rho^2(1+\rho^2)}{2(1-\rho^2)}$ (the steady rolling speed is ten times the minimum speed required for the disk to be wobble indefinitely). Results of numerical integration are shown in Figure 3.5. Note that, while the oscillations due to the initial disturbance die out, the bank angle ψ and and heading rate $\dot{\phi}$ approach constant non-zero steady-state values as predicted by the linearization. The linearization predicts that the steady-state value for the bank angle is

$$\psi_{ss} = \frac{S}{R} = \frac{\dot{\theta}_0\left[2(\hat{\psi}_0\dot{\theta}_0 + \dot{\hat{\phi}}_0) + \frac{2\rho^2(B\dot{\hat{\phi}}_0 + C\dot{\hat{\psi}}_0)}{1-\rho^2}\right]}{\left[(2\dot{\theta}_0^2 - \rho^2) - \frac{2B\rho^4}{1-\rho^2}\right]} = \frac{1}{990} \approx 0.001010101010 \tag{3.28}$$

The numerical simulation gives $\psi_{ss} \approx 0.001010101016$. The linearization predicts the steady-state solution for the heading rate as given by Equation (3.19)

$$\begin{aligned} \dot{\phi}_{ss} &= \frac{1}{1+\rho^2(2B-1)}\left[-2C\rho^2(\dot{\hat{\psi}} - \dot{\hat{\psi}}_0) - 2(1-\rho^2)\dot{\theta}_0(\hat{\psi} - \hat{\psi}_0)\right] + \dot{\phi}_0 \\ &\approx -0.00006734011. \end{aligned} \tag{3.29}$$

The numerical simulation gives $\dot{\phi}_{ss} \approx -0.00006734009$. Again, the numerical results for the disk with crooked masses are in good agreement with the results predicted by the linearization.

To a first order approximation, if there is no perturbation in the pitch rate, the linearization predicts that the pitch rate remains constant even if the bank or heading angle (or their rates) are perturbed. Upon closer inspection of the numerical results, however, the plots of the pitch rate show higher order effects that the linear approximation misses. For the uniform disk, the pitch rate oscillates about a value slightly higher than its initial value with amplitude about 80 times smaller than that of the bank angle, 750 times smaller than that of the bank rate, and about 1000 times smaller than that of the heading rate, but at the same frequency. For the uniform disk with crooked masses, the oscillations in the pitch rate die out at the the same rate and frequency of oscillation as the bank angle to a steady-state value whose difference from the initial pitch rate is about 150 times smaller than the difference of the steady-state bank angle from its initial value and about 1000 times smaller than the steady-state heading rate.

3.4.3 More General Crooked Masses

In this study, we have neither investigated the effects of (1) moving around the center-of-mass or (2) more general mass distributions of the crooked masses. Either of these enhancements might produce stability without rotational inertia of the disk.

3.5 Conclusions and Future Work

The altered disk is a conservative non-holonomic system. Although the damping term induced by the off-diagonal inertia terms causes the bank angle disturbances to die out, no energy can be lost. Introducing a small disturbance to the system increases the total energy of the system. When the disturbance dies out, where does the energy go? Due to the kinematic coupling between the lean and steer, the energy of the initial wobble is 're-directed' into an increase in the the heading rate and the pitch rate of the system, and energy is conserved.

This study gives evidence of how a device free to move in three dimensions may be made *more* stable in a purely passive manner by simply altering the distribution of mass in the system without

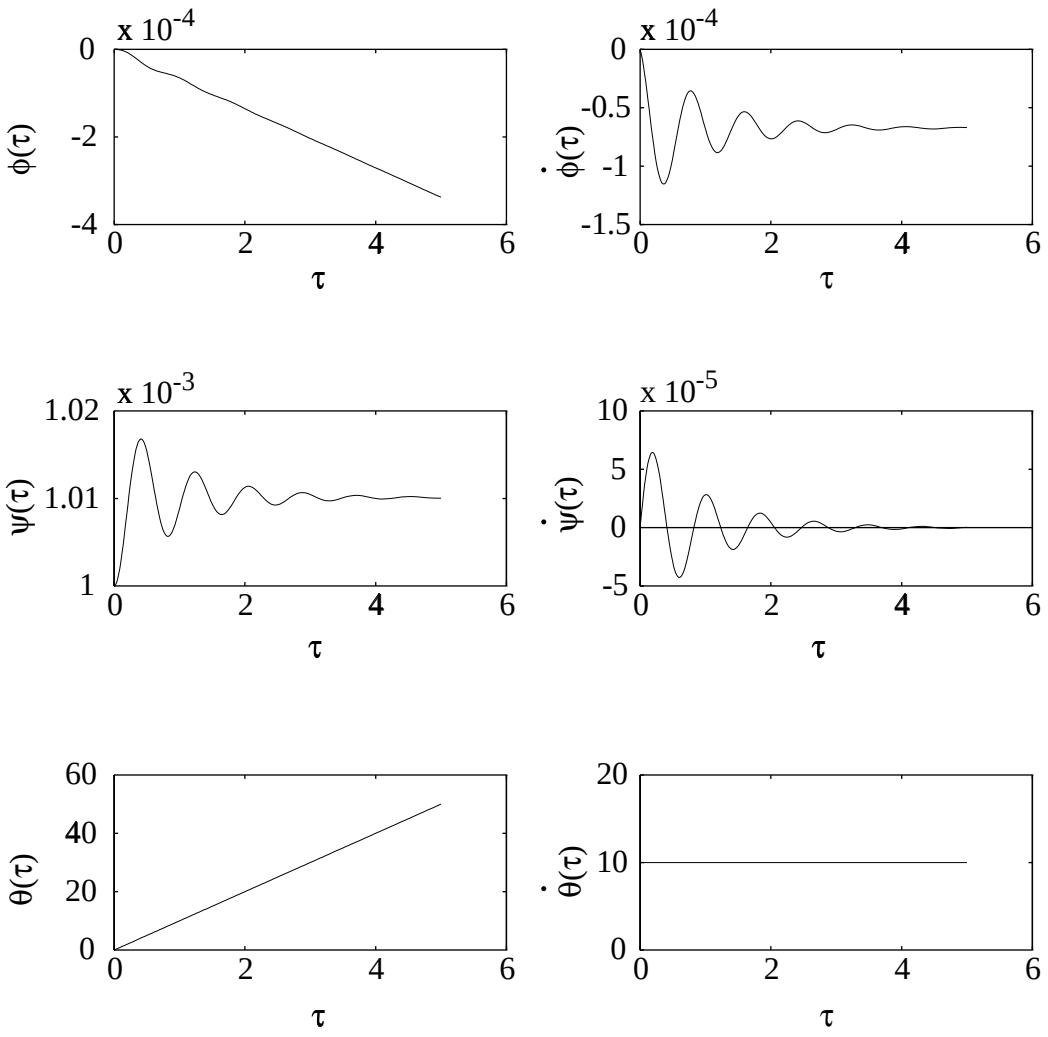

Figure 3.5: State of the uniform disk with crooked masses versus non-dimensional time τ up to $\tau = 5$ after it is perturbed from its steady vertical motion with an initial disturbance in the bank angle $\Delta\psi_0 = 0.001$. For this simulation, $2J = 0.5(\lambda^2 = 2/3)$, $A = 0.5$, $B = 0.5$, and $C = 0.25$.

any active control or energy input. The particular mass distribution investigated here, one that makes I_{xz} nonzero in the inertia matrix, changes the steady motions on circular paths at constant bank angle from stable to asymptotically stable. Thus, this study suggests that mass distribution is an important parameter in increasing the stability of the rolling disk, a conservative non-holonomic system. Perhaps the mass distribution may be adjusted in a similar way for walking mechanisms to add to or enhance stability in the presence of the dissipative foot collisions (non-conservative and piece-wise holonomic). We investigate this in our study of 3D passive-dynamic walkers in Chapter 6. But, the gyroscopic effect of the rolling disk is necessary for its asymptotic stability, a stability mechanism that counter oscillating swinging legs do not offer in walking models. So, it would be useful to consider how a more general mass distribution and center of mass location for the crooked masses might offer possibilities for greater stability of the rolling disk.

Next, as noted at the end of Chapter 2, we reconsider the rimless wheel, this time free to move in three dimensions. In the limit as the number of spokes gets very large and the slope very small, we check to see that the rimless wheel's behavior approaches that of the rolling disk. For a finite number of spokes, we compare stability of the rimless wheel to that of a rolling disk.

Chapter 4

'Step Three': Rimless Spoked Wheel Free to Move in Three Dimensions

I'm a spoke on a wheel. I am, and so are you.
Lefty in the movie *Donnie Brasco*

We now present an analysis of the three dimensional motions of a rimless spoked wheel, or polygon, 'rolling' downhill under the action of gravity. The 3D rimless wheel is shown in Figure 4.1 below to remind the reader of where it fits into the evolution of models in the research program. While preparing a talk on this work, the author was inspired to draw the cartoon shown in Figure 4.2.

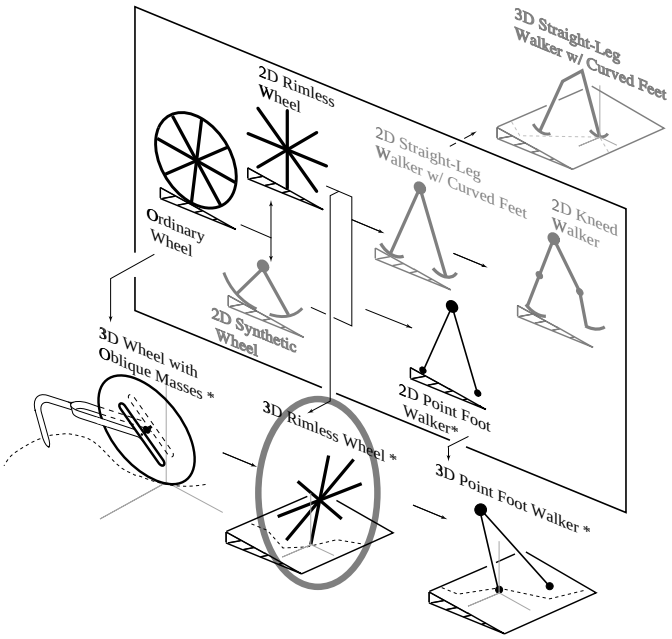

Figure 4.1: The place of the 3D rimless wheel in the passive-dynamic family tree.

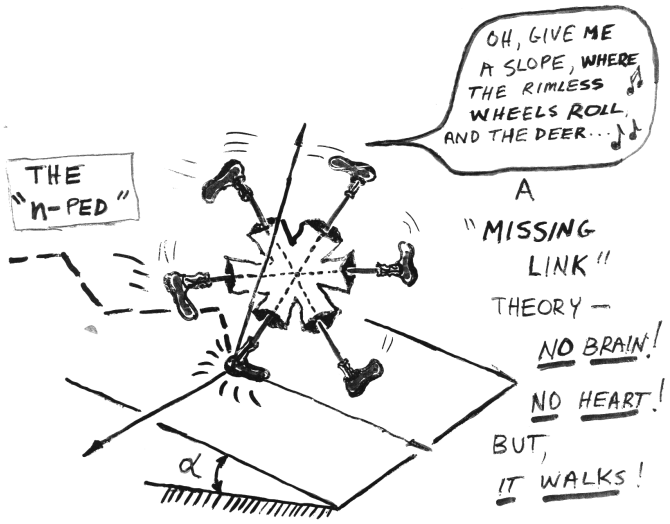

Figure 4.2: An anthropomorphized realization of the rimless spoked wheel free to move in three dimensions.

This chapter is an expanded version of the author's work reported on earlier in a paper published by Coleman, Chatterjee, and Ruina entitled *Motions of a Rimless Spoked Wheel: A Simple 3D System with Impacts* [74]. In particular: (1) Section 4.8.1 we add the details of a calculation on how to predict the steady state of the wheel using the numerically obtained Jacobian of the return map and (2) Section 4.8.2 includes much more of the details of the asymptotic expansion used to obtain an analytical approximation to the Jacobian of the return map.

We carry out three-dimensional numerical and analytical stability studies of steady motions of this system. At any fixed, large enough slope, the system has a one-parameter family of stable steady rolling motions. We find analytic approximations for the minimum required slope at a given heading for stable rolling in three dimensions, for the case of many spokes and small slope. The rimless wheel shares some qualitative features with passive-dynamic walking machines; it is a passive three dimensional system with intermittent impacts and periodic motions. In terms of complexity it lies between one dimensional impact oscillators and three dimensional walking machines. In contrast to a rolling disk on a flat surface which has steady rolling motions that are only *neutrally* stable at best, the rimless wheel can have asymptotic stability. In the limit as the number of spoke s n approaches infinity, the behavior of the rimless wheel approaches that of a rolling disk in an averaged sense and becomes neutrally stable. Also, in this averaged sense, the piecewise holonomic system (rimless wheel) approaches a nonholonomic system (disk).

4.1 Introduction

We study the three dimensional motions of a spoked, rimless wheel 'rolling' down a slope under the action of gravity (see Figure 4.3). A planar rimless wheel of mass m, with moment of inertia matrix $\mathbf{I}^C$ about the center of mass, and n evenly spaced identical spokes of length ℓ rolls down a slope of angle α. The orientation variables are 3-1-2 Euler angles representing pitch(θ), heading(ϕ), and bank(ψ). For 2D motions of the wheel at any fixed heading ϕ, the only non-constant variable is θ since the motion is then confined to a vertical plane aligned with gravity (ψ a constant).

By *rolling*, we mean motions in which the wheel pivots on one 'support' spoke until another

spoke collides with the ground, followed by transfer of support to that spoke, and so on. There is no power input (except gravity) and no control. For a given slope, the only free parameters of the system are the mass distribution and number of spokes.

4.1.1 Motivation

Our interest in the rimless wheel starts from an interest in the dynamics of human walking. Studies of the dynamics of walking motions sometimes involve mechanical systems with the following characteristics: **(a)** over certain periods, the systems have smooth motions that may be roughly described as unstable falling (near a statically unstable configuration); **(b)** these smooth motions are interrupted by collisions, at which velocities change quickly; and support might be transferred from one foot to another; and **(c)** after each collision, another phase of smooth motion begins.

Steady walking corresponds to periodic motions of these dynamic systems. Such systems have been studied with no actuation and control (McGeer, 1990, 1991 [43, 44, 4]; McMahon, 1984 [75]; Garcia, *et. al.*, 1996 [16]; Goswami, *et. al.*, 1996 [45]) as well as with various amounts and types of power input and active control (see, *e.g.*, Hemami and Chen, 1984 [76]; Furusho and Sano, 1990 [77]; Taga, 1991 [25]; Beletskii, 1990 [78]; Pandy and Berme, 1988 [79]; Hurmuzlu, 1993 [57, 58]; Yamaguchi, 1990 [19]; Zajac and Winters, 1990 [18]; Vukobratovic, *et. al.*, 1990 [80]).

One goal of studies of gait is to understand stability. McGeer's machines, and the walking toys that inspired them (McGeer, 1989) [11], are passive *and* dynamically stable. We are not aware of studies of systems that are simpler than McGeer's, yet retain the essential features mentioned above. Besides wobbling toys with low mass-centers and broad feet (McGeer, 1989) [11], passive dynamic walking machines that are stable in three dimensions have not yet been discovered in theory or simulation. We have developed the only such device in practice that we know of [14]; our device is based loosely on simulations of a similar model that is almost stable. We report on this device in more detail in Chapter 6.

Two dimensional motions of the rimless wheel were studied briefly by McGeer (note that in 2D motions, the system has only one degree of freedom). Although three-dimensional motions of a rolling regular polygons (the same as a rimless wheel) were studied by Goyal (1992) [7], three dimensional stability analyses of rolling polygons have not been conducted before. We hope that a 3D stability analysis of the wheel will provide some insight into possible stabilizing mechanisms which in turn might improve our understanding of the dynamics of passive walking in 3D. Like McGeer's walking machines, the rimless wheel has periodic motions in two dimensions which are stable if restricted to two dimensions. Also, like walking machines, the rimless wheel can fall down in 3D. The wheel is simpler to study than the walking machines for the following reasons: **(a)** if the slope is large enough, periodic motions always exist within some interval of heading angle ϕ; **(b)** if periodic motions exist, they are always stable if constrained to 2D; and **(c)** the motion is simpler because the system consists of a single rigid body, unlike the walking machines, which are made of interconnected rigid bodies.

Another reason why the rimless wheel is of interest is that its rolling motion resembles that of a disk, especially so as the number of spokes becomes large. Steady rolling of a disk on a level surface is not asymptotically stable; if slightly disturbed, the wheel wobbles forever (e.g., see Greenwood [6] and Chapter 3 of this dissertation). The similarity of the rolling motions, leads to the question of whether steady motions of the rimless wheel can be asymptotically stable.

4.2 Description of the System

A wheel of net mass m with the rim removed and n evenly spaced identical spokes of length ℓ rolls down a slope of angle α (see Figure 4.3). Assuming n-fold symmetry and that all mass is in the plane, the moment of inertia matrix about the center of mass with the y-axis normal to the plane

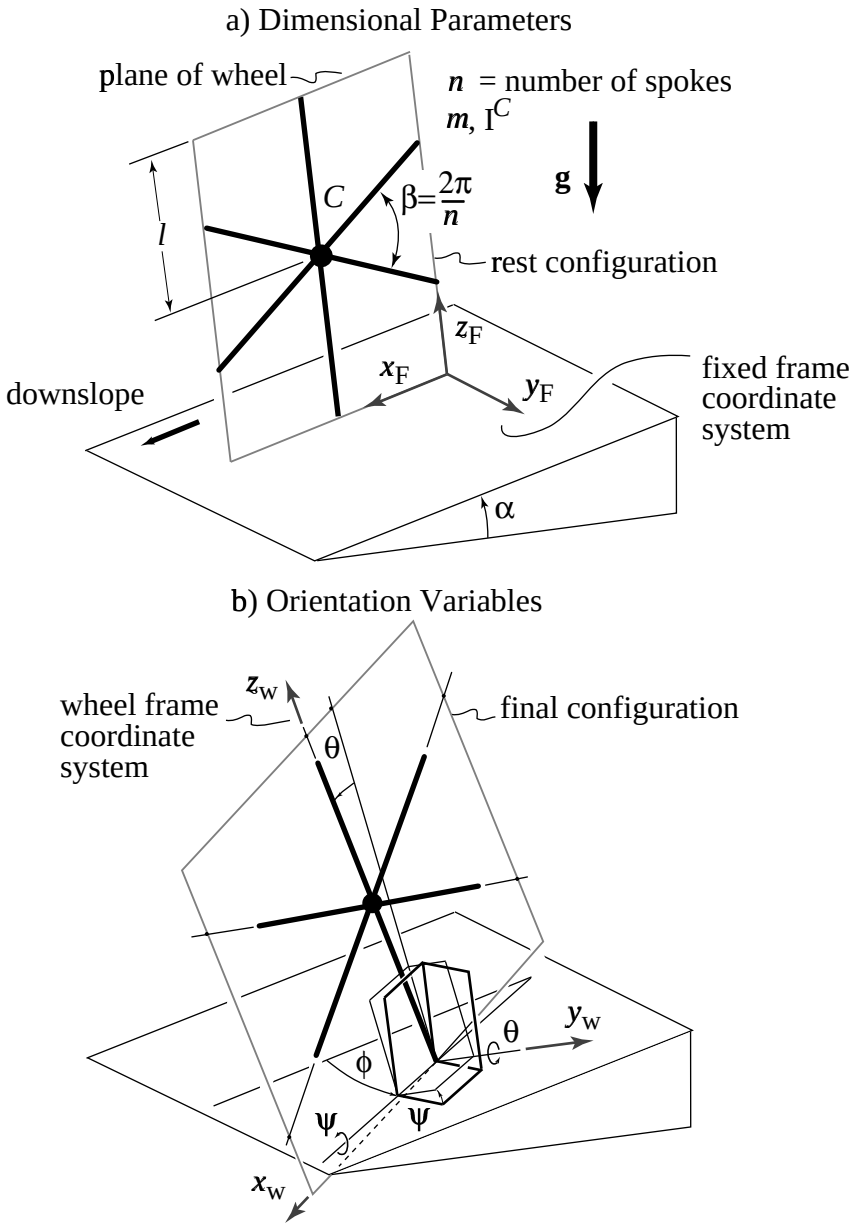

Figure 4.3: (a) Parameters and (b) orientation variables of the 3D rimless wheel model.

of the wheel is

$$\mathbf{I}^C = \begin{bmatrix} D & 0 & 0 \\ 0 & 2D & 0 \\ 0 & 0 & D \end{bmatrix}, \text{ for some } D > 0. \tag{4.1}$$

Unlike a wheel with a rim, since this device loses energy at collisions, it cannot roll steadily on a level surface. Here, we only consider downhill rolling.

It is possible that appreciably elastic and/or sliding collisions will make the dynamics of the system more complicated, and perhaps change its stability. We do not consider such cases here. Once a spoke contacts the ground, we assume that it pivots about the contact point until the next spoke collides and we do not allow slip and/or loss of contact between collisions.

The perfectly plastic, instantaneous collision assumption is reasonable when the distance of rebound or sliding is small compared to the distance between neighboring spoke tips, and the time of collisional interaction is small compared to the time between collisions. The perfectly plastic assumption reduces nicely to the rolling disk as $n \to \infty$.

4.2.1 Configuration and State Spaces

We characterize the configuration of the wheel between collisions using 3-1-2 Euler angles as shown in Figure 4.3 (see Appendix D). The heading angle is the rotation ϕ about the original z axis, the bank angle is the rotation ψ about the new x axis, and the pitch angle is the rotation θ about the newest y axis.

Globally, the system has five generalized coordinates, like a rolling disk: two for contact position and three for the three-dimensional orientation. Unlike the rolling wheel, the contact point is stationary between collisions and shifts discontinuously during collisions. The velocity at any instant is fully determined by only three generalized coordinates, the Euler angle rates. Thus, the nonholonomy of the system – the dimension of the configuration space has dimension two more than that of the instantaneously accessible velocity space ($5 > 3$).

In our stability analysis, we do not keep track of the foot contact position over several foot collisions; we just keep track of the orientation variables ϕ, ψ, and θ. We use equations of motion for a rimless wheel pivoting on one spoke (holonomic system with three degrees of freedom), and use angular momentum-balance-deduced jump conditions to map the state variables from just before a foot collision to just after. Thus, in our analysis, the state space is six dimensional and $\mathbf{q}$, the state vector, is defined to be

$$\mathbf{q} = \{\phi, \psi, \theta, \dot{\phi}, \dot{\psi}, \dot{\theta}\}^T. \tag{4.2}$$

4.2.2 Indexing Scheme

We move the origins of each of the frames instantaneously with each collision, from the tip of spoke i to the tip of spoke $i+1$ currently in contact with the ground at collision $i+1$. After a collision, then, we redefine the wheel orientation with the respect to the newly positioned frames. With our choice of 3-1-2 Euler angles, the heading and bank frames are translated after a collision yet maintain their orientations with respect to each other and the fixed frame.

As the origins of the various frames i are moved to the tip of the colliding spoke $i+1$, however, we not only translate the wheel frame but also rotate it by $-\frac{2\pi}{n}$ about the y_b-axis with respect to the bank frame so that the z_w-axis of the new wheel frame is aligned with spoke $i+1$. The spoke presently on the ground in some sense characterizes the orientation of the wheel frame with respect to the bank frame. Thus, the pitch angle changes from $\frac{\pi}{n}$ to $-\frac{\pi}{n}$ through a downhill collision.

The relationships between frames and their associated bases from before to after collision $i+1$ are

$${}^{i+1}\mathcal{H}^+ = {}^{i+1}\mathcal{H}^-, \; {}^{i+1}\mathbf{e}_h^+ = {}^{i+1}\mathbf{e}_h^-$$

$$
\begin{aligned}
{}^{i+1}\mathcal{B}^{+} &= {}^{i+1}\mathcal{B}^{-},\ {}^{i+1}\mathbf{e}_b^{+} = {}^{i+1}\mathbf{e}_b^{-} \\
{}^{i+1}\mathcal{W}^{+} &\neq {}^{i+1}\mathcal{W}^{-},\ {}^{i+1}\mathbf{e}_w^{+} = \mathbf{R}_2(\theta = -\frac{2\pi}{n})\ {}^{i+1}\mathbf{e}_w^{-},
\end{aligned} \tag{4.3}
$$

where the upper left superscript $i+1$ refers to collision $i+1$ and the upper right superscript refers the instants just before (-) or just after (+) collision.

4.2.3 Cycle of Motion

A *cycle* of the wheel is the motion from one spoke collision through the next. A schematic of one cycle, for downhill rolling, is shown in Figure 4.4. As before with the 2D wheel, we pick as the

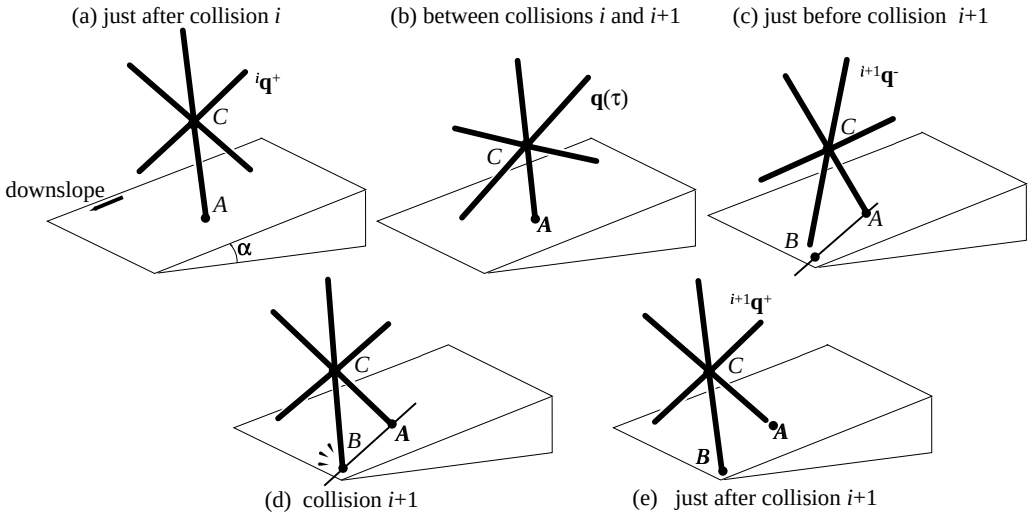

Figure 4.4: Schematic over one cycle of motion showing: (a) the state of the wheel just after collision i with point A, (b) the state of the wheel between collisions, (c) the state of the wheel just before collision $i+1$ at point B, (d) collision $i+1$ at point B, and (e) the state of the wheel just after collision $i+1$ at point B.

starting point the instant when the trailing spoke leaves the ground. The wheel rotates over the 'stance' spoke, spoke i , as an inverted pendulum with initial state ${}^{i}\mathbf{q}^{+}$. The initial pitch angle is known and is ${}^{i}\theta^{+} = -\frac{\pi}{n}$. The non-collisional portion of the stride ends just before the next spoke in sequence, spoke $i+1$, analogous to the swing leg in walking, strikes the ground when the pitch angle is also known, ${}^{i+1}\theta^{-} = \frac{\pi}{n}$. instantaneously transferring support from the trailing spoke to the leading spoke. The state of the wheel is ${}^{i+1}\mathbf{q}^{-}$. After impact, the wheel is now poised for the next start-of-cycle at pitch angle ${}^{i+1}\theta^{+} = {}^{i}\theta^{+} = -\frac{\pi}{n}$ and state ${}^{i+1}\mathbf{q}^{+}$.

4.3 Governing Equations

The beginning and end of the cycle is determined by the pitch angle θ. The pitch angle of the wheel *between collisions* is restricted to the interval $[-\frac{\pi}{n}, \frac{\pi}{n}]$ by resetting the pitch angle at each downhill collision to $\theta = -\frac{\pi}{n}$. When we are concerned with the overall motion of the system (position of the center of mass versus time), then the net total pitch angle and the position of the tip of the spoke currently on the ground are also important.

4.3.1 Equations of Motion between Collisions

Referring to Figure 4.4 and the description of the Euler angle frames in Appendix D, the equation of motion is derived from angular momentum balance about the contact point of the spoke currently touching the ground, say, point A,

$$\Sigma \mathbf{M}_{/A} =^{\mathcal{F}} \dot{\mathbf{H}}_{/A}, \tag{4.4}$$

where

$$\begin{aligned}
\Sigma \mathbf{M}_{/A} &= \mathbf{r}_{C/A} \times m\mathbf{g}, && (4.5)\\
\mathbf{g} &= g(\sin\alpha\ \mathbf{i}_f - \cos\alpha\ \mathbf{k}_f) && (4.6)\\
{}^{\mathcal{F}}\dot{\mathbf{H}}_{/A} &= {}^{\mathcal{W}}\dot{\mathbf{H}}_{/A} + \boldsymbol{\omega}_{\mathcal{W}/\mathcal{F}} \times \mathbf{H}_{/A}, \text{ and} && (4.7)\\
\boldsymbol{\omega}_{\mathcal{W}/\mathcal{F}} &= \boldsymbol{\omega}_{\mathcal{H}/\mathcal{F}} + \boldsymbol{\omega}_{\mathcal{B}/\mathcal{H}} + \boldsymbol{\omega}_{\mathcal{W}/\mathcal{B}} && (4.8)\\
&= \dot{\phi}\ \mathbf{k}_f + \dot{\psi}\ \mathbf{i}_h + \dot{\theta}\ \mathbf{i}_b. && (4.9)
\end{aligned}$$

The non-dimensionalized equations for motion between collisions are:

$$\begin{aligned}
\mathrm{s}\alpha\,(\mathrm{c}\theta\ \mathrm{c}\phi - \mathrm{s}\theta\ \mathrm{s}\psi\ \mathrm{s}\phi) + \mathrm{s}\theta\ \mathrm{c}\psi\ \mathrm{c}\alpha &= \frac{1}{\lambda^2}(\mathrm{c}\psi\ \dot{\psi}\dot{\phi} + \mathrm{s}\psi\ \ddot{\phi} + \ddot{\theta}) + \\
&\quad (\mathrm{c}\theta\ \mathrm{c}\psi\ \dot{\phi} + \mathrm{s}\theta\ \dot{\psi})(-\mathrm{s}\theta\ \mathrm{c}\psi\ \dot{\phi} + \mathrm{c}\theta\ \dot{\psi}) \\
0 &= \Big[\mathrm{s}\theta\ \mathrm{c}\psi\ \dot{\theta}\dot{\psi} - \mathrm{c}\theta\ \mathrm{s}\psi\ \dot{\psi}\dot{\phi} + \mathrm{c}\theta\ \mathrm{c}\psi\ \ddot{\phi} + \mathrm{c}\theta\ \dot{\theta}\dot{\psi} \\
&\quad + \mathrm{s}\theta\ \ddot{\psi} + (\mathrm{s}\psi\ \dot{\phi} + \dot{\theta})(-\mathrm{s}\theta\ \mathrm{c}\psi\ \dot{\phi} + \mathrm{c}\theta\ \dot{\psi})\Big] \\
\mathrm{c}\psi\ \mathrm{s}\phi\ \mathrm{s}\alpha + \mathrm{s}\psi\ \mathrm{c}\alpha &= -\frac{1+\lambda^2}{2\lambda^2}\Big[\mathrm{c}\theta\ \mathrm{c}\psi\ \dot{\phi} - \mathrm{s}\theta\ \mathrm{s}\psi\ \dot{\psi}\dot{\phi} + \\
&\quad \mathrm{s}\theta\ \mathrm{c}\psi\ \ddot{\phi} + \mathrm{s}\theta\ \dot{\theta}\dot{\psi} - \mathrm{c}\theta\ \ddot{\psi} + \\
&\quad (\mathrm{s}\psi\ \dot{\phi} + \dot{\theta})(\mathrm{c}\theta\ \mathrm{c}\psi\ \dot{\phi} + \mathrm{s}\theta\ \dot{\psi})\Big]
\end{aligned} \tag{4.10}$$

where 's'and 'c' are used to denote 'sin' and 'cos', and $\lambda^2 = \dfrac{1}{2J+1}$ with the square of the radius of gyration $J = \frac{D}{m\ell^2}$ (non-dimensionalized with respect to ℓ). An overdot indicates differentiation with respect to non-dimensional time $\tau = t\sqrt{g/\ell}$. The Maple® codes for generating the equations of motion between collisions are given in Appendix E. These equations are simply those of an inverted rigid body pendulum. This set of equations can be converted to a first order system of the form This set of equations can be converted to a first order system of the form

$$\dot{\mathbf{q}} = \mathbf{g}(\mathbf{q}, \mathbf{p}) \tag{4.11}$$

where $\mathbf{p}$ is a vector of the parameters

$$\mathbf{p} = (\lambda^2, \alpha). \tag{4.12}$$

We do not restate the equations in first order form for brevity. Henceforth, the dependence on the parameters $\mathbf{p}$ will not be explicitly stated.

As a brief aside, the parameter α could be eliminated from the equations of motion by a change of variable using angles measured with with respect to a fixed frame whose z-axis is aligned with gravity rather than the normal to the plane. By including α here in Equation (4.10), we eliminate it from the collision transition equations that we develop below.

4.3.2 Collision Transition Conditions

Collision Rule for Configuration Variables

Due to our choice of Euler angles, the heading and bank angles do not change through a collision. The pitch angle is reset at each collision as support is transferred from one spoke to the next according to the following mapping:

$$\theta \mapsto -\theta \text{ or } {}^{i}\theta^{+} = {}^{i}\theta^{-}. \tag{4.13}$$

Thus, we can write

$$\begin{Bmatrix} \phi^{+} \\ \psi^{+} \\ \theta^{+} \end{Bmatrix} = \mathbf{S} \begin{Bmatrix} \phi^{-} \\ \psi^{-} \\ \theta^{-} \end{Bmatrix}, \text{ where } \mathbf{S} = \begin{bmatrix} 1 & 0 & 0 \\ 0 & 1 & 0 \\ 0 & 0 & -1 \end{bmatrix}. \tag{4.14}$$

Collision Rule for Angular Rates

We model the collision as instantaneous. When a spoke collides with the ground, we assume that the trailing spoke instantaneously loses contact with the ground so that only one spoke is in contact with the ground at any time. We assume that no impulse is transmitted at the trailing spoke and that the collision of the new spoke with the ground is perfectly plastic.

Ignoring the impulse due to gravity during collision, the condition relating the angular velocity of the wheel before and after collision is derived from the conservation of angular momentum during collision about the incipient point of spoke contact. Referring to Figure 4.4, we can write this as

$$\mathbf{H}_{B}^{-} = \mathbf{H}_{B}^{+} \tag{4.15}$$

where $\mathbf{H}$ is angular momentum and

$$\begin{aligned} \mathbf{H}_{B}^{-} &= \mathbf{H}_{C}^{-} + \mathbf{r}_{C/B} \times m\mathbf{v}_{C}^{-} && (4.16) \\ \mathbf{H}_{C}^{-} &= \left[I^{C}\right] \boldsymbol{\omega}_{\mathcal{W}/\mathcal{F}}^{-} \\ \mathbf{v}_{C}^{-} &= \boldsymbol{\omega}_{\mathcal{W}/\mathcal{F}}^{-} \times \mathbf{r}_{C/A}, \\ \mathbf{H}_{B}^{+} &= \left[I^{B}\right] \boldsymbol{\omega}_{\mathcal{W}/\mathcal{F}}^{+}. && (4.17) \end{aligned}$$

Under the assumptions above, the angular rates before and after a collision are related as follows:

$$\begin{Bmatrix} \dot{\phi}^{+} \\ \dot{\psi}^{+} \\ \dot{\theta}^{+} \end{Bmatrix} = \mathbf{T} \begin{Bmatrix} \dot{\phi}^{-} \\ \dot{\psi}^{-} \\ \dot{\theta}^{-} \end{Bmatrix}, \tag{4.18}$$

where

$$\mathbf{T} = \begin{bmatrix} 1 + \frac{2\lambda^2}{1+\lambda^2}(\cos\frac{2\pi}{n} - 1) & 0 & 0 \\ -\frac{\lambda^2}{1+\lambda^2}\cos\psi\sin(\frac{2\pi}{n}) & 1 & 0 \\ 2\lambda^2\frac{1-\lambda^2}{1+\lambda^2}\sin\psi\sin^2(\frac{\pi}{n}) & 0 & \underbrace{1 + \lambda^2(\cos\frac{2\pi}{n} - 1)}_{\mu} \end{bmatrix}. \tag{4.19}$$

The $(3,3)$ element of the matrix $\mathbf{T}$ appears again in the stability calculations. We call it $\mu \equiv 1 + \lambda^2(\cos\frac{2\pi}{n} - 1)$ which is exactly the collision quantity that appears in the 2D analysis.

Total Collision Rule

Finally, we can merge the transition rules for the orientation variables and their rates into one map from the state of the system just before a collision to just after:

$$\begin{Bmatrix} \phi^+ \\ \psi^+ \\ \theta^+ \\ \dot{\phi}^+ \\ \dot{\psi}^+ \\ \dot{\theta}^+ \end{Bmatrix} = \mathbf{L} \begin{Bmatrix} \phi^- \\ \psi^- \\ \theta^- \\ \dot{\phi}^- \\ \dot{\psi}^- \\ \dot{\theta}^- \end{Bmatrix}, \text{ where } \mathbf{L} = \begin{bmatrix} \mathbf{S} & 0 \\ 0 & \mathbf{T} \end{bmatrix}. \tag{4.20}$$

We can rewrite this collision law that maps the state of the wheel just before to just after a collision as

$$\mathbf{q}^+ = \mathbf{h}(\mathbf{q}^-) = \left[\mathbf{L}(\mathbf{q}^-)\right] \mathbf{q}^-, \tag{4.21}$$

where the matrix $[\mathbf{L}(\mathbf{q}^-)]$ depends only on the orientation variables and not their rates. The Maple® code for for generating the total collision rule is presented in Appendix E.

4.4 Poincaré Section, Return Map, and Fixed Points

To study this system, we use again a Poincaré section as we did with the 2D rimless wheel in Chapter 2. Ignoring the absolute position of the wheel on the plane, the rimless wheel has a six-dimensional phase space with coordinates $(\phi, \psi, \theta, \dot{\phi}, \dot{\psi}, \dot{\theta})$. The Poincaré section for this autonomous system cannot be taken, say, at the period of some forcing function. Instead, a natural place to sample this space is at the points of discontinuity, the collisions, where we know the pitch angle of the wheel to be $\theta = \frac{\pi}{n}$ as for the 2D rimless wheel in Chapter 2. The map we use, say $\mathbf{f}$, takes the state of the wheel from just after one collision to just after the next collision.

In addition, we assume that the surface of the slope is not curved or bumpy so that the wheel must rotate through the same angle $\theta = \frac{2\pi}{n}$ between collisions; thus, the Poincaré section is taken at the same θ for every collision.

The state of the system *after* each collision i on the Poincaré section is ${}^i\mathbf{q}^+$. The map from one point to the next can be written as $\mathbf{q} \mapsto \mathbf{f}(\mathbf{q})$ or

$${}^{i+1}\mathbf{q}^+ = \mathbf{f}({}^i\mathbf{q}^+), \tag{4.22}$$

where we call $\mathbf{f}$ the *return map* (or Poincaré map) and ${}^i\mathbf{q}^+$ is the state vector of the system at the start of a cycle, just after the i_{th} collision.

The map $\mathbf{f}$ may be looked upon as a composition of two maps, $\mathbf{f} = \mathbf{h} \circ \mathbf{d}$; here, $\mathbf{d}$ governs the motion from just after collision i to just before collision $i+1$, obtained by integrating the equations of motion between collisions, and $\mathbf{h}$ governs support transfer, from just before to just after collision $i+1$.

For periodic or steady motion, we must find fixed points of the return map, $\mathbf{q}^* = \mathbf{f}(\mathbf{q}^*)$.

4.5 Stability of Periodic Motions

In this chapter we consider a system that, with fixed system parameters, $(m,\ n,\ \ell,\ J)$, exhibits a one-parameter family of periodic motions corresponding to rolling down the slope at different headings. On a Poincaré section, periodic motions appear as fixed points; thus a 1 parameter family of periodic motions appears as a curve on the Poincaré section.

Since we have a one-parameter family of fixed points, one eigenvalue will always be exactly equal to one. If all the *other* eigenvalues are smaller than one in magnitude, then the fixed point is asymptotically stable in the weak sense described in AppendixA.

For the system we consider in this chapter, the Poincaré section is five dimensional (the phase space is six dimensional). Thus, the Jacobian is a 5×5 matrix which can be numerically computed by five calculations using independent perturbations $\mathbf{q}_0 - \mathbf{q}^*$ for each case. Naturally, the perturbed point $\mathbf{q}_0$ must lie *on* the Poincaré section in each case. For no special reason, we chose to do *six* (dimension of the phase space) calculations, where the perturbed point $\mathbf{q}_0$ *need not* lie on the Poincaré section in each case, resulting in a 6×6 Jacobian matrix. **Note:** Our six dimensional calculation yields a Jacobian with six eigenvalues; one eigenvalue is exactly zero, and reflects the fact that the initially perturbed point might lie off the Poincaré section, but the next iterate $\mathbf{q}_1$ will lie exactly on the Poincaré section. The remaining five eigenvalues of our 6×6 Jacobian matrix are identical to the eigenvalues of the 5×5 Jacobian obtained by selecting initial perturbations only on the Poincaré section. Since our system has a one-parameter family of fixed points, one eigenvalue is exactly equal to one. Thus, there remain four eigenvalues to be examined. We apply the same approach for stability calculations to the 2D and 3D point-foot walkers in Chapters 5 and 6, respectively.

4.6 Motion Restricted to 2D: Some Results

A detailed analysis of all possible 2D motions of the rimless wheel may be found in Chapter 2. A simple analysis is described in McGeer (1990) [43]. Here, we consider only the motions near steady downhill rolling motions. If the rimless wheel completes a downhill cycle, the kinetic energy of the wheel at the end-of-cycle, just before collision $i+1$, is greater than the kinetic energy at the start-of-cycle, just after collision i, due to the downhill slope ($(K.E.)_{i+1}^{-} > (K.E.)_{i}^{+}$). The kinetic energy of the wheel drops instantaneously at impact.

For downhill motions, three distinct outcomes are possible when **(a)** the slope is big enough and **(b)** the wheel has enough initial kinetic energy make it past the vertical position ($\theta = -\gamma$) in its cycle of motion to the next downhill collision:

1. Periodic motion occurs if the energy lost in collision is exactly balanced by the kinetic energy gained in falling. In this case, the state variables are equal to those at the start of the previous cycle. The wheel is in periodic or limit cycle motion that repeats indefinitely.

2. The wheel slows down towards a periodic motion, which may be shown to be unique; this happens if more energy is lost in collision than gained in moving downhill.

3. The wheel speeds up towards the periodic motion; this happens if more energy is gained in moving downhill than lost in collision.

In Chapter 2, it is shown that condition **(a)** is satisfied if the effective slope angle $\gamma > \gamma_c$ where γ_c satisfies

$$1 - \cos\frac{\pi}{n}\cos\gamma - \frac{1+\mu^2}{1-\mu^2}\sin\frac{\pi}{n}\sin\gamma = 0, \tag{4.23}$$

and that condition **(b)** is satisfied if the the pitch rate just after a collision ${}^{i}\dot{\theta}^{+} > \dot{\theta}_c$ where $\dot{\theta}_c$ is given by

$$\dot{\theta}_c = \sqrt{2\lambda^2(1 - \cos(\gamma - \frac{\pi}{n}))}. \tag{4.24}$$

Based on the observations above, key aspects of the 2D motions that are relevant to steady rolling motions in 3D are stated below:

1. For large enough slopes, $\gamma > \gamma_c$, unique steady 2D rolling motions *always exist.*

2. The steady 2D motions (restricted to 2D) are asymptotically stable. The eigenvalue of the linearization of the map about the fixed point is $\mu^2 < 1$.

4.7 3D Motions

The solutions found in 2D will satisfy the 3D equations of motion; i.e., all 2D solutions are also 3D solutions. There is a family of 2D periodic motions restricted to different vertical planes; i.e., the wheel may roll downhill at different heading angles ϕ^*. We call these steady 3D motions *planar* (or 2D) *limit cycles*. A planar limit cycle is illustrated schematically in Figure 4.5. Corresponding to

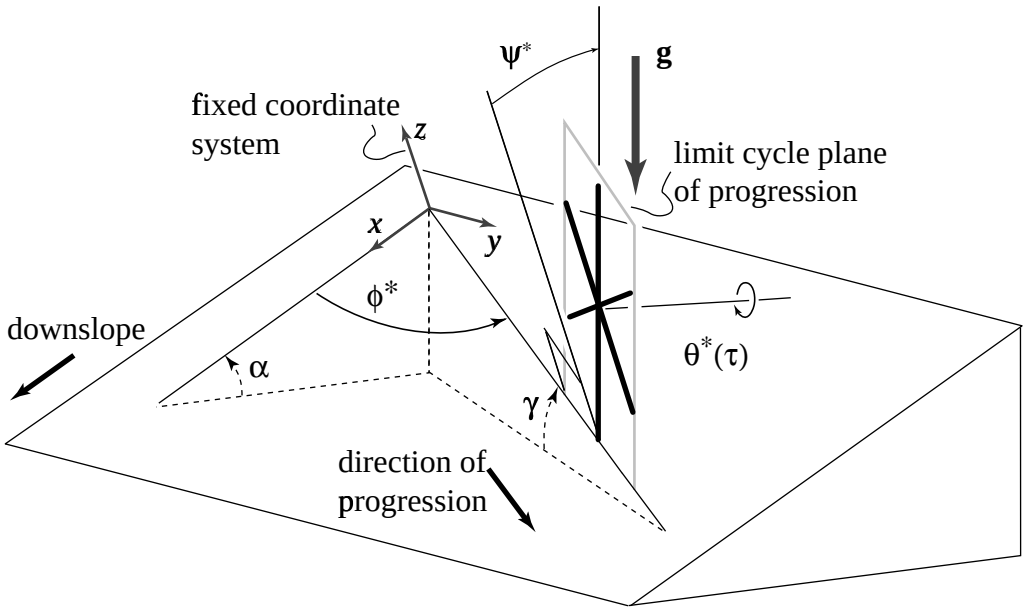

Figure 4.5: The schematic here depicts the planar limit cycle motion, for the 3D wheel, showing how the plane of the wheel at heading ϕ^* is aligned with the force acting on the wheel due to gravity.

each fixed point $\mathbf{q}^*$ is a trajectory $\mathbf{q}^*(\tau)$ in phase space, between collisions, which we call the 2D *limit cycle trajectory* (see Figure A.2 in Appendix A). The fixed point $\mathbf{q}^*$ and its associated 2D limit cycle trajectories between collisions are summarized in Table 4.1. For motions of the wheel restricted to two dimensions, the plane of the wheel is parallel to the line of action of the net gravity force acting on the wheel. In terms of the 3D variables, this gives the bank angle ψ^* of the wheel as a function of the slope angle α and the heading angle ϕ^*

$$\psi^* \equiv \psi(\phi^*, \alpha) = \tan^{-1}(-\sin\phi^* \ \tan\alpha). \tag{4.25}$$

The effective slope γ at a particular heading is given by

$$\gamma \equiv \gamma(\phi^*) = \sin^{-1}(\sin\alpha \ \cos\phi^*). \tag{4.26}$$

The heading angle ϕ^* may be looked upon as a free parameter that determines a one-parameter family of steady rolling motions. Finally, the *limit cycle pitch rate*, as sampled on the Poincaré section, and the *limit cycle period* τ^* are, respectively,

$$\dot{\theta}^* \equiv \dot{\theta}^*(\gamma, n, \lambda^2) \quad = \quad \sqrt{\frac{4\mu^2\lambda^2 \sin\frac{\pi}{n}\sin\gamma}{1-\mu^2}} \text{ and} \tag{4.27}$$

Table 4.1: The planar limit cycle in three dimensions. The limit cycle time histories $\phi^*(\tau)$, $\dot{\phi}^*(\tau)$, $\psi^*(\tau)$, and $\dot{\psi}^*(\tau)$ are constant over a cycle and equal to the corresponding fixed point values at the start-of-cycle. The limit cycle pitch angle $\theta^*(\tau)$ and rate $\dot{\theta}^*(\tau)$ are not constant.

State Variable	Limit Cycle Trajectory (in time)	Fixed Point of $\mathbf{f}$ (on Σ)
Heading Angle	$\phi^*(\tau) = \phi^*$	ϕ^*
Heading Rate	$\dot{\phi}^*(\tau) = 0$	$\dot{\phi}^* = 0$
Bank Angle	$\psi^*(\tau) = \psi^*$	$\psi^* \equiv \psi^*(\phi^*, \gamma)$
Bank Rate	$\dot{\psi}^*(\tau) = 0$	$\dot{\psi}^* = 0$
Pitch Angle	$\theta^*(\tau)$	$\theta^* = -\frac{\pi}{n}$
Pitch Rate	$\dot{\theta}^*(\tau)$	$\dot{\theta}^* \equiv \dot{\theta}^*(\gamma, n, \lambda^2)$

$$\tau^* = \int_{-\frac{\pi}{n}}^{\frac{\pi}{n}} \frac{d\theta}{\sqrt{(\dot{\theta}^*)^2 + 2\lambda^2(\cos(\frac{\pi}{n}) - \cos\theta)}}. \tag{4.28}$$

both of which can be found using a simple 2D energy analysis. As the number of spokes n gets large, various planar limit cycle quantities (the limit cycle pitch rate $\dot{\theta}^*$, the limit cycle time between collisions τ^*, the critical effective slope angle γ_c, and the collision parameter μ) scale with n as follows:

$$\dot{\theta}^* \simeq \sqrt{\frac{n \sin\gamma}{\pi}}, \quad \tau^* \simeq \frac{2(\frac{\pi}{n})^{\frac{3}{2}}}{\sqrt{\sin\gamma}}, \quad \gamma_c \simeq \frac{\lambda^2\pi^3}{n^3}, \quad \text{and } \mu \simeq 1 - 4\frac{\lambda^2\pi^2}{n^2}. \tag{4.29}$$

Here, γ_c is the minimum required slope for steady rolling motions to exist. The limit cycle pitch angle, equal to half the angle between the spokes, is $\theta^* = -\pi/n$ which obviously scales as $\theta^* \sim O(1/n)$.

For our 3D analytical stability study, we take the effective slope to be inversely proportional to the number of spokes,

$$\gamma = \frac{\bar{\gamma}}{n} + O(\frac{1}{n^3}) \gg \gamma_c \sim O(\frac{1}{n^3}) \tag{4.30}$$

where $\bar{\gamma} \sim O(1)$ is a constant. For such slopes, the limit cycle period scales as $\tau^* \sim O(1/n)$ and the limit cycle pitch rate tends to a constant $\dot{\theta}^* \simeq \sqrt{\bar{\gamma}/\pi}$. As $n \to \infty$, we obtain a disk on a flat surface rolling at constant speed proportional to $\bar{\gamma}$.

4.8 3D Stability of the 2D Limit Cycle

For a rimless wheel restricted to planar motions, asymptotically stable fixed points exist if the effective slope is big enough. The limit cycle pitch rate $\dot{\theta}^*$ is a function of the number of spokes, the radius of gyration of the wheel, and the effective slope angle. We determine the three-dimensional stability of this planar limit cycle whose 2D characteristics we already know in closed form from a nonlinear analysis of the rimless wheel restricted to two dimensions, as summarized in the previous section (for details, see Chapter 2).

In this chapter, we focus on the three-dimensional stability of the planar limit cycle. Though the 3D rimless wheel may have other periodic motions other than 2D limit cycles, such as zig-zagging or looping motions, we did not look for these solutions or investigate their stability.

Unlike the 2D case, we cannot find explicitly the 3D return map, its non-planar fixed points, or the stability of fixed points. Instead, we approximate the Jacobian of the map at the planar fixed point both numerically and analytically. In the analytical approach, the approximation is based on a perturbation expansion for a wheel with many spokes and small slopes. (See Appendix A and Appendix E for details.)

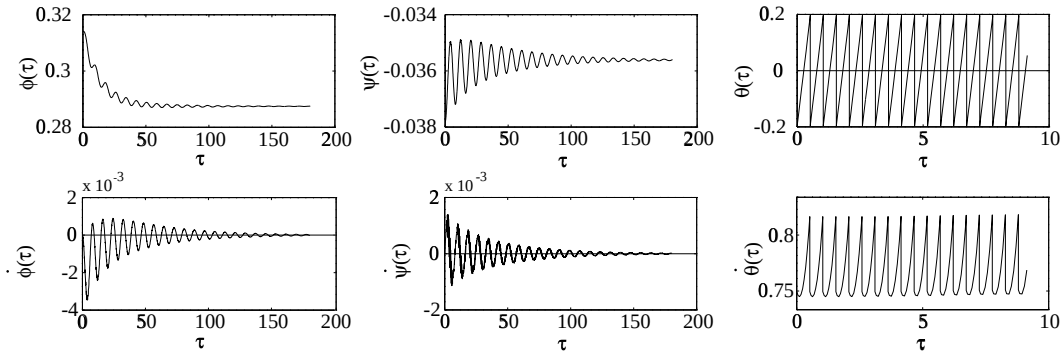

Figure 4.6: State of the rimless wheel plotted versus τ for 350 collisions after it is perturbed from its limit cycle with a disturbance in the bank angle $\Delta\psi_0 = 0.001$. For this simulation, $2J = 0.5$, $n = 16$, $\alpha = 2/n$, and $\phi_0^* = \pi/10$. Note that θ and $\dot{\theta}$ are plotted over only about 25 collisions since their variation with τ is at too high a frequency to be seen over 350 collisions. The discontinuities in the graphs of angular rates are due to the collisions.

4.8.1 Numerical Approximation

We integrated the fully nonlinear equations of motion using `int_henon_temp_3D.m`, a version of MATLAB®'s `ode45.m` (a 4th-5th order automatic step-sizing routine) modified to detect spoke collisions using Henon's [62] method (see Appendix A). We used an integration tolerance 10^{-8} in the automatic step-sizing routine. We use the same routine in Chapters 5 and 6. Figure 4.6 shows the state of the rimless wheel disturbed slightly from a planar limit cycle over many collisions. For the parameter values used, the steady rolling motion is stable. The disturbance eventually decays and the rimless wheel enters into a new planar limit cycle at a slightly different heading (and corresponding bank angle) across the slope.

We found fixed points and the Jacobian eigenvalues using a MATLAB® routine `newton_3D.m` (see Appendix A). We use the same routines in Chapters 5 and 6. The finite difference step size used to compute the Jacobian numerically was 10^{-4} and error tolerance for the fixed point search was 10^{-6}. The six numerically evaluated eigenvalues for the case in Figure 4.6 are: $\sigma_0 = 0$, $\sigma_1 = 1$ (see discussion in Section 4.5), $\sigma_2 = 0.9011$, $\sigma_{3,4} = 0.9108 \pm 0.3839i = 0.9884\, e^{\pm 0.3989 i}$, and $\sigma_5 = 0.96133$. The numerically evaluated Jacobian is

$$[\mathbf{J}] = \begin{pmatrix} 0.9975 & 0.4658 & -0.0206 & -0.1950 & 0 & 0 \\ -0.0181 & 0.6529 & -0.1515 & -0.6950 & -0.0000 & -0.0000 \\ 0.0125 & 0.1968 & 1.1050 & 0.4840 & 0 & 0 \\ 0.0525 & 0.5312 & 0.4403 & 1.0274 & 0.0000 & 0.0000 \\ 0 & 0 & 0 & 0 & 0 & 0 \\ -0.0127 & -0.0141 & -0.0057 & -0.0250 & 0.0620 & 0.9011 \end{pmatrix} \tag{4.31}$$

We will compare the numerical estimates of the eigenvalues for this case to asymptotic estimates in a later section. Since $|\sigma| \leq 1$, and only one eigenvalue is exactly equal to one, the planar limit cycle motion is asymptotically stable.

Given the initial perturbed state of the wheel from its limit cycle, we can predict approximately the subsequent motion of the wheel, using $\mathbf{J}$. We can do this as follows. To the linear approximation, the small initial perturbation to the fixed point of the return map propagates over k collisions as

$$\Delta\mathbf{q}_k = \mathbf{J}^k \cdot \Delta\mathbf{q}_0 \tag{4.32}$$

where $\Delta\mathbf{q}_0$ is the perturbation to the fixed point $\mathbf{q}_0^*$.

The new limit cycle of the wheel after many collisions is given by

$$\mathbf{q}^* = \mathbf{q}_0^* + \lim_{k\to\infty} \mathbf{J}^k \Delta\mathbf{q}_0. \tag{4.33}$$

In this numerical example,

$$\mathbf{q}_0^* = \{\phi^* = 0.3142, \psi^* = -0.0378, \theta^* = -0.1963, \dot{\phi}^* = 0, \dot{\psi}^* = 0, \dot{\theta}^* = 0.7496\}^T$$

and $\Delta\mathbf{q}_0 = \{\Delta\phi_0 = 0, \Delta\psi_0 = 0.001, \Delta\theta_0 = 0, \Delta\dot{\phi}_0 = 0, \Delta\dot{\psi} = 0, \Delta\dot{\theta} = 0\}^T$. Therefore, we estimate the state vector after 350 collisions to be

$$\mathbf{q}_0^* + \mathbf{J}^{350}\Delta\mathbf{q}_0 = \{0.2872,\ -0.0356,\ -0.1963,\ 0.0000,\ 0.0000,\ 0.7529\}^T. \tag{4.34}$$

In comparison, we obtained the state vector from numerical integration as

$$\mathbf{q}^* = \{0.2875,\ -0.0356,\ -0.1963,\ \ 0.0000,\ 0.0000,\ 0.7527\}^T \tag{4.35}$$

after 350 collisions, rather close agreement as expected.

Alternatively, we know

$$\mathbf{J}^k = \mathbf{X}\,\mathbf{C}^k\,\mathbf{X}^{-1} \tag{4.36}$$

where $\mathbf{X}$ is a matrix whose i_{th} column is the eigenvector associated with the i_{th} element of the diagonal matrix $\mathbf{C}$ whose elements are the eigenvalues of the Jacobian matrix $\mathbf{J}$ of the map $\mathbf{f}$ evaluated at the fixed point of the return map.

The matrix of eigenvalues of the Jacobian evaluated at $\mathbf{q}_0^*$ is

$$\mathbf{C} = \begin{pmatrix} \sigma_3 & 0 & 0 & 0 & 0 & 0 \\ 0 & \sigma_4 & 0 & 0 & 0 & 0 \\ 0 & 0 & \sigma_1 & 0 & 0 & 0 \\ 0 & 0 & 0 & \sigma_5 & 0 & 0 \\ 0 & 0 & 0 & 0 & \sigma_2 & 0 \\ 0 & 0 & 0 & 0 & 0 & \sigma_0 \end{pmatrix} \tag{4.37}$$

and the corresponding matrix of eigenvectors is

$$\mathbf{X} = \begin{pmatrix} 0.6518 + 0.2802i & -0.6518 - 0.2802i & -0.9858 & & \\ -0.1935 - 0.4866i & -0.1935 + 0.4866i & 0.0000 & & \\ 0.1833 + 0.3051i & 0.1833 - 0.3051i & 0.1176 & \cdots & \\ -0.2200 + 0.2136i & -0.2200 - 0.2136i & 0.0000 & & \\ 0.0000 & 0.0000 & 0.0000 & & \\ -0.0088 - 0.0406i & -0.0088 + 0.0406i & 0.1201 & & \end{pmatrix}$$

$$\begin{pmatrix} 0.9781 & 0.0000 & 0.0000 \\ -0.0718 & 0.0000 & 0.0000 \\ \cdots\ -0.0321 & 0.0000 & 0.0000 \\ 0.0134 & 0.0000 & 0.0000 \\ 0.0000 & 0.0000 & 0.9976 \\ -0.1923 & 1.0000 & -0.0686 \end{pmatrix}. \tag{4.38}$$

Upon inspection of $\mathbf{C}$, we see that

$$\lim_{k\to\infty} \mathbf{C}^k = \begin{pmatrix} 0 & 0 & 0 & 0 & 0 & 0 \\ 0 & 0 & 0 & 0 & 0 & 0 \\ 0 & 0 & 1 & 0 & 0 & 0 \\ 0 & 0 & 0 & 0 & 0 & 0 \\ 0 & 0 & 0 & 0 & 0 & 0 \end{pmatrix} \tag{4.39}$$

Thus, upon further inspection, we have

$$\lim_{k\to\infty} \mathbf{X}\,\mathbf{C}^k\,\mathbf{X}^{-1}\,\Delta\mathbf{q}_0 \tag{4.40}$$

$$= \Delta\psi_0 \cdot \mathbf{X}^{-1}(3,3) \cdot (\text{`}3_{rd} \text{ column of } \mathbf{X}\text{'})$$

$$= \{-0.0270,\ 0.0000,\ 0.0032,\ 0.0000,\ 0.0000,\ 0.0033\}^T. \tag{4.41}$$

Finally, according to Equation (4.33) we estimate the attracting fixed point to be

$$\mathbf{q}^* = \mathbf{q}_0^* + \lim_{k\to\infty} \mathbf{X}\,\mathbf{C}^k\,\mathbf{X}^{-1}\Delta\mathbf{q}_0$$

$$= \{0.2872,\ -0.0356,\ -0.1963,\ 0.0000,\ 0.0000, 0.7529\}^T. \tag{4.42}$$

exactly as we obtained above.

Also, note that, for the new limit cycle, the numerically calculated heading and bank angles are in the proper relationship and the numerically calculated limit cycle pitch rate is correct for the effective slope at the final heading:

$$\psi^* = \tan^{-1}(-\sin\phi^*\,\tan\alpha) = -0.0356 \text{ and } \dot{\theta}^* = \sqrt{\frac{4\mu^2\lambda^2 \sin\frac{\pi}{n}\sin\gamma}{1-\mu^2}} = 0.7527$$

where γ is defined by Equation (4.26).

More qualitatively, we note that the eigenvalues of largest magnitude less than 1 are $\sigma_{3,4}$, whose magnitude is about 0.99. These eigenvalues cause the slow, oscillatory decay in the disturbance. Note that the period of oscillation $2\pi/0.3989$ is about 16, and so there are about 22 oscillations over 350 collisions. After, say, 80 collisions, we have $(\sigma_2)^{80} < 0.0003$, $(\sigma_5)^{80} < 0.05$, and $|\sigma_{3,4}|^{80} \approx 0.39$. Therefore, the decay in the disturbance after about five oscillations (80 collisions) is almost solely governed by $\sigma_{3,4}$, and the decay per oscillation (per 16 collisions) thereafter is roughly given by $|\sigma_{3,4}|^{16} \approx 0.83$, which agrees with Figure 4.6.

The good agreement between the linearized dynamics (Equation (4.34)) and the numerical solution (Equation (4.35), Figure 4.6) are an indication that the numerical calculations are worthy The good agreement between the linearized dynamics (Equation (4.34)) and the numerical solution (Equation (4.35), Figure 4.6) are an indication that the numerical calculations are worthy and the asymptotic stability is genuine.

4.8.2 Analytical Approximation

In order to analytically determine the 3D stability of the steady rolling motion, we use a perturbation method with $\zeta = 1/n$ as a small parameter.

A numerical study of the eigenvalues of the Jacobian of the map for large n shows that two eigenvalues are of the form $1 + k\zeta^2$ for some constant k, so the Jacobian needs to be found at least up to $O(\zeta^2)$.

Our approach is based on the following observations: **(a)** we cannot find an analytical approximation of the full 3D return map; **(b)** we can find an analytical approximation to the steady rolling or periodic motion as a power series in ζ, up to arbitrary orders; **(c)** we can solve the first order (or linearized) variational equations for motions close to the limit cycle, also up to arbitrary orders in ζ; and, **(d)** using **(b)** and **(c)**, we can find the Jacobian of the return map at the fixed point up to arbitrary orders in ζ.

Asymptotic Expansion

We define

$$\zeta \equiv \frac{1}{n} \tag{4.43}$$

and note that ζ is small but finite and, hence, much larger than the variations used in the stability calculations. An overview of the general perturbation analysis procedure applied to this problem may be found in Appendix A. We summarize below the calculation of the three matrices comprising the approximation to the Jacobian, $\mathbf{A} = \mathbf{BDE}$, which have the following interpretations: $\mathbf{B}$ represents an approximation to the collision transition map. Matrix $\mathbf{D}$ represents a correction to the perturbation map to account for the perturbed time between collisions. Matrix $\mathbf{E}$ represents the map of the perturbations just after a collision to just before the next. The Maple® codes for generating these three matrices, finding the approximate Jacobian, and calculating the eigenvalue approximations are are provided in Appendix E.

For a small slope, taken to be $\alpha = \frac{2}{n}$, the eigenvalues of the Jacobian of the map are shown in the complex plane in Figure 4.7 and the modulus of the difference of the eigenvalues from one is shown in Figure 4.8. Figure 4.8 shows that the eigenvalues scale with δ as

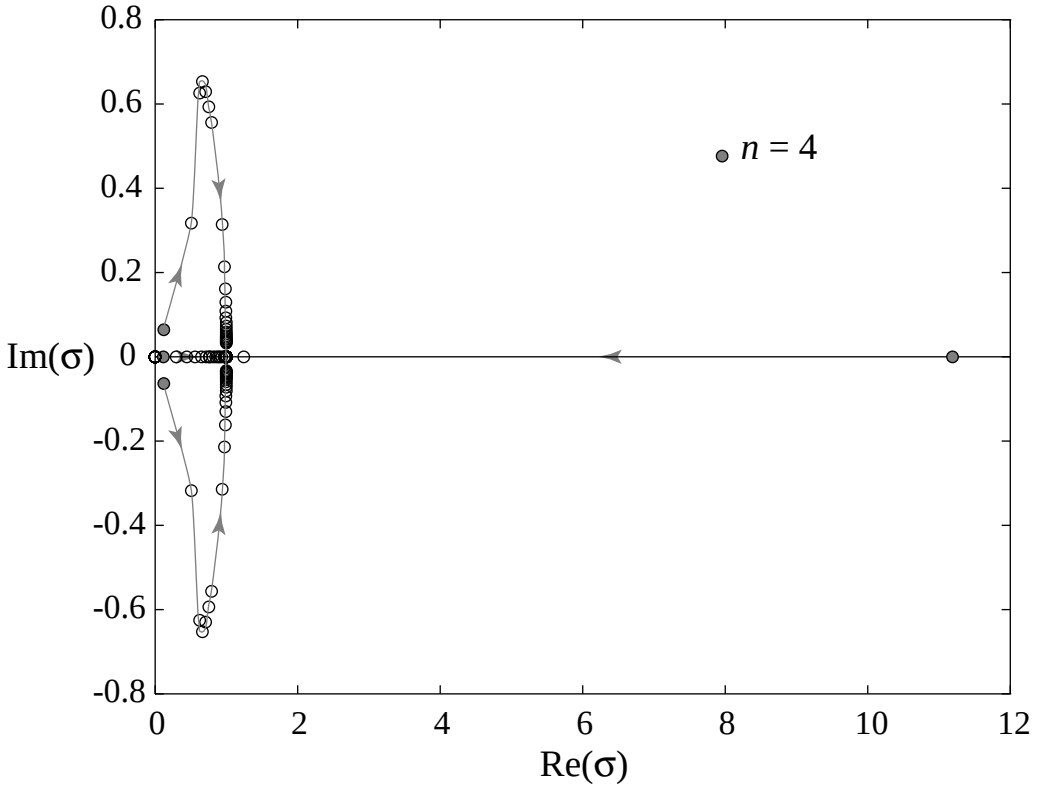

Figure 4.7: The eigenvalues of the Jacobian evaluated at the limit cycle fixed point are shown for increasing numbers of spokes n, slope angle $\alpha = \frac{2}{n}$, and inertia parameter $\lambda^2 = \frac{2}{3}$. The path of the eigenvalues as n increases is indicated with arrows.

1. $\sigma_0 = 0$
2. $\sigma_1 = 1 + O(\delta^3)$
3. $\sigma_2 \approx 1 + A\delta^2$
4. $\sigma_{3,4} \approx 1 \pm B_1\delta + B_2\delta^2$

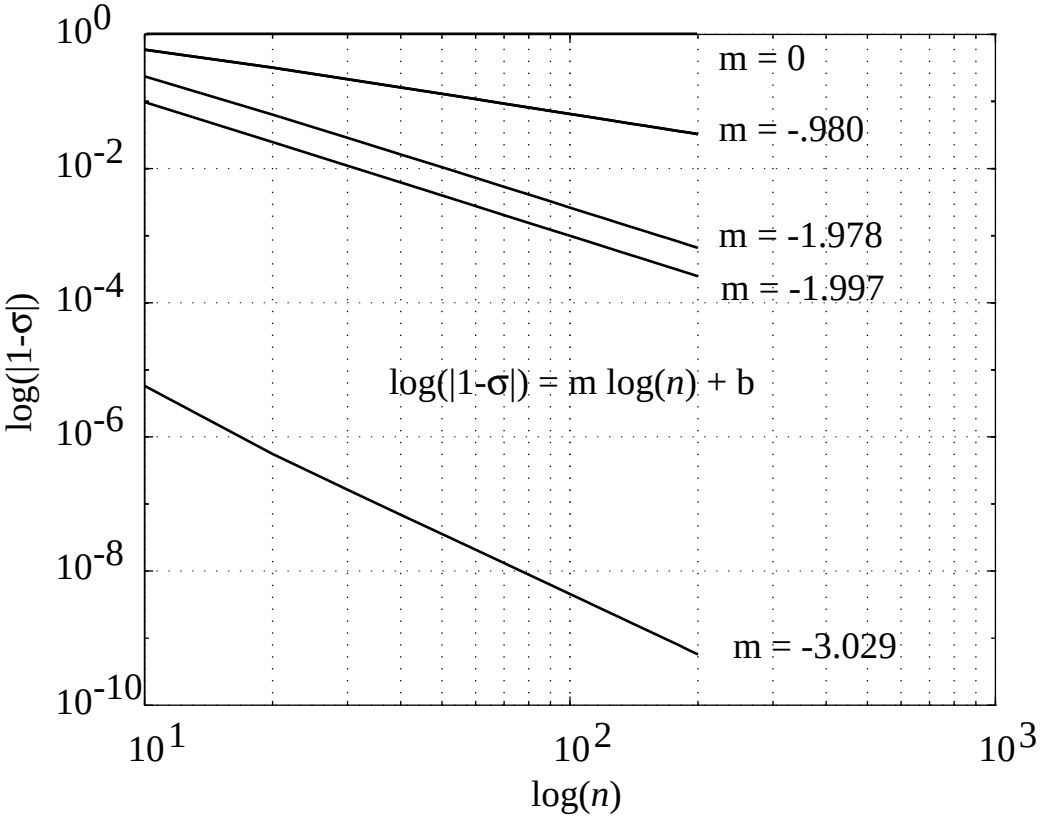

Figure 4.8: The modulus of the difference of the eigenvalues of the Jacobian evaluated at the fixed point from one are shown on a log-log plot as a function of number of spokes n with slope angle $\alpha = \frac{2}{n}$ and inertia parameter $\lambda^2 = \frac{2}{3}$.

5. $\sigma_5 \approx 1 + C\delta^2$.

From the numerics we assume that, in order to get the modulus of the difference of the eigenvalues from one to $O(\delta^2)$, we must find the approximation to the Jacobian $[\mathbf{A}]$ to $O(\delta^2)$. (The reasoning is as follows. Suppose, for example, we perturb the identity matrix to $O(\delta^m)$ to get a new matrix $[\mathbf{M}] = [\mathbf{I}] + O(\delta^m)$. The roots of the characteristic polynomial of $([\mathbf{M}] - \sigma\,[\mathbf{I}])$ will then be $O(\delta^m)$.)

We rescale the non-dimensional time τ, pitch angle θ, and slope angle as follows:

$$\begin{aligned} \tau &= \zeta T \\ \theta(\tau) &= \zeta \Theta(T) \\ \alpha &= \zeta \bar{\alpha}. \end{aligned} \tag{4.44}$$

Using these new scalings, we write the variational equations for small perturbations using

$$\begin{aligned} \phi(T) &\approx \phi^* + \epsilon\hat{\phi}(T), \\ \psi(T) &\approx \psi^* + \epsilon\hat{\psi}(T), \text{ and} \\ \Theta(T) &\approx \Theta^*(T) + \epsilon\hat{\Theta}(T), \end{aligned} \tag{4.45}$$

where

$$\psi^* \equiv \psi^*(\phi^*, \bar{\alpha}) = \tan^{-1}(-\sin\phi^* \ \tan(\zeta\bar{\alpha})) \tag{4.46}$$

and

$$\epsilon \ll \zeta. \tag{4.47}$$

The Perturbed Equations of Motion

We need to find the perturbed motions of the system up to strictly first order in ϵ. Recall that the equations of motion for the system are of the form $\dot{\mathbf{q}} = \mathbf{g}(\mathbf{q})$. The variational equations have time-varying coefficients which involve the limit cycle period $\Theta^*(T)$,

$$\dot{\hat{\mathbf{q}}}(T) \simeq D\mathbf{g}(\mathbf{q}^*(T))\hat{\mathbf{q}}(T). \tag{4.48}$$

Substituing Equations (4.44), (4.45), and (4.46) into the three nonlinear equations of motion (4.10) and truncating the resulting equations to first order in ϵ yields the following six ϵ^0 and ϵ^1order variational equations that govern the evolution of perturbations from the planar limit cycle:

ϵ^0:

$$0 = O(\zeta^7) \tag{4.49}$$

$$0 = \ddot{\Theta} - \lambda^2(\Theta + \bar{\alpha}\cos(\phi^*)\zeta^2, \text{ and} \tag{4.50}$$

$$0 = 0. \tag{4.51}$$

ϵ^1:

$$\begin{aligned} 0 = {} & \frac{1}{2}(1+\lambda^2)\ddot{\hat{\psi}} - (1+\lambda^2)\left[\left(\dot{\Theta}\dot{\hat{\phi}} + \frac{1}{2}\Theta\ddot{\hat{\phi}}\right)\right]\zeta - \\ & \left[(1+\lambda^2)\left(\dot{\Theta}\Theta\dot{\hat{\psi}} + \frac{1}{4}\Theta^2\ddot{\hat{\psi}}\right) - \lambda^2\hat{\psi}\right]\zeta^2 + \\ & \left[\frac{1}{12}(1+\lambda^2)\left(6\dot{\Theta}\left(\Theta^2 + \bar{\alpha}^2\sin^2(\phi^*)\right)\dot{\hat{\phi}} + \right.\right. \\ & \left.\left.\Theta\left(3\bar{\alpha}^2\sin^2(\phi^*) + \Theta^2\right)\ddot{\hat{\phi}}\right) - \bar{\alpha}\lambda^2\cos(\phi^*)\hat{\phi}\right]\zeta^3 \end{aligned} \tag{4.52}$$

$$
\begin{aligned}
0 &= \ddot{\Theta} - \bar{\alpha}\sin(\phi^*)\ddot{\hat{\phi}}\zeta - \lambda^2\hat{\theta}\zeta^2 + \\
&\quad \bar{\alpha}\sin(\phi^*)\left[\lambda^2\hat{\phi} + \frac{1}{6}\bar{\alpha}^2\left(\sin^2(\phi^*) - 2\cos^2(\phi^*)\right)\ddot{\hat{\phi}}\right]\zeta^3 \qquad (4.53)\\
0 &= \frac{1}{2}(1-\lambda^2)\ddot{\hat{\phi}} + \frac{1}{2}(1-\lambda^2)\left(2\dot{\Theta}\dot{\hat{\psi}} + \Theta\ddot{\hat{\psi}}\right)\zeta - \\
&\quad \frac{1}{4}(1-\lambda^2)\left[4\dot{\Theta}\Theta\dot{\hat{\phi}} + \left(\Theta^2 + \bar{\alpha}^2\sin^2(\phi^*)\right)\ddot{\hat{\phi}}\right]\zeta^2 - \\
&\quad \frac{1}{12}\Theta^2\left(6\dot{\Theta}\dot{\hat{\psi}} + \Theta\ddot{\hat{\psi}}\right)\zeta^3 \qquad (4.54)
\end{aligned}
$$

Equation(4.49) shows that the zeroth order term in the first variational equations has only $O(\zeta^7)$ and higher and Equation(4.49) shows that the zeroth order term third variational equation is identically zero. From Equation 4.50, we get an equation for $\Theta(T)$

$$\ddot{\Theta} - \lambda^2\left(\Theta + \bar{\alpha}\cos(\phi^*)\right)\zeta^2 = 0. \qquad (4.55)$$

The motions between collisions can be found in terms of a power series in ζ, which we truncate beyond third order. We expand $\Theta^*(T)$ as

$$\Theta^*(T) = \Theta^*(T,\zeta) \approx \Theta_0(T) + \zeta\Theta_1(T) + \cdots + \zeta^m\Theta_m(T) + \cdots. \qquad (4.56)$$

Upon substitution of Equation(4.56) into Equation(4.55), after applying the start-of-cycle condition $\Theta(0) = -\pi$ and end-of-cycle conditions in order for a limit cycle to exist, $\Theta(T^*) = \pi$ and $\mu\dot{\Theta}(T^*) = \dot{\Theta}(0)$ to solve for $\Theta_0(T)$ and $\Theta_1(T)$, and expanding in ζ, we get an approximate solution for limit cycle pitch angle $\Theta^*(T)$ and limit cycle period T^* accurate up to $O(\zeta^3)$

$$
\begin{aligned}
\Theta^*(T) &= \left(\sqrt{\frac{\bar{\gamma}}{\pi}}T - \pi\right) + \left[\frac{1}{6}\lambda^2\sqrt{\frac{\bar{\gamma}}{\pi}}T^3 + \frac{1}{2}\lambda^2(\bar{\gamma}-\pi)T^2 + \right.\\
&\quad \left.\frac{1}{12}\left(\sqrt{\bar{\gamma}\pi^3}(1-18\lambda^2) - \frac{\sqrt{\bar{\gamma}^5}}{\sqrt{\pi}\cos^2\phi^*}\right)T\right]\zeta^2 + O(\zeta^4) \qquad (4.57)\\
T^* &= 2\sqrt{\frac{\pi^3}{\bar{\gamma}}} + \left(\frac{2}{3}\sqrt{\frac{\pi^9}{\bar{\gamma}^3}} + \frac{1}{6}\sqrt{\frac{\pi^7}{\bar{\gamma}}}(6\lambda^2-1) + \frac{1}{6}\frac{\sqrt{(\pi\bar{\gamma})^3}}{\cos^2\phi^*}\right)\zeta^2 \\
&\quad + O(\zeta^4) \qquad (4.58)
\end{aligned}
$$

where (see Equation (4.30))

$$\bar{\gamma} \equiv \bar{\alpha}\cos\phi^*, \qquad (4.59)$$

and we have expanded the limit cycle period T^* in the power series

$$T^* = T_0 + T_1\zeta + \cdots + T_m\zeta^m\cdots. \qquad (4.60)$$

Now that we have used the ϵ^0 variational equations to obtain approximations to the pitch angle $\Theta^*(T)$ between collisions and the limit cycle period T^*, we can return to the ϵ^1 equations to solve for approximations to the perturbations to the limit cycle, $\hat{\phi}(T)$, $\hat{\psi}(T)$, and $\hat{\theta}(T)$. To do this, we first substitute the expression for $\Theta^*(T)$ into Equations(4.54), expand up to $O(\zeta^3)$, and solve for the second derivatives $\ddot{\hat{\phi}}(T)$, $\ddot{\hat{\psi}}(T)$, and $\ddot{\hat{\theta}}(T)$. The equations are too cumbersome so we do not display them here.

Next, we expand the perturbations in power series in ζ up to $O(\zeta^2)$, substitute the expansions into the equations for the second derivatives, and obtain simple uncoupled ordinary differential equations for each expansion coefficient which are easily solved.

Then, once we have the expressions for the expansion coefficients, we can construct the power series solutions for the perturbations in the Euler angles and differentiate them once to get their rates.

Finally, we can obtain the state of the perturbations just before the next collision $i+1$ in terms of the perturbations just after collision i by substituting the limit cycle period into the solutions for the evolution of the perturbations. The solved equations can be represented somewhat compactly in a matrix equation relating the perturbations to the limit cycle just after collision i to the state of those perturbations just before the next collision $i+1$

$$\hat{\mathbf{q}}(T^*) =^{1+i} \hat{\mathbf{q}}^- = \mathbf{E}(\zeta, \lambda^{\mathbf{2}}, \phi*, \bar{\alpha}) \ {}^{\mathbf{i}}\hat{\mathbf{q}}^+ \tag{4.61}$$

We do not show the components of $\mathbf{E}$ due to their complexity.

The Approximate Collision Map

Now, we calculate the matrix $\mathbf{B} \equiv \mathbf{Dh}(\mathbf{q}^*(\mathbf{T}^*))$ that approximates the collision function $\mathbf{h}$ defined by Equation(4.21). To obtain $\mathbf{B}$, we first simply find the Jacobian of $\mathbf{h}$ (using Maple®) and then evaluate it at $\mathbf{q}^*(\mathbf{T}^*)$. Without yet expanding the elements of the matrix in ζ, we get

$$\mathbf{B} = \begin{pmatrix} 1 & 0 & 0 & 0 & 0 & 0 \\ 0 & \frac{1+\lambda^2(4\cos^2(\pi\zeta)-3)}{1+\lambda^2} & 0 & 0 & 0 & 0 \\ 0 & 10 & 0 & 0 & 0 & \\ 0 & -\frac{4\lambda^2\cos(\bar{\alpha}\zeta\sin(\phi^*))\sin(\pi\zeta)\sin(\pi\zeta)}{1+\lambda^2} & 0 & 1 & 0 & 0 \\ 0 & 0 & 0 & 0 & 0 & 0 \\ 0 & 0 & 0 & 0 & 0 & 0 \end{pmatrix} \tag{4.62}$$

Perturbation to the Limit Cycle Period

Finally, we calculate the matrix that accounts for the perturbed limit cycle time

$$\mathbf{D} \equiv \mathbf{I} - \frac{\dot{\mathbf{q}}^*(\tau^*) \cdot Dr(\mathbf{q}^*(\tau^*))}{Dr(\mathbf{q}^*(\tau^*)) \cdot \dot{\mathbf{q}}^*(\tau^*)} \tag{4.63}$$

The collision detection function is

$$r(\mathbf{q}^-) = \theta - \frac{\pi}{n} \tag{4.64}$$

and its gradient is simply

$$Dr(\mathbf{q}^*(\tau^*)) = \{0,0,0,0,1,0\}^T. \tag{4.65}$$

We do not display the matrix $\mathbf{D}$ here due to its size.

Eigenvalues of the Approximate Jacobian

We approximate the Jacobian evaluated at the fixed point of the return map to $O(\zeta^2)$ as (see Appendix A and Appendix E)

$$\mathbf{A} \equiv \mathbf{BDE} = \tag{4.66}$$

(4.67)

$$
\begin{pmatrix}
1 & 2\frac{\pi^{\frac{3}{2}}\zeta}{\sqrt{\bar{\gamma}}} & 0 \\
0 & 1-8\frac{\zeta^2\pi^2}{1+\lambda^2}-12\frac{\zeta^2\pi^2\lambda^2}{1+\lambda^2} & -8\frac{\pi^{\frac{5}{2}}\lambda^2\zeta^2}{(1+\lambda^2)\sqrt{\bar{\gamma}}} \\
0 & 4\frac{\pi^{\frac{5}{2}}\zeta^2}{\sqrt{\bar{\gamma}}} & 1+4\frac{\pi^3\lambda^2\zeta^2}{(1+\lambda^2)\bar{\alpha}\cos(\phi^*)} \\
4\frac{\pi^{\frac{3}{2}}\zeta^2\sqrt{\bar{\gamma}}}{1+\lambda^2} & 4\frac{\pi\zeta}{1+\lambda^2} & 4\frac{\pi^{\frac{3}{2}}\zeta\lambda^2}{(1+\lambda^2)\sqrt{\bar{\gamma}}} \\
0 & 0 & 0 \\
-2\frac{\pi^{\frac{3}{2}}\zeta^2\lambda^2\sin(\phi^*)\sqrt{\bar{\alpha}}}{\sqrt{\cos(\phi^*)}} & 0 & 0
\end{pmatrix} \cdots
$$

$$
\begin{pmatrix}
-4\frac{\pi^{\frac{5}{2}}\zeta^2}{\sqrt{\bar{\gamma}}} & 0 & 0 \\
-4\pi\zeta & 0 & 0 \\
2\frac{\pi^{\frac{3}{2}}\zeta^2}{\sqrt{\bar{\gamma}}} & 0 & 0 \\
1+4\frac{\pi^3\zeta^2\lambda^2}{(1+\lambda^2)\bar{\gamma}}-8\frac{\pi^2\zeta^2(1-\lambda^2)}{1+\lambda^2} & 0 & 0 \\
0 & 0 & 0 \\
-4\pi\zeta^2\bar{\alpha}\sin(\phi^*) & \left(\frac{\lambda^2\pi^{\frac{3}{2}}}{\sqrt{\bar{\gamma}}}-\lambda^2\sqrt{\pi\bar{\gamma}}\right)\zeta & 1-4\pi^2\lambda^2\zeta^2
\end{pmatrix} \tag{4.68}
$$

Factoring the characteristic equations of the matrix $\mathbf{A}$, we get the approximation to the eigenvalues σ of the Jacobian as

$$
\begin{aligned}
\sigma_0 &= 0 \\
\sigma_1 &= 1+O(\zeta^3) \qquad \text{(in fact, this eigenvalue is exactly 1)} \\
\sigma_2 &\approx 1-(4\pi^2\lambda^2)\zeta^2 \approx \mu^2 < 1 \\
\sigma_{3,4} &\approx 1 \pm \beta_0\zeta+\beta_1\zeta^2 \\
\sigma_5 &\approx 1-\beta_2\zeta^2
\end{aligned} \tag{4.69}
$$

where

$$
\begin{aligned}
\beta_0 &= 2\pi\sqrt{2}\sqrt{\frac{\pi\lambda^2-2\bar{\gamma}}{\bar{\gamma}(1+\lambda^2)}}, \\
\beta_1 &= \frac{2(-\bar{\gamma}^2\lambda^4+2\pi^2\lambda^4-8\pi\lambda^2\bar{\gamma}+\bar{\gamma}^2\lambda^2+8\bar{\gamma}^2)\pi^2}{\bar{\gamma}(\pi\lambda^2-2\bar{\gamma})(1+\lambda^2)}, \text{ and} \\
\beta_2 &= \frac{4(\pi\lambda^2-\lambda^2\bar{\gamma}-\bar{\gamma})\pi^2\lambda^2}{(\pi\lambda^2-2\bar{\gamma})(1+\lambda^2)}.
\end{aligned}
$$

The numerical and asymptotic estimates of the eigenvalues are compared in Figure 4.9 and show the convergence to near-perfect agreement as the number of spokes gets large. Note that the approximation is based on the assumption of large n and the expressions for β_1 and β_2 show that accurate estimates are not expected for $\pi\lambda^2-2\bar{\gamma}$ close to zero. For the particular case presented in sub-section 4.8.1, we compare the numerical and asymptotic estimates of the eigenvalues from Equations (4.69) in Table 4.2 below. In addition, we compare the numerical and asymptotic estimates of the non-dimensional limit cycle period from Equation (4.58); the numerically computed value is $\tau^* = 0.5155$ and the asymptotic estimate is $\tau^* = \zeta T^* = 0.5203$.

Stability Criteria

The eigenvalues of the Jacobian of the map have the following interpretations:

- $\sigma_0 = 0$ and $\sigma_1 = 1$ for reasons discussed in Section 4.5.

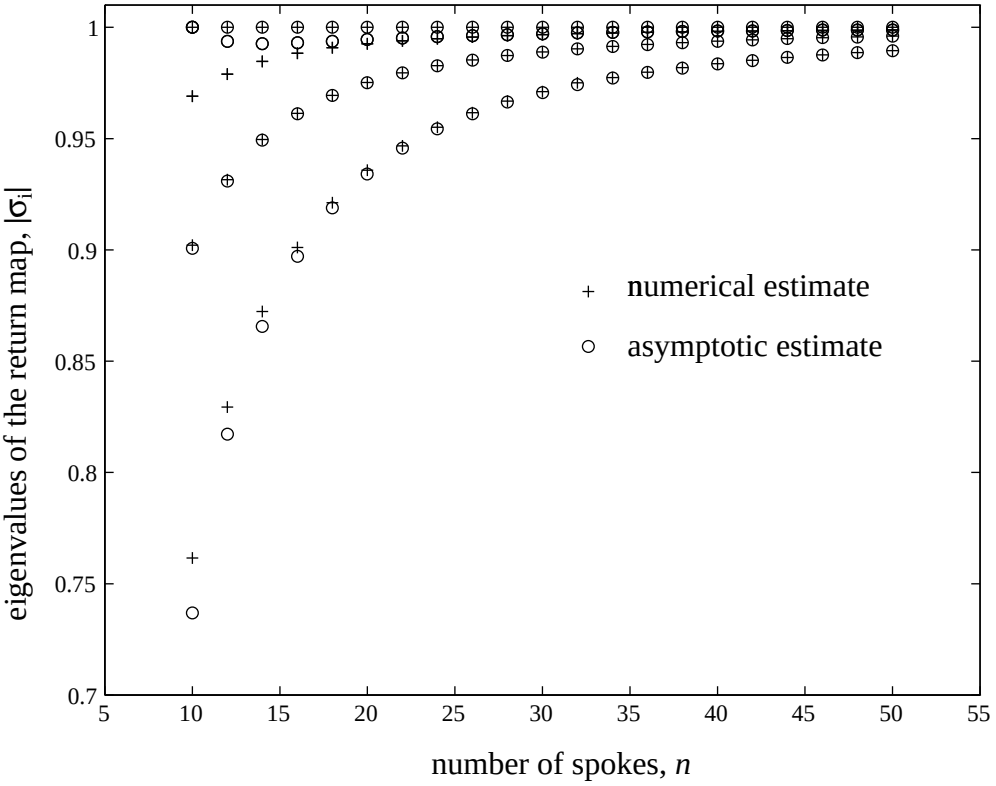

Figure 4.9: The modulus of the eigenvalues $|\sigma|$ of the Jacobian evaluated at the limit cycle fixed point are shown for different n, with $\alpha = 2/n$, and the arbitrarily chosen values $\lambda^2 = 2/3$, and $\phi_0^* = \pi/10$. The zero eigenvalue is not shown.

Table 4.2: Comparison of the numerical and perturbation estimates of the limit cycle eigenvalues for the case presented in Section 4.8.1 where $2J = 0.5$, $n = 16$, $\alpha = 2/n$, and $\phi_0^* = \pi/10$. Better agreement is found for larger n (see Figure 4.9).

	σ_0	σ_1	σ_2	$\sigma_{3,4}$	σ_5
Numerical	0	1	0.9011	$0.9884\, e^{\pm 0.3989 i}$	0.9613
Asymptotic	0	1	0.8972	$0.9930\, e^{\pm 0.4232 i}$	0.9612

- $\sigma_2 \approx 1 - (4\lambda^2\pi^2)\zeta^2 < 1$ comes from the 2D motion. In fact, σ_2 is exactly μ^2, where $\mu \equiv 1 + \lambda^2(\cos\frac{2\pi}{n} - 1)$.
- $|\sigma_{3,4}| < 1$ and $|\sigma_5| < 1$ determine necessary and sufficient conditions for asymptotic stability.

For asymptotic stability of steady planar rolling in 3D (for a wheel of many spokes on a small slope α and effective slope $\gamma \simeq O(\zeta)$), from Equations (4.69) we may conclude the following.

1. If β_0 is real, then one of $\sigma_{3,4}$ is greater than 1 by an amount $O(\zeta)$. On the other hand, if β_0 is imaginary, then the magnitudes of of $\sigma_{3,4}$ as well as σ_5 are $1 + O(\zeta^2)$ ($|\sigma_{3,4}| \approx 1 + 1/2(2\beta_1 + |\beta_0|^2)\zeta^2$). Therefore, for stability to $O(\zeta)$ we require $\pi\lambda^2 - 2\bar{\gamma} < 0$, or
$$\bar{\gamma} > \pi\lambda^2/2. \tag{4.70}$$
2. For stability to $O(\zeta^2)$ we require both **(i)** $\beta_2 > 0$ and **(ii)** $2\beta_1 + |\beta_0|^2 < 0$. Condition **(i)** is satisfied if $\bar{\gamma} > \pi\lambda^2/(1+\lambda^2)$. Note that in this case even Equation (4.70) above is automatically satisfied since $\lambda^2 = 1/(2J+1) < 1$. Finally, given $\bar{\gamma} > \pi\lambda^2/(1+\lambda^2)$, condition **(ii)** is automatically satisfied. Therefore, condition **(i)** is both necessary and sufficient to ensure stability, to $O(\zeta^2)$.

So, the asymptotic analysis estimates the condition for asymptotic stability of the planar limit cycle to be
$$\bar{\gamma} > \pi\lambda^2/(1+\lambda^2). \tag{4.71}$$

Since $\dot{\theta}^*$, the limit cycle pitch rate or rolling speed, is known in terms of $\gamma = \zeta\bar{\gamma}$, the stability results may be expressed in terms of this pitch rate (to lowest order). In terms of limit cycle pitch rate, the two stability criteria (4.70) and (4.71) reduce to
$$(\dot{\theta}^*)^2 > \frac{\lambda^2}{2}, \text{ and} \tag{4.72}$$
$$(\dot{\theta}^*)^2 > \frac{\lambda^2}{1+\lambda^2} \tag{4.73}$$
where, for $0 < \lambda^2 < 1$, criterion (4.73) is more stringent than (4.72) but (4.72) turns out to be important as discussed below.

Comparison to a Rolling Disk

The criterion on the forward speed for neutral stability of a uniform disk with polar moment of inertia $2J$ rolling in a vertical plane is $(\dot{\theta}^*)^2 > \lambda^2/2$, where $\lambda^2 = 1/(2J+1)$ (see e.g., Greenwood, 1965 [6]). This criterion is the same as the $O(\zeta)$ stability criterion (4.72) above, i.e., β_0 being imaginary. That the rolling disk criterion and criterion (4.72) should agree may be seen as follows. If Equation (4.72) is not met for the rimless wheel, i.e., $(\dot{\theta}^*)^2 < \lambda^2/2$ or β_0 is real, then one eigenvalue takes the form
$$|\sigma| = 1 + a\zeta, \text{ for some real } a > 0. \tag{4.74}$$
If Equation 4.72 is met, but Equation 4.73 is not necessarily met, then the eigenvalues take the form
$$|\sigma| = 1 + b\zeta^2, \text{ for some real } b, \text{ positive or negative.} \tag{4.75}$$
As $n \to \infty$, the rimless wheel approaches a rolling disk rolling with a constant speed on a level surface; the speed is decided by $\bar{\gamma}$. In order to compare the rimless wheel and the disk, we examine the propagation of small disturbances not through one spoke collision but rather through one revolution of the wheel at some constant limit cycle pitch rate; i.e., we look at the magnitude of σ_i^n as $n \to \infty$.

In the first case, the eigenvalue iterates through one revolution as

$$(1 + a\zeta)^{\frac{1}{\zeta}}. \tag{4.76}$$

Taking the limit as the number of spokes gets large, we get

$$\lim_{\zeta \to 0} (1 + a\zeta)^{\frac{1}{\zeta}} = \lim_{\zeta \to 0} \left[(1 + a\zeta)^{\frac{1}{a\zeta}} \right]^{a} = e^{a}. \tag{4.77}$$

Thus, as the number of spokes approaches infinity and the rimless wheel approaches a disk, small disturbances to the limit cycle grow exponentially with each revolution of the wheel.

In the second case, the eigenvalue iterates through one revolution as

$$\left(1 + b\zeta^2\right)^{\frac{1}{\zeta}}. \tag{4.78}$$

Taking the limit as the number of spokes gets large, we get

$$\lim_{\zeta \to 0} \left(1 + b\zeta^2\right)^{\frac{1}{\zeta}} = \lim_{\zeta \to 0} \left[\left(1 + b\zeta^2\right)^{\frac{1}{b\zeta}} \right]^{b} = \lim_{\zeta \to 0} e^{b\zeta} = 1. \tag{4.79}$$

Thus, it is seen that the $O(\zeta^2)$ stability criterion, Equation (4.73) above, becomes irrelevant in the limit as $n \to \infty$ and the associated eigenvalue goes to 1 (from above or below). On the other hand, the $O(\zeta)$ stability criterion, Equation (4.72), predicts instability if β_0 is real, and neutral stability if β_0 is imaginary in the limit as $n \to \infty$, just like the rolling disk. Therefore, Equation (4.72) governs the stability of the rimless wheel, as $n \to \infty$, and agrees with the stability calculations for a rolling disk.

In other words, for a large number of spokes but still finite, disturbances grow slowly. Yet, as the number of spokes approaches infinity and the rimless wheel approaches a disk, small disturbances neither grow nor decay through each revolution, like the rolling disk. Thus, the necessary condition for lateral stability of the rimless wheel on small slopes matches that for neutral stability of the rolling disk on a flat surface as the number of spokes approaches infinity.

4.8.3 Aside: Existence of Other Limit Cycles

In the case of 3D motions, if we vary the slope as a parameter for fixed n, then for some slope the eigenvalue σ_5 will be exactly 1. At that particular slope, the eigenvalue 1 has multiplicity two. Therefore, one might expect that at that slope two limit cycles merge.

We do not believe that there are such limit cycles. Our reasoning is as follows. **(a)** As n gets large, the dynamic behavior of the rimless wheel approaches that of a disk on a flat plane (in a suitably averaged sense). Small deviations from pure rolling, for a disk, are limited to small, periodic wobbles. These wobbles occur over a time scale of $O(1)$. For the rimless wheel, this means such wobbles occur over $O(n)$ collisions, which is consistent with the imaginary parts of $\sigma_{3,4}$ being $O(1/n)$. Such 'long-period' motions will not be fixed points of the single-spoke-collision return map we consider. Intuitively, we do not foresee any other types of fixed points of the return map except the one-parameter family of steady rolling motions we have considered. **(b)** Note that fixed points are solutions to the equation $\mathbf{f}(\mathbf{x}) = \mathbf{x}$, or $\mathbf{g}(\mathbf{x}) := \mathbf{f}(\mathbf{x}) - \mathbf{x} = 0$. The Jacobian of the function $\mathbf{g}(\mathbf{x})$ differs from that of $\mathbf{f}(\mathbf{x})$ by the identity, and a double eigenvalue of 1 for $\mathbf{f}$ corresponds to a double-zero eigenvalue for $\mathbf{g}$. However, for another solution branch in addition to the known one-parameter family to appear at that point, the rank of $D\mathbf{g}$, the Jacobian of $\mathbf{g}$, should be 4 (2 less than 6). Based on some numerical checks using the singular value decomposition, we believe that (at least typically) the rank of $D\mathbf{g}$ is 5 (1 less than 6). In other words, the double eigenvalue has algebraic multiplicity 2 but geometric multiplicity 1. This means that the already known one-parameter family of steady rolling solutions (i.e., limit cycles) is all there is.

4.9 Conclusions and Future Work

In this chapter, we have presented an analysis of a 3D dynamic system with intermittent impacts, that shares some qualitative features with passive dynamic walking machines. A viable computer-algebra based analytical technique for stability studies of systems with intermittent impacts was demonstrated for this moderately complex system. In another work, this same approach has been successfully used to study the stability of a simple walking machine in 2D (Garcia, *et. al.*, 1996[16]). The rimless wheel behaves like a disk, on $O(1)$ time scales, as the number of spokes get infinitely large.

We note that the rimless wheel can be stable in 2D on slopes of $O(1/n^3)$, essentially due to the energy dissipation in collisions. However, the 3D system, with more degrees of freedom, is only stable on slopes of $O(1/n)$. Hence, energy dissipation alone is not sufficient for stability in 3D. The intermittent collisions are somehow crucial to the asymptotic stability that the rimless wheel has but that the rolling disk does not have.

A question of general interest to us is the cause of balance stability of 'passive-dynamic' walking machines. Two known mechanisms for asymptotic stability of passive mechanical systems are dissipation and nonholonomic constraints. For the rimless wheel, the natural comparison system is a rolling disk, a classic nonholonomic system. The rolling disk, due to its symmetry with respect to motion reversal, is not asymptotically stable. Thus, we do not know of a simple way to explain the asymptotic balance stability of the system discussed here.

We would like to compare the rimless wheel with crooked masses attached to the disk with crooked masses in Chapter 3 to show how a nonconservative piecewise holonomic system with asymptotic stability approaches an asymptotically stable conservative nonholonomic system in the limit as the number of spokes gets large.

In addition, it would be interesting to search for other stable steady motions besides the planar limit cycle, like zig-zagging or looping behavior.

Next, Chapter 5 presents an analysis of a planar straight-legged point-foot walker constrained to move in two dimensions. We find stable 2D limit cycles for this device and use these as starting points for the 3D analysis in Chapter 6.

Chapter 5

'Step Four': Two-dimensional Straight-legged Point-foot Walker

In terms of its mechanics, walking is nothing more than a series of stumbles caught in the nick of time, a continuous, rhythmic loss and recovery of balance. Gravitation, no less, is the force that we harness to our service when we walk.
A. Sussman and R. Goode, *The Magic of Walking, 1967*

5.1 Introduction

We now present a study of our first walking model, in 2D. We will use 2D fixed points as 'seeds' for finding fixed points of a 3D version of the 2D model presented here as well as to get a feel for how a passive point-foot straight-leg model model behaves. We consider a two-dimensional straight-legged point-foot walking device, one only touched on by McGeer [43], a simplification of his 2D straight-legged walker with round feet. This is one of the simplest 2D models we can study, with only three parameters after non-dimensionalization. This model is a slightly more complicated version of the of the double-pendulum ('compass-gait') point-foot models being studied by [45, 81, 82]. The 2D straight-legged point-foot walking model is shown in Figure 5.1 below to remind the reader of where it fits into the evolution of models in the research program.

We find stable 2D passive gaits for a variety of parameters. We have also discovered an illustrative limiting case, a stable one-parameter (slope angle) model, the simplest walking model. This simple walking model displays stable chaotic walking as well as a case of funny walking (highly-unstable periodic gait with multiple leg swings between foot collisions). The details of the analysis of this model are presented in a paper by Garcia, Chatterjee, Ruina, and Coleman [16]. This model is a limiting case of the the simple straight-legged walkers of [4] and [45, 81, 82]. This model, described below in Section 5.5, has a special mass distribution that further simplifies the underlying mechanics and mathematics

5.1.1 Description of the 2D System

The 2D point-foot version of the 3D model is shown in Figure 5.2. It has two identical rigid legs of length ℓ, mass M, center of mass location (X_{cm}, Z_{cm}) in stance leg frame coordinates, and moment of inertia with respect to the center of mass I^{cm}. A frictionless hinge at the hip connects the legs. The system of links moves on a rigid ramp of slope α. As we assumed for a rimless wheel spoke, when a foot hits the ground (ramp surface) at *heel-strike*, it has a plastic (no-slip, no bounce) collision and its velocity jumps to zero. The foot remains on the ground, acting like a hinge joint, until the

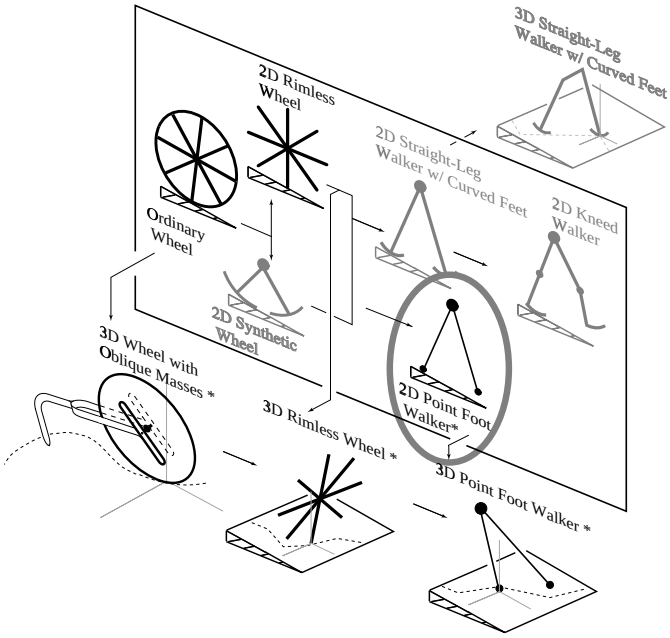

Figure 5.1: The place of the 2D straight-legged point-foot walking model in the passive-dynamic family tree.

swinging foot reaches heel-strike. During walking, only one foot is in contact with the ground at any time; double support occurs instantaneously. A 2D cartoon of the model's motion over one step is shown in Figure 5.3. Between collisions, the model's motion is governed by the classical laws of rigid-body mechanics. We make the non-physical assumption the swing foot can briefly pass through the ramp surface when the stance leg is near vertical. This concession is made to avoid the inevitable scuffing problems of straight-legged walkers. This clearance problem, while trivial in theory, can be solved in practice by providing suitable 'stepping stones' for the physical model or by adding knees or retractable feet (McGeer [4], Mochon [13]).

Configuration and State Spaces

We characterize the configuration of the walker between collisions using the stance and swing leg angles as shown in Figure 5.2. The stance leg angle θ_{st} is the angle of the stance leg with respect to the normal to the slope and the swing leg angle θ_{sw} is the angle of the swing leg with respect to the stance leg.

Between collisions, the system is holonomic and position is defined by two generalized coordinates, the stance and swing leg angles. Globally, the position is described by three generalized coordinates while the instantaneous velocity space is determined by only two angular rates; in this sense, it is nonholonomic.

In our stability analysis, we do not keep track of the foot contact position over several foot collisions; we just keep track of the orientation variables θ_{st} and θ_{sw}. We use equations of motion for a double pendulum (holonomic system with two degrees of freedom), and use angular momentum-balance-deduced jump conditions to map the state variables from just before a foot collision to just after. Thus, in our analysis, the state space is four dimensional and $\mathbf{q}$, the state vector, is defined to be

$$\mathbf{q} = \{\theta_{st}, \theta_{sw}, \dot{\theta}_{st}, \dot{\theta}_{sw}\}^T. \tag{5.1}$$

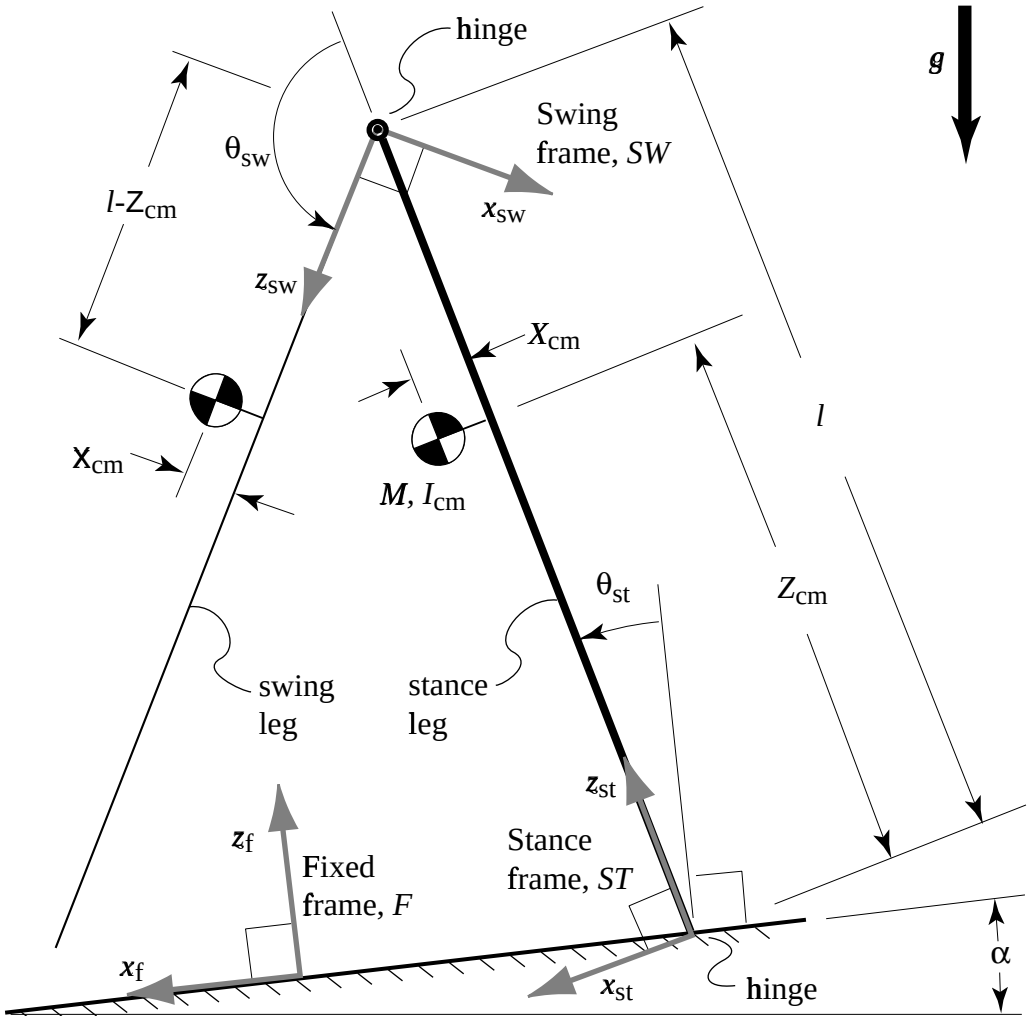

Figure 5.2: The point-foot walking model: parameters and configuration variables. Leg lines are drawn with different line weights to correspond to the plot of Figure 5.5. The leg mass is designated by M, the moment of inertia with respect to the center of mass by I^{cm}, the leg length by ℓ, the ramp angle with respect to the horizontal by α, and the acceleration due to gravity by g. The angle of the stance leg with respect to the slope normal is θ_{st} and the angle of the swing leg relative to the stance leg is θ_{sw}.

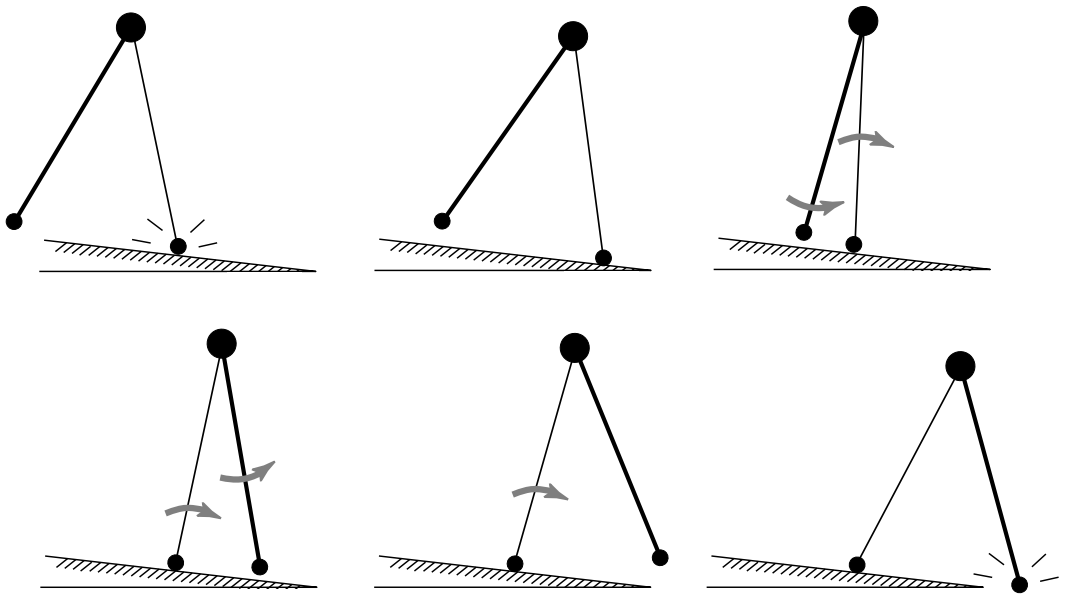

Figure 5.3: A typical passive walking step. The new stance leg (lighter line) has just made contact with the ramp in the upper left picture. The old stance leg becomes the new swing leg (heavier line). The new stance leg swings until the next heel-strike (bottom right picture). At heel-strike, the new swing leg becomes the newest stance leg.

5.1.2 Indexing Scheme

We have chosen a set of angles to describe the orientation of the walking device between collisions. We next present an indexing scheme to denote the state of the system just before and after the collision i of the i_{th} swing leg. We use the indexing scheme to define a 'cycle' of the walker — from just after a swing leg collision (heel-strike) to just after the next.

The i_{th} stance and swing legs are so designated after the i_{th} collision. Thus, the names of the legs are exchanged through a collision. That is, the i_{th} stance leg becomes the $i+1_{th}$ swing leg and vice-versa for the i_{th} swing leg.

Special times of interest are just before and just after collision i. The minus and plus signs $(-)$ and $(+)$ are used as the superscripts to denote these times. For instance, ${}^{i}\theta_{st}^{+}$ is the stance leg angle just after collision i of swing leg $i-1$.

In defining the orientation of the walking device, we have defined fixed frame $\mathcal{F}$, stance leg frame $\mathcal{ST}$ (fixed to the stance leg), and swing leg frame $\mathcal{SW}$ (fixed to the swing leg). The stance leg frame ${}^{i}\mathcal{ST}$ has origin at the tip of the stance leg currently in contact with the ground after collision i. The swing leg frame ${}^{i}\mathcal{SW}$ has origin at the hip joint. The z_{st} and z_{sw} axes are aligned with the stance and swing legs, respectively.

We move the origin of the stance leg frame instantaneously with each swing leg collision from the tip of the pre-collision stance leg to the tip of the post-collision stance leg currently in contact with the ground after collision $i+1$. The origin of the swing leg frame remains at the hip joint.

As the origin of stance leg frame i is moved to the tip of the colliding leg, however, we not only translate the stance leg frame but also rotate it by $-2\ {}^{i+1}\theta_{st}^{-}$ about the y-axis with respect to the fixed frame so that the z_{st}-axis of stance leg frame $i+1$ is aligned with stance leg $i+1$. Thus, the stance leg angle changes instantaneously from θ_{st} to $-\theta_{st}$ through a downhill swing leg collision. Likewise, the swing leg frame rotates by $-2\ {}^{i+1}\theta_{sw}^{-}$ about the y axis with respect to the stance leg frame so that the z_{sw}-axis of the swing leg frame $i+1$ is aligned with swing leg $i+1$.

After a collision, then, we redefine the absolute orientation with respect to the fixed frame using the newly positioned frames. The relationships between frames and their associated bases from before to after collision $i+1$ are

$$ {}^{i+1}\mathcal{ST}^{+} \neq {}^{i+1}\mathcal{ST}^{-},\ {}^{i+1}\mathbf{e}^{+}_{st} = \mathbf{R}_2(\theta = -2\ {}^{i+1}\theta^{-}_{st})\ {}^{i+1}\mathbf{e}^{-}_{st}, \tag{5.2} $$

$$ {}^{i+1}\mathcal{SW}^{+} \neq {}^{i+1}\mathcal{SW}^{-},\ {}^{i+1}\mathbf{e}^{+}_{sw} = \mathbf{R}_2(\theta = -2\ {}^{i+1}\theta^{-}_{sw})\ {}^{i+1}\mathbf{e}^{-}_{sw}. \tag{5.3} $$

5.1.3 Cycle of Motion

A 'cycle' of the walking device is the motion from one swing foot collision through the next. A schematic of one cycle, for downhill walking, is shown in Figure 5.4. As before with the 2D and

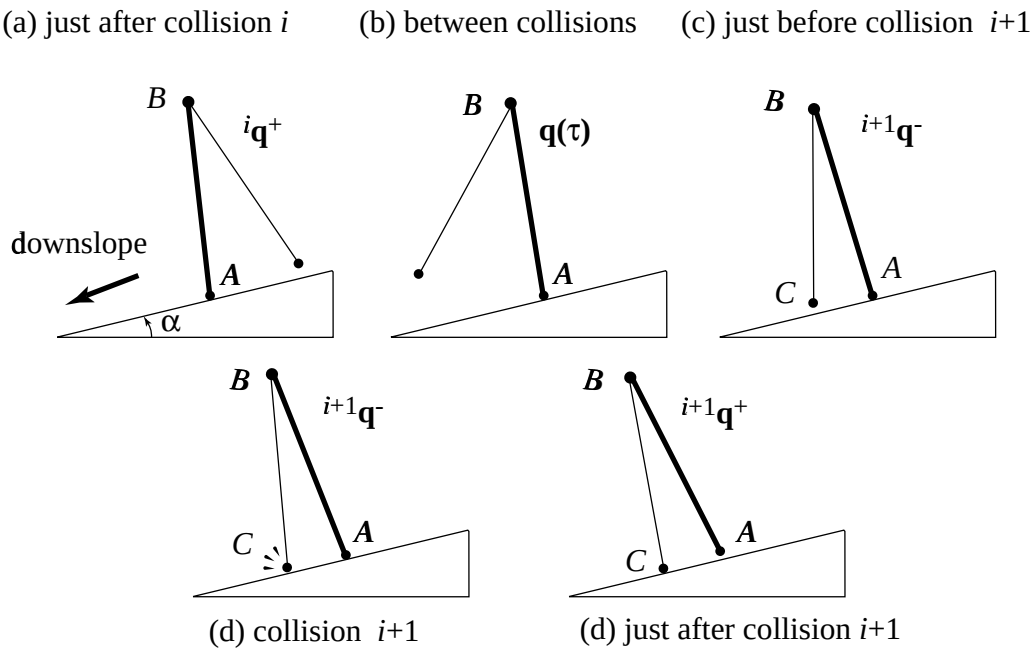

Figure 5.4: Schematic showing: (a) the state of the walking device over one stride just after collision i of swing leg i with point A, (b) the state of the walking device between collisions, (c) the state of the walking device just before collision $i+1$ of swing leg foot i at point B, (d) collision $i+1$ of swing foot i at point B, and (e) the state of the walking device just after collision $i+1$ of swing leg foot i at point B. The stance leg is denoted by the heavy line and the swing leg by the thin line.

3D rimless wheels, we pick as the starting point the instant when the trailing stance leg i leaves the ground *and* and the leading swing leg i simultaneously collides with the ground. The walking device rotates over the stance leg i , as an inverted double pendulum with initial state ${}^{i}\mathbf{q}^{+}$. The non-collisional portion of the stride ends just before swing leg i strikes the ground at collision $i+1$ instantaneously transferring support from the trailing stance leg to the leading swing leg. The state of the walker is now${}^{i+1}\mathbf{q}^{-}$. After impact, the walking device is now poised for the next start-of-cycle at state ${}^{i+1}\mathbf{q}^{+}$.

5.2 Governing Equations

Now that we have defined a cycle of motion, we can derive the equations that describe the motion between collisions and the collision transition rule.

5.2.1 Equations of Motion between Collisions (During the Swing Phase)

The two coupled second-order differential equations of motion are given below for the swing phase of the motion, where θ_{st} and θ_{sw} are functions of time non-dimensional time $\tau = t\sqrt{g/\ell}$. These equations are derived by taking angular momentum balance for (1) the whole mechanism about the contact point of the stance leg with the ground and for (2) the swing leg about the hip joint. Appendix B describes this procedure in detail.

$$\mathbf{M}(\mathbf{q}) \left\{ \begin{array}{c} \ddot{\theta}_{st} \\ \ddot{\theta}_{sw} \end{array} \right\} + \mathbf{V}(\mathbf{q}) \left\{ \begin{array}{c} \dot{\theta}_{st}^2 \\ \dot{\theta}_{sw}^2 \\ \dot{\theta}_{st}\dot{\theta}_{sw} \end{array} \right\} + \mathbf{G} \left\{ \begin{array}{c} \cos(\alpha + \theta_{st}) \\ \sin(\alpha + \theta_{st}) \\ \cos(\alpha + \theta_{st} + \theta_{sw}) \\ \sin(\alpha + \theta_{st} + \theta_{sw}) \end{array} \right\} = \left\{ \begin{array}{c} 0 \\ 0 \end{array} \right\} \tag{5.4}$$

The matrices in Equation (5.4) are

$$\mathbf{M}(\mathbf{q}) = \left[\begin{array}{cc} M_{11} & M_{12} \\ M_{21} & M_{22} \end{array} \right], \tag{5.5}$$

where

$$\begin{aligned} M_{11} &= 2\left[(1 + z^2 + x^2 - 2z) + I + (1 - z)\ c\theta_{sw}) + x\ s\theta_{sw}\right], \\ M_{12} &= \frac{1}{2}M_{11} - z, \\ M_{21} &= M_{12}, \text{ and} \\ M_{22} &= M_{12} - (1 - z)\ c\theta_{sw} - x\ s\theta_{sw}; \end{aligned} \tag{5.6}$$

$$\mathbf{V}(\mathbf{q}) =$$

$$\left[\begin{array}{ccc} 0 & x\ c\theta_{sw} - (1-z)\ s\theta_{sw} & -2(x\ c\theta_{sw} - (1-z)\ s\theta_{sw}) \\ x\ c\theta_{sw} - (1-z)\ s\theta_{sw} & 0 & 0 \end{array} \right], \tag{5.7}$$

and

$$\mathbf{G} = \left[\begin{array}{cccc} -x & -(1+z) & x & -(1-z) \\ 0 & 0 & x & -(1-z) \end{array} \right]. \tag{5.8}$$

Note that $V_{13} = -2V_{12}$, $V_{21} = V_{12}$, $G_{11} = -G_{13} = -G_{23}$, and $G_{14} = G_{24}$. These are the equations of motion for a planar rigid-body double pendulum. In Equations 5.23, we have rescaled time by $\sqrt{\ell/g}$. The moment of inertia, and coordinates of the center of mass are non-dimensionalized as follows: $I = \dfrac{I_{cm}}{M\ell^2}$ and $(x, z) = \left(\dfrac{X_{cm}}{\ell}, \dfrac{Z_{cm}}{\ell}\right)$.

5.2.2 Collision Transition Conditions

Collision Detection Rule

The collision occurs when the geometric collision condition

$$\mathbf{r}_{C/A} \cdot \hat{\mathbf{k}}_f = \cos(\theta_{st} + \theta_{sw}) + \cos(\theta_{st}) = 0. \tag{5.9}$$

is met. Equation 5.9 describes the values of θ_{sw} and θ_{st} for which the swing leg foot is coincident with the ramp surface. Solving Equation (5.9) for θ_{st} and θ_{sw}, we get an equivalent geometric collision condition

$$\pi - (\theta_{sw} + 2\theta_{st}) = 0. \tag{5.10}$$

which is easily seen from the collision configuration.

We also impose the additional condition that the stance leg be sufficiently past vertical (Equation (5.9) is also true at least once when the legs are nearly parallel, but we ignore scuffing).

Collision Rule for Configuration Variables

At the instant of swing foot collision, the pre-collision stance leg switches to the post-collision swing leg and vice-versa. So, the stance and swing angle are reset at each swing foot collision as support is transferred from the stance foot to the swing foot according to the following mapping:

$$\left\{ \begin{array}{c} \theta_{st} \\ \theta_{sw} \end{array} \right\} \mapsto \left\{ \begin{array}{c} -\theta_{st} \\ -\theta_{sw} \end{array} \right\} \tag{5.11}$$

Thus, we can write

$$\left\{ \begin{array}{c} \theta_{st}^{+} \\ \theta_{sw}^{+} \end{array} \right\} = \mathbf{S} \left\{ \begin{array}{c} \theta_{st}^{-} \\ \theta_{sw}^{-} \end{array} \right\}, \text{ where } \mathbf{S} = \left[\begin{array}{cc} -1 & 0 \\ 0 & -1 \end{array} \right]. \tag{5.12}$$

Collision Rule for Angular Rates

The swing foot contact point receives an impulse at foot-strike (point C). Due to the swing foot collision, an impulse is also transmitted to the swing leg at the hip joint (point B). We assume that, during collision, other smaller forces (e.g., gravity) acting on the system are negligible in comparison to the collision impulses. We also assume there are no impulsive ground contact torques. At the instant of collision at the hip, we assume that the former stance leg loses contact with the ground (at the same instant the swing foot makes contact) and that it has no impulsive reaction with the ground as it leaves. Based on these assumptions, angular momentum is conserved for the entire system about the swing foot contact point C during the collision process. Angular momentum is also conserved for the new swing leg (formerly the stance leg) about the hip joint, point B. These statements of angular momentum conservation during the collision process yield the transition rules for velocities from just before to just after foot-strike. Referring to Figure 5.4, we can write these conservation statements as

$$\mathbf{H}_{C}^{-} = \mathbf{H}_{C}^{+} \tag{5.13}$$

for the whole system and

$$^{\mathrm{st}}\mathbf{H}_{B}^{-} = ^{\mathrm{sw}}\mathbf{H}_{B}^{+} \tag{5.14}$$

for the the pre-collision stance leg which becomes the post-collision swing leg. Applying angular momentum balance as prescribed above through heel-strike gives the following collision rule for angular rates where the '+' superscript means 'just after heel-strike', and the '$-$' superscript means 'just before heel-strike'. Appendix B describes this procedure in detail. The jump equations are non-dimensionalized in the same way as the equations of motion between foot collisions.

$$\left\{ \begin{array}{c} \dot{\theta}_{st}^{\ +} \\ \dot{\theta}_{sw}^{\ +} \end{array} \right\} = \mathbf{T} \left\{ \begin{array}{c} \dot{\theta}_{st}^{-} \\ \dot{\theta}_{sw}^{-} \end{array} \right\} \tag{5.15}$$

where the transition matrix $\mathbf{T}$ is

$$\mathbf{T} = \frac{1}{D} \left[\begin{array}{cc} T_{11} & T_{12} \\ T_{21} & T_{22} \end{array} \right] \tag{5.16}$$

and its components are

$$\begin{aligned}
T_{11} &= \left((1+z)I - z^2(2-z) + x^2 + z(1+x^2)\right)\cos(2\theta_{st}^{-}) + \\
&\quad x\left(I - z(1-z) + x^2\right)\sin(2\theta_{st}^{-}) + T_{12}, \\
T_{12} &= I\left(I + 2x^2 + (2z-1)(z-1)\right) + x^2(x^2 - 3z + 1) + \\
&\quad z^2\left(z^2 + 3(1-z)\right) - z, \\
T_{21} &= \left[2z^2(2-z) - 2z(1+x^2)I + 2xz\sin(2\theta_{st}^{-}) + 2z(1-z)cos(2\theta_{st}^{-})\right]cos(2\theta_{st}^{-}) \\
&\quad -2z^2(1-z) + 2z(x^2 + I),
\end{aligned}$$

$$
\begin{aligned}
T_{22} &= \left((1-z)I + z^2(2-z) + x^2 - z(1+x^2)\right)\cos(2\theta_{st}^-) + \\
&\quad x\left(I + z(1-z) + x^2\right)\sin(2\theta_{st}^-) - T_{12}, \text{ and} \\
D &= \left(x^2 + (1-z)^2\right)\cos^2(2\theta_{st}^-) - x(1-z)\sin(4\theta_{st}^-) + \\
&\quad I\left(I + 2\left(x^2 - z(1-z) + 1\right)\right) + z^2\left((1-z)^2 + 2x^2 + 1\right) + \\
&\quad x^2(x^2 - 2z + 1) - 2z + 1.
\end{aligned} \tag{5.17}
$$

The jump equations are non-dimensionalized in the same way as the equations of motion between foot collisions.

Total Collision Rule

Finally, we can merge the transition rules for the orientation variables and their rates into one map from the state of the system just before a collision to just after:

$$
\begin{Bmatrix} \theta_{st}^+ \\ \theta_{sw}^+ \\ \dot{\theta}_{st}^+ \\ \dot{\theta}_{sw}^+ \end{Bmatrix} = \mathbf{L} \begin{Bmatrix} \theta_{st}^- \\ \theta_{sw}^- \\ \dot{\theta}_{st}^- \\ \dot{\theta}_{sw}^- \end{Bmatrix}, \text{ where } \mathbf{L} = \begin{bmatrix} \mathbf{S} & 0 \\ 0 & \mathbf{T} \end{bmatrix}. \tag{5.18}
$$

We can rewrite this collision law that maps the state of the walker just before to just after a collision as

$$
\mathbf{q}^+ = \mathbf{h}(\mathbf{q}^-) = \mathbf{L}(\mathbf{q}^-)\,\mathbf{q}^- \tag{5.19}
$$

where the matrix $[\mathbf{L}(\mathbf{q}^-)]$ depends only on the orientation variables and not their rates.

5.3 2D Return Map, Fixed Points and Stability of Walking Motions

This time, the straight-legged point-foot walker constrained to move in two dimensions has an four-dimensional phase space with coordinates $\{\theta_{st}, \theta_{sw}, \dot{\theta_{st}}, \dot{\theta_{sw}}\}^T$. Again, a natural place to sample this space is at the points of discontinuity, the collisions. We construct a map $\mathbf{f}$ that takes the state of the walker just after a collision to just after the next. The map from one state to the next can be written as before as $\mathbf{q} \mapsto \mathbf{f}(\mathbf{q})$ or

$$
{}^{i+1}\mathbf{q}^+ = \mathbf{f}({}^{i}\mathbf{q}^+), \tag{5.20}
$$

where $\mathbf{f}$ is the return map and ${}^{i}\mathbf{q}^+$ is the state vector of the system at the start of a cycle, just after the i_{th} collision.

Since we know the relationship of the stance leg angle to the swing leg angle on the Poincaré section(see Equation (5.10)), the map can be reduced to three dimensions. When making stability calculations in practice, as we did with the 3D rimless wheel in Chapter 4 (see note on page 98), we keep all four dimensions which always yields one eigenvalue of the Jacobian evaluated at a fixed point exactly zero.

Again, the map $\mathbf{f}$ may be looked upon as a composition of two maps $\mathbf{f} = (\mathbf{h} \circ \mathbf{d})$; here, $\mathbf{d}$ governs the motion from just after heel-strike i to just before heel-strike $i+1$, obtained by integrating the equations of motion between collisions, and $\mathbf{h}$ governs support transfer, from just before to just after heel-strike $i+1$.

For periodic or steady motion, we must again find fixed points of the return map,

$$
\mathbf{q}^* = \mathbf{f}(\mathbf{q}^*). \tag{5.21}
$$

5.4 Numerical Simulations and Results

5.4.1 Steady Motions and Stability

We integrated the fully nonlinear equations of motion using `int_henon2D.m`, a version of MATLAB®'s `ode45.m` (a 4th-5th order automatic step-sizing routine) modified to detect spoke collisions using Henon's [62] method. This routine is identical in nature to the 3D version `int_henon3D_temp.m` (see Appendix A). We used an integration tolerance 10^{-8} in the automatic step-sizing routine. A typical plot of θ_{st} and θ_{sw} over one step is shown in Figure 5.5. We found fixed points and the

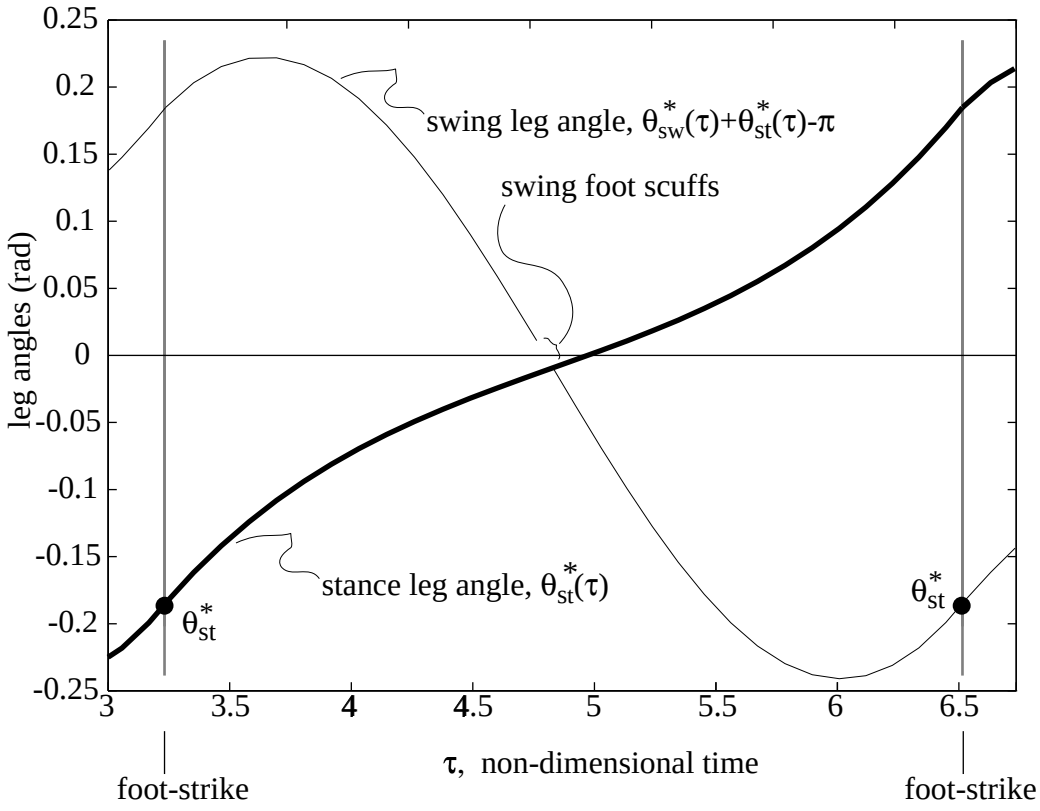

Figure 5.5: The 2D point-foot leg angles over one step at a gait cycle for $\alpha = 0.0090$, $I = 0.0827$, $x = 0.0000$, $z = 0.8780$. At a gait cycle, heel-strike returns the system to its initial conditions. The swing leg angle is more usefully plotted as measured from the vertical to the slope or $\theta^*_{sw}(\tau) + \theta^*_{st}(\tau) - \pi$. The stable fixed point for this case is $\mathbf{q}^* = \{-0.1847, 3.5110, 0.2080, -0.0220\}^T$; the maximum eigenvalue is $|\sigma_{max}| = 0.1611$ and the non-dimensional step period is $\tau^* = 3.278$. The stance leg curve is denoted by the heavy line and the swing leg curve by the thin line corresponding to Figure 5.2.

Jacobian eigenvalues using a MATLAB® routine `newton_2D.m`. THis routine is identical in nature to `newton_3D.m` (see Appendix A). The finite difference step size used to compute the Jacobian numerically was 10^{-4} and error tolerance for the fixed point search was 10^{-6}. The eigenvalues and eigenvectors for a particular case are shown in Table 5.1. Similar stability results are found over a wide range of parameter variations.

Table 5.1: Eigenvalues and eigenvectors for a stable periodic walking motion with $\alpha = \frac{\pi}{350}$, $I = 0.0827$, $x = -0.001$, and $z = 0.8780$.

Eigenvalues		
σ_1	σ_2	σ_3
0.2482	-0.0099	-.9607

Eigenvector			
θ^*_{st}	1	1	1
$\dot{\theta}^*_{st}$	-1.0143	-0.95	-0.7955
$\dot{\theta}^*_{sw}$	0.3837	-1.0581	0.3008

5.4.2 Effects of Parameters Variations on Steady Motions and Stability

We show how the step period τ^*, modulus of the maximum eigenvalue $|\sigma_{max}|$, and fixed point stance angle θ^*_{st} vary with each parameter while the others are held constant. No attempt is made here to exhaustively search the huge parameter space for stable periodic motions.

Leg Inertia, I

Increasing the non-dimensional leg inertia I (radius of gyration squared) increases the maximum eigenvalue, the step period, and the stance leg angle (as well as the inter-leg angle), as shown in Figure 5.6. Increasing the leg inertia lengthens the pendulum period of the swing leg and also slows the characteristic time of falling of the stance leg thereby decreasing the characteristic frequency of walking. Though lowering the leg inertia decreases the efficiency, according to Equation (2.8) for a comparable 2D rimless wheel, this does not make the walker unstable.

Mass Center Height along Leg, z

Raising z, the center of mass height along the leg, at first stabilizes walking, then destabilizes it as it nears the hip, and then stabilizes it again as it gets very close to the hip, as shown in Figure 5.7.

Mass Center Offset, x

As the center of mass is offset in either the fore or aft directions, the maximum eigenvalue increases while the periodic stance leg angle decreases; the step period decreases if the mass is moved forward and increases if it is moved backward (see Figure 5.8). A typical root-locus plot for the three return map eigenvalues are shown in Figure 5.9 for $-0.001 < x < 0.001$.

Slope Angle

The maximum eigenvalue, step period, and stance angle increase with increasing slope angle, as shown in Figure 5.10. No attempt is made here to estimate the basins of attraction for the stable periodic motions or the boundaries in parameters space that define the existence or non-existence of periodic motions.

Funny Walking

A typical plot of θ_{st} and θ_{sw} over one step for stable double-swing walking gait is shown in Figure 5.11 for $\alpha = 0.009$. (There are, in fact, an infinite number of solutions of n leg oscillations between leg foot collisions (see, Garcia, *et. al.* [16]).

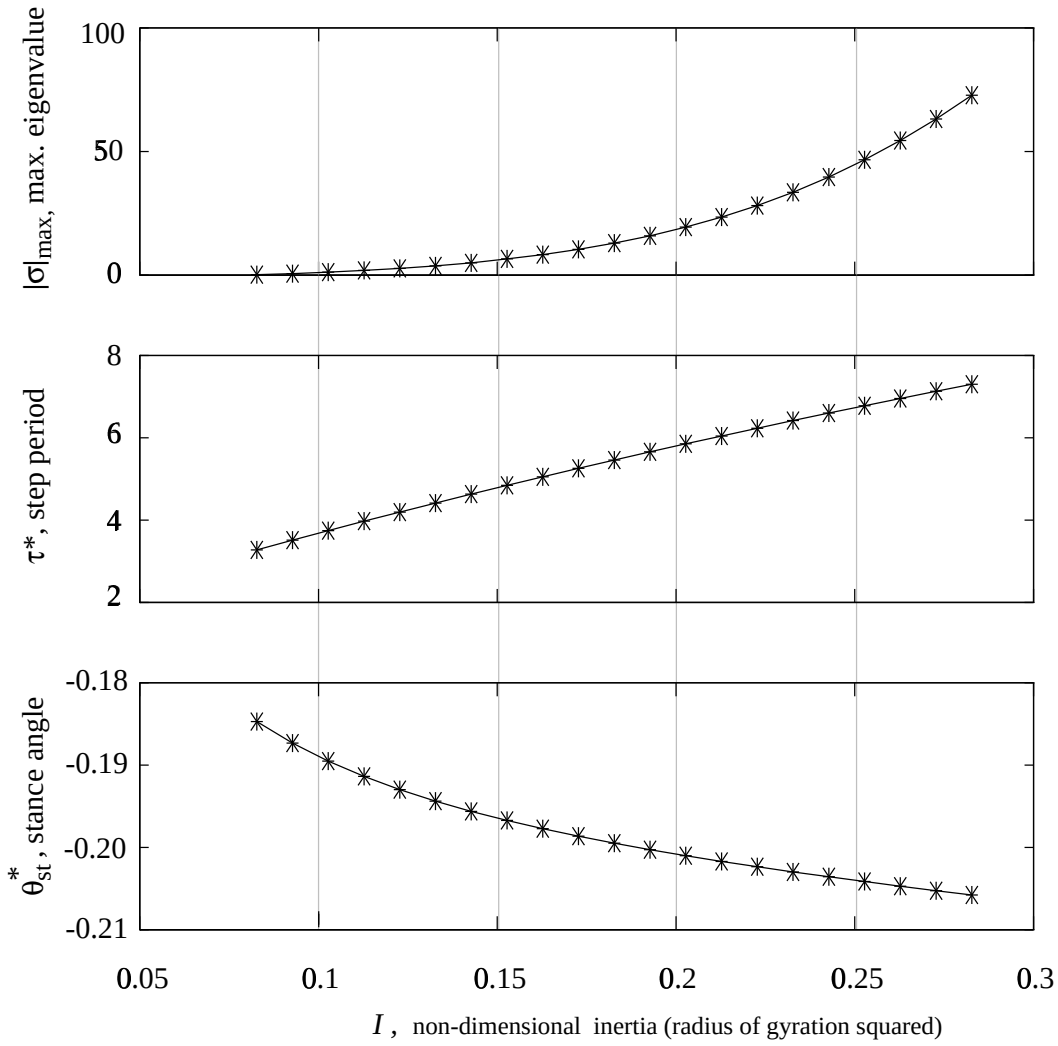

Figure 5.6: The variation of maximum eigenvalue, step period, and stance angle with non-dimensional inertia I for steady gait while slope angle and center of mass location are held constant at $\alpha = \frac{\pi}{350}$, $x = -0.001$, and $z = 0.8780$.

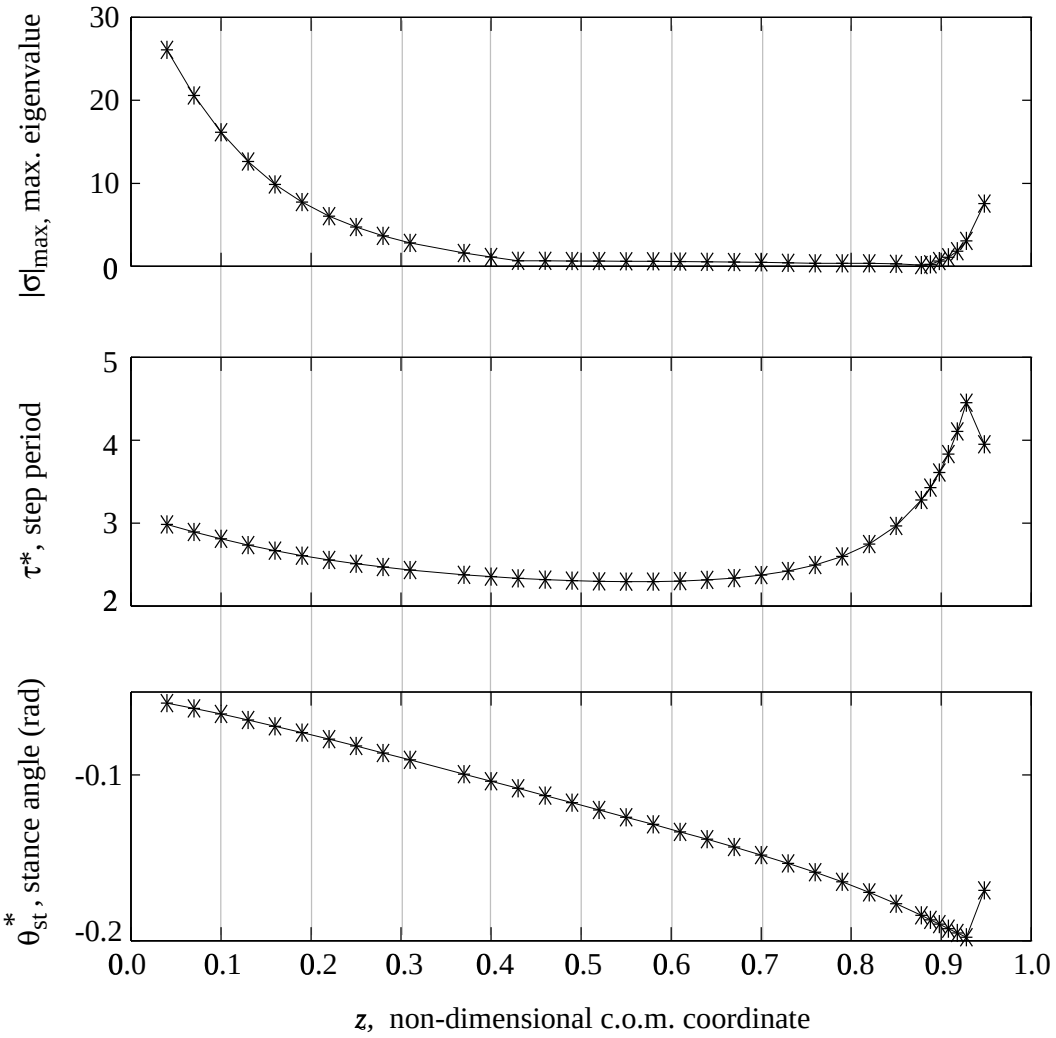

Figure 5.7: The variation of maximum eigenvalue, step period, and stance angle with non-dimensional center of mass position along the leg z for steady gait while slope angle, leg inertia, and center of mass offset are held constant at $\alpha = \frac{\pi}{350}$, $x = -0.001$, and $I = 0.0827$.

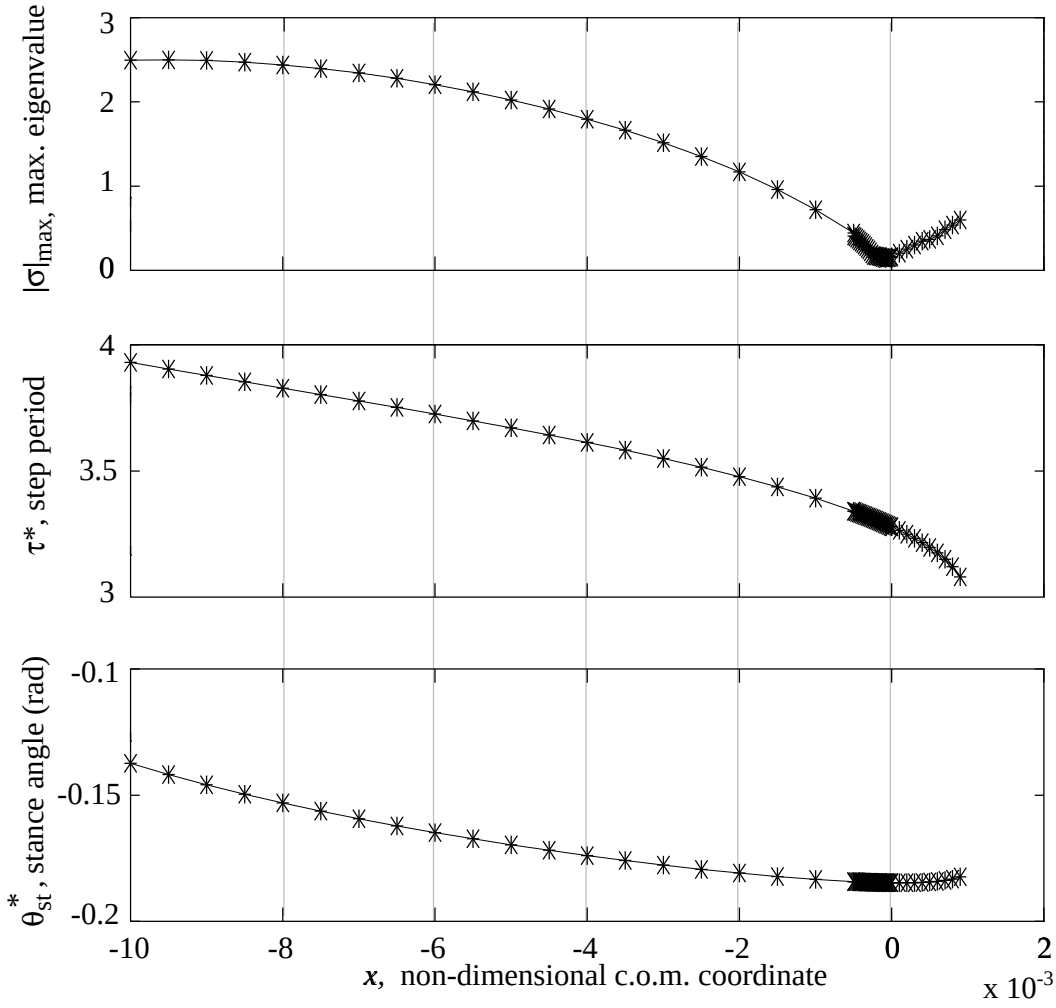

Figure 5.8: The variation of maximum eigenvalue, step period, and stance angle with non-dimensional center of mass offset x for steady gait while slope angle, leg inertia, and center of mass position along the leg are held constant at $\alpha = \frac{\pi}{350}$, $I = 0.0827$, and $z = 0.8780$.

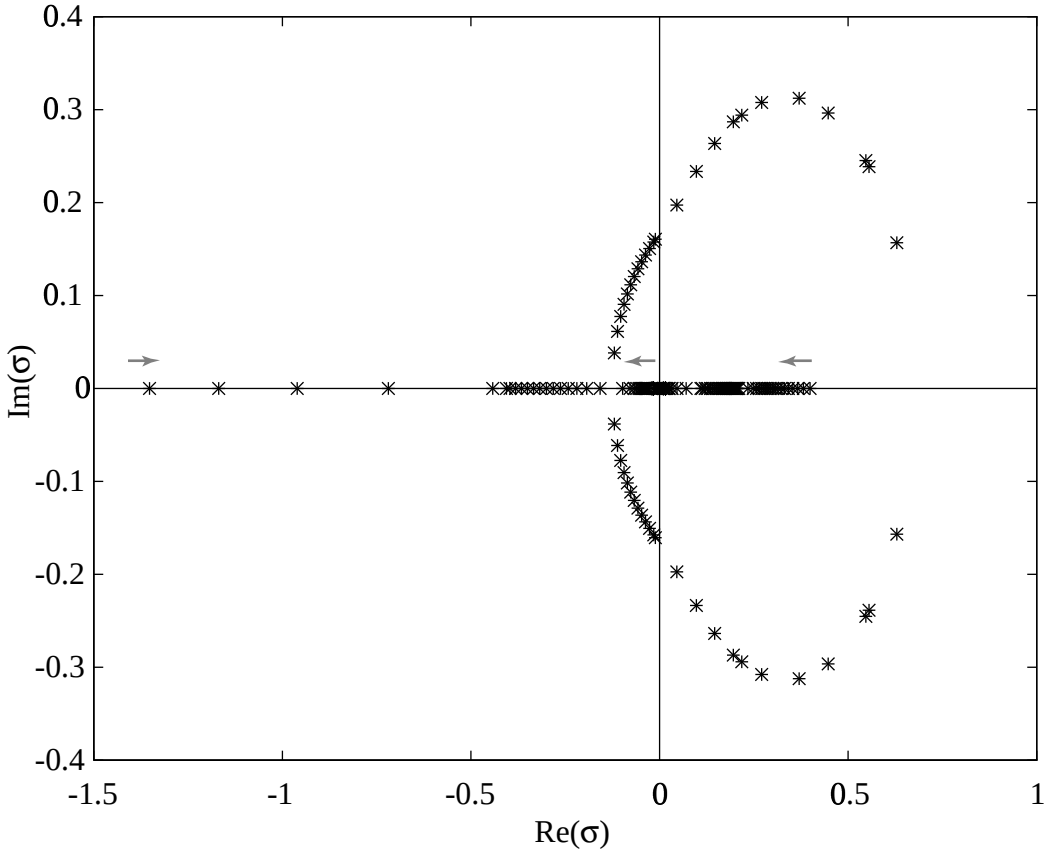

Figure 5.9: Root-locus of the three return map eigenvalues evaluated at periodic motions as the non-dimensional center of mass offset x is varied from -0.001 to 0.001 while the slope angle, leg inertia, and center of mass position along the leg are held constant at $\alpha = \frac{\pi}{350}$, $I = 0.0827$, and $z = 0.8780$. The small gray arrows indicate where the three eigenvalues start. The eigenvalue to the far right stays positive and real. The other two eigenvalues coalesce at $\sigma \approx -0.1$ and branch off into the complex plane. Periodic solutions for $x \geq 0.00105$ could not be found although an exhaustive search in smaller increments was not carried out.

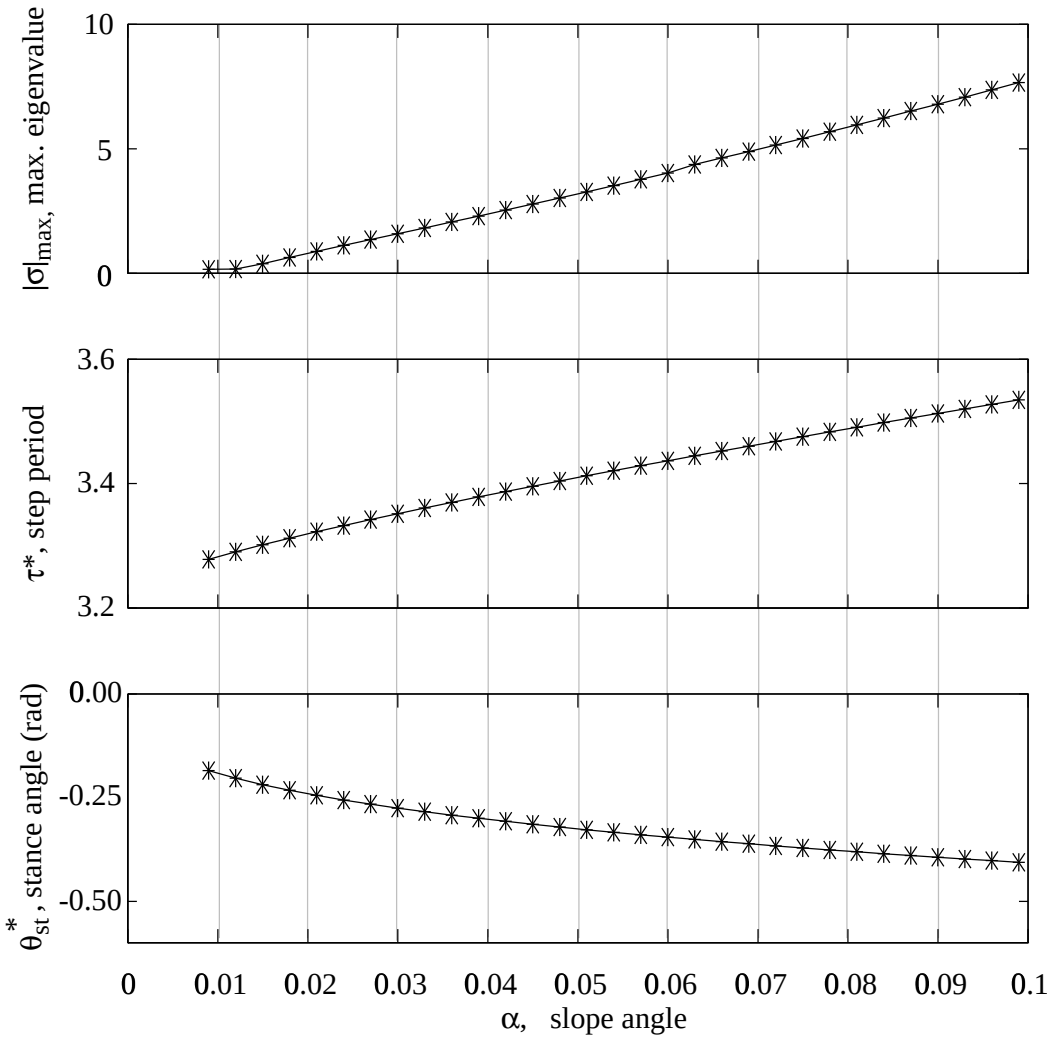

Figure 5.10: The variation of maximum eigenvalue, step period, and stance angle with slope angle α for steady gait while leg inertia center of mass position are held constant at $I = 0.0827$, $x = -0.001$, and $z = 0.8780$.

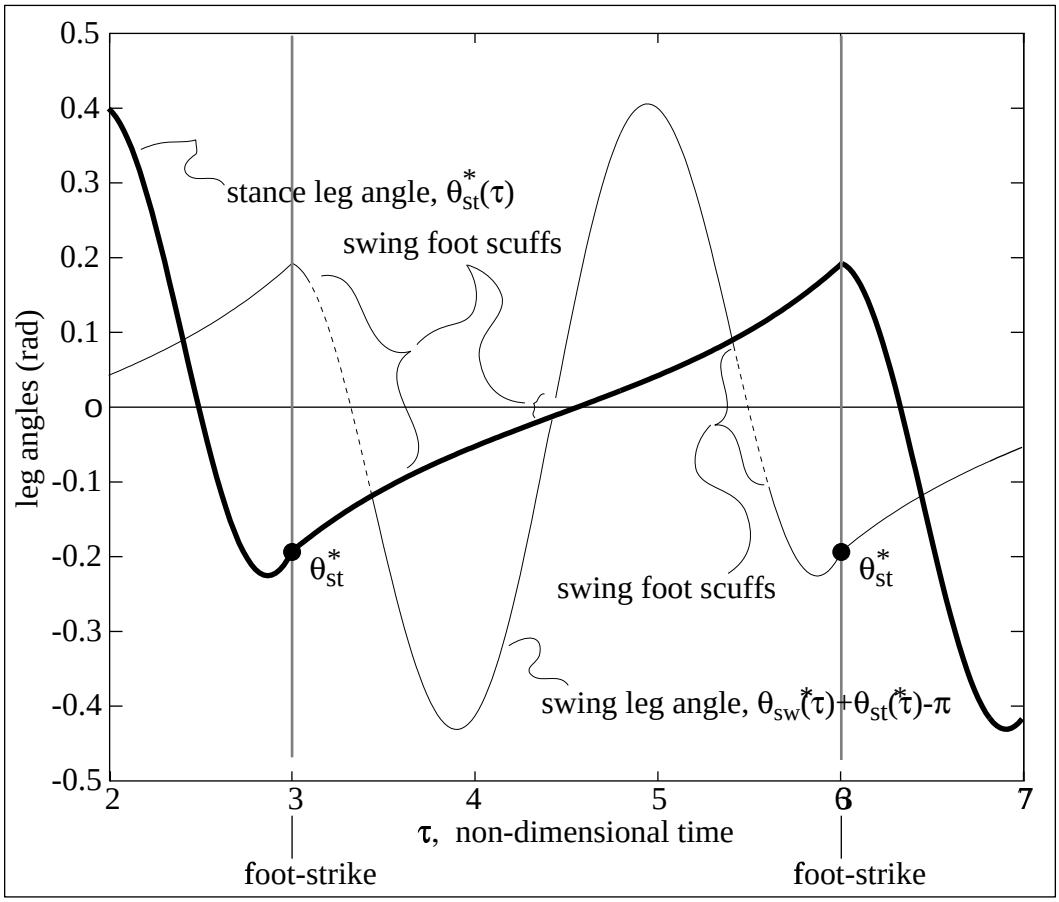

Figure 5.11: Point-foot leg angles for a double-swing gait mode over one step. for $\alpha = 0.0090$, $I = 0.0001922$, $x = 0.0000$, $z = 0.9980$. Again, the swing leg angle is more usefully plotted as measured from the vertical to the slope or $\theta^*_{sw}(\tau) + \theta^*_{st}(\tau) - \pi$. The stable fixed point for this case is $\mathbf{q}^* = \{-0.1924, 0.2043, 3.5264, -0.3061\}^T$; the maximum eigenvalue is $|\sigma_{max}| = 0.3503$; and the non-dimensional step period is $\tau^* = 4.0059$. The stance leg curve is denoted by the heavy line and the swing leg curve by the thin line corresponding to Figure 5.2. It is interesting to compare the double swing characteristics with those for the single swing with the same parameters: the stable fixed point for this case is $\mathbf{q}^* = \{-0.1255, 0.2615, 3.393, -0.1641\}^T$; the maximum eigenvalue is $|\sigma_{max}| = 0.8668$; and the non-dimensional step period is $\tau^* = 1.0271$. Surprisingly, the double-wing mode is more stable.

5.5 2D Special Case: The Simplest Walking Model

A simple case of the walking model above is one with point masses at the hip and foot, m_h and m_f, as shown in Figure 5.12. We assume that one-half of the hip mass is associated with one leg such

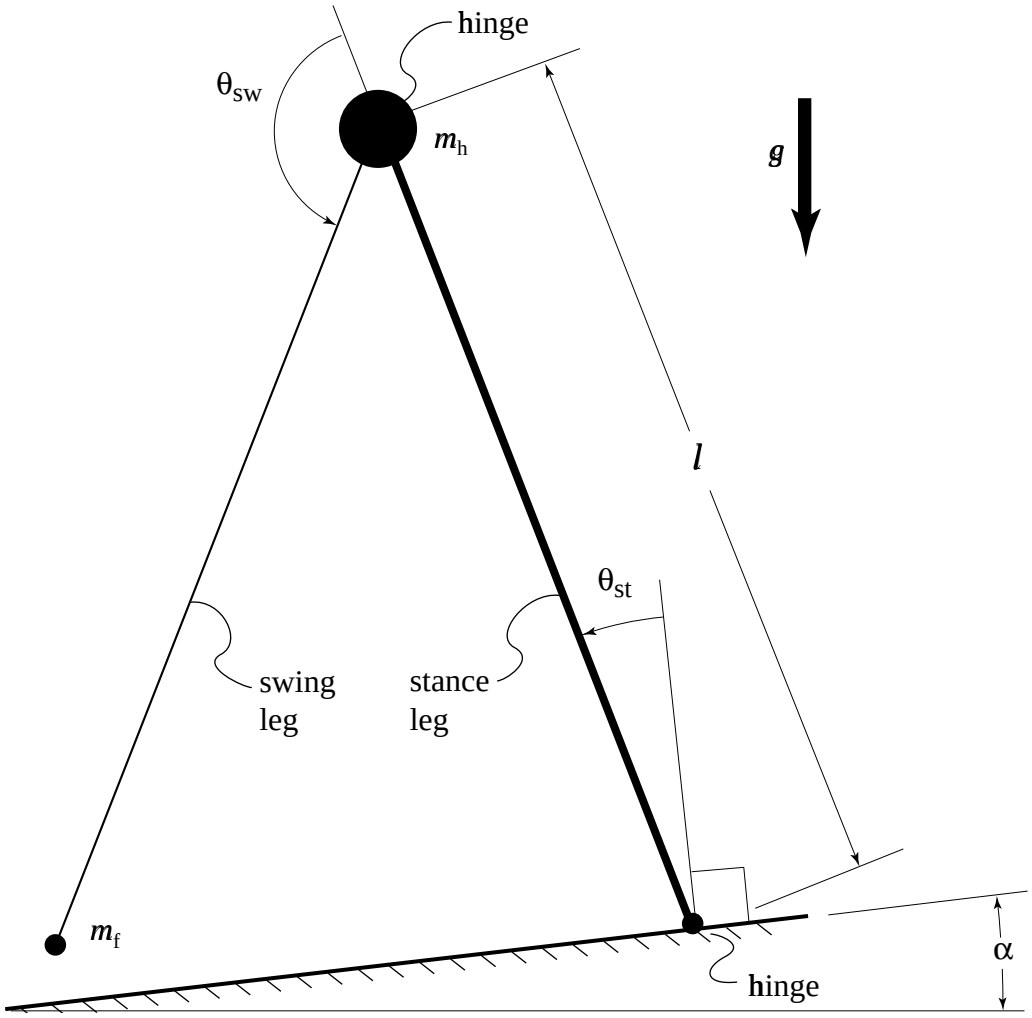

Figure 5.12: The simplest 2D point-foot walking model. Leg lines are drawn with different line weights to correspond to the plot of Figure 5.13.

that $M = m_f + \frac{1}{2}m_h$. In this case, the center of mass lies on the leg ($x = 0$) and $z = \frac{1}{1+\eta}$ where the mass ratio is $\eta = \frac{2m_f}{m_h}$. Each leg has non-dimensional moment of inertia $I = \frac{I_{cm}}{(m_f + \frac{1}{2}m_h)\ell^2} = \frac{1}{1+\eta}(1-z)^2 + \frac{\eta}{1+\eta}z^2 = \frac{\eta}{(1+\eta)^2}$. In particular, we study the simplest passive-dynamic walking model in which the hip mass is much greater than the foot mass ($m_h \gg m_f$), implying in the limit as the hip mass becomes infinitely large that $\eta \to 0$, $z \to 1$, and $I \to 0$. This model is studied in detail in Garcia, Chatterjee, Ruina, and Coleman [16]. The two coupled second-order differential equations of motion are given below for the swing phase of the motion for the simple model described

above.

$$\begin{bmatrix} 2\,(1+\eta(1+\cos\theta_{sw})) & \eta(1+\cos\theta_{sw}) \\ \eta(1+\cos\theta_{sw}) & \eta \end{bmatrix} \begin{Bmatrix} \ddot{\theta}_{st} \\ \ddot{\theta}_{sw} \end{Bmatrix}$$
$$+ \quad \eta\sin\theta_{sw} \begin{bmatrix} 0 & -1 & -2 \\ 1 & 0 & 0 \end{bmatrix} \begin{Bmatrix} \dot{\theta}_{st}^2 \\ \dot{\theta}_{sw}^2 \\ \dot{\theta}_{st}\dot{\theta}_{sw} \end{Bmatrix}$$
$$+ \quad \begin{bmatrix} -(2+\eta) & -\eta \\ 0 & -\eta \end{bmatrix} \begin{Bmatrix} \sin(\alpha+\theta_{st}) \\ \sin(\alpha+\theta_{st}+\theta_{sw}) \end{Bmatrix} = \begin{Bmatrix} 0 \\ 0 \end{Bmatrix} \tag{5.22}$$

Setting $\eta = 0$ (the limit as hip mass dominates foot mass) in the first equation of motion and dividing through by η in the second yields two simpler equations.

$$\ddot{\theta}_{st} - \sin(\alpha+\theta_{st}) = 0 \tag{5.23}$$
$$\ddot{\theta_{sw}} + \left(\dot{\theta}_{st}^2 - \cos(\alpha+\theta_{st})\right)\sin\theta_{sw} + \sin(\alpha+\theta_{st}) = 0. \tag{5.24}$$

The equations describe an inverted simple pendulum (the stance leg) whose motion is totally decoupled from the the motion of the swing leg. The swing leg, on the other hand, is a driven simple pendulum whose support motion at the hip is determined completely by the motion of the stance leg. Note that there is only one free parameter in Equations (5.23) and (5.24): the ramp slope α.

5.5.1 Collision Rule

The collision detection rule is unchanged. The collision rule for angular rates for the case of point foot and hip masses is

$$\begin{Bmatrix} \dot{\theta}_{st}^{+} \\ \dot{\theta}_{sw}^{+} \end{Bmatrix} = \mathbf{T} \begin{Bmatrix} \dot{\theta}_{st}^{-} \\ \dot{\theta}_{sw}^{-} \end{Bmatrix} \tag{5.25}$$

where the transition matrix $\mathbf{T}$ is

$$\mathbf{T} = \frac{1}{2+\eta\sin^2(2\theta_{st}^{-})} \begin{bmatrix} 2\cos(2\theta_{st}^{-}) & 0 \\ 2\cos(2\theta_{st}^{-})(\cos(2\theta_{st}^{-})-1) & 0. \end{bmatrix} \tag{5.26}$$

Setting $\eta = 0$ in Equation (5.26) yields the collision rule for angular rates

$$\begin{Bmatrix} \dot{\theta}_{st}^{+} \\ \dot{\theta}_{sw}^{+} \end{Bmatrix} = \begin{bmatrix} \cos(2\theta_{st}^{-}) & 0 \\ \cos(2\theta_{st}^{-})\left(\cos(2\theta_{st}^{-})-1\right) & 0 \end{bmatrix} \begin{Bmatrix} \dot{\theta}_{st}^{-} \\ \dot{\theta}_{sw}^{-} \end{Bmatrix}. \tag{5.27}$$

5.5.2 Numerical Simulations

A typical plot of θ_{st} and θ_{sw} over one step is shown in Figure 5.13 for $\alpha = 0.009$.

Dependence of Fixed Points and Stability on Slope Angle α

An in-depth stability analysis and of the simplest walking model can be found in Garcia, *et. al.* [16]; they show the existence of 2-cycle (or 'limping' gaits) and 4-cycle gaits and higher ('staggering gaits').

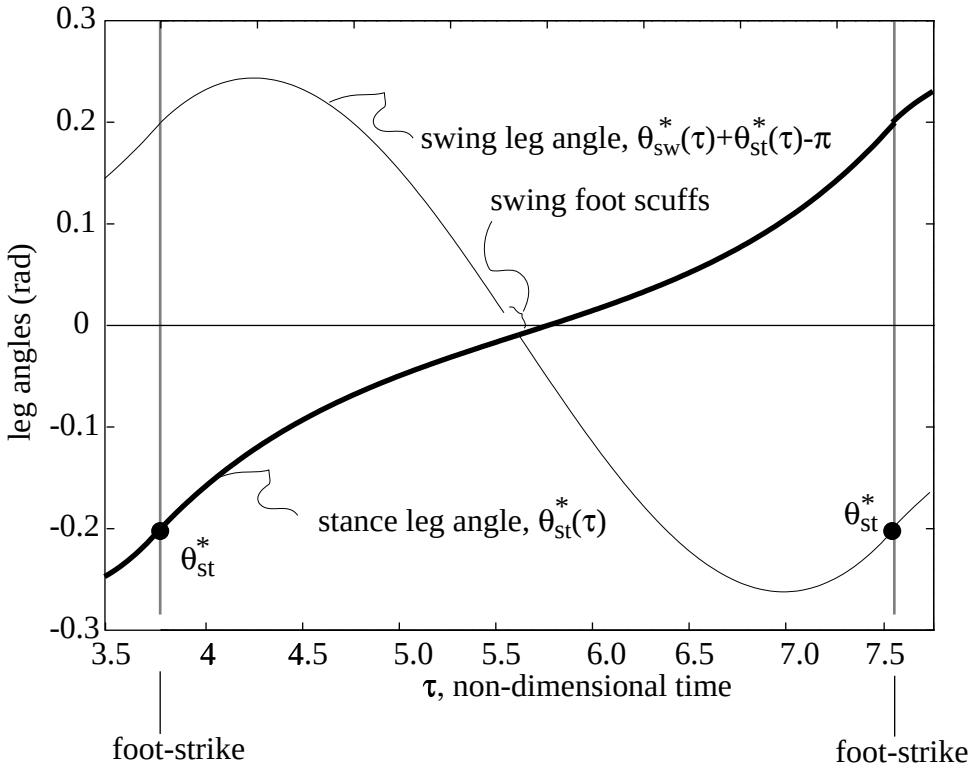

Figure 5.13: The simplest 2D point-foot walker leg angles over one step at a gait cycle for $\alpha = 0.009$ radians. The swing leg angle is more usefully plotted as measured from the vertical to the slope or $\theta^*_{sw}(\tau) + \theta^*_{st}(\tau) - \pi$. The fixed point for this case is $\mathbf{q}^* = \{-0.1999, 0.2002, 3.5414, -0.0158\}^T$; the maximum eigenvalue is $|\sigma_{max}| = 0.5182$ and the non-dimensional step period is $\tau^* = 3.7987$. The line weights correspond to those of Figure 5.12. The asterisks in the superscripts indicate fixed points and their corresponding leg angle trajectories.

5.6 Conclusions

For the two-dimensional four-parameter straight-legged point-footed walking model, we have found stable walking for a variety of parameters. Parameter studies turned up that a small polar moment of inertia I and high center of mass location z for the legs are good for stability but that fore/aft displacement of the center of mass is destabilizing. But, will the same be true for 3D versions of this model?

We also discovered an elegant one-parameter simplification of our model that has a huge hip mass and tiny point feet that has stable motions. Extensive investigations of this model can be found in Garcia, *et. al.* [16].

Finally, the 2D studies have provided a good starting point for our investigations into 3D passive-dynamic walking. We will first use the 2D numerical routines two search for 2D fixed points that will then serve as the initial guesses for the 3D fixed point searches, the subject of the next and final chapter.

Chapter 6

'Step Five': Three-dimensional Straight-legged Point-foot Walker

That's one small step for man . . . one giant leap for mankind.
Neil Armstrong *first step on moon, 10:56:15 p.m. EDT, July 20, 1969*

6.1 Introduction

We begin this final chapter with a review of McGeer's [4] 3D passive-dynamic walking model and his numerical results; unless noted otherwise, all of the references to McGeer in this section refer to this citation.

We then describe our 3D model and present the results. Almost by accident, we built a simple two-leg toy that can walk stably in 3D with no control system (see Coleman and Ruina [14] and [15]). It walks downhill powered only by gravity. It seems be the first McGeer-like passive-dynamic walker that is statically unstable in all standing positions, yet is stable in motion. It is one of few known mechanical devices that are stable near a statically unstable configuration but do not depend on spinning parts. Its design is loosely based on our 3D model simulations which do not predict its observed stability. We describe it later in this chapter.

6.1.1 McGeer's 3D Passive-Dynamic Biped Model

To evolve his understanding and models into the three-dimensional world,
McGeer [4] first pondered the idea of a *planar* biped free to move in three dimensions. Planar means that the biped would have no lateral thickness (no out-of-plane mass distribution). It would have two straight legs connected by a hinge whose axis of rotation is parallel to the plane of the biped. The biped can thus swing its legs past each other in the plane of the hinge. The biped's steady two-dimensional motions are also steady three-dimensional motions. The question arises as for the planar rimless wheel, however, whether *stable* steady gait in 2D is stable in 3D or can be stabilized if it is not. That is, can the biped demonstrate lateral stability since, when standing still or walking slowly, it acts essentially as an inverted pendulum? McGeer [4] noted that, for a given mass distribution, thin (planar) rolling disks owe their lateral stability entirely to spin (about the axis through the center of mass and normal to the disk); thus, he reasoned that, since a planar biped does not have the necessary store of angular momentum due to the counter-oscillation of its legs, it would be probably not be laterally stable. Like the side-ways inverted pendulum instability of the biped in three-dimensions, the biped confined to two dimensions also exhibits inverted pendulum behavior in the plane of progression (saggital plane) but it manages to stabilize itself through the

periodic exchange of support between its legs and repeated collisions. Based on this observation of stable 2D walking, McGeer envisioned lateral leg spacing (or hip width) to enable sideways falling-and-catching, or 'waddling', as a possible lateral stability mechanism for the 3D biped.

A schematic shows the configuration variables and parameters in Figure 6.1 of McGeer's 3D biped model with hip spacing. The model has nine parameters (center of mass position (3), principal radii

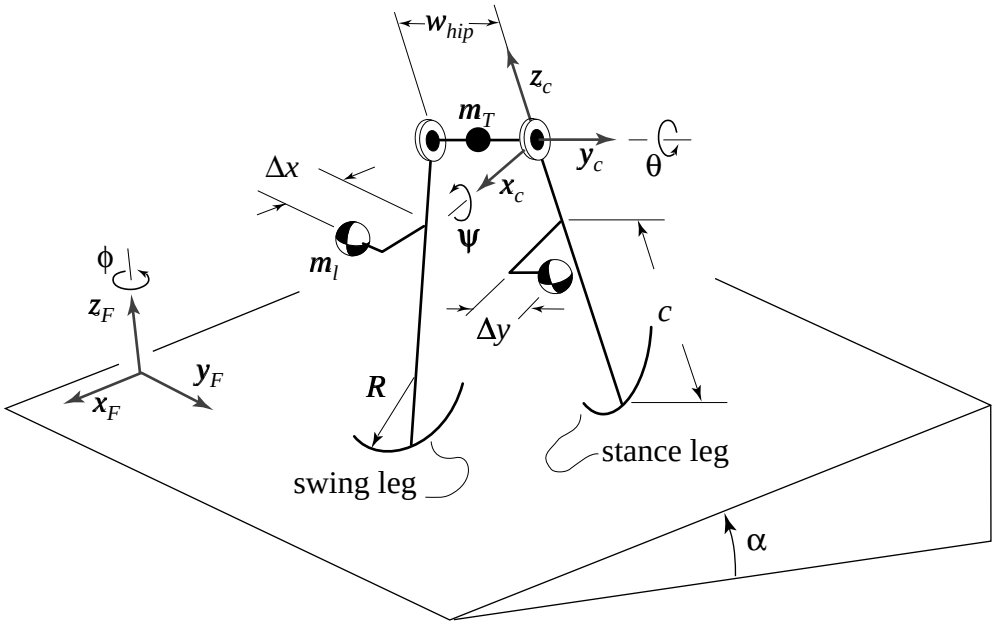

Figure 6.1: McGeer's 3D passive-dynamic walking model: parameters and configuration variables. Like McGeer's[4] 2D straight-legged model, it has two identical straight legs and semi-circular feet. Orientation of the stance leg relative to the ground frame is determined by the heading(ϕ), bank(ψ), and pitch(θ) sequence of rotations about the axes indicated. The swing and stance legs have the same heading and roll angles, but can pitch independently. The leg mass is m_l and has location Δx, Δy, and c (with respect to the stance leg frame) and the leg coordinates are aligned with its principal moments of inertia. The radii of gyration are r_{gyr_x}, r_{gyr_y}, and r_{gyr_z}. The hip has only a point mass, m_T. The radius of curvature of the feet is R.

of gyration (3), foot radius, hip mass, and leg mass) and eight state variables (heading (ϕ), bank (ψ), stance pitch(θ_{st}), swing pitch (θ_{sw}) and their rates). The leg coordinates shown in Figure 6.1 are aligned with its principal moments of inertia.

Stride Function, Periodic Gaits, and Stability

Using the fully non-linear dynamics, McGeer [4] composed the stride function from equations of motion generated using the *Autolev* program and from collision conditions derived by hand. He then encoded it in FORTRAN and wrapped it in a multi-dimensional Newton's method fixed point search procedure.

To find fixed points of with McGeer's 3D model over one step, the search algorithm must look for initial conditions which do not repeat after each foot collision but instead produce a mirror image. Heading and bank in fixed point motions must switch sign from collision to collision. Likewise, the algorithm could search for fixed points over two collisions which repeat but with a proper exchange

of leg parameters after the first collision.

McGeer's search procedure found unstable periodic motions with both long and short step periods. Figure 6.2 shows plots of the stance and swing leg pitch angles, heading and bank angles, the foot paths viewed from above, and the swing foot height above the ground for a typical steady motion. The longitudinal motion of the 3D periodic gait is qualitatively the same as for the 2D case.

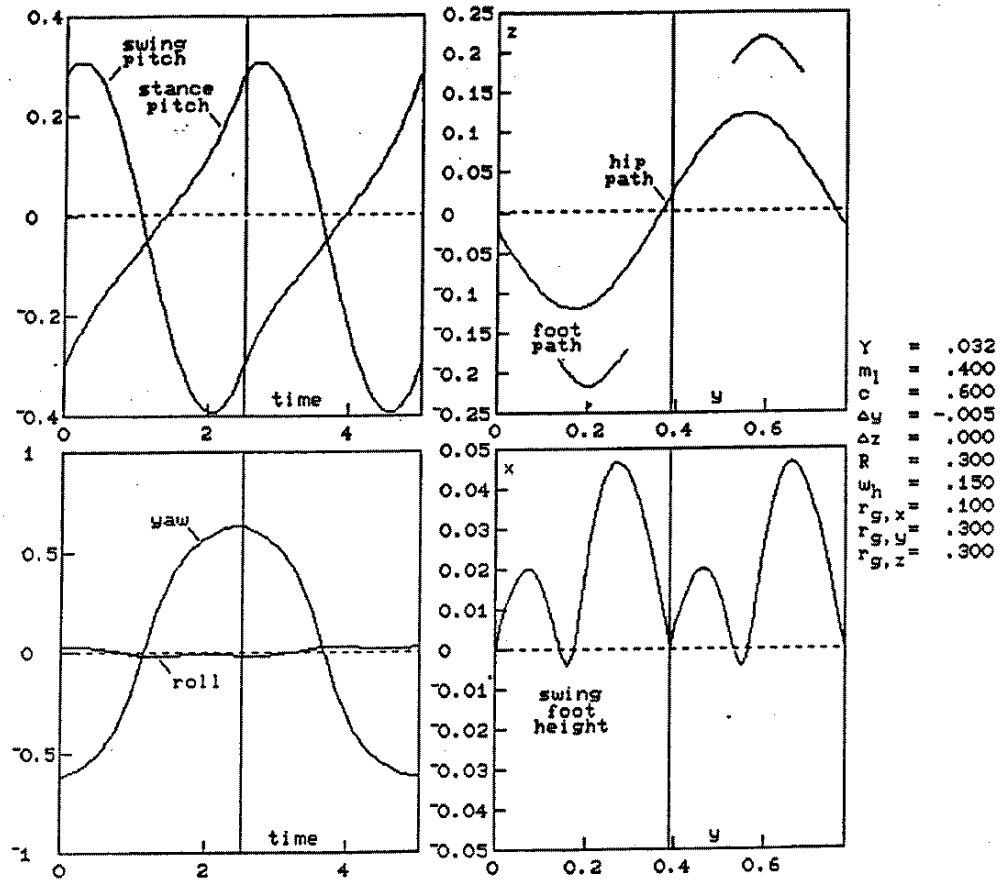

Figure 6.2: Three-dimensional passive cycle, as calculated for a straight-legged biped having legs separated by 15% of leg length. The slope is 3.2%. (Reprinted with permission from McGeer [4])

Figure 6.3 shows the variation of step periods, equilibrium slopes, and the modulus of dominant eigenvalues with hip width for fixed hip-to-leg mass ratio, foot radius, leg center-of-mass position, and principal radii of gyration. Note the existence in the plots of long and short period solutions.

Stability and Parameter Variation

As with McGeer's 2D models, McGeer [4] found fore/aft offset in the leg's center of mass a powerful parameter for modulating gait; putting it slightly aft of the leg axis permitted gaits with substantially wider hips than if the offset were zero.

As noted before, the *static* planar biped has a strong inverted pendulum instability. One would hope that the moving biped could be at least more stable than simply falling over sideways. In other words, if you perturb a steady gait cycle laterally and do the same to the standing biped, in which

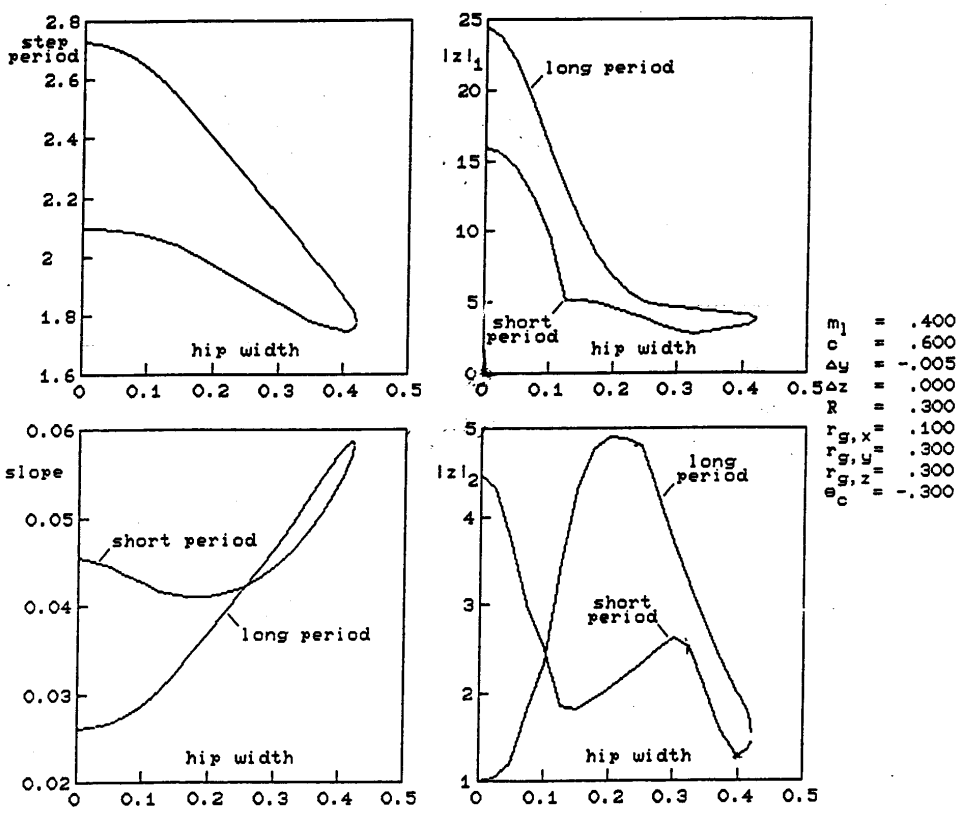

Figure 6.3: Step periods, equilibrium slopes, and dominant eigenvalues calculated for 3D passive bipeds walking with a stride of about 0.6 leg length (initial $\theta_C = -0.3$). $|z_1|$ and $|z_2|$ are the dominant eigenvalues. Results for both short- and long-period cycles are plotted against hip width. (Reprinted with permission from McGeer [4])

case would the biped fall over less during one gait period? McGeer [4] investigated the pendulum instability of the biped model as follows. Neglecting the coupling of the lateral to longitudinal motion, the equation of motion governing perturbations $\hat{\psi}$ in bank angle for small motions is (normalized by $\sqrt{g/\ell}$)

$$\ddot{\hat{\psi}} - p^2\hat{\psi} \approx 0 \tag{6.1}$$

where p is the inverted pendulum frequency given by

$$p = \sqrt{\frac{2m_{leg}c + m_T}{2m_{leg}(c^2 + r_{gyr_y}^2) + m_T}}. \tag{6.2}$$

Given a small initial lateral disturbance, the dominant term in the banking solution is

$$\hat{\psi} \simeq \hat{\psi}_0 e^{p\tau}. \tag{6.3}$$

Similarly, for the full model, the map governing the evolution of a perturbation in the bank eigendirection over one gait period is given by

$$\hat{\psi} \simeq \hat{\psi}_0 \sigma \tag{6.4}$$

where σ is the eigenvalue, whose corresponding eigenvector corresponds to perturbation in the bank angle, of the Jacobian evaluated at a fixed point. Thus, comparing the lateral instability of the biped in a steady gait to its inverted pendulum instability can be made by comparing σ to $e^{p\tau_0}$ where τ_0 is the gait period.

In the example reprinted from McGeer [4] in Figure 6.3, the inverted pendulum frequency is $p = 1.10$ and $e^{p\tau_0} = 9.96$ for the short-period gait and $e^{p\tau_0} = 20.1$ for long period gait. From Figure 6.3, the corresponding return map eigenvalues are $\sigma = 16$ and $\sigma = 24$, respectively. This data is summarized in Table 6.1. So, looking at the ratios in the third column of Table 6.1, we

Table 6.1: Comparison between falling-over-sideways eigenvalues for the McGeer 3D walker (1) standing still and (2) in a gait cycle. The data comes from Figure 6.3.

	Lateral Stability Eigenvalues		
	Standing	Walking	Ratio
	$e^{p\tau_0}$	σ	$\sigma/e^{p\tau_0}$
short period gait	9.96	16	1.61
long period gait	20.1	24	1.19

see that walking makes it harder to stay upright than just standing still; i.e., for the configuration examined, a sideways perturbation to the McGeer 3D walker while walking unstably grows more over a gait period than the same disturbance applied to the walker over the same period while standing still unstably in a vertical position. Specifically, for the short period gait, a lateral perturbation applied at the beginning of a step grows approximately 1.61 times as much as the same disturbance applied to the walker standing still grows over the step period.

In the best case, obtained again from the example reprinted from Mceer's [4] plots reprinted in Figure 6.3, for long period gait at $w_{hip} \approx 0.42$, $e^{p\tau_0} = 6.8$ and $\sigma \approx 5$; and for short period gait at $w_{hip} \approx 0.32$, $e^{p\tau_0} = 7.65$ and $\sigma \approx 3$. So, though in best case reported here (the short period gait above) the walker is unstable, it still beats falling over sideways from a standstill, if only by a little ($\sigma/e^{p\tau_0} = 0.39$)! Further searches through parameter space failed to yield much improvement in stability.

McGeer's Observations

McGeer observes that the bank to heading amplitude ratio is very small, the heading motions much to large by human standards. McGeer suggested the following change in the model construction to reduce large changes in heading. Based on human construction, replace the hinges at the hips with roll joints to add a rolling degree of freedom which can be used to reduce lateral leg separation and thus eliminate most of the rolling torque; to keep the model from collapsing as soon as the swing leg is unsupported, stiff torsional springs would have to be added at the roll joint.

McGeer had no further suggestions for passive 3D gait stabilization. He proposed actively stabilizing the model with roll joints at the hips by varying the equilibrium positions of the roll springs and suggested a control law algorithm to do so. As far as this author knows, McGeer did not pursue this work further.

6.1.2 Our 3D Passive Dynamic Gait Model

With the proper combination of gyroscopic coupling, due to mass distribution or mechanical devices, and the dissipative foot collisions, alternative methods to hip spacing might exist to stabilize the planar 3D biped in ways that bicycles, skate-boards, skates, and other are self-stabilizing, both with and without dissipation. For instance, a 3D planar biped might be stabilized in the way that the 3D rimless wheel and the 3D rolling disk are more stable than a uniform rolling disk, due to dissipative spoke collisions and asymmetric mass distribution, respectively, and in both cases due perhaps, in some way, to the the nonholonomic motion constraints.

So, we study a planar 3D model with two straight legs, point feet (ball joint contact with the ground between collisions), and a hinge joint at the hip. We lose complexity in the foot design but gain greater flexibility by allowing non-axisymmetric leg mass distributions. In simplifying the model by making point foot contact and removing the hip axle, we have hoped that more basic and more deeply insightful mechanics interpretations of 3D motions and mechanisms for stability (or instability) would be more readily available to us. The 3D straight-legged point-foot walking model is shown in Figure 6.4 below to remind the reader of where it fits into the evolution of models in the research program.

To date, we have not found stable 3D passive gaits. We have only slightly improved upon McGeer's stability results and discovered an illustrative limiting case: a 'tight-rope walking' 3D model that is neutrally stable in the limit as the length of the 'balance bar' goes to infinity. Like the 3D rimless wheel, there exists a one parameter family of fixed points, where we think of the heading as the parameter.

6.2 Description of System

The 3D point-foot model is shown in Figure 6.5 and Figure 6.6. It has two symmetric rigid legs of length ℓ, mass M, symmetrically located center of mass locations ((X_{cm}, Y_{cm}, Z_{cm}) in stance leg frame coordinates), and mirror-symmetry related moments of inertia with respect to the center of mass $\mathbf{I}^{cm}$. A frictionless hinge at the hip connects the legs and has orientation $\hat{\mathbf{n}}$ normal to the symmetry plane of the legs. Each of the two legs can make point contact with the ground (slope $= \alpha$) with no contact couples. The gravitational acceleration is $\mathbf{g}$.

As we assumed for a rimless wheel spoke, when a foot hits the ground (ramp surface) at *heel-strike*, it has a plastic (no-slip, no bounce) collision and its velocity jumps to zero. The foot remains on the ground, acting like a ball-and-socket joint, until the swinging foot reaches heel-strike. During walking, only one foot is in contact with the ground at any time; double support occurs instantaneously.

Between collisions, the model's motion is governed by the classical laws of rigid-body mechanics. As with the 2D walker, we make the non-physical assumption the swing foot can briefly pass through

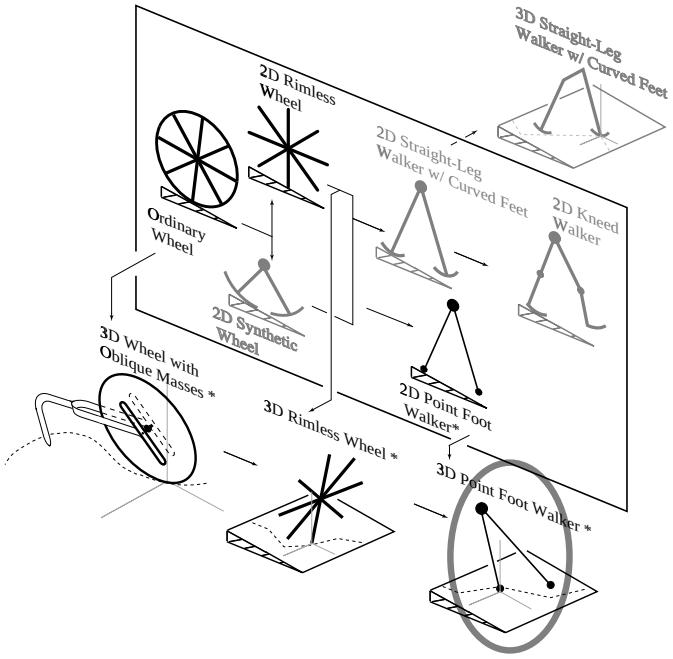

Figure 6.4: The place of the 3D straight-legged point-foot walking model in the passive-dynamic family tree.

the ramp surface when the stance leg is near vertical.

6.2.1 Configuration, State Space, and Nonholonomic Constraints

We characterize the configuration of the stance leg between collisions using 3-1-2 Euler angles as shown in Figure 6.21, the same angles we used to describe the orientation of the 3D rimless wheel in Chapter 4. The heading angle is the rotation ϕ about the original z axis, the bank angle is the rotation ψ about the new x axis, and the stance-leg pitch angle is the rotation θ_{st} about the newest y axis. The Euler angles are described in detail in Appendix D. The stance leg angle θ_{st} is the angle of the stance leg with respect to the normal to the slope. Due to the hinge at the hip, the swing leg has the same heading and bank as the stance leg — it can only change its pitch relative to the stance leg. The the swing leg angle θ_{sw} is the pitch angle of the swing leg with measured with respect to the stance leg. The absolute position of the walker on the plane does not enter into the governing equations.

Between collisions, the (reduced) state space is eight dimensional and $\mathbf{q}$, the state vector, is

$$\mathbf{q} = \{\phi, \psi, \theta_{st}, \theta_{sw}, \dot{\phi}, \dot{\psi}, \dot{\theta}_{st}, \dot{\theta}_{sw}\}^T. \tag{6.5}$$

The unreduced accessible configuration space is six-dimensional (the above Euler angles plus position on the slope) whereas at any instant in time the accessible velocity space is four-dimensional (the four dynamical state variables). Hence the overall nonholonomicity ($6 > 4$) of this system which is smooth and holonomic between instants of collision.

6.2.2 Indexing Scheme

We have chosen a set of angles to describe the orientation of the walking device between collisions. We next present an indexing scheme to denote the state of the system just before and after the

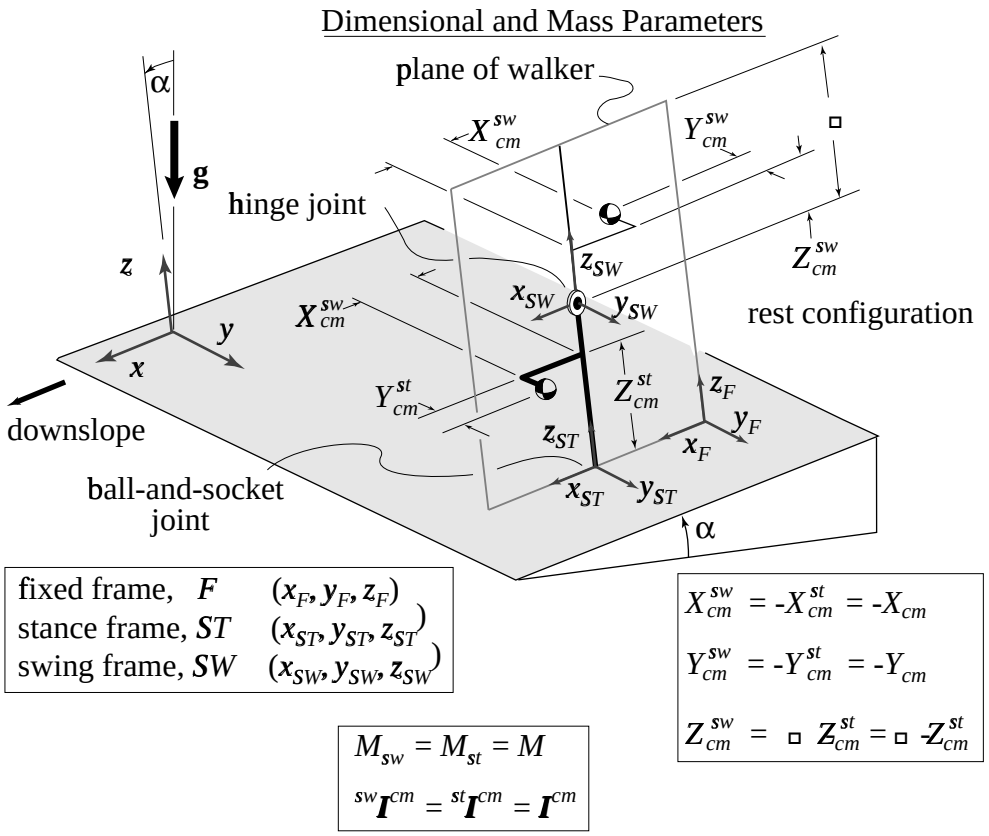

Figure 6.5: The 3D point-foot walking model parameters. The leg mass is designated by M, the moment of inertia with respect to the center of mass by $\mathbf{I}^{cm}$, the leg length by ℓ, the ramp angle with respect to the horizontal by α, and the acceleration due to gravity by g.

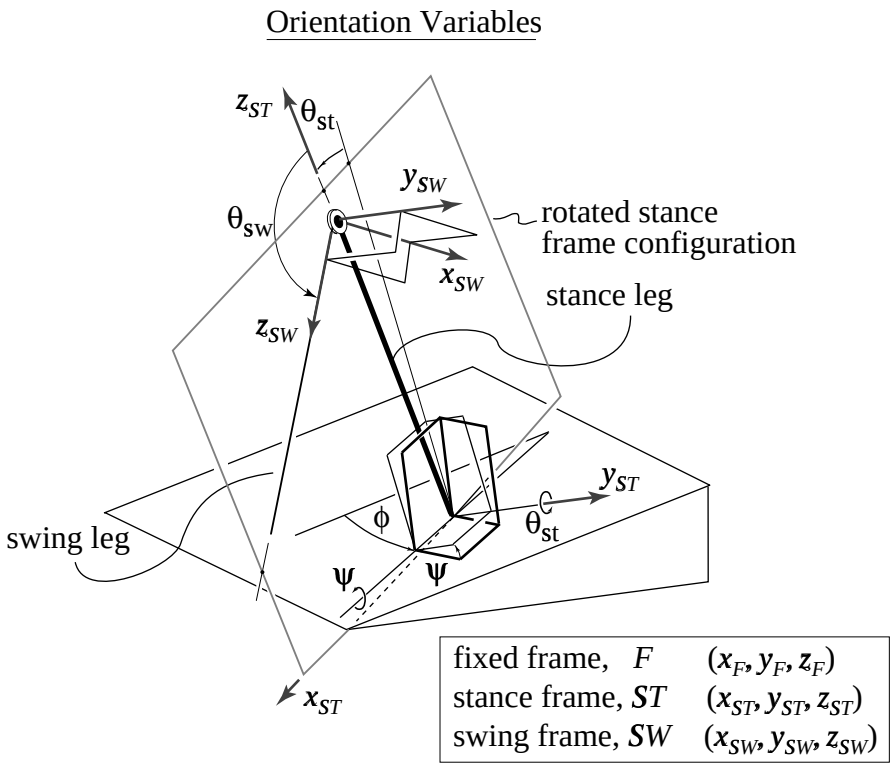

Figure 6.6: The 3D point-foot walking model configuration variables. The heading angle is the rotation ϕ about the original z axis, the bank angle is the rotation ψ about the new x axis, and the stance-leg pitch angle is the rotation θ_{st} about the newest y axis. The stance leg angle θ_{st} is the angle of the stance leg with respect to the normal to the slope. The the swing leg angle θ_{sw} is the pitch angle of the swing leg measured with respect to the stance leg.

collision i of the i_{th} swing leg. We use the indexing scheme to define a 'cycle' of the walker — from just after a swing leg collision (heel-strike) to just after the next. The indexing scheme presented here is identical to the one presented for the 2D walker but is repeated here for clarity.

The i_{th} stance and swing legs are so designated after the i_{th} collision. Thus, the names of the legs are exchanged through a collision. That is, the i_{th} stance leg becomes the $i+1_{th}$ swing leg and vice-versa for the i_{th} swing leg.

Special times of interest are just before and just after collision i. The minus and plus signs $(-)$ and $(+)$ are used as the superscripts to denote these times. For instance, ${}^{i}\theta_{st}^{+}$ is the stance leg angle just after collision i of swing leg $i-1$.

In defining the orientation of the walking device, we have defined fixed frame $\mathcal{F}$, stance leg frame $\mathcal{ST}$ (fixed to the stance leg), and swing leg frame $\mathcal{SW}$ (fixed to the swing leg). The stance leg frame ${}^{i}\mathcal{ST}$ has origin at the tip of the stance leg currently in contact with the ground after collision i. The swing leg frame ${}^{i}\mathcal{SW}$ has origin at the hip joint. The z_{st} and z_{sw} axes are aligned with the stance and swing legs, respectively.

We move the origin of the stance leg frame instantaneously with each swing leg collision from the tip of the pre-collision stance leg to the tip of the post-collision stance leg currently in contact with the ground after collision $i+1$. The origin of the swing leg frame remains at the hip joint.

As the origin of stance leg frame i is moved to the tip of the colliding leg, however, we not only translate the stance leg frame but also rotate it by $-2\ {}^{i+1}\theta_{st}^{-}$ about the y-axis with respect to the fixed frame so that the z_{st}-axis of stance leg frame $i+1$ is aligned with stance leg $i+1$. Thus, the stance leg angle changes instantaneously from θ_{st} to $-\theta_{st}$ through a downhill swing leg collision. Likewise, the swing leg frame rotates by $-2\ {}^{i+1}\theta_{sw}^{-}$ about the y axis with respect to the stance leg frame so that the z_{sw}-axis of the swing leg frame $i+1$ is aligned with swing leg $i+1$.

After a collision, then, we redefine the absolute orientation with respect to the fixed frame using the newly positioned frames. The relationships between frames and their associated bases from before to after collision $i+1$ are

$$
\begin{aligned}
{}^{i+1}\mathcal{ST} &\neq {}^{i}\mathcal{ST},\ {}^{i+1}\mathbf{e}_{st} = \mathbf{R}_2(\theta = -2\ {}^{i+1}\theta_{st}^{-})\ {}^{i}\mathbf{e}_{st}, && (6.6)\\
{}^{i+1}\mathcal{SW} &\neq {}^{i}\mathcal{SW},\ {}^{i+1}\mathbf{e}_{sw} = \mathbf{R}_2(\theta = -2\ {}^{i+1}\theta_{sw}^{-})\ {}^{i}\mathbf{e}_{sw}. && (6.7)
\end{aligned}
$$

At at a swing foot collision, in addition to updating the state of the system, we must also be careful to update the leg parameters to take into account the reflection symmetry of the legs. When the swing leg collides with the ground and becomes the new stance leg, its y center of mass position is different from that of the previous stance leg:

$$
y \mapsto -y \text{ or } {}^{i}y^{+} = -\,{}^{i}y-. \tag{6.8}
$$

Recall that, in between collisions, the inertia matrices for the stance and swing legs are the same. In between collisions, the x and y coordinates of the center of mass of each leg are opposite in sign but only the y coordinate for each changes sign through a collision.

6.2.3 Cycle of Motions

A 'cycle' of the walking device is the motion from one swing foot collision through the next. A schematic of one cycle, for downhill walking, is shown in Figure 6.7. As before with the 2D and 3D rimless wheels and the 2D walker, we pick as the starting point the instant when the trailing stance leg i leaves the ground *and* and the leading swing leg i simultaneously collides with the ground. The walking device rotates over the stance leg i , as an inverted double pendulum with initial state ${}^{i}\mathbf{q}^{+}$. The non-collisional portion of the stride ends just before swing leg i strikes the ground at collision $i+1$ instantaneously transferring support from the trailing stance leg to the leading swing leg. The state of the walker is now ${}^{i+1}\mathbf{q}^{-}$. After impact, the walking device is now poised for the next start-of-cycle at state ${}^{i+1}\mathbf{q}^{+}$.

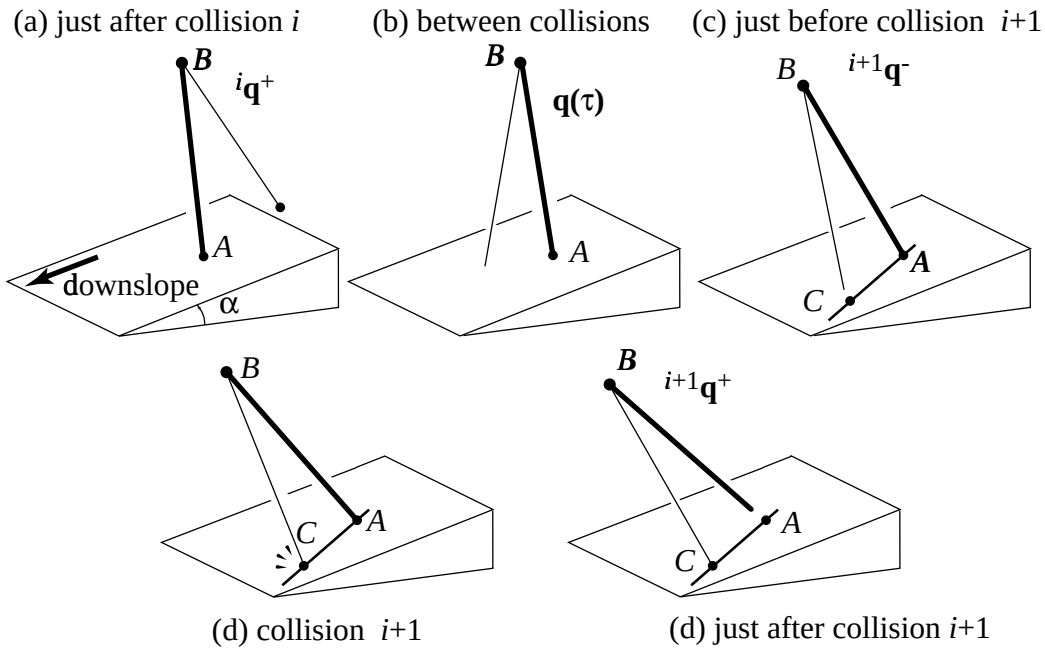

Figure 6.7: Schematic showing: (a) the state of the walking device over one stride just after collision i of swing leg i with point A, (b) the state of the walking device just before collision $i+1$ of swing leg foot i at point B, (c)collision $i+1$ of swing foot i at point B, and (d) the state of the walking device just after collision $i+1$ of swing leg foot i at point B. The stance leg is denoted by the heavy line and the swing leg by the thin line.

6.3 Governing Equations

Now that we have defined a cycle of motion, we can derive the equations that describe the motion between collisions and the collision transition rule. We present the details of the methodology to derive the governing equations in Appendix B.

6.3.1 Equations of Motion between Collisions (During the Swing Phase)

The four coupled second-order differential equations of motion are given below for the swing phase of the motion, where θ_{st} and θ_{sw} are functions of time non-dimensional time $\tau = t\sqrt{g/\ell}$. These equations are derived exactly as for the 2D version of this 3D model by taking angular momentum balance for (1) the whole mechanism about the contact point of the stance leg with the ground and for (2) the swing leg about the hip joint hinge axis.

$$\mathbf{M}(\mathbf{q}) \begin{Bmatrix} \ddot{\phi} \\ \ddot{\psi} \\ \ddot{\theta}_{st} \\ \ddot{\theta}_{sw} \end{Bmatrix} + \mathbf{V}(\mathbf{q}) \begin{Bmatrix} \dot{\phi}^2 \\ \dot{\psi}^2 \\ \dot{\theta}_{st}^2 \\ \dot{\theta}_{sw}^2 \\ \dot{\phi}\dot{\psi} \\ \dot{\phi}\dot{\theta}_{st} \\ \dot{\phi}\dot{\theta}_{sw} \\ \dot{\psi}\dot{\theta}_{st} \\ \dot{\psi}\dot{\theta}_{sw} \\ \dot{\theta}_{st}\dot{\theta}_{sw} \end{Bmatrix} + \mathbf{G}(\mathbf{q}) = \begin{Bmatrix} 0 \\ 0 \\ 0 \\ 0 \end{Bmatrix} \tag{6.9}$$

For brevity, we do not include the full equations here since they are too long and would not add to the clarity of the text. We do, however, include in Appendix B the Maple® code used to derive the governing equations. The moment of inertia, and coordinates of the center of mass are non-dimensionalized as follows: $\mathbf{I} = \dfrac{\mathbf{Icm}}{M\ell^2}$ and $(x, y, z) = \left(\dfrac{X_{cm}}{\ell}, \dfrac{Y_{cm}}{\ell}, \dfrac{Z_{cm}}{\ell}\right)$

6.3.2 Collision Transition Conditions

Collision Detection Rule

The collision occurs when the geometric collision condition

$$\mathbf{r}_{C/A} \cdot \hat{\mathbf{k}}_f = \cos(\theta_{st} + \theta_{sw}) + \cos(\theta_{st}) = 0. \tag{6.10}$$

is met. Equation (6.10) describes the values of θ_{sw} and θ_{st} for which the swing leg foot is coincident with the ramp surface. Solving Equation (6.10) for θ_{st} and θ_{sw}, we get an equivalent geometric collision condition

$$\pi - (\theta_{sw} + 2\theta_{st}) = 0. \tag{6.11}$$

which is easily seen from the collision configuration.

We also impose the additional condition that the stance leg be sufficiently past vertical (Equation (6.10) is also true at least once when the legs are nearly parallel, but we ignore scuffing).

Collision Rule for Configuration Variables

At the instant of swing foot collision, the pre-collision stance leg switches to the post-collision swing leg and vice-versa. The heading and bank angles remain the same through collision. So, the stance

and swing angle are reset at each swing foot collision as support is transferred from the stance foot to the swing foot according to the following mapping:

$$\left\{ \begin{array}{c} \theta_{st} \\ \theta_{sw} \end{array} \right\} \mapsto \left\{ \begin{array}{c} -\theta_{st} \\ -\theta_{sw} \end{array} \right\} \tag{6.12}$$

Thus, we can write

$$\left\{ \begin{array}{c} \phi^+ \\ \psi^+ \\ \theta_{st}^+ \\ \theta_{sw}^+ \end{array} \right\} = \mathbf{S} \left\{ \begin{array}{c} \phi^- \\ \psi^- \\ \theta_{st}^- \\ \theta_{sw}^- \end{array} \right\}, \text{ where } \mathbf{S} = \left[\begin{array}{cccc} 1 & 0 & 0 & 0 \\ 0 & 1 & 0 & 0 \\ 0 & 0 & -1 & 0 \\ 0 & 0 & 0 & -1 \end{array} \right]. \tag{6.13}$$

Collision Rule for Angular Rates

The swing foot contact point receives an impulse at foot-strike (point C). Due to the swing foot collision, an impulse is also transmitted to the swing leg at the hip joint (point B). We assume that, during collision, other smaller forces (e.g., gravity) acting on the system are negligible in comparison to the collision impulses. We also assume there are no impulsive ground contact torques. At the instant of collision at the hip, we assume that the former stance leg loses contact with the ground (at the same instant the swing foot makes contact) and that it has no impulsive reaction with the ground as it leaves. Based on these assumptions, angular momentum is conserved for the entire system about the swing foot contact point C during the collision process. Angular momentum is also conserved for the new swing leg (formerly the stance leg) about the hip joint hinge axis. These statements of angular momentum conservation during the collision process yield the transition rules for velocities from just before to just after foot-strike. Referring to Figure 6.7, we can write these conservation statements as

$$\mathbf{H}_C^- = \mathbf{H}_C^+ \tag{6.14}$$

for the whole system and

$${}^{\mathrm{st}}\mathbf{H}_B^- = {}^{\mathrm{sw}}\mathbf{H}_B^+ \tag{6.15}$$

for the the pre-collision stance leg which becomes the post-collision swing leg. The quantity $\mathbf{H}$ is angular momentum. Applying angular momentum balance as prescribed above through heel-strike gives the following collision rule for angular rates where the '+' superscript means 'just after heel-strike', and the '−' superscript means 'just before heel-strike'. The jump equations are non-dimensionalized in the same way as the equations of motion between foot collisions.

Collision Rule for Parameters

While the parameters for the walker are not changed by the collision dynamics, they are changed in the collision bookkeeping. When a stance leg becomes a swing leg and vice-versa, they must each remain a left or right leg due to their mirror reflection symmetry. What this amounts to is only a sign change in the c.o.m. y coordinate. All other parameters, including the inertia matrix, remain the same.

Total Collision Rule

Finally, we can merge the transition rules for the orientation variables and their rates into one map from the state of the system just before a collision to just after:

$$\begin{Bmatrix} \phi^+ \\ \psi^+ \\ \theta_{st}^+ \\ \theta_{sw}^+ \\ \dot{\phi}^+ \\ \dot{\psi}^+ \\ \dot{\theta}_{st}^+ \\ \dot{\theta}_{sw}^+ \end{Bmatrix} = \mathbf{L} \begin{Bmatrix} \phi^- \\ \psi^- \\ \theta_{st}^- \\ \theta_{sw}^- \\ \dot{\phi}^- \\ \dot{\psi}^- \\ \dot{\theta}_{st}^- \\ \dot{\theta}_{sw}^- \end{Bmatrix}, \text{ where } \mathbf{L} = \begin{bmatrix} \mathbf{S} & 0 \\ 0 & \mathbf{T} \end{bmatrix}. \tag{6.16}$$

We can rewrite this collision law that maps the state of the walker just before to just after a collision as

$$\mathbf{q}^+ = \mathbf{h}(\mathbf{q}^-) = \mathbf{L}(\mathbf{q}^-)\,\mathbf{q}^- \tag{6.17}$$

where the matrix $\mathbf{L}(\mathbf{q}^-)$ depends only on the orientation variables and not their rates. We do not include the collision rule here for brevity's sake but, again, we include in Appendix B the Maple® code used to derive the collision rule.

6.4 Return Map, Fixed Points and Stability of Walking Motions

The straight-legged point-foot walker free to move in three dimensions has an eight-dimensional phase space with coordinates $\{\phi, \psi, \theta_{st}, \theta_{sw}, \dot{\phi}, \dot{\psi}, \dot{\theta_{st}}, \dot{\theta_{sw}}\}^T$. Ag-
, a natural place to sample this space is at the points of discontinuity, the collisions. Because of the reflection symmetry of the legs about the $x-z$ plane, however, we construct a map $\mathbf{f}$ that takes the state of the walker just after a collision to just after the *two* successive collisions; i.e., through two cycles as defined above. Thus, the section of interest is taken after every two cycles of motion. The map from one state to the next can be written then as $\mathbf{q} \mapsto \mathbf{f}(\mathbf{q})$ or

$${}^{i+2}\mathbf{q}^+ = \mathbf{f}({}^{i}\mathbf{q}^+), \tag{6.18}$$

where $\mathbf{f}$ is the return map and ${}^{i}\mathbf{q}^+$ is the state vector of the system at the start of a cycle, just after the i_{th} collision.

Since we know the relationship of the stance leg angle to the swing leg angle on the Poincaré section (see Equation (6.11)), the map can be reduced to seven dimensions. In practice, when making stability calculations, we keep all eight dimensions which always yields one eigenvalue of the Jacobian evaluated at a fixed point exactly zero.

Again, the map $\mathbf{f}$ may be looked upon as a composition of two maps, but this time applied twice, $\mathbf{f} = (\mathbf{h} \circ \mathbf{d})^2$; here, $\mathbf{d}$ governs the motion from just after heel-strike i to just before heel-strike $i+1$, obtained by integrating the equations of motion between collisions, and $\mathbf{h}$ governs support transfer, from just before to just after heel-strike $i+1$.

For periodic or steady motion, we must again find fixed points of the return map,

$$\mathbf{q}^* = \mathbf{f}(\mathbf{q}^*). \tag{6.19}$$

We will use 2D fixed points as 'seeds' for finding 3D fixed points.

6.5 Re-parameterization of the Inertia Matrix

The inertia matrix for a rigid body must satisfy the following criteria:

1. all its eigenvalues are positive and
2. the sum of any two eigenvalues must be greater than or equal to the third; i.e., they must satisfy the triangle inequality.

In parameter studies, various components of the inertia matrix for the legs are varied. To guarantee that the components are varied in a way such that the inertia matrix satisfies the above constraints, we re-parameterize the inertia matrix in the following way.

Let the arrangement of six masses of mass $M/6$ at the ends of rigid massless rods as shown in Figure 6.8 represent the distribution of leg mass where M is the leg mass. In the configuration shown, the axes are aligned with the principal directions of the moment of inertia matrix for the arrangement. Suppose the principal moment of inertia matrix for each leg is

$$\mathbf{I} = \begin{bmatrix} I_1 & 0 & 0 \\ 0 & I_2 & 0 \\ 0 & 0 & I_3 \end{bmatrix} \tag{6.20}$$

where, I_1, I_2, and I_3 are positive and $I_1 \leq I_2 + I_3$, $I_2 \leq I_1 + I_3$, and $I_3 \leq I_1 + I_2$. Then, we can re-parameterize the inertia matrix in terms of the locations of the six masses, d_1, d_2, and d_3 as follows:

$$\begin{aligned} I_1 &= (d_2 + d_3^2)/3, \\ I_2 &= (d_1^2 + d_3^2)/3, \text{ and} \\ I_3 &= (d_1^2 + d_2^2)/3 \end{aligned} \tag{6.21}$$

where the inertia terms have been non-dimensionalized with respect to $M\ell^2$. This re-parameterization ensures that the eigenvalues of the inertia matrix are positive since d_1, d_2, and d_3 are positive. (Even if any of the d_1, d_2, and d_3 are negative, the eigenvalues will still be positive since the squares of each are taken in Equations (6.21)).

In terms of the inertia quantities, the distances can be found as

$$\begin{aligned} d_1 &= \sqrt{\frac{3}{2}(-I_1 + I_2 + I_3)}, \\ d_2 &= \sqrt{\frac{3}{2}(I_1 - I_2 + I_3)}, \text{ and} \\ d_3 &= \sqrt{\frac{3}{2}(I_1 + I_2 - I_3)}. \end{aligned} \tag{6.22}$$

Since, I_1, I_2, and I_3 satisfy the triangle inequality, d_1, d_2, and d_3 are guaranteed to be positive. Thus far, given any d_1, d_2, and d_3, we obtain a legitimate diagonal inertia matrix.

To obtain a more general matrix with product of inertia terms we simply find the components of the inertia matrix in the same coordinate system for an arbitrary rotation of the body about the origin. In terms of a rotation matrix $\mathbf{R}$ and the principal inertia matrix $\mathbf{I}$, the inertia matrix $\mathbf{I}'$ for the body rotated from its initial configuration relative to the coordinate axes is given by

$$\mathbf{I}' = \mathbf{R}^T \mathbf{I} \mathbf{R}, \tag{6.23}$$

where we use the 3-1-2 Euler angles κ, ν and ρ to form the rotation matrix (see Appendix D). In numerical simulations, locations d_1, d_2, and d_3 and the rotation angles κ, ν and ρ are used rather than the moment of inertia matrix components themselves.

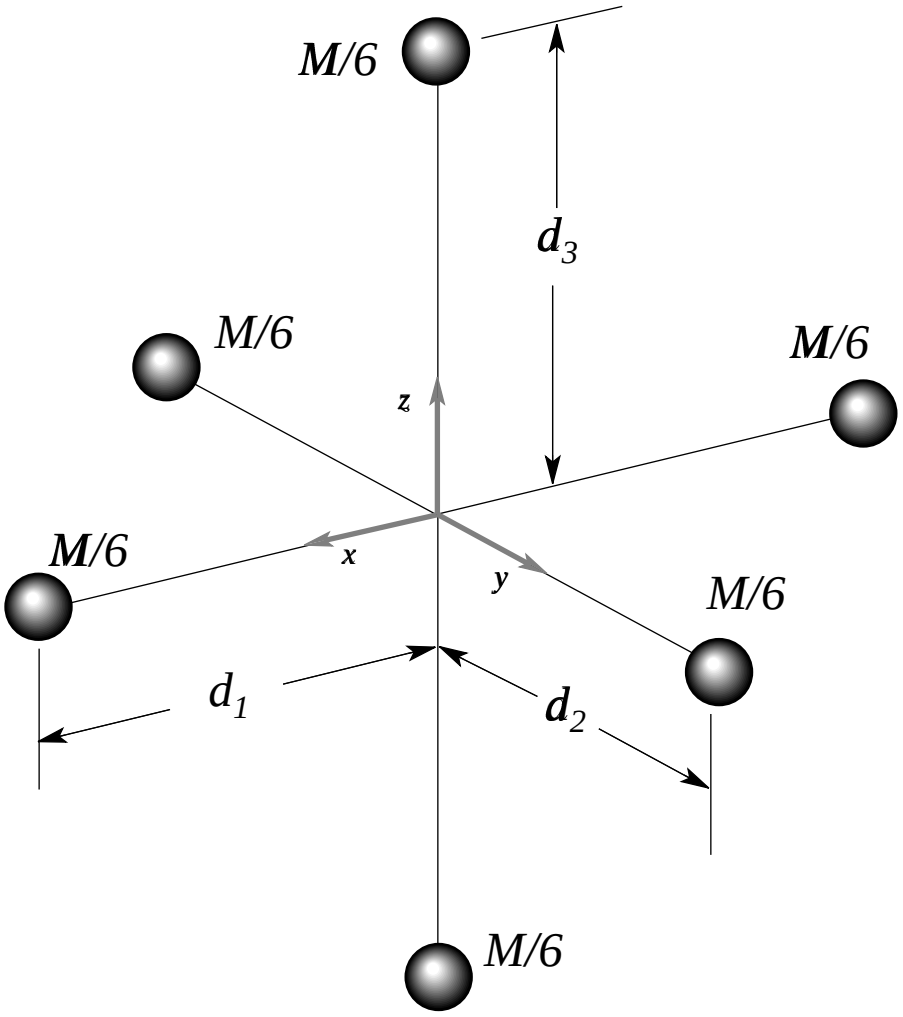

Figure 6.8: Re-parameterization of the leg moment of inertia matrix by making the transforming the leg into the equivalent structure shown in the figure: six equal masses $M/6$ with each pair of masses arranged symmetrically along each axis at the distances d_1, d_2, and d_3.

6.6 Numerical Simulations and Results

6.6.1 Steady Motions and Stability

We integrated the fully nonlinear equations of motion using `int_henon_temp_3D.m`, a version of MATLAB®'s `ode45.m` (a 4th-5th order automatic step-sizing routine) modified to detect spoke collisions using Henon's [62] method(see Appendix A). We used an integration tolerance 10^{-8} in the automatic step-sizing routine.

Because there exists a family of periodic solutions at each heading angle for the planar 3D walker, we constrain the heading angle to return to where it started after the two collisions of each map iteration so that we may find 3D fixed points; otherwise, the Newton's method search will not converge on any particular member of the family of solutions. For simplicity, we look for solutions at zero heading. This does not mean, however, that the walker walks in a straight line – only that it points in the same heading after two steps.

A typical plot of the state of the 3D walker over two steps (one map iteration) is shown in Figure 6.9. We found fixed points and the Jacobian eigenvalues using a MATLAB® routine `newton_3D.m` (see Appendix A). We use the same routines in Chapters 5 and 6. The finite difference step size used to compute the Jacobian numerically was 10^{-4} and error tolerance for the fixed point search was 10^{-6}. The eigenvalues and eigenvectors for a particular case are shown in Table 6.2. The maximum eigenvalue is associated with falling over laterally or in the bank direction. Figure 6.10 shows the

Table 6.2: Eigenvalues and eigenvectors for the case plotted in Figure 6.9.

	Eigenvalues							
	σ_1	σ_2	σ_3	σ_4	σ_5	σ_6	σ_7	σ_8
	2.5827	0.3871	0.1289	0.8992	0.8495	1.0000	0.9904	0.0000
Eigenvector								
ϕ^*	0.0006	0.0004	-0.0045	0.00037	0.0002	1.0000	1.0000	0.0038
ψ^*	-0.7833	-0.7750	0.0008	0.0000	0.0000	-0.0037	-0.0022	-0.0001
θ^*_{st}	-0.0087	-0.0233	0.1379	-0.0125	-0.0060	0.0000	-0.0001	-0.0535
θ^*_{sw}	0.0174	0.0466	-0.2759	0.0251	0.0129	0.0001	0.0001	0.2442
$\dot{\phi}^*$	0.0043	0.0056	-0.0147	-0.0154	-0.0154	0.0000	-0.008	0.0153
$\dot{\psi}^*$	-0.6190	0.6122	-0.0014	0.0003	0.0002	0.0000	0.0003	0.0000
$\dot{\theta}^*_{st}$	-0.0047	0.0016	-0.0801	-0.0006	-0.0228	0.0000	0.0001	0.0569
$\dot{\theta}^*_{sw}$	0.0525	0.1473	-0.9477	-0.9995	-0.9995	-0.0011	-0.0011	0.9664

leg angles; comparison of the heading and bank angles; swing leg height; and swing foot and hip paths over two foot collisions.

6.6.2 Dynamic Stability versus Falling Over: A Criteria For 'Goodness' of Instability

In terms of our model parameters, the inverted pendulum frequency Equation (6.2) discussed in the chapter introduction is given by

$$p = \sqrt{\frac{z}{(I_{xx} + y^2 + z^2)}}. \tag{6.24}$$

To reiterate, comparing the lateral instability of the biped in a steady gait to its inverted pendulum instability can be made by comparing σ to $e^{p\tau_0}$ where τ_0 is the gait period.

6.6.3 Effects of Parameters Variations on Steady Motions and Stability

We show how the step period τ^*, modulus of the maximum eigenvalue $|\sigma_{max}|$, fixed point stance angle θ^*_{st}, and the ratio of return map to falling-over-eigenvalue vary with each parameter while the

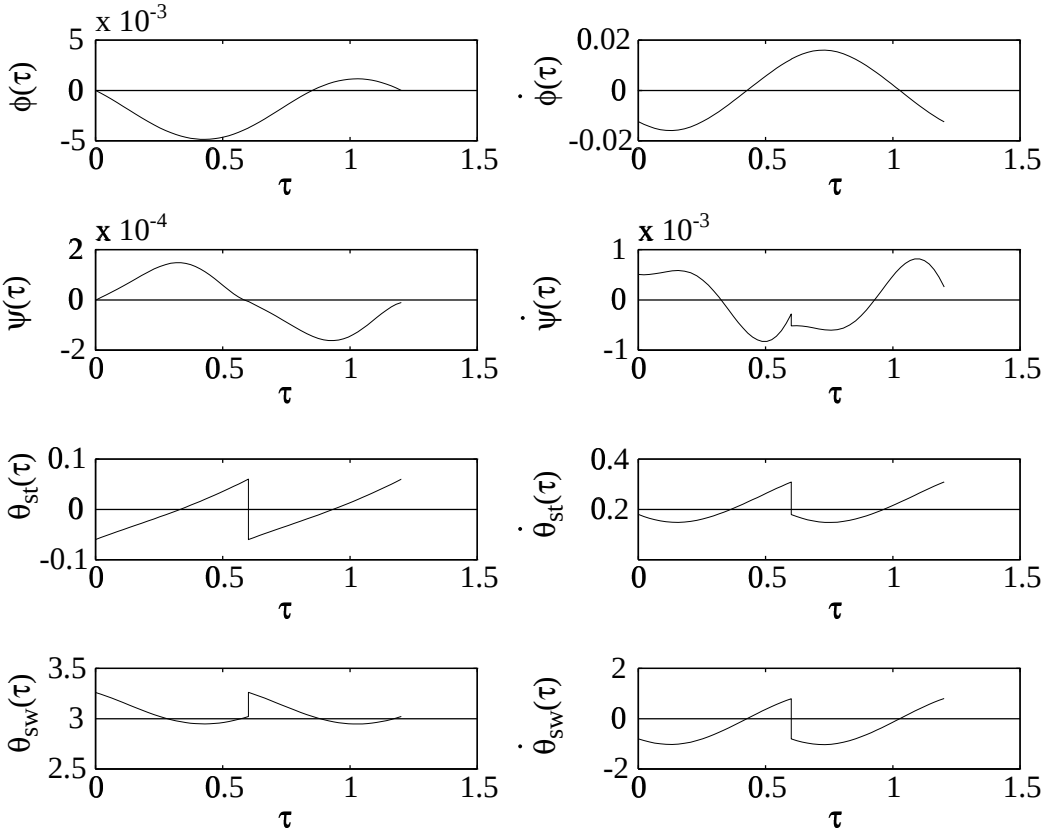

Figure 6.9: The state of the 3D walker over two steps in a periodic motion for $I_{xx} = 0.5577$, $I_{yy} = 0.00021$, $I_{zz} = 0.5579$, $I_{xy} = 0.0000$, $I_{xz} = 0.0000$, $I_{yz} = 0.0000$, $\alpha = 0.0037$, $x = 0.0$, $y = 0.2706$, and $z = 0.9270$. In a periodic motion, every other foot-strike returns the system to its initial conditions. The swing leg angle is more usefully plotted as measured from the vertical to the slope or $\theta^*_{sw}(\tau) + \theta^*_{st}(\tau) - \pi$. The fixed point for this case is $\mathbf{q}^* = \{0.0000\ 0.000008\ -\ 0.0597\ 3.2610\ -\ 0.0132\ 0.00051\ 0.1866\ -0.8523\}^T$; the maximum eigenvalue is $|\sigma_{max}| = 2.58$ and the non-dimensional step period is $\tau^* = 1.2031$.

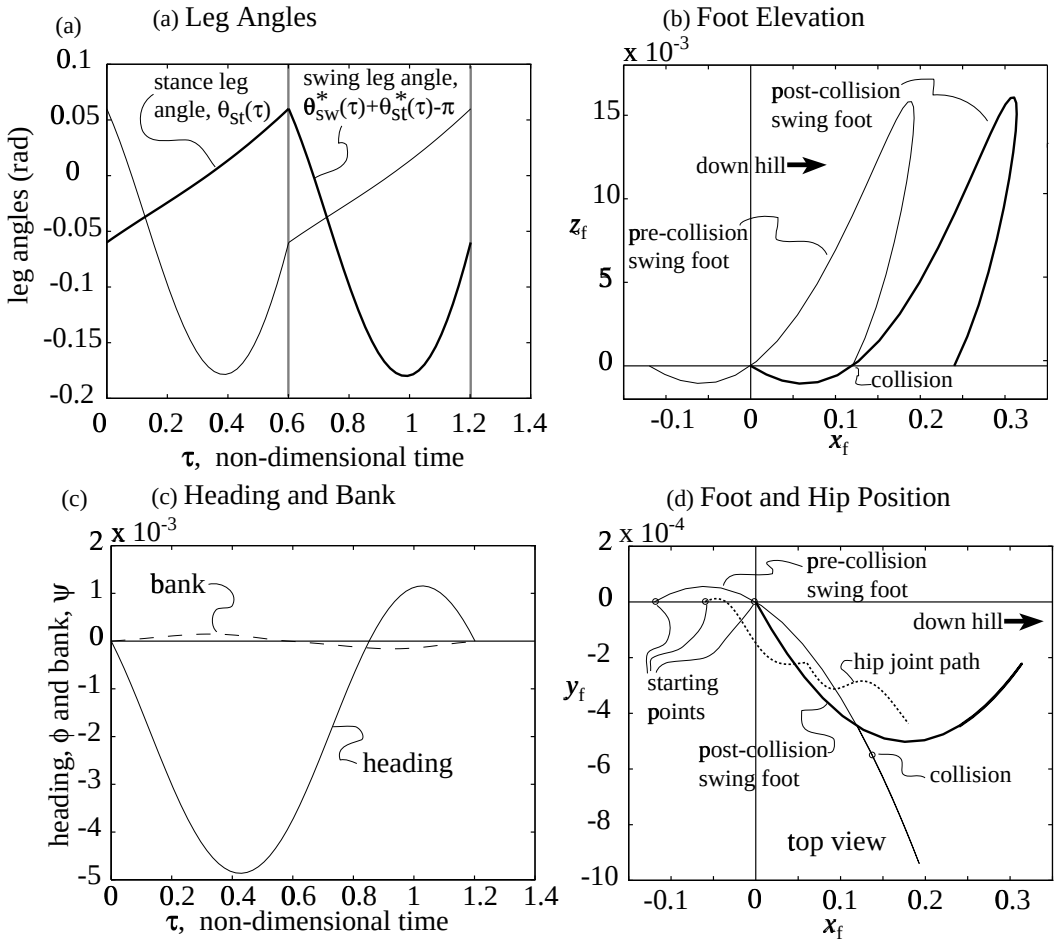

Figure 6.10: Typical periodic gait cycle behavior over two steps for $I_{xx} = 0.5577$, $I_{yy} = 0.00021$, $I_{zz} = 0.5579$, $I_{xy} = 0.0000$, $I_{xz} = 0.0000$, $I_{yz} = 0.0000$, $\alpha = 0.0037$,$x = 0.0$, $y = 0.2706$, and $z = 0.9270$. The fixed point for this case is $\mathbf{q}^* = \{0.0000\ 0.000008\ -\ 0.0597\ 3.2610\ -\ 0.0132\ 0.00051\ 0.1866\ -0.8523\}^T$; the maximum eigenvalue is $|\sigma_{max}| = 2.58$ and the non-dimensional step period is $\tau^* = 1.2031$. (a) The periodic gait cycle leg angles are very similar to those for 2D walking. The stance leg curve is denoted by the heavy line and the swing leg curve by the thin line corresponding to Figure 6.21. (b) The plots show how the swing foot passes through the floor momentarily between collisions. (c) The plots show the relationship of the heading and the bank angle of the walker over two steps. (d) The plots show the path of the hip joint and the swing foot viewed from above over two steps.

others are held constant. No attempt is made here to exhaustively search the huge parameter space for stable periodic motions.

Leg Moment of Inertia Matrix, $\mathbf{I}^{cm}$

The effect of varying the components of the inertia matrix of the legs is shown in Figures 6.11–6.14. We vary the re-parameterization quantities d_1, d_2, d_3, κ, ν, and ρ instead of the inertia components themselves.

Increasing the distribution of mass in the fore and aft directions, by increasing d_1, destabilizes the walker and increases its step period and stance leg angle. Note in Figure 6.11 that double solutions exist for the same values of d_1 in the range d_1 =0.016 to 0.025 that are much less stable and have much longer step periods and step lengths. In light of the results in Garcia *et al.* [3] showing that, even for the one-parameter 2D straight-legged point-foot walking model (see Section 5.5), multiple solutions at the same slope angle exist, such behavior most certainly exists for the 3D straight-legged point-foot model, but we did not investigate this possibility further. McGeer [4] also found short and long period solutions for the zero hip spacing (see Figure 6.3). Increasing the mass distribution of the

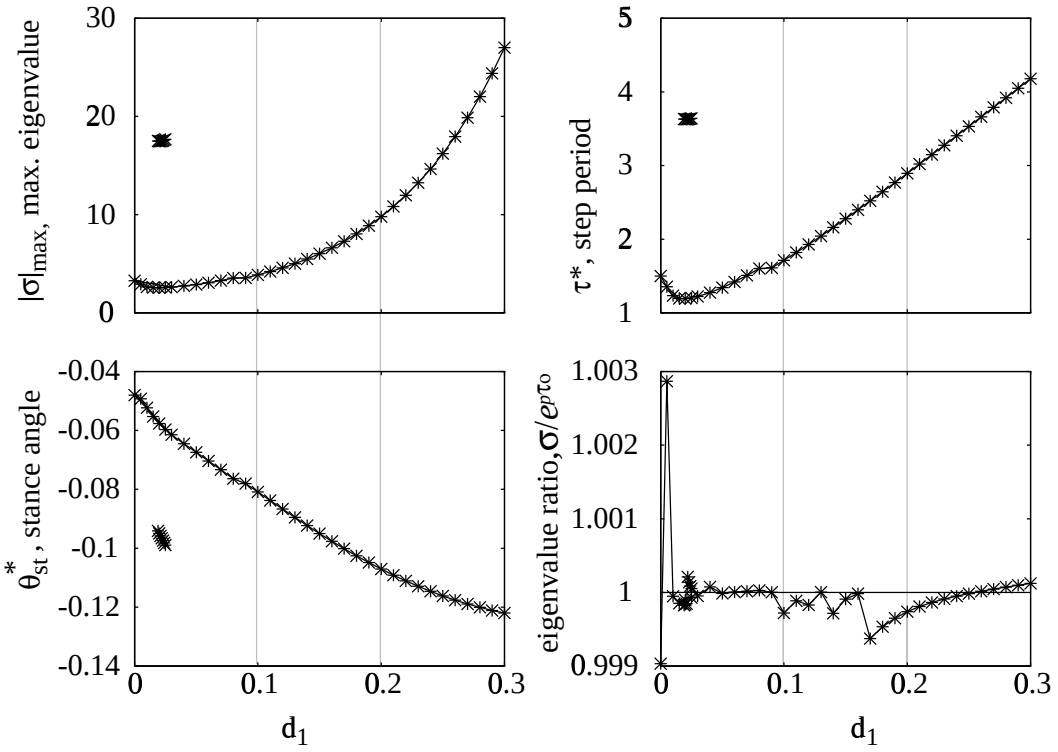

Figure 6.11: The variation of maximum eigenvalue, step period, stance angle, and the ratio of return map to falling-over-eigenvalue with non-dimensional inertia parameter d_1 for steady gait while the other parameters are held constant at $d_2 = 1.2935$, $d_3 = 0.00006$, $\kappa = 0$, $\nu = 0$, $\rho = 0$, $x = 0$, $y = 0.2706$, $z = 0.9270$, and $\alpha = 0.0038$.

legs in the lateral (y) direction by increasing d_2 has a strong effect on the stability and motion of the walker – the maximum eigenvalue decreases fairly rapidly and the step period and stance leg angles increase. Increasing the distribution of mass in the vertical (z) direction by increasing d_3 rapidly destabilizes the walker and increases its step period while at first increasing its stance leg angle and

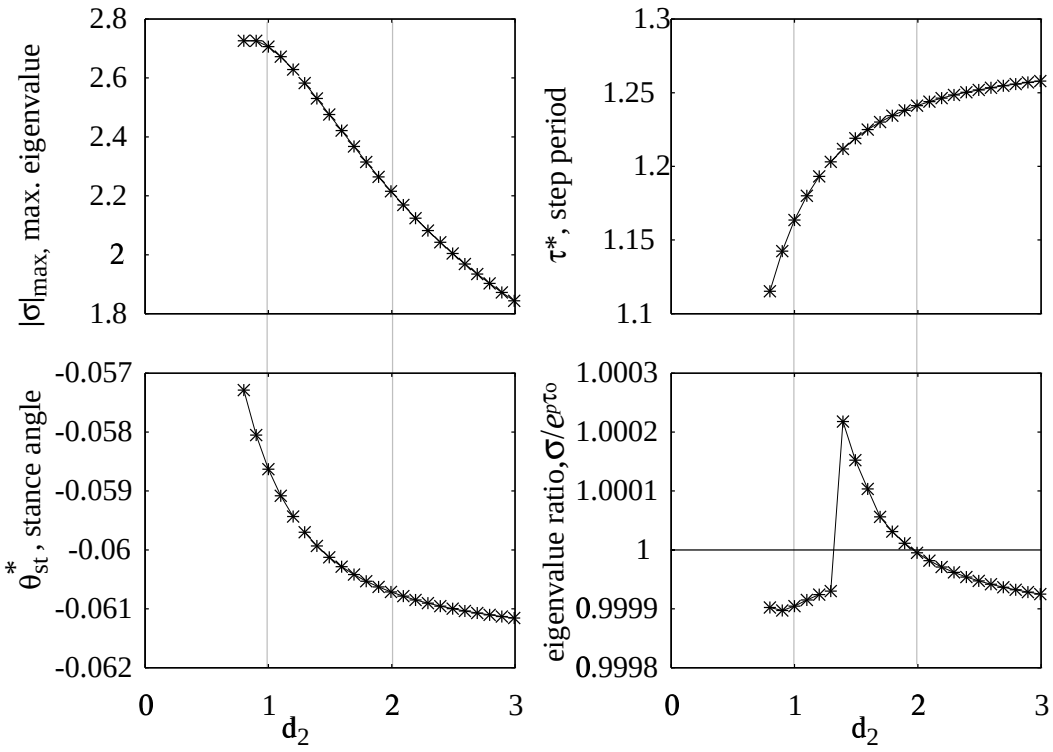

Figure 6.12: The variation of maximum eigenvalue, step period, stance angle, and the ratio of return map to falling-over-eigenvalue with non-dimensional inertia parameter d_2 for steady gait while the other parameters are held constant at $d_1 = 0.025$, $d_3 = 0.00006$, $\kappa = 0$, $\nu = 0$, $\rho = 0$, $x = 0$, $y = 0.2706$, $z = 0.9270$, and $\alpha = 0.0038$.

then finally decreasing it. That increasing d_1 and d_2 destabilizes the 3D walker corresponds to the instability of the 2D walker due to increasing its polar moment of inertia.

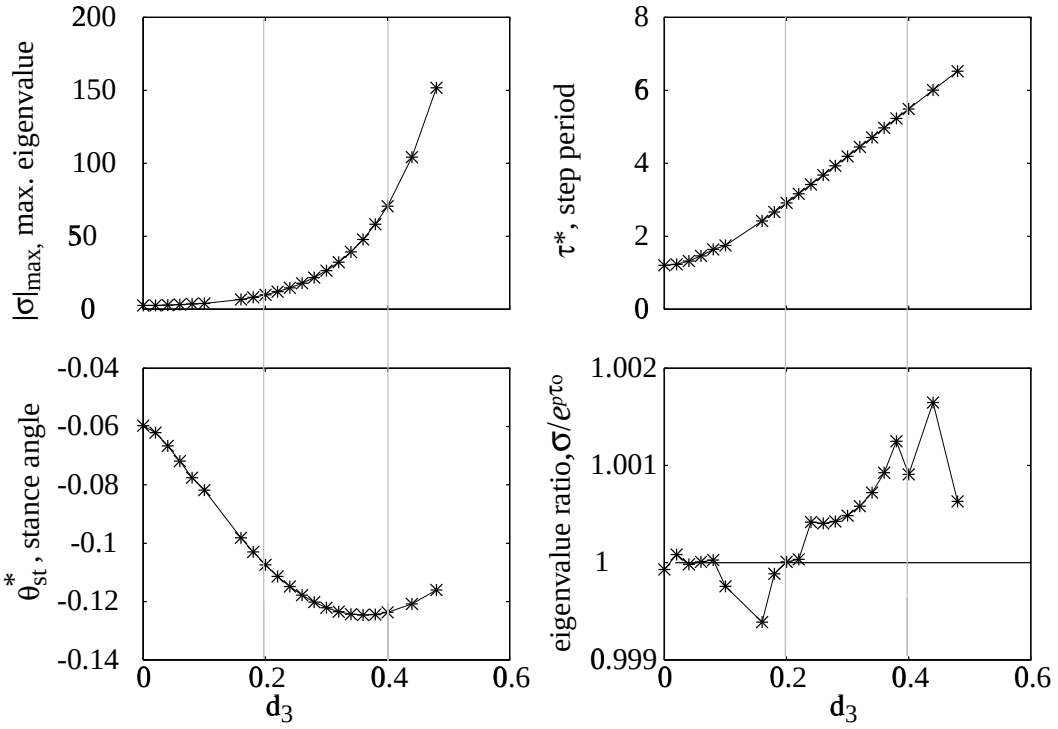

Figure 6.13: The variation of maximum eigenvalue, step period, stance angle, and the ratio of return map to falling-over-eigenvalue with non-dimensional inertia parameter d_3 for steady gait while the other parameters are held constant at $d_1 = 0.025$, $d_2 = 1.2935$, $\kappa = 0$, $\nu = 0$, $\rho = 0$, $x = 0$, $y = 0.2706$, $z = 0.9270$, and $\alpha = 0.0038$.

We found no fixed points for $\kappa \geq 0.00000001$ or $\nu \geq 0.00000001$. Chatterjee [83] suggested the following strategy for checking that this result makes sense. First, to make sure this was not a numerical artifact, we checked that the Newton's method error calculation was the same as we decreased the integration tolerance while holding all other parameters constant. Then, we checked to see that the condition number of the Newton's method Jacobian matrix was not too large (cond($\mathbf{J}$)$<$ 10^8). Finally, we checked to see that as we let κ and ν go to zero, that cond($\mathbf{J}$) remained nearly constant. So, it seems that no walking solutions may exist for non-zero I_{xy} and I_{yz}, at least for the parameter set considered here.

As the distribution of mass of the leg is rotated in the xz-plane of the walker about its y-axis by an amount ρ, the maximum eigenvalue decreases, increasing stability, just as crooked masses in the plane of a rolling disk enhance its stability (see Figure 6.14). But, the changes in stability, step period, and stance leg angle are small despite the wide variation in values for ρ because the distribution of mass in the x-direction and z-direction for the given parameter set, controlled by d_1 and d_3, is small.

Center of Mass Position

The effect of varying the coordinates of the center of mass of the legs is shown in Figures 6.15–6.16.

As the center of mass is offset in the forward directions, the maximum eigenvalue decreases while the periodic stance leg angle decreases, just the opposite of the 2D model! The step period decreases

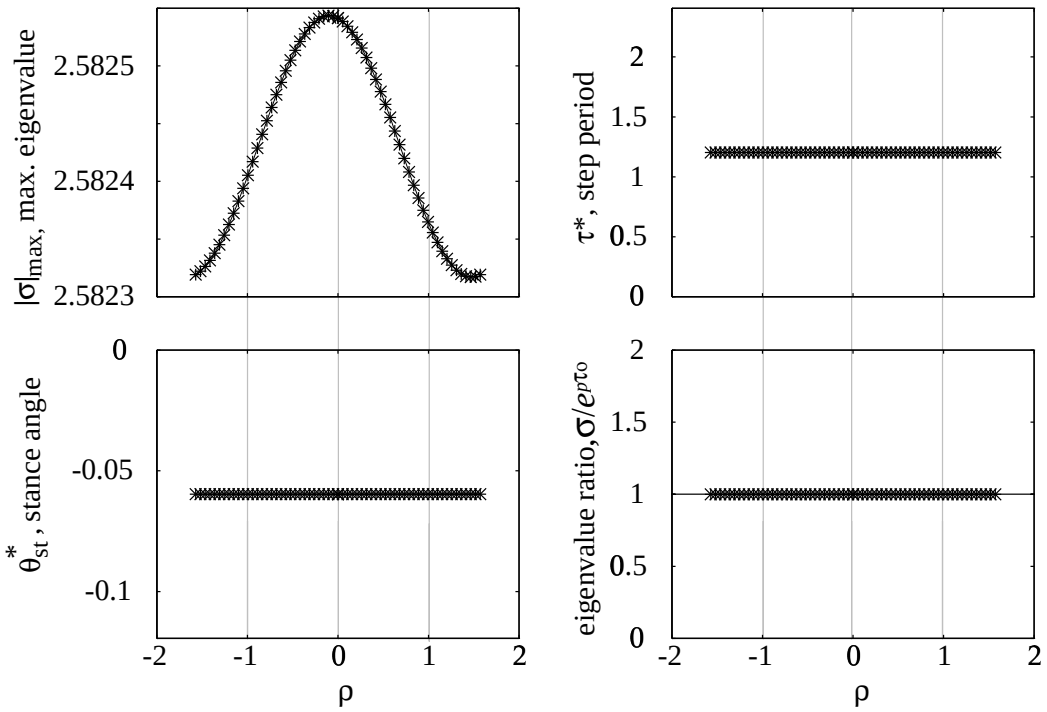

Figure 6.14: The variation of maximum eigenvalue, step period, stance angle, and the ratio of return map to falling-over-eigenvalue with non-dimensional inertia parameter ρ for steady gait while the other parameters are held constant at $d_1 = 0.025$, $d_2 = 1.2935$, $d_3 = 0.00006$, $\kappa = 0$, $\nu = 0$, $x = 0$, $y = 0.2706$, $z = 0.9270$, and $\alpha = 0.0038$.

if the mass is moved forward. Like increasing d_2, increasing the y offset of the walker has a powerful

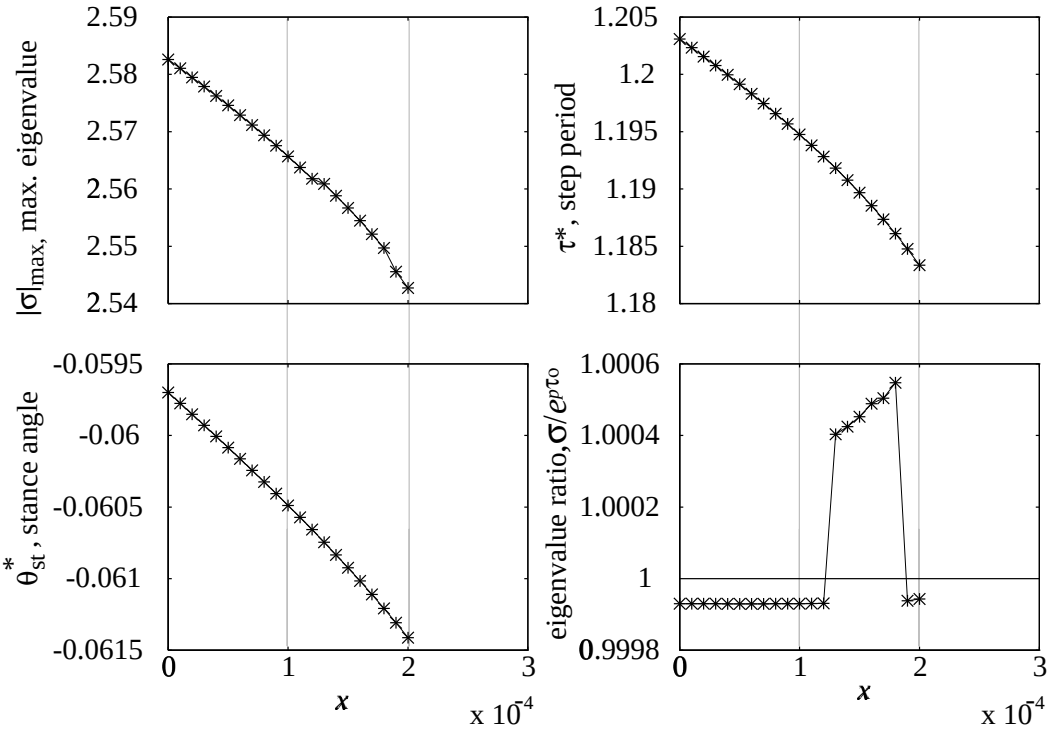

Figure 6.15: The variation of maximum eigenvalue, step period, stance angle, and the ratio of return map to falling-over-eigenvalue with non-dimensional coordinate of the center of mass x for steady gait while the other parameters are held constant at $d_1 = 0.025$, $d_2 = 1.2935$, $d_3 = 0.00006$, $\kappa = 0$, $\nu = 0$, $\rho = 0$, $y = 0.2706$, $z = 0.9270$, and $\alpha = 0.0038$.

effect on its steady motions and their stability – the maximum eigenvalue decreases. At first, as the y offset is increased, the maximum eigenvalue drops off rapidly and then decrease gradually as y gets large. But, while squeezing mass out along the y axis increases the step period and stance leg angle, sliding the center of mass out along the y axis decreases both. Raising z, the center of mass height along the leg, at first destabilizes walking, then stabilizes it as it nears the hip, also just the opposite of the effect of increasing z for the 2D walker with the same planar properties (see Figure 5.7 in Chapter 5)! In addition, as the center of mass gets very close to the hip, there is a sharp decrease in stability and increase in step period.

Slope Angle

The maximum eigenvalue, step period, and stance angle increase with increasing slope angle, are shown in Figure 6.18.

3D Special Case: Tight-rope Walking with a Balance Bar

For the case of large d_2 or y the 3D walker legs essentially have a mass distribution corresponding to laterally extended balance bars like what might be used for walking on a tight-rope. From Figures 6.12 and 6.16, it seems that, in the limit as d_2 or y get very large, the modulus of the maximum eigenvalue asymptotically approaches one, or neutral lateral stability, from above.

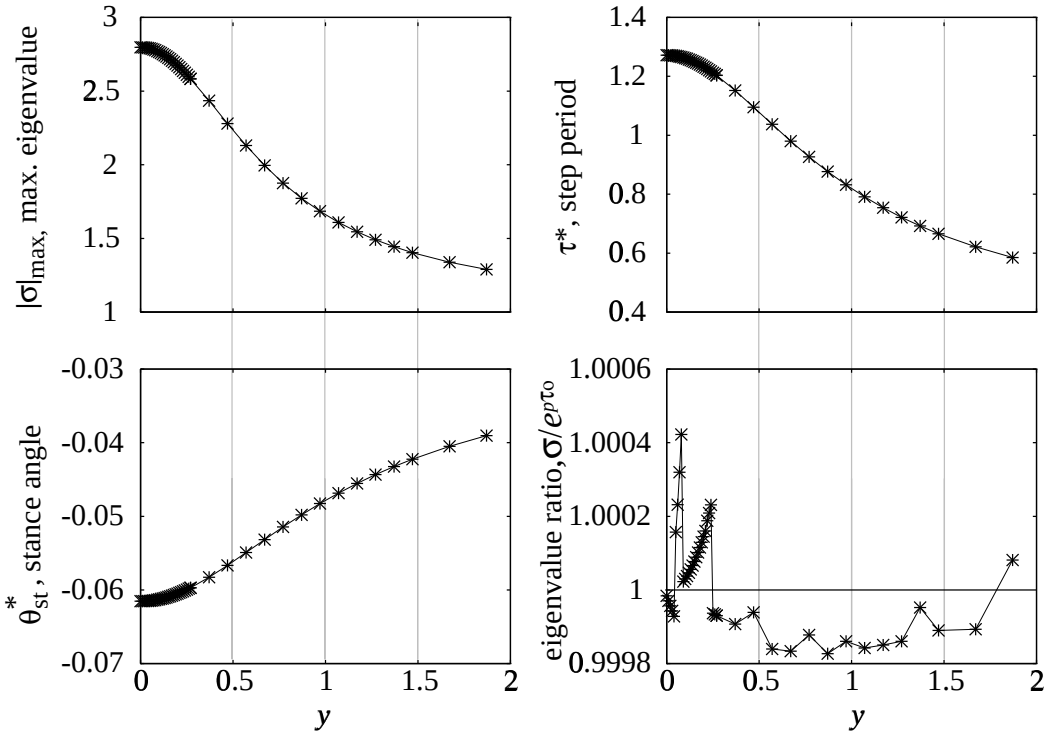

Figure 6.16: The variation of maximum eigenvalue, step period, stance angle, and the ratio of return map to falling-over-eigenvalue with non-dimensional coordinate of the center of mass y for steady gait while the other parameters are held constant at $d_1 = 0.025$, $d_2 = 1.2935$, $d_3 = 0.00006$, $\kappa = 0$, $\nu = 0$, $\rho = 0$, $x = 0$, $z = 0.9270$, and $\alpha = 0.0038$.

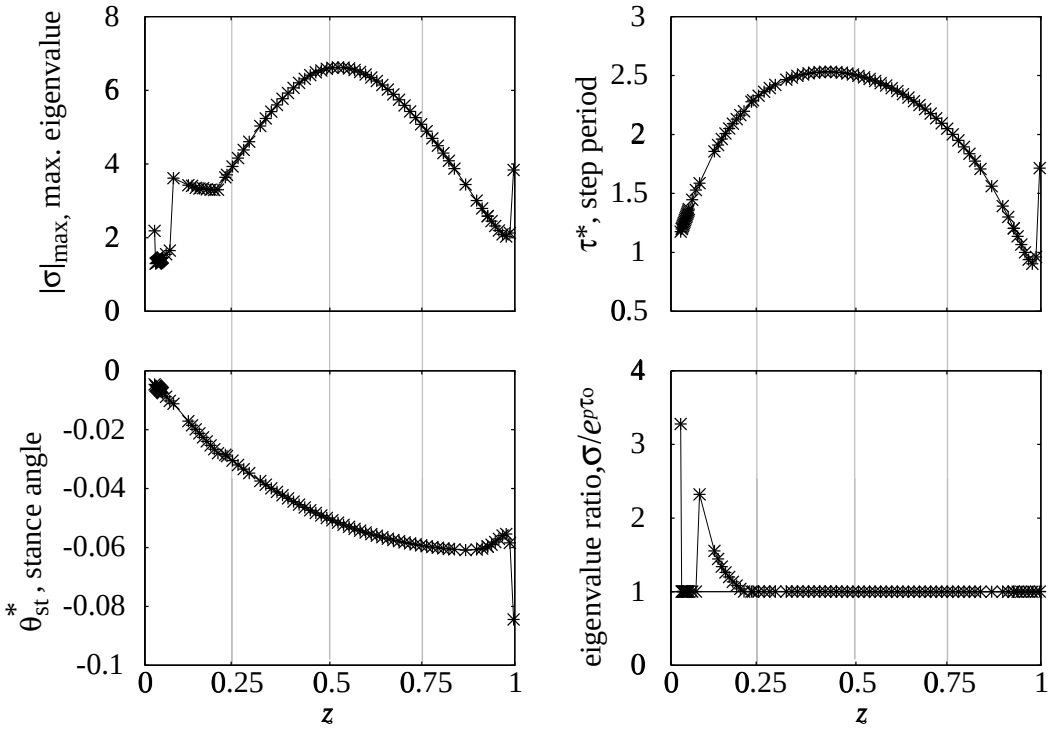

Figure 6.17: The variation of maximum eigenvalue, step period, stance angle, and the ratio of return map to falling-over-eigenvalue with non-dimensional coordinate of the center of mass z for steady gait while the other parameters are held constant at $d_1 = 0.025$, $d_2 = 1.2935$, $d_3 = 0.00006$, $\kappa = 0$, $\nu = 0$, $\rho = 0$, $x = 0$, $y = 0.2706$, and $\alpha = 0.0038$.

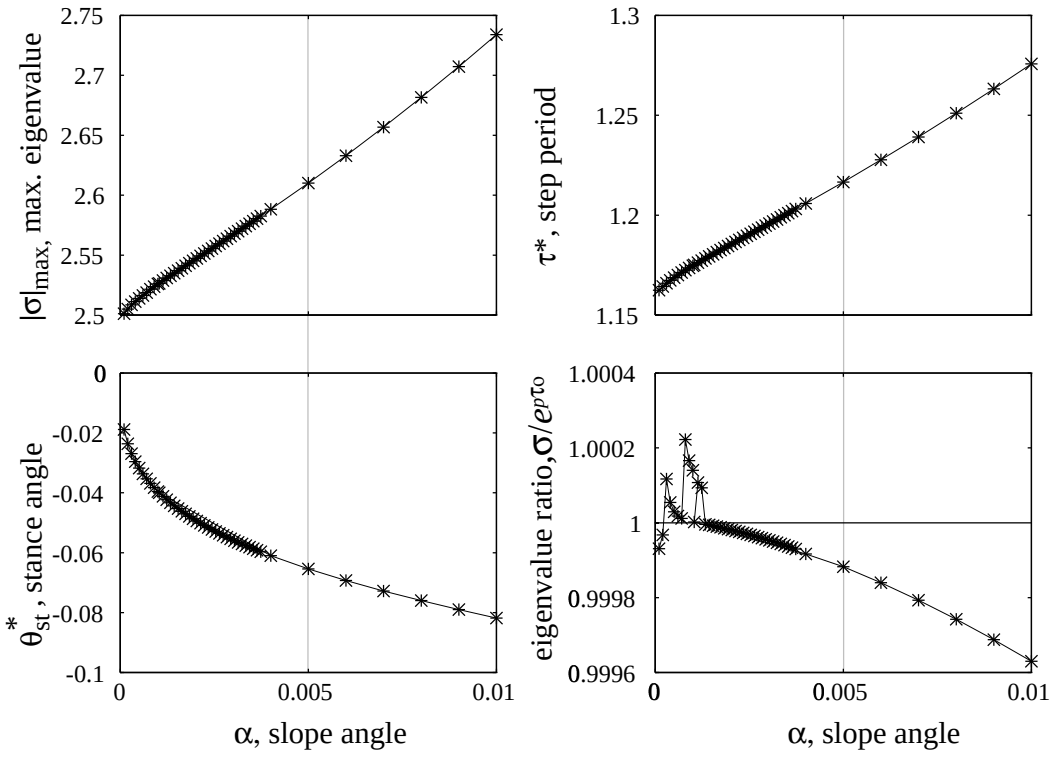

Figure 6.18: The variation of maximum eigenvalue, step period, stance angle, and the ratio of return map to falling-over-eigenvalue with slope angle α for steady gait while the other parameters are held constant at $d_1 = 0.025$, $d_2 = 1.2935$, $d_3 = 0.00006$, $\kappa = 0$, $\nu = 0$, $\rho = 0$, $x = 0$, $y = 0.2706$, $z = 0.9270$.

6.6.4 An Uncontrolled Walking Toy that Cannot Stand Still

As a non-working demonstration of the kinematics and mass distributions in our simulations, and not for walking experiments, we assembled a device similar to the one shown in Figure 6.19 (see Coleman and Ruina [14]). It has two straight legs, separated by simple hinges at the hips, laterally extending balance mass rods, and rounded feet. Playing, with no hopes of success, we placed the toy on a ramp. Surprisingly, it took a few serendipitous, if not very steady or stable, steps. After some non-quantifiable tinkering, we arrived at the functioning device shown in the photograph in Figure 6.19 and with more construction detail in Figure 6.20. Our physical model is constructed

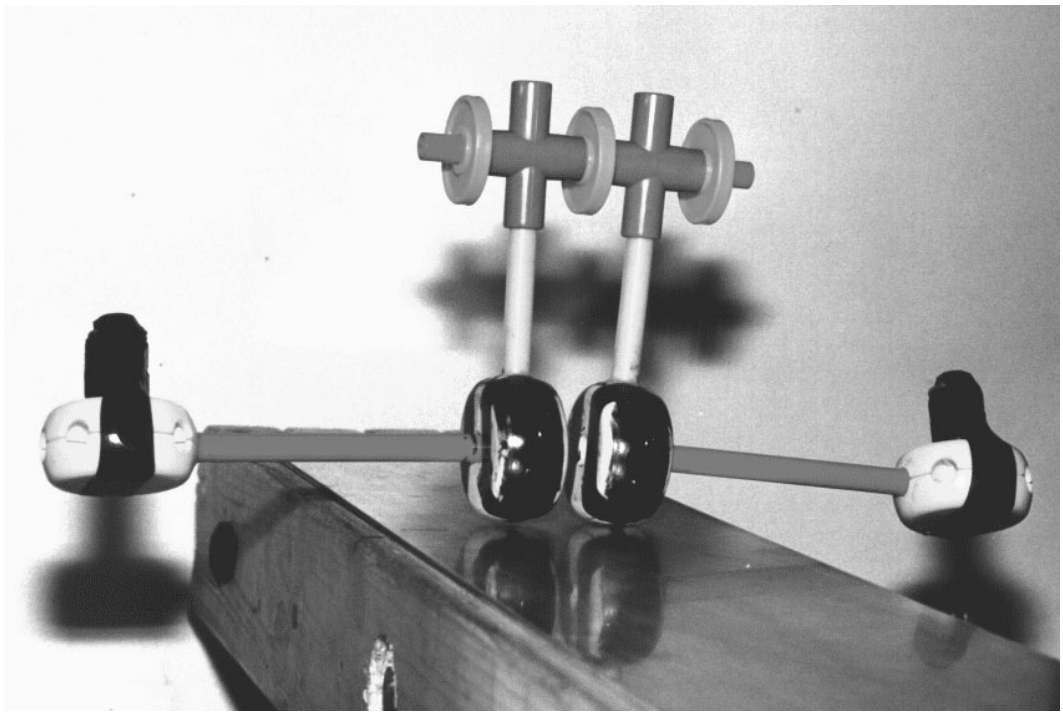

Figure 6.19: The 3D Tinkertoy® walking model shown out for a stroll in the lab.

from a popular American child's construction toy, brass strips to round the feet bottoms, and various steel nuts for balance masses. The walking ramp has about a 4.5 degree slope and is narrow enough to avoid making contact with the balance masses as the walker rocks side-to-side. Another more complex assembly of similar toy parts (not described here) walks on a wide ramp.

Construction Details

The device is built using the Playskool® Tinkertoy® Construction System: Colossal Constructions™, 1991 set. One leg is made from a yellow spool, a light green rod, and a dark green hinge (plus '+' shaped) glued together. Then, we slid the legs onto a red rod (loose fit) which acts as an axle. The green hinges are separated and kept from sliding apart by three orange washers friction-fit to the red axle. The legs and red axle can rotate independently.

To support the side weights, we glued a yellow spool rigidly to the end of a red rod and inserted the other end into the side of a yellow foot with a friction fit to allow for rotational adjustment.

We assembled each balance mass from two stacked steel nuts held together between two washers by a nut and bolt. Each nut assembly has a mass of about 50 grams. Then, each balance mass assembly was located on the yellow spools at the end of the balance rods and held in place with

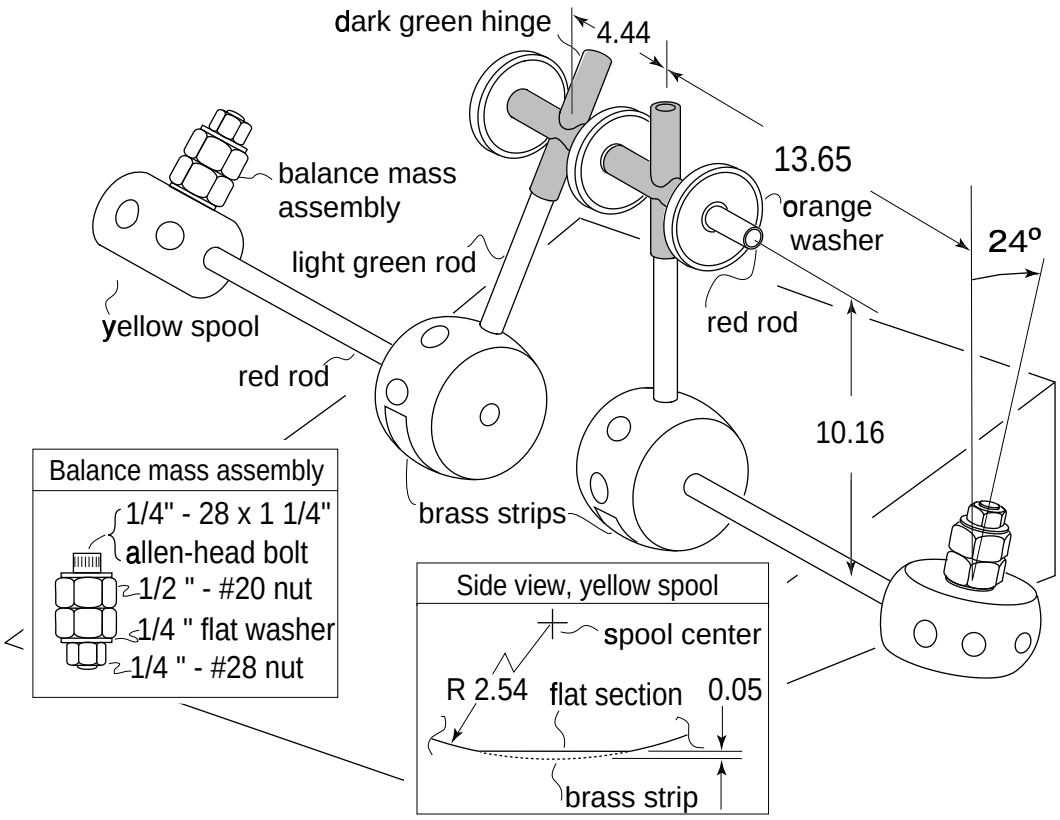

Figure 6.20: The 3D Tinkertoy® walking model with hardware description and dimensions (in centimeters, not drawn to scale). The balance masses and the brass strips are fastened with black electrical tape (not shown).

vinyl electrical tape. The balance mass assembly is tilted behind the leg. As a result, the legs have low mass centers located laterally at a distance comparable to the leg length, above the center of curvature of the feet, and just behind the leg axes. The mass of the fully assembled walking device is about 120 grams, only 20 grams more than the two balance masses. When the toy is in its unstable-equilibrium standing position the nominally-vertical legs are approximately orthogonal to the ramp.

Because a yellow spool has holes located radially around its circumference to accept rods, a small flat section is on the bottom at the foot contact point. To ensure that the walker is statically unstable (cannot stand on the flat sections or in any other way), a small (0.50 cm wide) strip of thin (0.013 cm) brass shim stock material was fastened over the flat section contacting the floor so as to restore its curvature there.

6.6.5 Observed motion.

Because the center of mass is above the center of curvature of the round feet, we cannot stably stand this device with parallel or with splayed legs. When placed aiming downhill on a ramp, tipped to one side, and released, the device rocks side-to-side and, coupled with swinging of the legs, takes tiny steps. When a foot hits the ground, it sticks and then rolls, until the swinging foot next collides with the ground. Except at the moment of foot collision, only one foot is in contact with the ground at any time. When the swinging foot collides with the ground, the trailing leg leaves the ground. The gait is more-or-less steady; after small disturbances the toy either falls or stumbles a few steps while returning to near-periodic gait. At a slope of 4.5 degrees, it takes a step about every 0.47 seconds and advances forward about 1.3 cm per step, where a step is measured from a foot collision to the next collision of that same foot. The side-to-side tilt is about 4 degrees, there is no visible variation in ϕ during a step, but there is slight directional drift (one way or another) over many steps. The rounded metal strips at the feet bottom deform during foot collision in a way that may or may not be essential; we do not know yet.

6.7 Conclusions and Future Work

The most stable case to date has maximum eigenvalue $|\sigma|_{max} = 1.145257$ with $d_1 = 0.025000$, $d_2 = 1.293532$, $d_3 = 0.00006$, $\kappa = 0$, $\nu = 0$, $\rho = 0$, $x = 0$, $y = 0.8706$, $z = 0.0290$, and $\alpha = 0.0037$. (The moments and products of inertia are $I_{xx} = 0.557742$, $I_{yy} = 0.000208$, $I_{zz} = 0.557950$, $I_{xy} = 0$, $I_{xz} = 0$, and $I_{yz} = 0$.) For these parameters, the ratio of the return map eigenvalue to the falling-over eigenvalue for the walker, however, is $p \approx 1$. The fixed point for this case is $\mathbf{q}^* = \{0.000000,\ 0.000012,\ -0.004765,\ 3.151124,\ -0.001196,\ 0.002499,\ 0.818076,$
$-0.003722\}^T$ The best ratio of map to falling-over eigenvalue is just less than one for any of the parameter ranges investigated here.

We have by no means exhausted the search through parameter space for stable walking and plan to continue searching with this model and more complicated ones as described below.

We have constructed a device which can balance while walking but cannot stand in any configuration. Although our new machine does not have a very human-like mass distribution, it does highlight the possibility that uncontrolled dynamics may not just contribute to fore-aft walking balance, as indicated by previous McGeer models, but also to side-to-side balance. The mechanism joins a small collection of statically unstable devices which dynamically balance without any rapidly spinning parts.

Our too-simple mathematical/computational model does not explain this behavior. We do not yet know what key modeling features need be included to predict the observed dynamic stability. Figure 6.21 shows a 3D model which probably captures the essential geometric and mass-distribution features of the physical model presented here, one we would like to study. The additions to the model

are hip spacing and now each of the two legs can make rolling and collisional contact with the ground (slope = α) with no contact couples. Based on McGeer's numerical 3D results, our 3D numerical results, and our physical 3D model, it seems a good place to continue would be a 3D straight-legged point-foot walker with hip spacing and balance bars.

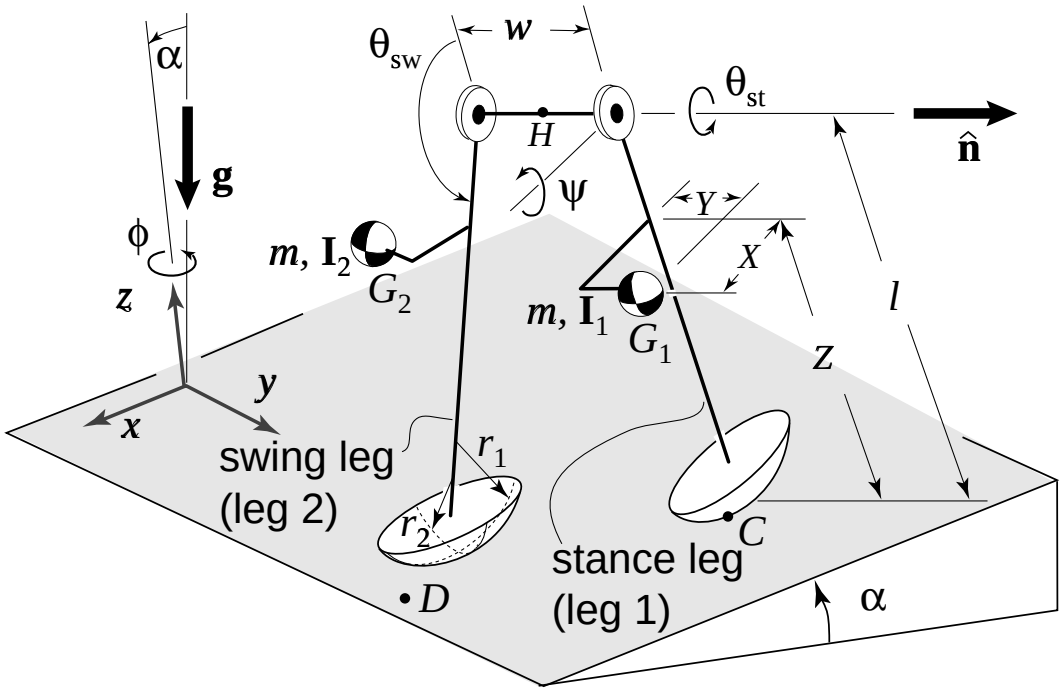

Figure 6.21: A more complicated rigid body model of the simple walker. The device, at least at the level of approximation which we believe is appropriate, is a pair of symmetric rigid bodies (leg 1 = stance leg, leg 2 = swing leg) that have mass m, symmetrically located (in the rest state) centers of mass $G_{1,2}$, and mirror-symmetry related moment of inertia matrices with respect to the center of mass $\mathbf{I}_{1,2}$. The legs are connected by a frictionless hinge at the hip with center point H and orientation $\hat{\mathbf{n}}$ normal to the symmetry plane of the legs. Each of the two legs can make rolling and collisional contact with the ground (slope = α) with no contact couples. The gravitational acceleration is $\mathbf{g}$. The model we studied is a simpler version of the one shown here: it had no hip spacing ($w = 0$) and point-feet ($r_1 = r_2 = 0$).

An open and possibly unanswerable question is whether the stability of this intermittently dissipative system can be explained, in part, by the fact that its piecewise holonomic constraints act somewhat like nonholonomic constraints.

Appendix A

Description of the Analysis, Numerical, and Simulation Procedures

Here we describe the gait analysis procedures using mathematical notation and the numerical simulation routines.

A.1 Return Map and Poincaré Section

Mathematically, a non-linear *function* or *map* is used to describe one stride of a walking device. This function can be written as $\mathbf{q} \mapsto \mathbf{f}(\mathbf{q}, \mathbf{p})$ or

$$ {}^{i+1}\mathbf{q}^{+} = \mathbf{f}({}^{i}\mathbf{q}^{+}, \mathbf{p}) \tag{A.1} $$

where ${}^{i}\mathbf{q}^{+}$ is a state vector describing the system at the start of a stride, say, the i_{th}, just after the last foot collision and $\mathbf{p}$ is a vector of geometric and inertia parameters. For instance, one component of $\mathbf{q}$ could be the angle of a leg measured with respect to the vertical and one element of $\mathbf{p}$ could be leg length. The mathematical description of the return map, fixed points, and stability is depicted in a phase space schematic (Figure A.1).

The definite 'point' at which the state of the system is sampled, just after a foot collision, is called the *Poincaré section* (typically denoted by Σ) and McGeer's stride function $\mathbf{f}$ is called a *Poincaré map*. The return map is a function of $\mathbf{q} \in \Sigma$, given by Equation (A.1). For any trajectory of the system, given an initial intersection with the Poincaré section, $\mathbf{q}_0$, the return map generates a sequence of iterates, $\mathbf{q}_1, \mathbf{q}_2, \mathbf{q}_3, \cdots$. The sequence of iterates on the section are called *orbits*.

The map $\mathbf{f}$ can be looked at as a composition of two maps, $\mathbf{f} = \mathbf{h} \circ \mathbf{d}$, which is convenient for analysis:

1. $\mathbf{d}$, which governs motion from just after collision i to just before collision $i + 1$, obtained by integrating the equation of motion $\mathbf{g}$ between collisions, and
2. $\mathbf{h}$, which governs support transfer, from just before to just after collision $i + 1$.

For more on the dynamics of maps see Hale and Kocak [84], Drazin [85], Devaney [86], and Guckenheimer and Holmes [51].

Numerically, $\mathbf{f}$ can cast as a subroutine incorporating integration of the nonlinear equations represented by $\mathbf{g}$, recognition of end-of-step contact, indexing of configuration variables and/or parameters at support transfer, and calculation of velocity changes due to the impulse at foot strike using $\mathbf{h}$.

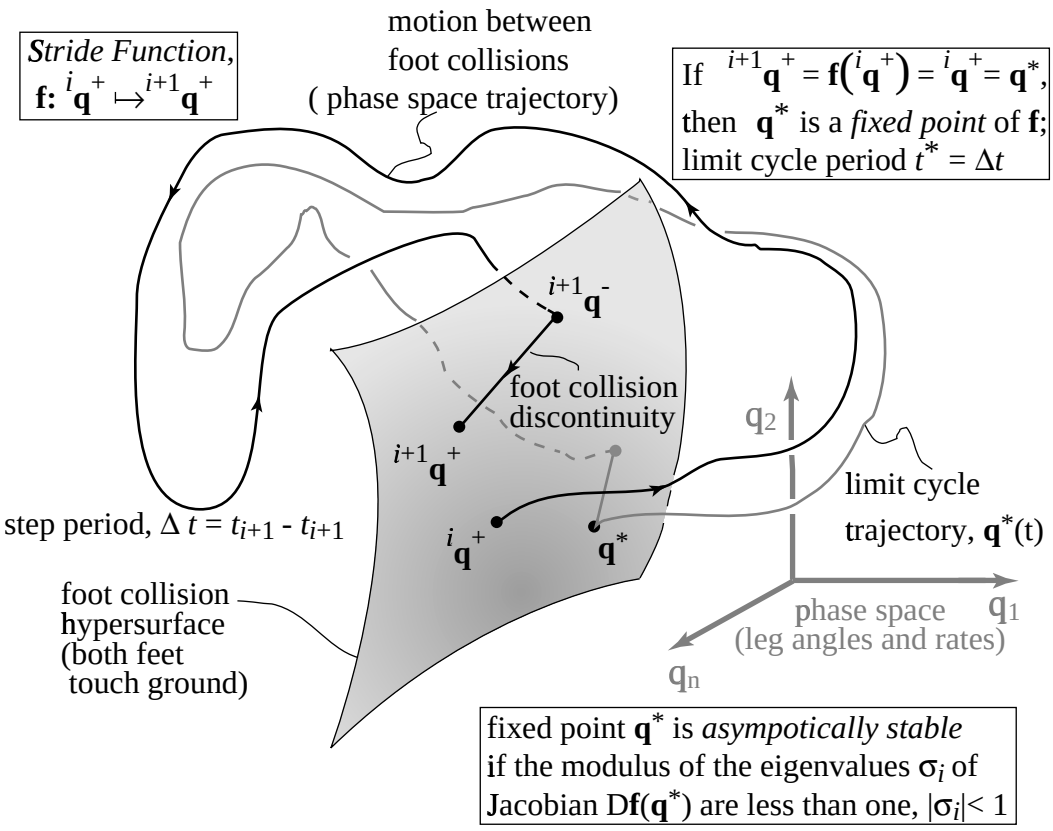

Figure A.1: Schematic of the stride function, fixed points, and stability in the phase space. The stride function takes as input the state of a system just after a collision, integrates forward in time along the phase space trajectory, detects a foot collision, determines the discontinuity in the state of the system due to the foot collision and returns as output the state of the system just after the next collision. When the output of the function equals the input, the state of the system is a fixed point of the stride map. If the moduli of the eigenvalues of the Jacobian of the stride function evaluated at a fixed point are all less than one, then the fixed point and its associated limit cycle motion are asymptotically stable.

Numerical Integration of the Equations of Motion and Collision Detection

We integrate the equations using a 4th-5th order automated step-sizing Runge-Kutta routine from MATLAB® modified to detect collisions. We detect collisions numerically using a method developed by Henon [62]. In Henon's method, the equations of motion between collisions $\mathbf{g}(\mathbf{q})$ are integrated until a collision detection inequality is violated (foot passes through the floor). Then, the equations of motion are recast in terms of the collision detection function (height of foot off of the floor) as the independent variable rather than time. Starting with the last integration step just before the foot passes through the floor, the equations are then integrated until the height of the foot off of the floor is zero to the Runge-Kutta tolerance.

The Henon algorithm is summarized as follows. First, we define a scalar *collision detection function* 'r' such that a collision occurs when

$$r(\mathbf{q}) = 0. \tag{A.2}$$

This function determines the surface of section. To the n state variables, we add an additional variable

$$q_{n+1} = r(\mathbf{q}) \tag{A.3}$$

and to the n dimensional system of differential equations of motion, $\dot{\mathbf{q}} = \mathbf{g}(\mathbf{q})$, we add the additional equation

$$\dot{q}_{n+1} = g_{n+1}(\mathbf{q}) \tag{A.4}$$

where

$$g_{n+1}(\mathbf{q}) = \nabla r \cdot \mathbf{g}. \tag{A.5}$$

Next, we divide the first n equations by the last $(n+1)_{th}$ one and inverting the last one to obtain

$$\begin{aligned} \frac{dq_1}{q_{n+1}} &= \frac{g_1}{g_{n+1}} \\ &\vdots \\ \frac{dq_n}{q_{n+1}} &= \frac{g_n}{g_{n+1}} \end{aligned} \tag{A.6}$$

$$\frac{d\tau}{q_{n+1}} = \frac{1}{g_{n+1}}. \tag{A.7}$$

In this way, time τ has now become a dependent variable and the collision detection function $q_{n+1} = r$ is now the independent variable.

In practice, we integrate $\mathbf{g}$ with respect to time τ until

$$q_{n+1} = r(\mathbf{q}) < 0 \tag{A.8}$$

and then switch to system (A.7). Using either the last computed point or the one before that, we integrate system (A.7) with respect to the new independent variable $q_{n+1} = r$ using the usual Runge-Kutta algorithm until the collision detection function is zeroed to the integration tolerance. The modified MATLAB® routine is called `int_henon3D_temp.m` and is displayed below. The routine also animates as it integrates; it calls `draw_walker3D`, for instance, to draw the 3D walker to the screen at each integration step. We have used this integration routine (as well as others using linear interpolation methods, e.g., method of false position) for simulating motions of the rimless wheels (Chapters 2 and 4), and the 2D and 3D walkers (Chapters 5 and 6). We show only the routines for the 3D walker below since the methods are the same for the others and the 2D walker is a special case of the 3D walker.

```
%************************************************************
%<><><><><><><><><><><><><><> int_henon3D_temp.m <><><><><><><><><><><
%************************************************************

% A modified 4th/5th order runge-kutta integrator based on the
% MATLAB function ode45.  This integrator integrates up until the
%  collision condition is met.   It stores the results in a matrix
% yout which has n columns for the Euler angles and their rates.

% Modified by Mike Coleman
%************************************************************

function [tout,yout,falls]=int_henon3D_temp(FunFcn,t0,tf,y0,...
contact,par,par1,trace);

% This program is a modified version of ODE45.  ODE45 is described
% below.

% ODE45  has been  modified to end when a collision detection
% function of the dependent  variables  reaches a desired final
% value, zero,  within the integration tolerance tol.  The program
% uses the automatic step size until the detection function becomes
% negative.  The program then uses the Henon method to  determine
% the state of the system at the collision, in several Runga-Kutta
% integration steps!  Henceforward, we will denote the collision
% detection function as s(x) and the collision detection condition
% as s(x)=0.  In simple terms, the collision detection function is
% elevation of the tip of the swing leg above the ground.

% ODE45 Integrate a system of ordinary differential equations using
% 4th and 5th order Runge-Kutta formulas.  See also ODE23 and
% ODEDEMO.M.
% [T,Y] = ODE45('yprime', T0, Tfinal, Y0) integrates the system
% of ordinary differential equations described by the M-file
% YPRIME.M over the interval T0 to Tfinal and using initial
% conditions Y0.
% [T, Y] = ODE45(F, T0, Tfinal, Y0, TOL, 1) uses tolerance TOL
% and displays status while the integration proceeds.
%
% INPUT:
% F     - String containing name of user-supplied problem description.
%         Call: yprime = fun(t,y) where F = 'fun'.
%         t      - Time (scalar).
%         y      - Solution column-vector.
%         yprime - Returned derivative column-vector;
%                  yprime(i) = dy(i)/dt.
% t0    - Initial value of t.
% tf- Final value of t.
% y0    - Initial value column-vector.
% tol   - The desired accuracy. (Default: tol = 1.e-6).
% trace - If nonzero, each step is printed. (Default: trace = 0).
%
% OUTPUT:
% T  - Returned integration time points (row-vector).
% Y  - Returned solution, one solution column-vector per tout-value.
%
% The result can be displayed by: plot(tout, yout).

%   C.B. Moler, 3-25-87.
%   Copyright (c) 1987 by the MathWorks, Inc.
%   All rights reserved.

%reset flops to zero
```

```
%flops(0)

% The Fehlberg coefficients:
alpha = [1/4  3/8  12/13  1  1/2]';
beta  = [ [    1      0      0     0      0    0]/4
          [    3      9      0     0      0    0]/32
          [ 1932  -7200   7296     0      0    0]/2197
          [ 8341 -32832  29440  -845      0    0]/4104
          [-6080  41040 -28352  9295  -5643    0]/20520 ]';
gamma =[[902880  0  3953664  3855735 -1371249 277020]/7618050
        [ -2090  0  22528  21970  -15048 -27360]/752400 ]';
pow = 1/5;
if nargin < 6, trace = 0; end
if nargin < 5, tol = 1.e-6; end


% Initialization
l=1;
t = t0;
hmax = (tf - t)/5;
hmin = (tf - t)/20000;
h = (tf - t)/100;

tol=par1(2);

y = y0(:);
ycheck=y;
f = y*zeros(1,6);

tout=t;
yout = y.';
tau = tol * max(norm(y, 'inf'), 1);

if trace
   clc, t, h, y
end

done = 0;

cnt=0;
cntr=0;

keep_going=0;
henon_const=1;

anim=par1(1);
%%%%%%%%%%%%%%%%%%%%%%%%%%%%%%%%%%%%%%%%%%%%%%%%%%%%%%%%%%%%%%%%%%%%%%%
%%%%%%%%%%%%%%%%%%%%%% DRAWING INITIALIZATION %%%%%%%%%%%%%
%%%%%%%%%%%%%%%%%%%%%%%%%%%%%%%%%%%%%%%%%%%%%%%%%%%%%%%%%%%%%%%%%%%%%%%
if (anim==0)        % If anim = 0, then do animation
  draw_flag = 0;
  [stanceleg,stancefoot,swingleg,swingfoot,hinge]=...
  draw_walker3D(y,draw_flag,contact);
end; % end conditional for animation
%%%%%%%%%%%%%%%%%%%%%%%%%%%%%%%%%%%%%%%%%%%%%%%%%%%%%%%%%%%%%%%%%%%%%%%
%%%%%%%%%%%%%%%%%%%%%%%%%%%%%%%%%%%%%%%%%%%%%%%%%%%%%%%%%%%%%%%%%%%%%%%
%<><><><><><><><><><><><><><><><><><><><><><><><><><><><><><><><><><><><
%% BEGIN MAIN INTEGRATION AND COLLISION DETECTION ROUTINE %%
%<><><><><><><><><><><><><><><><><><><><><><><><><><><><><><><><><><><><><
%%%%%%%%%%%%%%%%%%%%%%%%%%%%%%%%%%%%%%%%%%%%%%%%%%%%%%%%%%%%%%%%%%%%%%%

while done ~= 1 % main while loop

%%%%%%%%%%%%%%%%%%%%%%%%%%%%%%%%%%%%%%%%%%%%%%%%%%%%%%%%%%%%%%%%%%%%%%%
```

```
%%%%%%%%%%%%%%%%%% COMPUTE SLOPES %%%%%%%%%%%%%%%%%%%%%%%%
%%%%%%%%%%%%%%%%%%%%%%%%%%%%%%%%%%%%%%%%%%%%%%%%%%%%%%%%%%

 % Compute the slopes

 if henon_const==1             % If henon_const == 1, foot
                               % not passed through
                               % the ground yet.
   keep_going=0;
   temp = feval(FunFcn,yout(size(yout,1),:),par);
   f(:,1) = temp(:);
   for j = 1:5
    temp=feval(FunFcn,yout(size(yout,1),:)'+h*f*beta(:,j),par);
         f(:,j+1) = temp(:);
   end
 % Estimate the error and the acceptable error

      delta = norm(h*f*gamma(:,2),'inf');
    %  tau = tol*max(norm(y,'inf'),1.0);
       tau = tol*max(norm(yout(size(yout,1),:),'inf'),1.0);
      %error_crit=tau-delta
 else
              % If foot passes through the ground, back up
              % and detect the collision corresponding state
              % using the Henon method.

%%%%%%%%%%%%%%%%%%%%%%%%%%%%%%%%%%%%%%%%%%%%%%%%%%%%%%%%%%%
%%%%%%%%%%%% HENON METHOD - INNER WHILE LOOP %%%%%%%%%%%%%%%
%%%%%%%%%%%%%%%%%%%%%%%%%%%%%%%%%%%%%%%%%%%%%%%%%%%%%%%%%%%
%  The collision detection function s(x), up until now a
%  DEPENDENT variable, becomes instead the INDEPENDENT variable.
%  Time, on the other hand, becomes a DEPENDENT variable. Now
%  that we have entered this loop, we stay in it until the
%  collision is detected.  Then we exit and make a final update
%  to the time and state vector output arrays.

% Initialization for the inner Henon loop

tt = coll_crit0;      % Now, in the standard Runga-Kutta routine,
                      % s(x) has become the "time variable", "t".

hhmax = (coll_critf - tt);
hh = hhmax;
f = zeros(length(y),6);
k = 1;
touth(k) = tt;
youth(k,:) = y.';

% The inner Henon while loop

  while (tt > coll_critf) & (tt + hh < tt)

   if tt + hh < coll_critf,
     hh = coll_critf-tt;
   end

   % Compute the slopes
   temp = feval(FunFcn,y,par); % compute regular derivatives with
                               % time as independent variable at
                               % the current state.

   henon_const=temp(9);        % compute s'(x).

   temp = temp/henon_const;    % convert the derivatives to
```

```
                              % functions of the collision
                              % detection function as
                              % the independent variable
   f(:,1) = temp(:);

    for j = 1:5
      temp = feval(FunFcn,  y+hh*f*beta(:,j),par);
      henon_const=temp(9);
      temp = temp/henon_const;
      f(:,j+1) = temp(:);
   end

   % Estimate the error and the acceptable error

   delta = norm(hh*f*gamma(:,2),'inf');
   tau = tol*max(norm(y,'inf'),1.0);

   % Update the solution only if the error is acceptable

    if delta <= tau
      tt = tt + hh;
      y = y + hh*f*gamma(:,1);
      k = k+1;

      touth(k) = tt;
      youth(k,:) = y.';

    end

    if trace
      home, tt, hh, y
    end

   % Update the step size

    if delta ~= 0.0
      hh = max(hhmax, 0.8*hh*(tau/delta)^pow);
    end

  end;
%%%%%%%%%%%%%%%%%%%%%%%%%%%%%%%%%%%%%%%%%%%%%%%%%%%%%%%%%%%%%%%%%%%%%%%
%%%%%%%%%%%%%%% END INNER HENON WHILE LOOP %%%%%%%%%%%%%%%%%
%%%%%%%%%%%%%%%%%%%%%%%%%%%%%%%%%%%%%%%%%%%%%%%%%%%%%%%%%%%%%%%%%%%%%%%

if y(5)>tol & y(7)<pi-tol
  done=1;  % done is set to one after the Henon loop is done
           % to signal the main while loop to end once the
           % Henon calculation is done.
else
  keep_going=1;
  henon_const=1;
  start_check=0;
  yout(last+1,:)=y';
  tout(last+1)=youth(k,10);
end
  if (t < coll_critf)
   disp('Singularity likely.')
   t
  end
end; % end conditional loop for entering into the Henon
     % calculation.
%%%%%%%%%%%%%%%%%%%%%%%%%%%%%%%%%%%%%%%%%%%%%%%%%%%%%%%%%%%%%%%%%%%%%%%
%%%%%%%%% DECIDE IF READY TO CHECK FOR COLLISION  %%%%%%%%%
%%%%%%%%%%%%%%%%%%%%%%%%%%%%%%%%%%%%%%%%%%%%%%%%%%%%%%%%%%%%%%%%%%%%%%%
```

```
if keep_going == 0 & done ~= 1
% Calculate new time and state

           tcheck = tout(length(tout)) + h;
           ycheck = yout(size(yout,1),:)' + h*f*gamma(:,1);

% Check to see if walker falls over

 if delta<=tau & abs(ycheck(5))>pi/4 | abs(ycheck(1))>pi/4 |...
   abs(ycheck(3))>pi/4
             done=1;
             disp('falls over')
             falls=1;
 else
             falls=0;
 end;  % End falling over check.

% If stance and swing angles are appropriate, start to look
% for collisions.

if (delta <= tau) & (ycheck(5)>tol) & (ycheck(7)< pi - tol)
   start_check = 1;
end
%%%%%%%%%%%%%%%%%%%%%%%%%%%%%%%%%%%%%%%%%%%%%%%%%%%%%%%%%%%%%%%%%%%

%%%%%%%%%%%%%%%%%%%%%%%%%%%%%%%%%%%%%%%%%%%%%%%%%%%%%%%%%%%%%%%%%%%
%%%%%%%%%% COLLISION DETECTION AND SOLUTION UPDATE %%%%%%%%%%%
%%%%%%%%%%%%%%%%%%%%%%%%%%%%%%%%%%%%%%%%%%%%%%%%%%%%%%%%%%%%%%%%%%%
% As we integrate the equations of motion, we are also updating
% the collision detection function.  We seek to find when it
% passes through zero; i.e., when s(x) < 0. In the derivative
% file, the collision detection function is the ninth state
% variable (y(9)) and the tenth is time.

        %  As long as the collision detection function is > 0,
        %  we proceed with the usual Runga-Kutta routine.

  if start_check ==1 & done~=1 % Solution is already acceptable,
                               % delta <= tau.
       last=size(yout,1);

       if pi-ycheck(7)-(2*ycheck(5)) >tol

         tout = [tout; tcheck];    % Usual Runge-Kutta solution
                                   % update.
         yout = [yout; ycheck.'];

     %  If the collision detection function becomes less than
     %  zero, we stop with the usual routine and branch
     %  to the Henon loop, as long as we've taken a FORWARD
     %  step (y(5)>0) & (y(7)<pi).

       elseif pi-(2*yout(last,5))-yout(last,7)>tol

    %  If s(x) becomes < 0, (y(9) <0),  we stop with the usual
    % routine and branch to the Henon loop --- as long as
    %  we've taken a FORWARD step (y(5)>0) & (y(7)<pi) and
    % the in the last integration step, s(x)>0! That is,
    % after we are ready to check for a collision, the foot
    % has to be above the ground.
            y=yout(last,:)';
            temp = feval(FunFcn,y,par);
            henon_const= temp(9);
```

```
% We set the henon_const to be the to be the value of s'(x) at
% the state of the walker at the the last step BEFORE s(x)<0.
% The current value of s(x) BEFORE  s(x) < 0.

     coll_crit0=pi-(2*y(5))-y(7);

           coll_critf=0.0;      % The desired value of s(x).

       else

% If start_check = 1 but the  foot was not above the ground
% at the last integration step we record the current time
% and state here.

           tout = [tout; tcheck];
           yout = [yout; ycheck.'];
       end; %  Ends checking for forward collision.
   elseif (delta <= tau)

% If start_check ~= 1, then we  update.

        tout = [tout; tcheck];
        yout = [yout; ycheck.'];

   end; % Ends loop for collision detection and Runge-Kutta
        % solution update.

   % Update the step size

   if (delta ~= 0.0)
       h=0.8*h*(tau/delta)^pow;
   end

   if trace
       home, h, y
   end
end;
%%%%%%%%%%%%%%%%%%%%%%%%%%%%%%%%%%%%%%%%%%%%%%%%%%%%%%%%%%%%%%%%%%%%%%%
%%%%%%%%%% DRAW WALKER IN CURRENT CONFIGURATION %%%%%%%%%%%%
%%%%%%%%%%%%%%%%%%%%%%%%%%%%%%%%%%%%%%%%%%%%%%%%%%%%%%%%%%%%%%%%%%%%%%%
  if (anim==0) % do animation if anim = 0.
   if (delta<=tau) & henon_const == 1 % draw walker pre-Henon
                                      % method loop.
    draw_flag=1;
    draw_walker3D(yout(size(yout,1),:),draw_flag,contact,...
              stanceleg,stancefoot,swingleg,swingfoot,hinge);

   else                % draw walker post- Henon method loop.
    draw_flag=1;
    draw_walker3D(y,draw_flag,contact,stanceleg,stancefoot,...
                  swingleg,swingfoot,hinge);
   end;
  end;
%%%%%%%%%%%%%%%%%%%%%%%%%%%%%%%%%%%%%%%%%%%%%%%%%%%%%%%%%%%%%%%%%%%%%%%
end;  % end main while loop

%%%%%%%%%%%%%%%%%%%%%%%%%%%%%%%%%%%%%%%%%%%%%%%%%%%%%%%%%%%%%%%%%%%%%%%
%<><><><><><><><><><><><><><><><><><><><><><><><><><><><><><><><><><><><
%%% END  MAIN INTEGRATION AND COLLISION DETECTION ROUTINE  %%
%<><><><><><><><><><><><><><><><><><><><><><><><><><><><><><><><><><><><><
%%%%%%%%%%%%%%%%%%%%%%%%%%%%%%%%%%%%%%%%%%%%%%%%%%%%%%%%%%%%%%%%%%%%%%%

%%%%%%%%%%%%%%%%%%%%%%%%%%%%%%%%%%%%%%%%%%%%%%%%%%%%%%%%%%%%%%%%%%%%%%%
%%%%%%%%%%%%%%%%%% FINAL SOLUTION UPDATE %%%%%%%%%%%%%%%%%%%%
```

```
%%%%%%%%%%%%%%%%%%%%%%%%%%%%%%%%%%%%%%%%%%%%%%%%%%%%%%%%%%%%%%%%%%%%%%%

if done==1 & henon_const~=1

%  Catenate post- Henon method solutions to pre-Henon method
%  solutions.

tout = [tout; youth(2:k,10)];
yout = [yout; youth(2:k,:)];

end
%%%%%%%%%%%%%%%%%%%%%%%%%%%%%%%%%%%%%%%%%%%%%%%%%%%%%%%%%%%%%%%%%%%%%%%

%%%%%%%%%%%%%%%%%%%%%%%%%%%%%%%%%%%%%%%%%%%%%%%%%%%%%%%%%%%%%%%%%%%%%%%

%************************************************************
%<><><><><><><><><><><><> draw_walker3D  <><><><><><><><><><
%************************************************************
function [stanceleg,stancefoot,swingleg,swingfoot,hinge]= ...
draw_walker3D(y,draw_flag,contact,hand1,hand2,hand3,hand4,...
hand5);
%%%%%%%%%%%%%%%%%%%% BEGIN DRAWING INITIALIZATION %%%%%%%%%%
% Draw walker in initial state

leg=1;

stancepoints=[0,0,leg]'; % define stance leg

swingpoints=[0,0,leg]';  % define swing leg

%y(1)=20*y(1);
%y(3)=20*y(3);
%y(5)=3*y(5);
%y(7)=15*y(7);

%<><><><><><><><><THE ROTATION MATRICES><><><><><><><><><><><><><><>
% Define the rotation matrices with the current state from
% int_henon3D_temp.m

rot1st=[1,0,0;0,cos(y(3)),sin(y(3));0,-sin(y(3)),cos(y(3))];
rot2st=[cos(y(5)),0,-sin(y(5));0,1,0;sin(y(5)),0,cos(y(5))];
rot3st=[cos(y(1)),sin(y(1)),0;-sin(y(1)),cos(y(1)),0;0,0,1];
rot_st=rot2st*(rot1st*rot3st);

rotthetasw = [cos(y(7)),0,-sin(y(7)); 0,1,0; ...
              sin(y(7)), 0,cos(y(7))];

rotationmatrix_sw= rot_st*rotthetasw;

%############################################################
% Find coordinates of stance and swing legs at current state

rotstance=rot_st'*stancepoints;
rotswing_st= rotthetasw'*swingpoints;
swingpoint_st=rotswing_st+stancepoints;
swingpoint=rot_st'*swingpoint_st;

contactpoint=contact';
hingepoint=rotstance+contactpoint;
swingpoint=swingpoint + contactpoint ;
%############################################################
% Draw the walker in initial configuration using the line
%command  of Matlab's HandleGraphics.

if draw_flag ==0
```

```
view([1 1 1]);
axis([-1 1 -1 1 -1 1]);
axis equal
ylabel('y')
xlabel('x')
zlabel('z')
ground_line=...
   line('color','y','linestyle','-.','erase','none',...
                'xdata',[-1 1],...
                'ydata',[0 0],...
                'zdata',[0 0]);

stanceleg=...
line('color','y','linestyle','-','erase','background',...
                'xdata',[contactpoint(1),hingepoint(1)],...
                'ydata',[contactpoint(2),hingepoint(2)],...
                'zdata',[contactpoint(3),hingepoint(3)]);
stancefoot=...
line('color','y','linestyle','o','erase','background',...
                'xdata',contactpoint(1),...
                'ydata',contactpoint(2),...
                'zdata',contactpoint(3));

swingleg=...
line('color','y','linestyle',':','erase','background',...
               'xdata',[hingepoint(1),swingpoint(1)],...
               'ydata',[hingepoint(2),swingpoint(2)],...
               'zdata',[hingepoint(3),swingpoint(3)]);
%              'linewidth',[2.5],...
swingfoot=...
line('color','y','linestyle','o','erase','background',...
                'xdata',swingpoint(1),...
                'ydata',swingpoint(2),...
                'zdata',swingpoint(3));
hinge=...
line('color','y','linestyle','.','erase','background',...
                'markersize',[36],...
                'xdata',hingepoint(1),...
                'ydata',hingepoint(2),...
                'zdata',hingepoint(3));


else % if in midst of integration, reset the line data at
     %each step.

set(hand1,'xdata',[contactpoint(1),hingepoint(1)],...
                 'ydata',[contactpoint(2),hingepoint(2)],...
                 'zdata',[contactpoint(3),hingepoint(3)]);
set(hand2,'xdata',contactpoint(1),...
                 'ydata',contactpoint(2),...
                 'zdata',contactpoint(3));

set(hand3,'xdata',[hingepoint(1),swingpoint(1)],...
                 'ydata',[hingepoint(2),swingpoint(2)],...
                 'zdata',[hingepoint(3),swingpoint(3)]);

set(hand4,'xdata',swingpoint(1),...
                 'ydata',swingpoint(2),...
                 'zdata',swingpoint(3));

set(hand5,'xdata',hingepoint(1),...
                 'ydata',hingepoint(2),...
                 'zdata',hingepoint(3));
```

```
drawnow; redraw to the screen with new data.

end
%%%%%%%%%%%%% END DRAWING INITIALIZATION %%%%%%%%%%%%%%%%%%
```

A.2 Fixed points and Periodic Motions

For cyclic or *period-k* gait, we must find solutions to Equation (A.1) $\mathbf{q}^*$ which map to themselves after k steps

$$\mathbf{q}^* = \mathbf{f}^k(\mathbf{q}^*, \mathbf{p}). \tag{A.9}$$

A *period-one* gait cycle ($k = 1$) corresponds to a state that returns to itself after *one* step and is called a *fixed* point of $\mathbf{f}$. For a *period-two* gait cycle ($k = 2$), the state after a collision repeats itself after *two* steps, and so on. Henceforward, when we use the term *gait cycle* we mean *period-one* gait cycle.

On a Poincaré section, periodic motions appear as fixed points; thus a k parameter family of periodic motions appears as a k dimensional hypersurface or manifold on the Poincaré section.

We can fail to find walking solutions in numerical investigations (searches for fixed points of the stride map $\mathbf{f}$) if (1) the Jacobian becomes singular; (2) the initial guess for the Newton's method search is not good enough to converge to a limit cycle motion; and (3) no periodic motions exist for the given parameters [3].

Using the Newton-Raphson Method for Finding Fixed Points

Numerical procedures such as Newton's multi-dimensional root finding method, which we describe here, may be invoked to find fixed points numerically.

First, introduce a new function $\mathbf{S}(\mathbf{q}) = \mathbf{f}(\mathbf{q}) - \mathbf{q}$. Then, fixed points of $\mathbf{f}$ are roots of $\mathbf{S}(\mathbf{q}) = \mathbf{0}$. Let $\mathbf{q}_k$ be an initial guess at state of the system that is not a fixed point of $\mathbf{f}$. Then $\mathbf{S}(\mathbf{q}_k) = \mathbf{f}(\mathbf{q}_k) - \mathbf{q}_k \neq \mathbf{0}$. We would like to find corrections Δq_k such that, for $\mathbf{q}_{k+1} = \mathbf{q}_k + \Delta q_k$, $\mathbf{S}(\mathbf{q}_{k+1})$ converges to $\mathbf{0}$ as $k \to \infty$. To a linear approximation, $\mathbf{S}$ can expanded in a neighborhood of $\mathbf{q}$ as

$$\mathbf{S}(\mathbf{q}_{k+1}) = \mathbf{S}(\mathbf{q}_k) + D\mathbf{S}(\mathbf{q}_k)\,\Delta q_k \tag{A.10}$$

where $D\mathbf{S}(\mathbf{q}_k)$ is the Jacobian of $\mathbf{S}$ evaluated at $\mathbf{q}_k$. Setting $\mathbf{S}(\mathbf{q}_{k+1}) = \mathbf{0}$, we obtain a set of linear equations that can be solved for the corrections Δq_k

$$\Delta q_k = -\left[D\mathbf{S}(\mathbf{q}_k)\right]^{-1}\,\mathbf{S}(\mathbf{q}_k). \tag{A.11}$$

In terms of the original function $\mathbf{f}$, Δq_k is

$$\Delta q_k = -\left[D\mathbf{f}(\mathbf{q}_k) - \mathbf{I}\right]^{-1}\,\left(\mathbf{f}(\mathbf{q}_k) - \mathbf{q}_k\right). \tag{A.12}$$

The corrections Δq_k are added to the previous estimate of the root and the process is iterated to convergence. In practice, the iteration process terminates when the norm of $\mathbf{S}$ is less than some tolerance. In cases where the Jacobian of the function whose zeroes are to be found cannot be evaluated explicitly, it must be found numerically, using a finite difference approach, for instance. Section A.3.2 describes such a procedure. The Newton's method routine we use to study the 3D walker, `newton_3D.m`, is displayed below. In it is nested a Newton's method routine used to first find a 2D fixed point for a 3D walker constrained to planar walking. This fixed point is used as a starting point for the 3D fixed point search. This approach saves considerable computation effort. The routine finds roots of $g(x) = 0$ where $g(x) = f(x) - x$ and $f(x)$ is one evaluation of the return map. $g(x)$ is returned by `driver_fixedpt3D.m` which integrates the equations of motion and applies

the collision rules. `driver_fixedpt3D.m` calls `int_henon3D_temp.m` (described above) which in turn calls the derivative file `derivs_3D.m`. `derivs_3D.m` returns the derivative vector; it evaluates the derivatives using a `*.mex` file called `deriv_stuff3D_test.mex4`. The `*.mex` file was created from the `*.c` file called `deriv_stuff3D_test.c`. The collision rule is applied by calling `jump_walker3D`. Each of these routines is displayed below as well (except for the `deriv_stuff3D_test.mex4` which is not human-readable). We show only the routines for the 3D walker since 2D walker is a special case of the 3D walker and we did not search for fixed points for the 3D rimless wheel. The driver and collision rule routines are representative of those used for any other numerical simulations carried out in this dissertation.

```
%************************************************************
%<><><><><><><><><><><><>   newton_3D.m    <><><><><><><><><><><
%************************************************************
function [max_eig,fixed_pt,eigs,eigvs,t_final,falls]=...
                                        newton_3D(fun,init,par)

%This is a program used to solve  g(x)=0, for non-linear vector
%function g of several variables using Newton's method.  fun
% generates g(x).

x=init;

%First, search for 2D fixed point with given parameters and
%intial state.

x2D=init(5:8);
subset2D=[2 7 8 9 11];
par2D=par(subset2D);
[max_eig2D,fpt2D,eigs2D,eigvs2D,tf2D,falls]=...
newton_2D('driver_fixedpt2D',x2D,par2D)
%If find 2D fixed point, start search for 3D fixed point
%or else quit.

if falls == 0 % else, branch to end, no output.

x=[0 0 0 0, fpt2D']';
xx=x;
jac_iter0=0;
scale_factor=(1e-4*max(1,norm(x)));
length_x=length(x);
pert=eye(length_x)*scale_factor;
newt_incr=0;
newt_max=100;
delta_x=0;

% Make first 3D function evaluation, g(x0).

   [eval_fun,tf,falls,t_step]=feval(fun,x,par);
     % gives g(x) incl. constraint on  heading

    if falls == 0
%       mapstr=['one map iteration  completed'];
%       disp(mapstr);
    elseif falls == 1
       mapstr=['one map iteration not completed'];
       disp(mapstr);
       newt_incr=newt_max+1;
    end

% Remember, the function we are finding the solution
%to is g(x)=0 so that when g(x)[eval_fun(x)] < epsilon
%where epsilon is << 1, we have found a fixed point of
```

```
%g(x)=0 which is a solution to f(x)=x.

  if falls==0
   norm_g0=norm(eval_fun)
  end

  if norm_g0 <= 1.e-8 & falls == 0

   disp('no search needed')

   while jac_iter0<length_x
    jac_iter0=jac_iter0+1;
    [eval_fun1,tf1,falls,t_step]=...
                           feval(fun,x+pert(:,jac_iter0),par);
    jacobian_g(:,jac_iter0)=...
    (eval_fun1(1:length_x)-eval_fun(1:length_x))/scale_factor;
      if falls == 0
%      mapstr=...
         ['map iteration ',num2str(jac_iter0),' completed'];
%          disp(mapstr);
      elseif falls == 1
       mapstr=...
        ['map iteration ',num2str(jac_iter0),' not completed'];
          disp(mapstr);
          jac_iter0=length_x+1;
      end
    end
  end

  if falls==0
    jacobian_f=jacobian_g+eye(length_x);
    fixed_pt=x;  %store fixed points;
    [v,D]=eig(jacobian_f);
    eigs=diag(D);
    eigvs=v;
    max_eig=max(abs(diag(D)));
    t_final=tf;
  end
  norm_g_rec=norm_g0;
  while (norm(eval_fun)>1.e-8)&(newt_incr<newt_max)

    newt_incr=newt_incr+1  % update while loop counter

    norm_g=norm(eval_fun)
    norm_g_rec=[norm_g_rec,norm_g];
    save norm_stuff norm_g_rec

    % Calculate Jacobian of function numerically
    jac_iter=0;
    while jac_iter<length_x
     jac_iter=jac_iter+1;
     [eval_fun1,tf1,falls,t_step]=feval(fun,x+pert(:,jac_iter),par);
     jacobian_g(:,jac_iter)=...
          (eval_fun1(1:length_x)-eval_fun(1:length_x))/scale_factor;
    if falls == 0
%       mapstr=['map iteration ',num2str(jac_iter),' completed'];
%       disp(mapstr);
     elseif falls == 1
      mapstr=['map iteration ',num2str(jac_iter),' not completed'];
      disp(mapstr);
      jac_iter=length_x+1;
     end
    end
```

```
    % Compute new estimate of x.

    if jac_iter==length_x
      jacobian_aug=[jacobian_g;eye(1,length_x)];
    end % Jacobian is augmented with another row to account
        % for heading constraint

   if falls == 0
    cond(jacobian_aug)
    delta_x=(jacobian_aug\eval_fun)
    x=x-delta_x;
    xx=[xx,x];

   % Evaluate function at newest x for next iteration

    [eval_fun,tf,falls,t_step]=feval(fun,x,par);

   elseif delta_x~=0
    x=xx(:,size(xx,2)-1);
    damping=0.5
    delta_x=damping*delta_x;
    x_falls=x-delta_x;

    % Evaluate function at newest x for next iteration
    [eval_fun,tf,falls,t_step]=feval(fun,x_falls,par);

   else newt_incr=newt_max+1;

   end
end
if falls==0 & newt_incr <newt_max
  jacobian_f=jacobian_g+eye(length_x);

  fixed_pt=x;  %store fixed points
  [v,D]=eig(jacobian_f);
  eigs=diag(D);
  eigvs=v;
  max_eig=max(abs(diag(D)))
  t_final=tf;
end
   % Display to screen if method does not converge on a root.
     if newt_incr >= newt_max | falls == 1
       disp('did not converge')
       falls=1;
     end
else

falls=1
disp('Cannot step 2D, did not converge3D')
%%%%%%%%%%%%%%%%%%%%%%%%%%%%%%%%%%%%%%%%%%%%%%%%%%%%%%%%%%%%%%%%%%%%%%%
end

%<><><>
```

```
% The output of the function is g (the difference between the
% state of the system after two collisions and the initial
% state), t_final (the elapsed time over two steps = one map
% iteration), and falls (flag to indicate the walker has
% fallen over).

% At the end of the program there are small calculations for
% potential, kinetic and total energy for the entire time of
% simulation.

%Written by Mike Coleman
%***********************************************************
function [g,t_final,falls,t_step]=driver_fixedpt3D(x,params)
%***********************************************************

input=x;

% Reset the integration start time to zero.

t_initial=0;
t_final=0.1;

% Define initial input for use with Henon method which makes
% the collision detection funtion the (N+1)th state variable
% and time the (N+2)th state variable

x0_9=pi-(2*x(5))-x(7);

initial=[input',x0_9,t_initial];

anim=1;               % If anim=0, then animation is turned on.

do_energy=1;          % If do_energy=0, then do energy
                      % calculations and plots.
do_state=0;           % If do_state=0, then do state variable
                      % plots.
if anim==0
 clf reset
end

tol = 1.e-8;           % tolerances for integration;

collisions= 2  ;       % number of collisions to simulate

falls = 0;             % falling over flag initialized at 0
                       % for not falling over.

%Initialize position of current spoke on the ground.

contact=[0 0 0];     % Initialize position of current spoke
                     % on the ground.

params1=[anim tol];
%<><><><><><><><><><><><><><><><>< The Main Loop ><><><><><><><><

% Here is the algorithm...

for inc=1:collisions
t_init=t_initial;
  if falls == 0
% Integrate with the current initial conditions using
% derivs_3D.m.  The integration stops at a collision.
```

```
[t,x,falls]=int_henon3D_temp('derivs_3D',t_initial,...
        t_final+t_initial,initial,contact,params,params1,0);
length_x=size(x,1);
t_step=t(length(t))-t_init;
if do_energy ==0 | do_state == 0
 length_t=length(t);
 time=[time;t];
 output=[output;x];
 length_trec=[length_trec,length_t];
end

%Display collision to screen

if falls==0
     collisionstr=['collision ',num2str(inc),' detected'];
     %disp(collisionstr);
else
    collisionstr=['collision ',num2str(inc),' not detected'];
    disp(collisionstr);
end

%APPLICATION of the JUMP CONDITION

[newconsts3D,angdotp]=jump_walker3D(x,params);

xplus=[x(length_x,1) angdotp(1) x(length_x,3) angdotp(2) ...
   -x(length_x,5) angdotp(3) pi+2*x(length_x,5) angdotp(4)];

params=[newconsts3D,params(length(params))]';
params_rec=[params_rec,params];

t_initial=x(length_x,10);

x0_9=x(length_x,9);
initial=[xplus,x0_9,t_initial];

x1=x(length_x,1);
x3=x(length_x,3);
x5=x(length_x,5);
x7=x(length_x,7);

% Compute new x-y position of foot after a collision

deltax=sin(x5)*cos(x1)+cos(x5)*sin(x3)*sin(x1)+sin(x7)*...
   cos(x5)*cos(x1)-sin(x7)*sin(x5)*sin(x3)*sin(x1)+cos(x7)*...
   sin(x5)*cos(x1)+cos(x7)*cos(x5)*sin(x3)*sin(x1);

deltay=sin(x5)*sin(x1)-cos(x5)*sin(x3)*cos(x1)+sin(x7)*...
   cos(x5)*sin(x1)+sin(x7)*sin(x5)*sin(x3)*cos(x1)+cos(x7)*...
   sin(x5)*sin(x1)-cos(x7)*cos(x5)*sin(x3)*cos(x1);

     contact=contact+[deltax deltay 0];
  end; % end falling over conditional loop

end % end for loop to integrate over k collisions

g=xplus(1:8)-input(1:8)';
g=[g';input(1)-params(length(params))];
t_final=t_initial;

% Compute total energy

if do_energy == 0
 time=output(:,10);
```

```
 [pot,kin,tot]=energy_try(length_trec(1),params,...
                          output(1:length_trec(1),:));
 [pot1,kin1,tot1]=...
       energy_try(size(output,1),params_rec(:,1),...
       output(length_trec(1)+1:sum(length_trec),:));
  energy_data=[pot,kin,tot;pot1,kin1,tot1];
  eplot=energy_plots(time,energy_data(:,1),...
       energy_data(:,2),energy_data(:,3));
end

if do_state == 0
 time=output(:,10);
 plot(time,output(:,5),time,output(:,7)+output(:,5)-pi)
 plot(time,output(:,1),time,output(:,3))
 splot=state_var_plots(input,time,output);
end
%%%%%%%%%%%%%%%%%%%%%%%%%%%%%%%%%%%%%%%%%%%%%%%%%%%%%%%%%%%%%%%%%%%%%%%%%%%%%%%
%%%%%%%%%%%%%%%%%%%%%%%%%%%%%%%%%%%%%%%%%%%%%%%%%%%%%%%%%%%%%%%%%%%%%%%%%%%%%%%
%<><><><><><><><><><><> derivs_3D.m <><><><><><><><><><><><><>
%%%%%%%%%%%%%%%%%%%%%%%%%%%%%%%%%%%%%%%%%%%%%%%%%%%%%%%%%%%%%%%%%%%%%%%%%%%%%%%
%This file outputs the derivative vector for the 3D walker.

function xdot=derivs_3D(x,constants)

xdot=zeros(1,10);

coef_matrix=deriv_stuff3D_test(x(8),x,constants)';
               % the mex-file called here computes a
               % coef_matrix matrix and a right hand side
               % of a linear equation to be solved for the
               % second derivatives.

mass_matrix=coef_matrix(2:5,2:5);
rhs=coef_matrix(2:5,6);
ddot=(mass_matrix\rhs)';     % Using backslash to solve
         % to solve for 2nd derivs.

%  The first order system of equations of motion for the
%  3D walker  with point  feet.

xdot(1)=x(2);
xdot(2)=ddot(1);
xdot(3)=x(4);
xdot(4)=ddot(2);
xdot(5)=x(6);
xdot(6)=ddot(3);
xdot(7)=x(8);
xdot(8)=ddot(4);
%%%%%%%%%%%%%%%%%%%%%%%%%%%%%%%%%%%%%%%%%%%%%%%%%%%%%%%%%%%%%%%%%%%%%%%%%%%%%%%
%%%%% Additional Derivatives for the Henon Method %%%%%%%%%%%%
%%%%%%%%%%%%%%%%%%%%%%%%%%%%%%%%%%%%%%%%%%%%%%%%%%%%%%%%%%%%%%%%%%%%%%%%%%%%%%%
funs=xdot(1:8);% This is a vector containing the 8 first order
               % derivatives of the system of equations of
               % motion.

% Below is the gradient of the collision  detection function.

grad_coll_crit=[0 0 0 0 -2 0 -1 0];

xdot(9)= funs*grad_coll_crit';

%  The derivative of the collision detection
%  function, with respect to the state
%  variables, is equal to the dot product of
```

```
%  its gradient with their derivatives.

xdot(10)=1;         %  The tenth "state variable" is time which
                    %  is  updated here as well as in the
                    %  Runge-Kutta routine that calls this file.
%%%%%%%%%%%%%%%%%%%%%%%%%%%%%%%%%%%%%%%%%%%%%%%%%%%%%%%%%%%%%%%%%%%%%%%%%%%%
```

```
/* <><><>
```

```
      double alpha=constants[7];
      double x=constants[8];
      double y=constants[9];
      double z=constants[10];

      double x1=q[0];
      double q2=q[1];
      double x3=q[2];
      double q4=q[3];
      double x5=q[4];
      double q6=q[5];
      double x7=q[6];
      double q8=q[7];

      double sx1=sin(x1);
      double cx1=cos(x1);
      double sx3=sin(x3);
      double cx3=cos(x3);
      double sx5=sin(x5);
      double cx5=cos(x5);
      double sx7=sin(x7);
      double cx7=cos(x7);
      double ca=cos(alpha);
      double sa=sin(alpha);

 /*   c1sq=c1*c1;
      s1sq=s1*s1;
      c3sq=c3*c3;
      s3sq=s3*s3;
      c5sq=c5*c5;
      s5sq=s5*s5;
      c7sq=c7*c7;
      s7sq=s7*s7; */

      double xsq=x*x;
      double ysq=y*y;
      double zsq=z*z;

(For the sake of brevity, we do not include the
intermediate variables or the definitions of the
M(q), V(q), and G(q) matrices.  They are
produced as output of Maple$^{\circledR}$ in optimized format
and are too long to be useful to reproduce here.
We do, however, show how the data is stored in
coef_matrix to prepare it for derivs_3D.m)

/*  Coefficient Matrix Intermediate Variables     */
/*  Velocity Terms Matrix Intermediate Variables  */
/*  Applied Moment Vector Intermediate Variables  */
/*  Coefficient Matrix                            */
/*  Velocity Terms Matrix                         */
/*  Applied Moment Vector                         */

      vel_terms[1]=q2*q2;
      vel_terms[2]=q4*q4;
      vel_terms[3]=q6*q6;
      vel_terms[4]=q8*q8;
      vel_terms[5]=q2*q4;
      vel_terms[6]=q2*q6;
      vel_terms[7]=q2*q8;
      vel_terms[8]=q4*q6;
      vel_terms[9]=q4*q8;
      vel_terms[10]=q6*q8;
```

```
       for(i=1; i<5;i++){
         vel_vect[i]=0.;
       for(j=1;j<11;j++)
         vel_vect[i]=vel_vect[i]+vel_matrix[i][j]*vel_terms[j];
       }

       coef_matrix[1][5]=vel_vect[1]+applmom_vect[1];
       coef_matrix[2][5]=vel_vect[2]+applmom_vect[2];
       coef_matrix[3][5]=vel_vect[3]+applmom_vect[3];
       coef_matrix[4][5]=vel_vect[4]+applmom_vect[4];

     return;
}

#ifdef __STDC__
void mexFunction(
int nlhs,
Matrix *plhs[],
int nrhs,
Matrix *prhs[]
)
#else
mexFunction(nlhs, plhs, nrhs, prhs)
int nlhs, nrhs;
Matrix *plhs[], *prhs[];
#endif
{
double *coef_matrix;
double *t,*q,*constants;
unsigned int m,n;

        m=6;
        n=5;

/* Create a matrix for the return argument */

        COEF_MATRIX_OUT = mxCreateFull(m,n,REAL);

/* Assign pointers to the various parameters */

        coef_matrix=mxGetPr(COEF_MATRIX_OUT);

t = mxGetPr(T_IN);
q = mxGetPr(Q_IN);
        constants = mxGetPr(P_IN);


/* Do the actual computations in a subroutine */

deriv_stuff3D(coef_matrix,t,q,constants);
return;
}
/* <><><>
```

```
%driver_fixedpt3D.m. The pre- and post- collision matrices
%were derived using the Maple$^{\circledR}$ batch codes jump3D_ff_minus
%and jump3D_ff_plus.

last=size(q,1); %size of the input state vector.

% inertia matrix parameters

I11=constants(1);
I22=constants(2);
I33=constants(3);
I12=constants(4);
I13=constants(5);
I23=constants(6);

%mass

m=constants(7);

%slope angle

alpha=constants(8);

% c.o.m. position

x=constants(9);
y=constants(10);
z=constants(11);

% pre-collision and post-collision states needed to compute
% collision matrices

PHIm=q(last,1);
PSIm=q(last,3);
THETASTm=q(last,5);
THETASWm=q(last,7);
THETASWp=pi+2*THETASTm;

phi_dot_m=q(last,2);
psi_dot_m=q(last,4);
thetast_dot_m=q(last,6);
thetasw_dot_m=q(last,8);

%trig substitutions

s1=sin(PHIm);
c1=cos(PHIm);

s3=sin(PSIm);
c3=cos(PSIm);

s5m=sin(THETASTm);
s5p=-s5m;
c5m=cos(THETASTm);
c5p=c5m;

s7m=sin(THETASWm);
s7p=sin(pi+2*THETASTm);
c7m=cos(THETASWm);
c7p=cos(pi+2*THETASTm);
%%%%%%%%%%%%%%%%%%%%%%%%%%%%%%%%%%%%%%%%%%%%%%%%%%%%%%%%%%%%%%%%%%%%%%%
%components of the pre-collision matrix called coef_matrixm

(The components are omitted in this appendix for the sake
```

```
of brevity.)


%pre-collision matrix

coef_matrixm=[mm11 mm12 mm13 mm14;
              mm21 mm22 mm23 mm24;
              mm31 mm32 mm33 mm34;
              mm41 mm42 mm43 mm44];

%components of the post-collision matrix called coef_matrixp

(Again, the components are omitted in this appendix for the
sake of brevity)

%post-collision matrix

coef_matrixp=[mp11 mp12 mp13 mp14;
              mp21 mp22 mp23 mp24;
              mp31 mp32 mp33 mp34;
              mp41 mp42 mp43 mp44];
%%%%%%%%%%%%%%%%%%%%%%%%%%%%%%%%%%%%%%%%%%%%%%%%%%%%%%%%%%%%%%%%%%%
%post-collision Euler angle rates by solving
%coef_matrixp*angdotp = coef_matrixm*angdotm for angdotp.

% angdotp is vector of post-collision Euler angle rates.

angdotp=coef_matrixp\(coef_matrixm*...
         [phi_dot_m psi_dot_m thetast_dot_m thetasw_dot_m]');
%jumpmat=inv(coef_matrixp)*coef_matrixm

phi_dot_p=angdotp(1);
psi_dot_p=angdotp(2);
thetast_dot_p=angdotp(3);
thetasw_dot_p=angdotp(4);

%parameter up-date. Only change is in c.o.m. y coordinate.

I11=constants(1);
I22=constants(2);
I33=constants(3);
I12=constants(4);
I13=constants(5);
I23=constants(6);

m=constants(7);

alpha=constants(8);

x=constants(9);
y=-constants(10); %ONLY CHANGE
z=constants(11);

% newconsts3D is the vector of 11 updated parameters.

%%%%%%%%%     1   2   3   4   5   6  7   8   9 10 11
newconsts3D=[I11 I22 I33 I12 I13 I23 m alpha x  y  z ];
%%%%%%%%%%%%%%%%%%%%%%%%%%%%%%%%%%%%%%%%%%%%%%%%%%%%%%%%%%%%%%%%%%%
```

A.3 Fixed Point Stability

We use the following definitions of stability. Let $\mathbf{q} \in \Sigma$ be a fixed point. The fixed point $\mathbf{q}$ is *stable* if, for any $\epsilon > 0$, there exists $\delta > 0$ such that whenever $|\mathbf{q}_0 - \mathbf{q}| < \delta$, $|\mathbf{q}_n - \mathbf{q}| < \epsilon$ for all positive n. The fixed point $\mathbf{q}$ is *asymptotically stable* if, in particular, there exists $\delta > 0$ such that whenever $|\mathbf{q}_0 - \mathbf{q}| < \delta$, $|\mathbf{q}_n - \mathbf{q}| < \epsilon$ for all positive n and $\lim_{n\to\infty} \mathbf{q}_n = \mathbf{y}$ exists. Note that we do not insist that $\mathbf{y} = \mathbf{q}$, only that $|\mathbf{y} - \mathbf{q}| < \epsilon$; *therefore, our use of the term asymptotic stability is less restrictive than usual.* Clearly, if $\mathbf{y}$ exists, it must be a fixed point. Thus, we call a periodic motion asymptotically stable if, when slightly disturbed from this motion, the system asymptotically approaches some 'nearby' periodic motion. This is the strongest type of stability possible when there is a family of periodic motions, since the perturbed point $\mathbf{q}_0$ could just as well be a perturbation of $\mathbf{y}$ as a perturbation of $\mathbf{q}$.

Stability of periodic motions can be investigated by linearizing the return map about the fixed point $\mathbf{q}^*$ and studying the evolution of small disturbances from the fixed point. The linearization of $\mathbf{f}$ near $\mathbf{q}^*$ is given by

$$\mathbf{q}^* + \Delta\mathbf{f} = \mathbf{f}(\mathbf{q}^* + \Delta\mathbf{q}, \mathbf{p}) \simeq \mathbf{f}(\mathbf{q}^*, \mathbf{p}) + D\mathbf{f}(\mathbf{q}^*, \mathbf{p})\Delta\mathbf{q} \tag{A.13}$$

where $D\mathbf{f}(\mathbf{q}^*, \mathbf{p})$ is the Jacobian matrix, $\mathbf{J}$, called the linearization of the map $\mathbf{f}$ at the fixed point $\mathbf{q}^*$ whose components are $\dfrac{\partial f_i}{\partial q_j}$. Since $\mathbf{q}^* = \mathbf{f}(\mathbf{q}^*, \mathbf{p})$, we obtain

$$\Delta^{i+1}\mathbf{q}^+ = \Delta\mathbf{f} \simeq \mathbf{J}\Delta^i\mathbf{q}^+, \tag{A.14}$$

a set of linear difference equations which govern the evolution of the perturbation $\Delta\mathbf{q}$ from the fixed point $\mathbf{q}^*$.

If the eigenvalues σ_i of the Jacobian of the map evaluated at a fixed point have magnitudes less than one, $|\sigma_i| < 1$, then small perturbations to the limit cycle state vector at the start of a step will decay to $\mathbf{0}$ and we say the fixed point is *asymptotically stable.* If at least one eigenvalue is outside the unit circle, $|\sigma_i| > 1$, then any perturbation along the corresponding eigenvector will bump the system off of the limit cycle and we say the system is *unstable.* If the eigenvalues are of magnitude less than or equal to one, $|\sigma_i| \leq 1$, then the limit cycle is *neutrally stable* for tiny perturbations along the eigenvectors for which $|\sigma_i| = 1$; such perturbations will neither grow nor die.

We get the Jacobian of the return map evaluated at a fixed point as a 'free' by-product of the fixed point search since the Jacobian is evaluated at each Newton iteration. Once we find a fixed point, we find the the eigenvalues of the last Newton step Jacobian iteration. So, we use the MATLAB® routine `newton_3D.m` above to numerically calculate the map eigenvalues.

A.3.1 Eigenvaules of the Jacobian of the Map Evaluated at the Fixed Point

Why do the moduli of the eigenvalues of the Jacobian matrix $\mathbf{J}$ representing the linearization of $\mathbf{f}$ near the fixed points $\mathbf{q}^*$ have to be to be less than one for the fixed points to be asymptotically stable? The reasoning is as follows. After k collisions, an initial perturbation $\Delta\mathbf{q}_0$ becomes

$$\Delta\mathbf{q}_k = \underbrace{\mathbf{J}(\mathbf{J}(\cdots(\mathbf{J}}_{k}\,\Delta\mathbf{q}_0)). \tag{A.15}$$

Assume $\mathbf{J}$ has n eigenvectors, $\mathbf{v}^1, \ldots, \mathbf{v}^n$ and n eigenvalues, $\sigma_1, \ldots, \sigma_n$. Then, we have

$$\mathbf{J}\mathbf{v}^1 = \sigma_1\mathbf{v}^1 \cdots \mathbf{J}\mathbf{v}^i = \sigma_i\mathbf{v}^i \cdots \mathbf{J}\mathbf{v}^n = \sigma_n\mathbf{v}^n. \tag{A.16}$$

Now, we may write the initial perturbation as a linear combination of the eigenvectors

$$\Delta \mathbf{q}_0 = C_1 \mathbf{v}^1 + \cdots + C_n \mathbf{v}^n. \tag{A.17}$$

For, say, $k = 1$,

$$\begin{aligned} \Delta \mathbf{q}_1 &= \mathbf{J} \Delta \mathbf{q}_0 \\ &= \mathbf{J}\{C_1 \mathbf{v}^1 + \cdots + C_n \mathbf{v}^n\} \\ &= C_1 \mathbf{J}\mathbf{v}^1 + \cdots + C_n \mathbf{J}\mathbf{v}^n \\ &= C_1 \sigma_1 \mathbf{v}^1 + \cdots + C_n \sigma_n \mathbf{v}^n. \end{aligned} \tag{A.18}$$

By induction, then, for any k,

$$\Delta \mathbf{q}_k = C_1 \sigma_1^k \mathbf{v}^1 + \cdots + C_n \sigma_n^k \mathbf{v}^n. \tag{A.19}$$

If any $|\sigma_i| > 1$, $|\sigma_i|^k$ blows up as $k \to \infty$ which implies that $\Delta \mathbf{q}_k$ and $\Delta \mathbf{q}_0$ blow up as well. Therefore, $\mathbf{q}^*$ is unstable to small perturbations if any $|\sigma_i| > 1$.

If there is known to be a one-parameter family of steady rolling or periodic motions, and if only one eigenvalue is exactly equal to one while the others have magnitude less than one, then we call the periodic motion asymptotically stable in the sense described above. That is, the slightly disturbed system exponentially converges to a nearby periodic motion. This stability is not as strong as the usual definition of asymptotic stability.

A.3.2 Stability Calculations

Here, we describe numerical and analytical procedures for evaluating the Jacobian of a return map at a fixed point.

Numerical approximation to the Jacobian

We numerically approximate the Jacobian of the stride map evaluated at a fixed point using a finite-difference approach. For an n-dimensional state space, the linearization of the map $\mathbf{f}$ at the fixed points $\mathbf{q}^*$ can be obtained numerically by starting with n initial state vectors $\{\Delta \mathbf{q}_0\}_m$ in the neighborhood of $\mathbf{q}^*$, with perturbations in only one state variable at a time, say, the m_{th}, Δq_m, while the others are kept fixed at zero in each of the n vectors,

$$\{\Delta \mathbf{q}_0\}_m = \begin{Bmatrix} 0 \\ 0 \\ 0 \\ \vdots \\ \Delta q_m \\ \vdots \\ 0 \\ 0 \end{Bmatrix}, \quad m = 1, \ldots, n. \tag{A.20}$$

The subscript m outside the square brackets indicates an initial state vector with a non-zero m_{th} component. Numerically integrating the equations of motion for each of the n initial state vectors and applying the collision transition function, we can obtain n final state vectors $\{\mathbf{q}_1\}_m$,

$$\begin{aligned} \{\mathbf{q}_1\}_m &= \mathbf{f}(\mathbf{q}^* + \{\Delta \mathbf{q}_0\}_m, \mathbf{p}) \\ &\simeq \mathbf{f}(\mathbf{q}^*) + \mathbf{J}\{\Delta \mathbf{q}_0\}_m, \quad m = 1, \ldots, n. \end{aligned} \tag{A.21}$$

Subtracting the cyclic term $\mathbf{f}(\mathbf{q}^*)$ from both sides and letting $\{\mathbf{q}_1\}_m - \mathbf{q}^* = \{\Delta\mathbf{q}_1\}_m$, we get

$$\begin{aligned} \{\Delta\mathbf{q}_1\}_m &\simeq \mathbf{J}\{\Delta\mathbf{q}_0\}_m \\ &\simeq \Delta q_m(\text{`}m_{\text{th}} \text{ column of } \mathbf{J}\text{'}). \end{aligned} \tag{A.22}$$

Thus, the difference between the output vector and the fixed point, $\{\Delta\mathbf{q}_1\}_m$, is a numerical approximation, scaled by Δq_m, to the m_{th} column of the Jacobian matrix $\mathbf{J}$ of $\mathbf{f}$ evaluated at the fixed point. After n numerical integrations of the n initial perturbation vectors, we can then assemble all of the columns of an approximation to $\mathbf{J}$. The stability of the fixed points is determined by the eigenvalues of $\mathbf{J}$.

Analytical Approximation to the Jacobian

An analytical approximation to the Jacobian of the return map can be obtained as follows. Recall that we have the differential equation of motion between collisions

$$\dot{\mathbf{q}} = \mathbf{g}(\mathbf{q}), \tag{A.23}$$

subject to the initial condition $\mathbf{q}(0) = {}^i\mathbf{q}^+$.

We also have the collision transition rule

$${}^i\mathbf{q}^+ = \mathbf{h}({}^i\mathbf{q}^-) = \mathbf{L}({}^i\mathbf{q}^-)\,{}^i\mathbf{q}^-. \tag{A.24}$$

We define a *collision detection function* 'r' such that a collision occurs when

$$r(\mathbf{q}^-) = 0. \tag{A.25}$$

For example, the collision detection function for the 2D or 3D rimless wheel is

$$r(\mathbf{q}^-) = \theta - \frac{\pi}{n}. \tag{A.26}$$

Assume a fixed point $\mathbf{q}^*$ of the system exists with corresponding limit cycle trajectory

$$\mathbf{q}^*(\tau). \tag{A.27}$$

The pre-collision state vector is

$${}^{i+1}\mathbf{q}^- = \mathbf{q}^*(\tau^*), \tag{A.28}$$

where τ^* is the limit cycle time between collisions. So, the collision detection and transition rules give

$$r(\mathbf{q}^*(\tau^*)) = 0, \text{ and} \tag{A.29}$$

$$\mathbf{h}(\mathbf{q}^*(\tau^*)) = \mathbf{q}^*. \tag{A.30}$$

For a particular system, we need to find the limit cycle trajectory $\mathbf{q}^*(\tau)$ and the time τ^* between collisions in the limit cycle. See figure A.2 for a schematic illustration of the limit cycle time history.

We wish to study the evolution of a perturbation from the fixed point, just after collision i, $\Delta\mathbf{q} = \epsilon\hat{\mathbf{q}}$, where ϵ is small. Henceforth, we shall use a 'hat' ($\hat{}$) to denote perturbed quantities. So, just after a collision, say the i_{th}, the perturbed state of the wheel is

$${}^i\mathbf{q}^+ = \mathbf{q}_0^* + \epsilon\hat{\mathbf{q}}_0 = \mathbf{q}_0^* + \epsilon({}^i\hat{\mathbf{q}}^+). \tag{A.31}$$

The perturbed solution to the differential equation between collisions with this perturbed initial condition, then, is

$$\mathbf{q}(\tau) = \mathbf{q}^*(\tau) + \epsilon\hat{\mathbf{q}}(\tau). \tag{A.32}$$

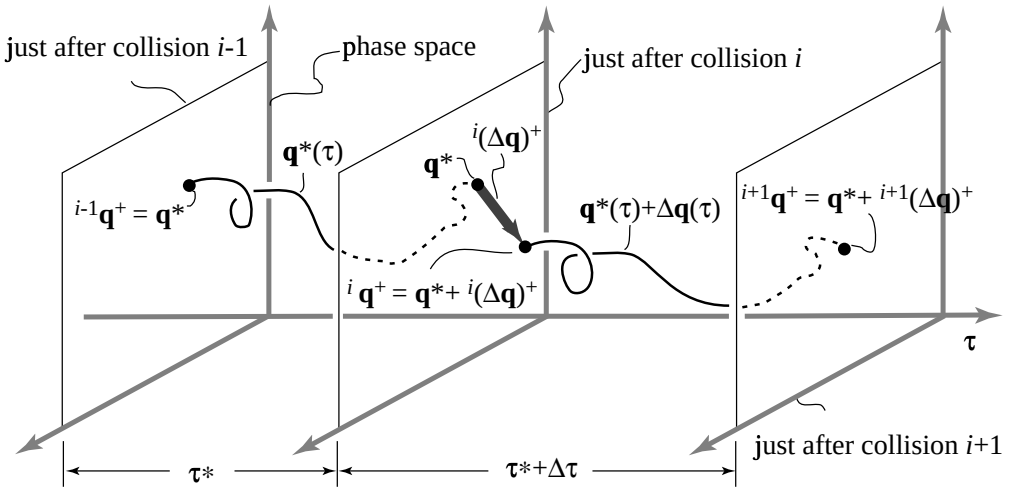

Figure A.2: Schematic of the perturbed limit cycle.

As a result of perturbing the fixed point, the limit cycle time between collisions is also perturbed.

$$\tau_f = \tau^* + \Delta\tau = \tau^* + \epsilon\hat{\tau}. \tag{A.33}$$

See figure A.2 for a schematic illustration of the perturbed limit cycle time history.

We summarize the derivation of an analytical approximation to the map governing the evolution of the perturbations from just after one collision to just after the next as follows. We substitute the perturbed quantities into the governing equation of motion, the collision detection function, and the collision transition rule. We then expand and truncate the resulting expressions to first order in epsilon. We obtain:

1. an expression governing the evolution of a perturbation to the limit cycle from just after a collision to just before the next, (a linear non-autonomous system)

$$\dot{\hat{\mathbf{q}}}(\tau) \simeq D\mathbf{g}(\mathbf{q}^*(\tau))\hat{\mathbf{q}}(\tau), \tag{A.34}$$

2. an expression for the perturbation to the time between collisions $\hat{\tau}$,

$$\hat{\tau} \simeq -\frac{Dr(\mathbf{q}^*(\tau^*))\hat{\mathbf{q}}^*(\tau^*)}{Dr(\mathbf{q}^*(\tau^*))\dot{\mathbf{q}}^*(\tau^*)}, \text{ and} \tag{A.35}$$

3. an expression for relating the perturbation to the limit cycle just before collision to just after,

$$^{i+1}\hat{\mathbf{q}}^+ \simeq D\mathbf{h}(\mathbf{q}^*(\tau^*)) \left[\mathbf{I} - \frac{\dot{\mathbf{q}}^*(\tau^*)\cdot Dr(\mathbf{q}^*(\tau^*))}{Dr(\mathbf{q}^*(\tau^*))\cdot\dot{\mathbf{q}}^*(\tau^*)}\right] \hat{\mathbf{q}}(\tau^*). \tag{A.36}$$

Putting these expressions together, we obtain an analytical approximation to the linear map governing the evolution of perturbations from collision to collision as a product of three special matrices

$$^{i+1}\hat{\mathbf{q}}^+ \simeq \underbrace{\mathbf{BDE}}_{\mathbf{A}} \, {}^i\hat{\mathbf{q}}^+ \tag{A.37}$$

where

$$\begin{aligned} \mathbf{B} &\equiv D\mathbf{h}(\mathbf{q}^*(\tau^*)), \\ \mathbf{D} &\equiv \mathbf{I} - \frac{\dot{\mathbf{q}}^*(\tau^*)\cdot Dr(\mathbf{q}^*(\tau^*))}{Dr(\mathbf{q}^*(\tau^*))\cdot\dot{\mathbf{q}}^*(\tau^*)}, \text{ and} \end{aligned} \tag{A.38}$$

$\mathbf{E}$ can be obtained by integrating Equation (A.34) with arbitrary initial condition ${}^{i}\hat{\mathbf{q}}^{+}$ forward up to time τ^{*},

$$\hat{\mathbf{q}}(\tau^{*}) \simeq \mathbf{E}\ {}^{i}\hat{\mathbf{q}}^{+}. \tag{A.39}$$

We can calculate analytical expressions for the eigenvalues of the approximation to the Jacobian $\mathbf{A} \simeq \mathbf{J}$ as functions of the rimless wheel parameters, or power series in ζ.

The three matrices comprising the approximation to the Jacobian, $\mathbf{A} = \mathbf{BDE}$, have the following interpretations. Matrix $\mathbf{B}$ represents an approximation to the collision transition map. Matrix $\mathbf{D}$ represents a correction to the perturbation map to account for the perturbed time between collisions. Matrix $\mathbf{E}$ represents the map of the perturbations just after a collision to just before the next.

In order to obtain this approximate Jacobian, we need to find the limit cycle trajectory $\mathbf{q}^{*}(\tau)$ and the limit cycle time between collisions τ^{*}. If we do not have explicit solutions for these two quantities, then we must use approximate methods to obtain them, guided by intuition and numerics.

If we know (1) the limit cycle trajectory $(\mathbf{q}^{*}(\tau))$, (2) the corresponding time between collisions (τ^{*}) , and (3) the map of the perturbations to the limit cycle just after a collision to just before the next (represented by the matrix $\mathbf{E}$) *explicitly*, then the matrix $\mathbf{A}$ is exactly equal to the Jacobian of the map $\mathbf{f}$ evaluated at the fixed point $\mathbf{q}^{*}(\tau)$. This is true even though we may not know the full return map $\mathbf{f}$ explicitly.

We carried out a analytical stability analysis, as decribed above, of the 3D rimless wheel in Chapter 4. The Maple® codes used for the analysis are displayed in Appendix E.

Appendix B

Derivation of the Governing Equations for the 3D Passive-Dynamic Walking Mechanism

In this appendix, we derive the equations of motion between foot collisions and the collision transition rules for the 3D straight-legged point foot walker.

B.1 Derivation of the Equations of Motion between Collisions

We derive the equations of motion for the 3D walker between collisions by writing angular momentum balance for the entire device about the contact point of the stance leg and also for the swing leg about the hinge joint axis at the hip.

B.1.1 Notation description

First, we define the following terms used to specify position, orientation, mass, and inertia quantities for a body b:

1. A body frame is denoted by a number b.
2. A coordinate system a is rigidly attached to frame b with origin a.
3. A standard basis $\left(\hat{\mathbf{X}}_b^c, \hat{\mathbf{Y}}_b^c, \hat{\mathbf{Z}}_b^c\right)$ is associated with frame b, aligned with coordinate system b, and written in basis c. (We use this notation to avoid confusion of the basis vectors with the indices i, j, and k and the moment of inertia matrix designation $\mathbf{I}$ or $\mathbf{J}$.)
4. The axis of rotation of a hinge (or revolute joint) b is aligned with $\hat{\mathbf{Y}}_b$.
5. $\mathbf{d}_{b/c}^e$ is the position vector of the center of mass of body b with respect to the origin of coordinate system c written in the basis of frame e.
6. $\mathbf{r}_{b/c}^e$ is the position vector of the origin of coordinate system b with respect to the origin of coordinate system c written in the basis of frame e.

7. $\mathbf{a}_b^c$ is the absolute acceleration of the center of mass of body b written in the basis of frame c.
8. $\mathbf{R}_b^c$ is the rotation matrix that transforms the components of a vector in frame b to its components in frame c.
9. $\boldsymbol{\omega}_{b/c}^e$ is the angular velocity of body b with respect to body c written in the basis of frame e.
10. m_b is the mass of body b.
11. ${}^c\mathbf{I}^b$ is the moment of inertia matrix for body b with respect to its center of mass and calculated with respect to frame c.
12. $\dot{\mathbf{H}}_{/b}^c$ is the absolute rate of change of angular momentum of body b about its center of mass written in the basis of frame c.
13. $\left(\dot{\mathbf{H}}_{/c}^b\right)^e$ is the absolute rate of change of angular momentum of body b about the origin of frame c written in the basis of frame e.
14. $\left(\mathbf{M}_{/c}^b\right)^e$ is the applied moment acting on body b about the origin of frame c written in the basis of frame e.
15. Sub-system b of an interconnected system of n bodies is the collection of $n-b+1$ bodies numbered from b to n.
16. $\sum_{s=b}^n \left(\dot{\mathbf{H}}_{/c}^s\right)^e$ is absolute rate of change of angular momentum of sub-system b about the origin of frame c written in the basis of frame e.
17. $\sum_{s=b}^n \left(\mathbf{M}_{/c}^s\right)^e$ is the applied moment on subs-system b about the origin of frame c written in the basis of frame e.
18. $\sum_{s=b}^n \left(\mathbf{M}_{/c}^s\right)^e = \sum_{s=b}^n \left(\dot{\mathbf{H}}_{/c}^s\right)^e$ is the equation of angular momentum balance for subs-system b about the origin of frame c written in the basis of frame e.

B.1.2 Equations of Angular Momentum Balance

The equations of angular momentum balance about the contact point of the stance leg for the 3D walker system are

$$\begin{aligned} \sum_{s=3}^{4} \left(\Sigma \mathbf{M}_{/0}^s\right) &= \sum_{s=3}^{4} \dot{\mathbf{H}}_{/0}^s \text{ or} \\ \Sigma \mathbf{M}_{/0}^3 + \Sigma \mathbf{M}_{/0}^4 &= \dot{\mathbf{H}}_{/0}^3 + \dot{\mathbf{H}}_{/0}^4. \end{aligned} \tag{B.1}$$

The equation of angular momentum balance of the swing leg about the axis of rotation of the hinge joint at the hip is

$$\left\{\Sigma \mathbf{M}_{/4}^4 = \dot{\mathbf{H}}_{/4}^4\right\} \cdot \hat{\mathbf{Y}}_4. \tag{B.2}$$

Below, we lay out the quantities needed to expand these equations.

B.1.3 Frame Kinematics

Referring to Figure B.1, we define the following kinematic quantities for the 3D walker needed to write the equations of angular momentum. We write all of the vector components in the fixed frame coordinates using appropriate transformations.

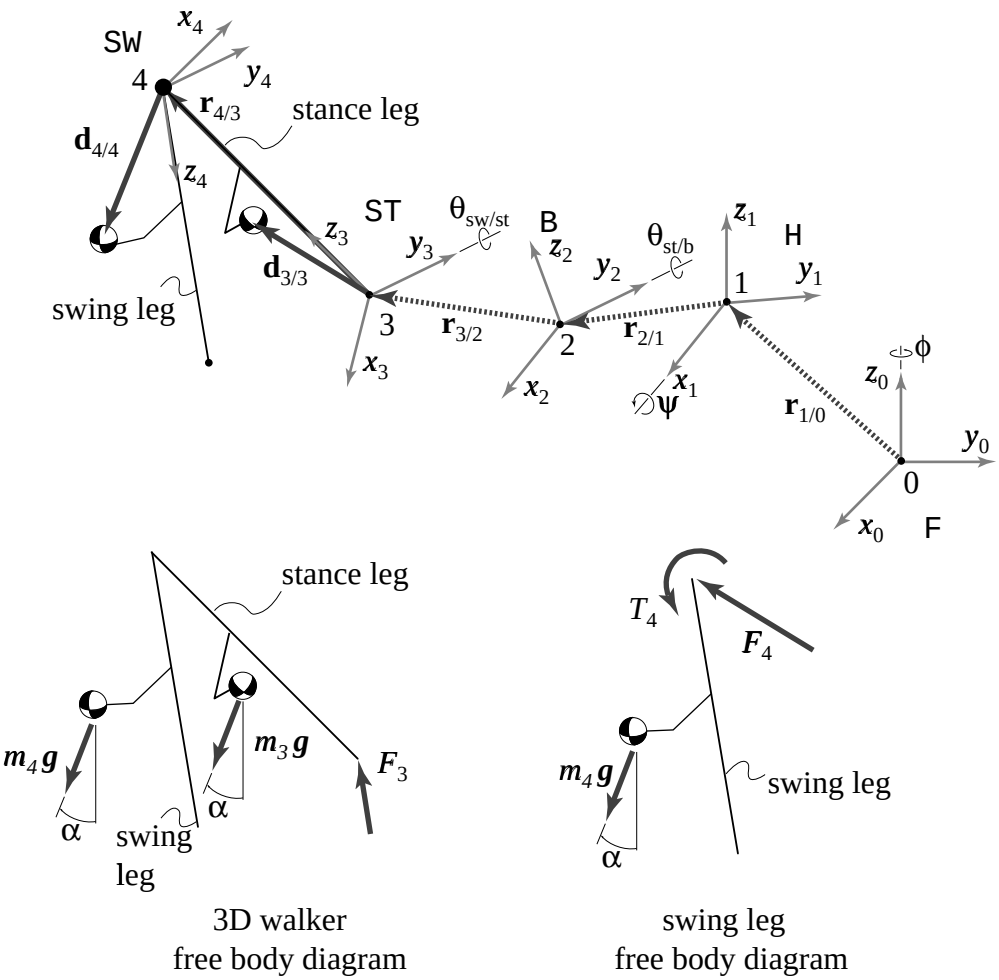

Figure B.1: Frame 0 is fixed frame $\mathcal{F}$, frame 1 is heading frame $\mathcal{H}$, frame 2 is bank frame $\mathcal{B}$, frame 3 is stance frame $\mathcal{ST}$, and frame 3 is swing frame $\mathcal{SW}$. The walking device makes ball-and-socket contact with the ground at point 3 which is physically coincident with points 0, 1, and 2 since, for the 3-1-2 Euler angle frames, $\mathbf{r}_{3/2} = \mathbf{r}_{2/1} = \mathbf{r}_{1/0} = \mathbf{0}$. The leg length is ℓ, g is the acceleration due to gravity, and α is the slope angle

Rotation Matrices

First, the rotation matrices between frames are:

$$\begin{aligned}
\mathbf{R}_0^1(\phi) &= \begin{bmatrix} c\phi & s\phi & 0 \\ -s\phi & c\phi & 0 \\ 0 & 0 & 1 \end{bmatrix}, \\
\mathbf{R}_1^2(\psi) &= \begin{bmatrix} 1 & 0 & 0 \\ 0 & c\psi & s\psi \\ 0 & -s\phi & c\phi \end{bmatrix}, \\
\mathbf{R}_2^3(\theta_{st}) &= \begin{bmatrix} c\theta_{st} & 0 & -s\theta_{st} \\ 0 & 1 & 0 \\ s\theta_{st} & 0 & c\theta_{st} \end{bmatrix}, \text{ and} \qquad \text{(B.3)} \\
\mathbf{R}_3^4(\theta_{sw}) &= \begin{bmatrix} c\theta_{sw} & 0 & -s\theta_{sw} \\ 0 & 1 & 0 \\ s\theta_{sw} & 0 & c\theta_{sw} \end{bmatrix}. \qquad \text{(B.4)} \\
& \qquad \text{(B.5)}
\end{aligned}$$

Then, the rotation matrices between each intermediate frame and the fixed frame are

$$\begin{aligned}
\mathbf{R}_0^2 &= \mathbf{R}_1^2 \cdot \mathbf{R}_0^1, \qquad \text{(B.6)} \\
\mathbf{R}_0^3 &= \mathbf{R}_2^3 \cdot \mathbf{R}_1^2 \cdot \mathbf{R}_0^1, \text{ and} \qquad \text{(B.7)} \\
\mathbf{R}_0^4 &= \mathbf{R}_3^4 \cdot \mathbf{R}_2^3 \cdot \mathbf{R}_1^2 \cdot \mathbf{R}_0^1. \qquad \text{(B.8)}
\end{aligned}$$

Angular Velocity

The relative angular velocities between each successive frame are

$$\begin{aligned}
\boldsymbol{\omega}_{1/0}^0 &= \dot{\phi}\hat{\mathbf{Z}}_0^0, \\
\boldsymbol{\omega}_{2/1}^1 &= \dot{\psi}\hat{\mathbf{X}}_1^1, \\
\boldsymbol{\omega}_{3/2}^2 &= \dot{\theta_{st}}\hat{\mathbf{Y}}_2^2, \text{ and} \\
\boldsymbol{\omega}_{4/3}^3 &= \dot{\theta_{st}}\hat{\mathbf{Y}}_3^3. \qquad \text{(B.9)}
\end{aligned}$$

The absolute angular velocity of the stance and swing legs written in the fixed frame basis are

$$\begin{aligned}
\boldsymbol{\omega}_{3/0}^0 &= \boldsymbol{\omega}_{1/0}^0 + \boldsymbol{\omega}_{2/1}^0 + \boldsymbol{\omega}_{3/2}^0 \text{ and} \qquad \text{(B.10)} \\
\boldsymbol{\omega}_{4/0}^0 &= \boldsymbol{\omega}_{4/3}^0 + \boldsymbol{\omega}_{3/0}^0 \qquad \text{(B.11)}
\end{aligned}$$

where

$$\begin{aligned}
\boldsymbol{\omega}_{1/0}^0 &= \boldsymbol{\omega}_{1/0}^0, \\
\boldsymbol{\omega}_{2/1}^0 &= [\mathbf{R}_0^1]^T \cdot \boldsymbol{\omega}_{2/1}^1, \\
\boldsymbol{\omega}_{3/2}^0 &= [\mathbf{R}_0^2]^T \cdot \boldsymbol{\omega}_{3/2}^2, \text{ and} \\
\boldsymbol{\omega}_{4/3}^0 &= [\mathbf{R}_0^3]^T \cdot \boldsymbol{\omega}_{4/3}^3. \qquad \text{(B.12)}
\end{aligned}$$

Center of Mass Position and Absolute Acceleration

The stance and swing leg center of mass positions with respect to the stance and swing frame origins are

$$\begin{aligned}
\mathbf{d}_{3/3}^3 &= x\hat{\mathbf{X}}_3^3 + y\hat{\mathbf{Y}}_3^3 + z\hat{\mathbf{Z}}_3^3 \text{ and} \\
\mathbf{d}_{4/4}^4 &= -x\hat{\mathbf{X}}_4^4 - y\hat{\mathbf{Y}}_4^4 + (\ell - z)\hat{\mathbf{Z}}_4^4. \qquad \text{(B.13)}
\end{aligned}$$

The position of the hip relative to the stance foot is

$$\mathbf{r}^3_{4/3} = \ell\,\hat{\mathbf{Z}}^3_3. \tag{B.14}$$

The stance and swing center of mass positions with respect to the origin of the fixed frame written in the fixed frame basis are

$$\begin{aligned}
\mathbf{d}^0_{3/0} &= \mathbf{d}^0_{3/3} + \mathbf{r}^0_{3/0} \\
&= [\mathbf{R}^3_0]\cdot\mathbf{d}^3_{3/3} + \overbrace{\sum_{s=0}^{3}\mathbf{r}^0_{s+1/s}}^{\mathbf{0}} \\
&= [\mathbf{R}^3_0]^T\cdot\mathbf{d}^3_{3/3} \text{ and} \\
\mathbf{d}^0_{4/0} &= \mathbf{d}^0_{4/4} + \mathbf{r}^0_{4/0} \\
&= [\mathbf{R}^4_0]^T\cdot\mathbf{d}^4_{4/4} + \overbrace{\underbrace{[\mathbf{R}^3_0]^T\cdot\mathbf{r}^3_{4/3}}_{\mathbf{r}^0_{4/3}} + \sum_{s=0}^{4}\mathbf{r}^0_{s+1/s}}^{} \\
&= [\mathbf{R}^4_0]^T\cdot\mathbf{d}^4_{4/4} + [\mathbf{R}^3_0]^T\cdot\mathbf{r}^3_{4/3}.
\end{aligned} \tag{B.15}$$

The accelerations of the center of mass of the stance and swing legs written in the fixed frame basis are, respectively,

$$\begin{aligned}
\mathbf{a}^0_3 &= \frac{d^2}{dt^2}\mathbf{d}^0_{3/0} \text{ and} \\
\mathbf{a}^0_4 &= \frac{d^2}{dt^2}\mathbf{d}^0_{4/0}.
\end{aligned} \tag{B.16}$$

B.1.4 Moment of Inertia Matrices

The moment of inertia matrices for the stance and swing legs calculated with respect to the fixed frame are, respectively

$$\begin{aligned}
{}^0\mathbf{I}^3 &= [\mathbf{R}^3_0]^T\cdot\ {}^3\mathbf{I}^3\cdot\ [\mathbf{R}^3_0] \text{ and} \\
{}^0\mathbf{I}^4 &= [\mathbf{R}^4_0]^T\cdot\ {}^4\mathbf{I}^4\cdot\ [\mathbf{R}^4_0]
\end{aligned} \tag{B.17}$$

where the inertia matrices calculated for each leg in the leg frames are identical

$${}^3\mathbf{I}^3 = {}^4\mathbf{I}^4 = \mathbf{I} = \begin{bmatrix} I_{xx} & I_{xy} & I_{xz} \\ I_{xy} & I_{yy} & I_{yz} \\ I_{xz} & I_{yz} & I_{zz} \end{bmatrix}. \tag{B.18}$$

B.1.5 Rate of Change of Angular Momentum

The rate of change of angular momentum for the stance leg about the origin of the fixed frame written in the fixed frame basis is

$$\left(\dot{\mathbf{H}}^3_{/0}\right)^0 = \dot{\mathbf{H}}^0_{/3} + \mathbf{d}^0_{3/0}\times m_3\,\mathbf{a}^0_3 \tag{B.19}$$

where

$$\begin{aligned} \mathbf{H}^0_{/3} &= {}^0\mathbf{I}^3 \cdot \boldsymbol{\omega}^0_{3/0}, \text{ and} \\ \dot{\mathbf{H}}^0_{/3} &= \frac{d}{dt}\mathbf{H}^0_{/3}. \end{aligned} \tag{B.20}$$

The rate of change of angular momentum for the swing leg about the origin of the fixed frame written in the fixed frame basis is

$$\left(\dot{\mathbf{H}}^4_{/0}\right)^0 = \dot{\mathbf{H}}^0_{/4} + \mathbf{d}^0_{4/0} \times m_4\, \mathbf{a}^0_4 \tag{B.21}$$

where

$$\begin{aligned} \mathbf{H}^0_{/4} &= {}^0\mathbf{I}^4 \cdot \boldsymbol{\omega}^0_{4/0}, \text{ and} \\ \dot{\mathbf{H}}^0_{/4} &= \frac{d}{dt}\mathbf{H}^0_{/4}. \end{aligned} \tag{B.22}$$

The component along the hinge axis at the hip of the rate of change of angular momentum for the swing leg about the origin of the swing frame, written in the fixed frame basis, is

$$\left\{ \left(\dot{\mathbf{H}}^4_{/4}\right)^0 = \dot{\mathbf{H}}^0_{/4} + \mathbf{d}^0_{4/4} \times \mathbf{a}^0_4 \right\} \cdot \hat{\mathbf{Y}}^0_4 \tag{B.23}$$

where

$$\hat{\mathbf{Y}}^0_4 = [\mathbf{R}^4_0]^T \cdot \hat{\mathbf{Y}}^4_4. \tag{B.24}$$

B.1.6 Applied Moments

Referring to the free body diagrams in Figure B.1, the applied moments acting on the stance and swing legs about the contact point of the stance frame written in the fixed frame basis are, respectively

$$\begin{aligned} \left(\mathbf{M}^3_{/0}\right)^0 &= \mathbf{d}^0_{3/0} \times m_3 \mathbf{g}^0, \text{ and} \\ \left(\mathbf{M}^4_{/0}\right)^0 &= \mathbf{d}^0_{4/0} \times m_4 \mathbf{g}^0 \end{aligned} \tag{B.25}$$

where $\mathbf{g}^0$ is the gravity vector

$$\mathbf{g}^0 = g(\sin\alpha\, \hat{\mathbf{X}}^0_0 - \cos\alpha\, \hat{\mathbf{Z}}^0_0). \tag{B.26}$$

The component along the hinge axis at the hip of the applied moments acting on the swing leg about the origin of the swing frame, written in the fixed frame basis, is

$$\left\{ \left(\mathbf{M}^4_{/4}\right)^0 = \mathbf{d}^0_{4/4} \times m_4 \mathbf{g}^0 \right\} \cdot \hat{\mathbf{Y}}^0_4. \tag{B.27}$$

B.1.7 Assembling the Equations of Motion

The two equations for angular momentum balance above yield four equations of motion. Collection terms appropriately, we can assemble three matrices $\mathbf{M}(\mathbf{q})$, $\mathbf{V}(\mathbf{q})$, and $\mathbf{G}(\mathbf{q})$ of Equation (6.9) in Chapter 6. The Maple® codes for generating these matrices are included in the next pages.

```
#####################################################################
#eqns3D_ff

#eqns3D_ff derives the four equations of motion from angular
#momentum balance. The output is:

#H0dot_0, the rate of change of angular momemtum about point
  $0$(3x1 vector);
#M0dot_0, the applied moment about point $0$ due to
   gravity(3x1 vector);
#H4dot_0, the rate of change of angular momemtum about point $4$
  dotted with the hinge axis(scalar);
#M0dot_0, the applied moment about point $4$ due to
  gravity dotted with the hinge axis(scalar).

#The output is stored in eqns3D_ff.m

#The three matrices M(q), V(q), and G(q) are extracted in
#the files arrange_mass_ff, arrange_vel_ff, and
#arrange_applmom_ff, respectively.

#Invoke linear algebra package
with(linalg):
#Kinematics
#Rotation Matrices

rot_0_1:=matrix([[cos(phi(t)),sin(phi(t)),0],
                 [-sin(phi(t)),cos(phi(t)),0],
                 [0,0,1]]):
rot_1_2:=matrix([[1,0,0],
                 [0,cos(psi(t)),sin(psi(t))],
                 [0,-sin(psi(t)),cos(psi(t))]]):
rot_2_3:=matrix([[cos(thetast(t)),0,-sin(thetast(t))],
                 [0,1,0],
                 [sin(thetast(t)),0,cos(thetast(t))]]):
rot_3_4:=matrix([[cos(thetasw(t)),0,-sin(thetasw(t))],
                 [0,1,0],
                 [sin(thetasw(t)),0,cos(thetasw(t))]]):
rot_0_2:=multiply(rot_1_2,rot_0_1):
rot_0_3:=multiply(rot_2_3,multiply(rot_1_2,rot_0_1)):
rot_0_4:=multiply(rot_3_4,multiply(rot_2_3,
            multiply(rot_1_2,rot_0_1))):

#Angular velocity

w3_0_0:=add(array([0,0,diff(phi(t),t)]),
         add(multiply(transpose(rot_0_1),
              array([diff(psi(t),t),0,0])),
               multiply(transpose(rot_0_2),
                 array([0,diff(thetast(t),t),0])))):

w4_0_0:=add(w3_0_0,multiply(transpose(rot_0_3),
               array([0,diff(thetasw(t),t),0]))):

#Position Vectors

d3_0_0:=multiply(transpose(rot_0_3),array([x,y,z])):
d4_0_0:=add(multiply(transpose(rot_0_3),array([0,0,1])),
            multiply(transpose(rot_0_4),array([-x,-y,1-z]))):
d4_4_0:=multiply(transpose(rot_0_4),array([-x,-y,1-z])):

#Rate of change of angular momenta
#Moment of Inertia Matrices
```

```
#w.r.t d3
Id3_3:=matrix([[I11,I12,I13],
               [I12,I22,I23],
               [I13,I23,I33]]):

#w.r.t d4
Id4_4:=matrix([[I11,I12,I13],
               [I12,I22,I23],
               [I13,I23,I33]]):

#About point 0...

H0dot_0:=add(
          add(
         map(diff,multiply(
                  multiply(transpose(rot_0_3),
                      multiply(Id3_3,rot_0_3)),
                                      w3_0_0),t),
           crossprod(d3_0_0,evalm(m*map(diff,d3_0_0,t$2)))),

          add(
           map(diff,multiply(
                  multiply(transpose(rot_0_4),
                      multiply(Id4_4,rot_0_4)),
                                      w4_0_0),t),
           crossprod(d4_0_0,evalm(m*map(diff,d4_0_0,t$2))))):

#About point 4...

H4dot_0:=innerprod(
          add(
           map(diff,multiply(
                     multiply(transpose(rot_0_4),
                       multiply(Id4_4,rot_0_4)),
                                      w4_0_0),t),
           crossprod(d4_4_0,evalm(m*map(diff,d4_0_0,t$2)))),
          multiply(transpose(rot_0_4),array([0,1,0]))):

#gravity vector

grav_0:=array([sin(alpha),0,-cos(alpha)]):

#Appied moments About point 0...

M0_0:=add(
       crossprod(d3_0_0,evalm(m*grav_0)),
       crossprod(d4_0_0,evalm(m*grav_0))):

#about point 4...

M4_0:=innerprod(
        crossprod(d4_4_0,evalm(m*grav_0)),
        multiply(transpose(rot_0_4),array([0,1,0]))):
#####################################################################

#####################################################################
#arrange_mass_ff

#arrange_mass_ff extracts the matrix M(q) from the equations
#of motion stored in eqns3D_ff.m.
#The output is final_coef_matrix.

with(linalg):
read `eqns3D_ff.m`:
```

```
ddot:=array([diff(phi(t),t$2),diff(psi(t),t$2),
          diff(thetast(t),t$2), diff(thetasw(t),t$2)]):

Hdot:=array([H0dot_0[1],H0dot_0[2],H0dot_0[3],H4dot_0]):

for i from 1 by 1 to 4 do
 for j from 1 by 1 to 4 do
 mp[i,j]:=coeff(expand(Hdot[i]),ddot[j],1):

 od:
 od:
g:=(i,j) ->mp[i,j]:
coef_matrix:=matrix(4,4,g):

for r from 1 by 1 to 4 do
for s from 1 by 1 to 4 do
Twocoef_matrix[r,s]:=
    simplify(subs(phi(t)=x1,psi(t)=x3,thetast(t)=x5,
                  thetasw(t)=x7, coef_matrix[r,s])):
Threecoef_matrix[r,s]:=
    subs(sin(x1)=sx1,sin(x3)=sx3,sin(x5)=sx5,sin(x7)=sx7,
         cos(x1)=cx1,cos(x3)=cx3,cos(x5)=cx5,cos(x7)=cx7,
                          Twocoef_matrix[r,s]):
od:
od:

gg:=(r,s) ->Threecoef_matrix[r,s]:
temp_matrix:=matrix(4,4,gg):

#interface(screenwidth=60);

finalcoef_matrix:=
map(collect,map(collect,map(collect,map(collect,map(collect,
map(collect,map(collect,map(collect,map(collect,map(collect,
map(collect,map(collect,map(collect,map(collect,map(collect,
map(collect,map(collect,map(collect, temp_matrix
       ,sx1),cx1),sx3),cx3),sx5),cx5),cx7),sx7)
       ,x),y),z),m)
       ,I11),I12),I13),I22),I23),I33);
######################################################################

######################################################################
#arrange_vel_ff

#arrange_vel_ff extracts the matrix V(q) from the equations of
#motion stored in eqns3D_ff.m.  The output is vel_matrix.

#This file calls vel_tot_ff.m and vel_sw_ff.m which
#``preprocesses'' the equations of motion in order to reduce
#the memory required by this file to complete its computations.

with(linalg):

read `vel_tot_ff.m`:
read `vel_sw_ff.m`:

vv11:=coeff(collect(Threebb[1],q2),q2,2):
vv12:=coeff(collect(Threebb[1],q4),q4,2):
vv13:=coeff(collect(Threebb[1],q6),q6,2):
vv14:=coeff(collect(Threebb[1],q8),q8,2):
vv15:=coeff(collect(coeff(collect(Threebb[1],q2),q2,1),q4),q4,1):
vv16:=coeff(collect(coeff(collect(Threebb[1],q2),q2,1),q6),q6,1):
vv17:=coeff(collect(coeff(collect(Threebb[1],q2),q2,1),q8),q8,1):
vv18:=coeff(collect(coeff(collect(Threebb[1],q4),q4,1),q6),q6,1):
vv19:=coeff(collect(coeff(collect(Threebb[1],q4),q4,1),q8),q8,1):
```

```
vv10:=coeff(collect(coeff(collect(Threebb[1],q6),q6,1),q8),q8,1):

vv21:=coeff(collect(Threebb[2],q2),q2,2):
vv22:=coeff(collect(Threebb[2],q4),q4,2):
vv23:=coeff(collect(Threebb[2],q6),q6,2):
vv24:=coeff(collect(Threebb[2],q8),q8,2):
vv25:=coeff(collect(coeff(collect(Threebb[2],q2),q2,1),q4),q4,1):
vv26:=coeff(collect(coeff(collect(Threebb[2],q2),q2,1),q6),q6,1):
vv27:=coeff(collect(coeff(collect(Threebb[2],q2),q2,1),q8),q8,1):
vv28:=coeff(collect(coeff(collect(Threebb[2],q4),q4,1),q6),q6,1):
vv29:=coeff(collect(coeff(collect(Threebb[2],q4),q4,1),q8),q8,1):
vv20:=coeff(collect(coeff(collect(Threebb[2],q6),q6,1),q8),q8,1):

vv31:=coeff(collect(Threebb[3],q2),q2,2):
vv32:=coeff(collect(Threebb[3],q4),q4,2):
vv33:=coeff(collect(Threebb[3],q6),q6,2):
vv34:=coeff(collect(Threebb[3],q8),q8,2):
vv35:=coeff(collect(coeff(collect(Threebb[3],q2),q2,1),q4),q4,1):
vv36:=coeff(collect(coeff(collect(Threebb[3],q2),q2,1),q6),q6,1):
vv37:=coeff(collect(coeff(collect(Threebb[3],q2),q2,1),q8),q8,1):
vv38:=coeff(collect(coeff(collect(Threebb[3],q4),q4,1),q6),q6,1):
vv39:=coeff(collect(coeff(collect(Threebb[3],q4),q4,1),q8),q8,1):
vv30:=coeff(collect(coeff(collect(Threebb[3],q6),q6,1),q8),q8,1):

vv41:=coeff(collect(Threedd,q2),q2,2):
vv42:=coeff(collect(Threedd,q4),q4,2):
vv43:=coeff(collect(Threedd,q6),q6,2):
vv44:=coeff(collect(Threedd,q8),q8,2):
vv45:=coeff(collect(coeff(collect(Threedd,q2),q2,1),q4),q4,1):
vv46:=coeff(collect(coeff(collect(Threedd,q2),q2,1),q6),q6,1):
vv47:=coeff(collect(coeff(collect(Threedd,q2),q2,1),q8),q8,1):
vv48:=coeff(collect(coeff(collect(Threedd,q4),q4,1),q6),q6,1):
vv49:=coeff(collect(coeff(collect(Threedd,q4),q4,1),q8),q8,1):
vv40:=coeff(collect(coeff(collect(Threedd,q6),q6,1),q8),q8,1):

temp_matrix:=
matrix([[vv11,vv12,vv13,vv14,vv15,vv16,vv17,vv18,vv19,vv10],
         [vv21,vv22,vv23,vv24,vv25,vv26,vv27,vv28,vv29,vv20],
         [vv31,vv32,vv33,vv34,vv35,vv36,vv37,vv38,vv39,vv30],
         [vv41,vv42,vv43,vv44,vv45,vv46,vv47,vv48,vv49,vv40]]):
vel_matrix:=
       map(collect,map(collect,map(collect,map(collect,
       map(collect,map(collect,map(collect,map(collect,
       map(collect,map(collect,map(collect,map(collect,
       map(collect,map(collect,map(collect,map(collect,
       map(collect,map(collect,map(simplify,
       subs(sx1^2=1-cx1^2,sx3^2=1-cx3^2,sx5^2=1-cx5^2,
            sx7^2=1-cx7^2,subs(sx1^3=sx1*(1-cx1^2),
            sx1^4=sx1^2*(1-cx1^2),sx3^3=sx3*(1-cx3^2),
            sx3^4=sx3^2*(1-cx3^2),sx5^3=sx5*(1-cx5^2),
            sx5^4=sx5^2*(1-cx5^2),sx7^3=sx7*(1-cx7^2),
            sx7^4=sx7^2*(1-cx7^2),subs(s1=sx1,s3=sx3,
            s5=sx5,s7=sx7,c1=cx1,c3=cx3,c5=cx5,c7=cx7,
                                  op(1,temp_matrix)))))
          ,sx1),sx3),sx5),sx7),cx1),cx3),cx5),cx7)
          ,m),x),y),z)
          ,I11),I12),I13),I22),I23),I33);

#interface(screenwidth=60);
#######################################################################

#######################################################################
#vel_tot_ff
#prepares the equations of motion for arrange_vel_ff
```

```
with(linalg):
read `eqns3D_ff.m`:

bb:= subs(diff(phi(t),t$2)=0,diff(psi(t),t$2)=0,
          diff(thetast(t),t$2)=0,diff(thetasw(t),t$2)=0,
                                    evalm(-1*H0dot_0)):

Onebb:=subs(diff(phi(t),t)=q2,diff(psi(t),t)=q4,
            diff(thetast(t),t)=q6, diff(thetasw(t),t)=q8,
                                                 op(1,bb)):
Twobb:=map(simplify,subs(phi(t)=x1,psi(t)=x3,thetast(t)=x5,
                         thetasw(t)=x7,op(1,Onebb))):

Threebb:= subs(
          sin(phi(t))    =sx1,   cos(phi(t))    =cx1,
          sin(psi(t))    =sx3,   cos(psi(t))    =cx3,
          sin(thetast(t))=sx5,   cos(thetast(t))=cx5,
          sin(thetasw(t))=sx7,   cos(thetasw(t))=cx7,
          op(1,Onebb)):
Threebb:= map(collect,map(collect,map(collect,map(collect,
          map(collect,map(collect,map(collect,map(collect,
          map(collect,map(collect,map(collect,map(collect,
          map(collect,map(collect,map(collect,map(collect,
          map(collect,map(collect,map(collect,map(collect,
          map(collect,map(collect,
     subs(sin(x1)    =sx1,   cos(x1)    =cx1,
          sin(x3)    =sx3,   cos(x3)    =cx3,
          sin(x5)    =sx5,   cos(x5)    =cx5,
          sin(x7)    =sx7,   cos(x7)    =cx7,
          op(1,Onebb))
       ,q2),q4),q6),q8)
       ,sx1),cx1),sx3),cx3),sx5),cx5),cx7),sx7)
       ,x),y),z),m)
       ,I11),I12),I13),I22),I23),I33):
#####################################################################

#####################################################################
#vel_swing_ff
#prepares the equations of motion for arrange_vel_ff

with(linalg):
read `eqns3D_ff.m`:

dd:= subs(diff(phi(t),t$2)=0,diff(psi(t),t$2)=0,
          diff(thetast(t),t$2)=0,diff(thetasw(t),t$2)=0,
                                           -1*H4dot_0):

Onedd:=subs(diff(phi(t),t)=q2,diff(psi(t),t)=q4,
            diff(thetast(t),t)=q6, diff(thetasw(t),t)=q8,dd):

Threedd:=  collect   (collect  (collect  (collect  (collect
           (collect  (collect  (collect  (collect  (collect
           (collect  (collect  (collect  (collect  (collect
           (collect  (collect  (collect  (collect  (collect
           (collect(collect(
     subs(sin(phi(t))    =sx1,   cos(phi(t))    =cx1,
          sin(psi(t))    =sx3,   cos(psi(t))    =cx3,
          sin(thetast(t))=sx5,   cos(thetast(t))=cx5,
          sin(thetasw(t))=sx7,   cos(thetasw(t))=cx7,
          Onedd)
       ,x),y),z),m)
       ,I11),I12),I13),I22),I23),I33)
       ,q2),q4),q6),q8)
       ,sx1),cx1),sx3),cx3),sx5),cx5),cx7),sx7):
#####################################################################
```

B.2 Energy Calculation

The total kinetic energy of the 3D walking system between collisions is

$$E_K = \frac{1}{2} m_3 \left(\mathbf{v}_3^0 \cdot \mathbf{v}_3^0 \right) + \frac{1}{2} \boldsymbol{\omega}_{3/0}^0 \cdot \ {}^0\mathbf{I}^3 \cdot \ \boldsymbol{\omega}_{3/0}^0 + \frac{1}{2} m_4 \left(\mathbf{v}_4^0 \cdot \mathbf{v}_4^0 \right) + \frac{1}{2} \boldsymbol{\omega}_{4/0}^0 \cdot \ {}^0\mathbf{I}^4 \cdot \ \boldsymbol{\omega}_{4/0}^0 \tag{B.28}$$

where the velocities of the center of mass of the stance and swing legs written in the fixed frame basis are, respectively,

$$\begin{aligned} \mathbf{v}_3^0 &= \frac{d}{dt} \mathbf{d}_{3/0}^0 \text{ and} \\ \mathbf{v}_4^0 &= \frac{d}{dt} \mathbf{d}_{4/0}^0. \end{aligned} \tag{B.29}$$

The total potential energy of the 3D walking system between collisions is

$$E_P = - \left(m_3 \left(\mathbf{d}_{3/0}^0 \cdot \mathbf{g}^0 \right) + m_4 \left(\mathbf{d}_{4/0}^0 \cdot \mathbf{g}^0 \right) \right). \tag{B.30}$$

The Maple® codes for generating the total energy equation is given below.

```
######################################################################
with(linalg):
read `eqns3D_ff.m`:

ke_st_cm:=(1/2)*m*innerprod(map(diff,d3_0_0,t),
                            map(diff,d3_0_0,t)):
ke_st_rot:=(1/2)*innerprod(w3_0_0,
         multiply(multiply(transpose(rot_0_3),
              multiply(Id3_3,rot_0_3)),w3_0_0)):
ke_sw_cm:=(1/2)*m*innerprod(map(diff,d4_0_0,t),
                              map(diff,d4_0_0,t)):
ke_sw_rot:=(1/2)*innerprod(w4_0_0,
         multiply(multiply(transpose(rot_0_4),
                             multiply(Id4_4,rot_0_4)),w4_0_0)):

ke_st_cm1:=subs(diff(phi(t),t)=q2,diff(psi(t),t)=q4,
                diff(thetast(t),t)=q6, diff(thetasw(t),t)=q8,
      ke_st_cm):
ke_st_cm2:=
   subs(sin(phi(t))    =s1,   cos(phi(t))    =c1,
        sin(psi(t))    =s3,   cos(psi(t))    =c3,
        sin(thetast(t))=s5,   cos(thetast(t))=c5,
        sin(thetasw(t))=s7,   cos(thetasw(t))=c7,ke_st_cm1):


ke_sw_cm1:=subs(diff(phi(t),t)=q2,diff(psi(t),t)=q4,
                diff(thetast(t),t)=q6, diff(thetasw(t),t)=q8,
ke_sw_cm):
ke_sw_cm2:=
   subs(sin(phi(t))    =s1,   cos(phi(t))    =c1,
        sin(psi(t))    =s3,   cos(psi(t))    =c3,
        sin(thetast(t))=s5,   cos(thetast(t))=c5,
        sin(thetasw(t))=s7,   cos(thetasw(t))=c7,ke_sw_cm1):

ke_st_rot1:=subs(diff(phi(t),t)=q2,diff(psi(t),t)=q4,
                 diff(thetast(t),t)=q6, diff(thetasw(t),t)=q8,
ke_st_rot):
ke_st_rot2:=
   subs(sin(phi(t))    =s1,   cos(phi(t))    =c1,
        sin(psi(t))    =s3,   cos(psi(t))    =c3,
```

```
        sin(thetast(t))=s5,   cos(thetast(t))=c5,
        sin(thetasw(t))=s7,   cos(thetasw(t))=c7,ke_st_rot1):

ke_sw_rot1:=subs(diff(phi(t),t)=q2,diff(psi(t),t)=q4,
                 diff(thetast(t),t)=q6, diff(thetasw(t),t)=q8,
ke_sw_rot):
ke_sw_rot2:=
   subs(sin(phi(t))    =s1,   cos(phi(t))    =c1,
        sin(psi(t))    =s3,   cos(psi(t))    =c3,
        sin(thetast(t))=s5,   cos(thetast(t))=c5,
        sin(thetasw(t))=s7,   cos(thetasw(t))=c7,ke_sw_rot1):

ke:=ke_st_cm2+ke_sw_cm2+ke_st_rot2+ke_sw_rot2:
ke1:=
       collect(collect(collect(collect(collect(collect(
       collect (collect (collect (collect (collect (collect(
       collect (collect (collect (collect (collect (collect(
       subs(s1^2=1-c1^2,s3^2=1-c3^2,s5^2=1-c5^2,s7^2=1-c7^2,
       subs(s1^3=s1*(1-c1^2),s1^4=s1^2*(1-c1^2),s3^3=s3*(1-c3^2),
         s3^4=s3^2*(1-c3^2),s5^3=s5*(1-c5^2),s5^4=s5^2*(1-c5^2),
         s7^3=s7*(1-c7^2),s7^4=s7^2*(1-c7^2),ke))
        ,s1),s3),s5),s7),c1),c3),c5),c7)
         ,m),x),y),z)
        ,I11),I12),I13),I22),I23),I33);


pe:=-1*(m*innerprod(d3_0_0,grav_0)+m*innerprod(d4_0_0,grav_0)):

pe1:=subs(sin(phi(t))    =s1,   cos(phi(t))    =c1,
          sin(psi(t))    =s3,   cos(psi(t))    =c3,
          sin(thetast(t))=s5,   cos(thetast(t))=c5,
          sin(thetasw(t))=s7,   cos(thetasw(t))=c7,
          sin(alpha)     =sa,cos(alpha)     =ca,pe);
interface(screenwidth=60);
#####################################################################
```

B.3 Derivation of the Collision Rules for Angular Rates

To begin, we first state the rules for updating the walking system through a swing foot collision.

B.3.1 Indexing Scheme

We have chosen a set of angles to describe the orientation of the walking device between collisions. We next present an indexing scheme to denote the state of the system just before and after the collision i of the i_{th} swing leg. We use the indexing scheme to define a 'cycle' of the walker — from just after a swing leg collision (heel-strike) to just after the next.

The i_{th} stance and swing legs are so designated after the i_{th} collision. Thus, the names of the legs are exchanged through a collision. That is, the i_{th} stance leg becomes the $i + 1_{th}$ swing leg and vice-versa for the i_{th} swing leg.

Special times of interest are just before and just after collision i. The minus and plus signs $(-)$ and $(+)$ are used as the superscripts to denote these times. For instance, ${}^i\theta_{st}^+$ is the stance leg angle just after collision i of swing leg $i-1$.

In defining the orientation of the walking device, we have defined fixed frame 0, stance leg frame 3 (fixed to the stance leg), and swing leg frame 4 (fixed to the swing leg). The stance leg frame ${}^i3$ has origin at the tip of the stance leg currently in contact with the ground after collision i. The swing leg frame ${}^i4$ has i origin at the hip joint. The z_3 and z_4 axes are aligned with the stance and swing legs, respectively.

We move the origin of the stance leg frame instantaneously with each swing leg collision from the tip of the pre-collision stance leg to the tip of the post-collision stance leg currently in contact with the ground after collision $i+1$. The origin of the swing leg frame remains at the hip joint.

As the origin of stance leg frame i is moved to the tip of the colliding leg, however, we not only translate the stance leg frame but also rotate it by $-2\ {}^{i+1}\theta_{st}^{-}$ about the y-axis with respect to the fixed frame so that the z_3-axis of stance leg frame $i+1$ is aligned with stance leg $i+1$. Thus, the stance leg angle changes instantaneously from θ_{st} to $-\theta_{st}$ through a downhill swing leg collision. Likewise, the swing leg frame rotates by $-2\ {}^{i+1}\theta_{sw}^{-}$ about the y axis with respect to the stance leg frame so that the z_4-axis of the swing leg frame $i+1$ is aligned with swing leg $i+1$.

After a collision, then, we redefine the absolute orientation with respect to the fixed frame using the newly positioned frames. The relationships between frames and their associated bases from before to after collision $i+1$ are

$$ {}^{i+1}3 \neq {}^{i}3;\ {}^{i+1}\mathbf{e}_3 = \mathbf{R}_2^3(\theta = -2\ {}^{i+1}\theta_{st}^{-})\ {}^{i}\mathbf{e}_3, \tag{B.31} $$

$$ {}^{i+1}4 \neq {}^{i}4;\ {}^{i+1}\mathbf{e}_4 = \mathbf{R}_3^4(\theta = -2\ {}^{i+1}\theta_{sw}^{-})\ {}^{i}\mathbf{e}_4. \tag{B.32} $$

At a swing foot collision, in addition to updating the state of the system, we must also be careful to update the leg parameters to take into account the reflection symmetry of the legs. Just after collision $i+1$ of swing leg i when it becomes the new stance leg $i+1$ and stance leg i becomes swing leg $i+1$, their center of mass parameters are different from those of the previous stance and swing legs i. The parameters change as follows:

$$ {}^{+}y = -\left({}^{-}y\right), \text{ or} \tag{B.33} $$

$$ \begin{Bmatrix} {}^{+}x \\ {}^{+}y \\ {}^{+}z \end{Bmatrix} = \mathbf{C} \cdot \begin{Bmatrix} {}^{-}x \\ {}^{-}y \\ {}^{-}z \end{Bmatrix} \tag{B.34} $$

where

$$ \mathbf{C} = \begin{bmatrix} 1 & 0 & 0 \\ 0 & -1 & 0 \\ 0 & 0 & 1 \end{bmatrix}. \tag{B.35} $$

Here, $+$ and $-$ refer to the leg parameters just after and just before a collision, respectively. Recall that, in between collisions, the inertia matrices for the stance and swing legs are the same. In between collisions, the x and y coordinates of the center of mass of each leg are opposite in sign but only the y coordinate for each changes sign through a collision.

B.3.2 Angular Momentum – Impulse: Conservation of Angular Momentum

Referring to Figure B.2, at the collision of the swing leg with the ground, there is an impulse at the swing foot contact point (point 5^{-}) and, consequently, also on the swing leg at the hip joint (point 4). Point 5^{-} is coincident with the origin of the origin 0^{+} of the post-collision fixed frame and the contact point 3^{+} of the post-collision stance leg. We assume that, during collision, other smaller forces (e.g., gravity) acting on the system are negligible in comparison to the collision impulses. We also assume there are no impulsive ground contact torques. At the instant of collision at the hip, we assume that the former stance leg loses contact with the ground (at the same instant the swing foot makes contact) and that it has no impulsive reaction with the ground as it leaves. Based on these assumptions, angular momentum is conserved for the entire system about the swing foot contact point during the collision process. Angular momentum is also conserved for the new swing leg (formerly the stance leg) about the hip joint hinge axis. We can write these conservation statements

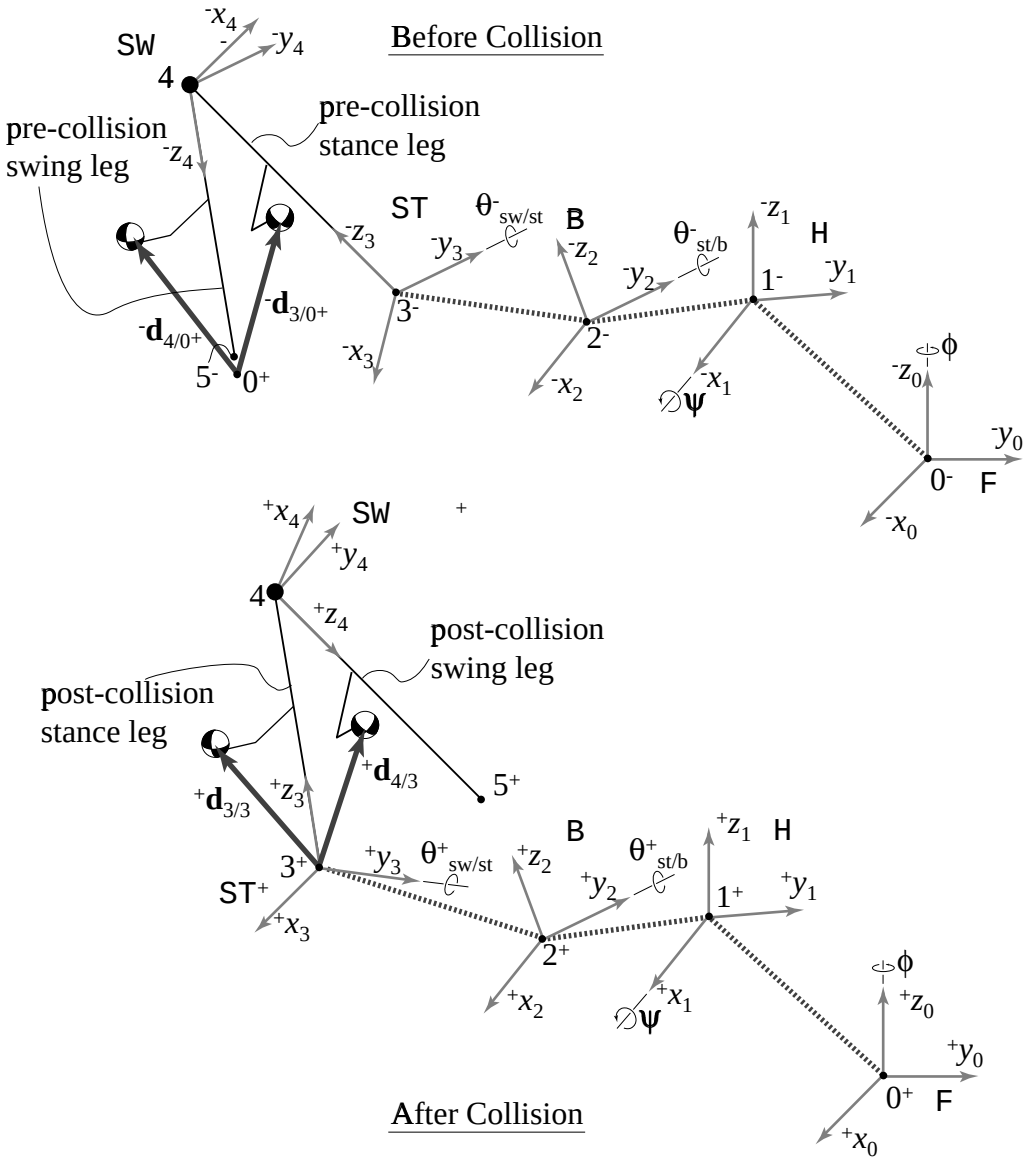

Figure B.2: A schematic showing the pre- and post-collision configurations of the 3D walking mechanisms.

as

$$\begin{aligned}
\sum_{s=3}^{4} {}^{+}\mathbf{H}^{s}_{/0+} &= \sum_{s=3}^{4} {}^{-}\mathbf{H}^{s}_{/0+} \text{ or} \\
{}^{+}\mathbf{H}^{3}_{/0+} + {}^{+}\mathbf{H}^{4}_{/0+} &= {}^{-}\mathbf{H}^{3}_{/0+} + {}^{-}\mathbf{H}^{4}_{/0+} \text{ and} \\
\left\{ {}^{+}\mathbf{H}^{4}_{/4} \right. &= \left. {}^{-}\mathbf{H}^{4}_{/4} \right\} \cdot \hat{\mathbf{Y}}_4. \qquad \text{(B.36)}
\end{aligned}$$

The plus (+) and minus (-) refer to the states of the system just before and just after the i_{th} collision of the the swing leg with the ground, respectively. Note that ${}^{+}\hat{\mathbf{Y}}_4 = {}^{-}\hat{\mathbf{Y}}_4$.

First, we write out the pre-collision (-) quantities and then the post-collision (+) ones needed for the angular momentum calculations.

B.3.3 Pre-collision Quantities

Rotation Matrices

The heading and bank angles remain the same through collision; i.e.,

$$\begin{aligned}
\phi^{+} &= \phi^{-} = \phi \text{ and} \\
\psi^{+} &= \psi^{-} = \psi. \qquad \text{(B.37)}
\end{aligned}$$

Thus, the pre-collision rotation matrices between frames are the same for the heading and bank frames as previously defined but different for the stance and swing frames as defined below:

$${}^{-}\mathbf{R}^{3}_{2}(\theta^{-}_{st}) = \begin{bmatrix} c\theta^{-}_{st} & 0 & -s\theta_{st}- \\ 0 & 1 & 0 \\ s\theta^{-}_{st} & 0 & c\theta^{-}_{st} \end{bmatrix}, \text{ and} \qquad \text{(B.38)}$$

$${}^{-}\mathbf{R}^{4}_{3}(\theta^{-}_{sw}) = \begin{bmatrix} c\theta^{-}_{sw} & 0 & -s\theta^{-}_{sw} \\ 0 & 1 & 0 \\ s\theta^{-}_{sw} & 0 & c\theta^{-}_{sw} \end{bmatrix}. \qquad \text{(B.39)}$$

$$\qquad \text{(B.40)}$$

Then, the rotation matrices between each intermediate frame and the fixed frame are

$$\begin{aligned}
\mathbf{R}^{2}_{0} &= \mathbf{R}^{2}_{1} \cdot \mathbf{R}^{1}_{0}, \qquad \text{(B.41)} \\
{}^{-}\mathbf{R}^{3}_{0} &= {}^{-}\mathbf{R}^{3}_{2} \cdot \mathbf{R}^{2}_{1} \cdot \mathbf{R}^{1}_{0}, \text{ and} \qquad \text{(B.42)} \\
{}^{-}\mathbf{R}^{4}_{0} &= {}^{-}\mathbf{R}^{4}_{3} \cdot \ {}^{-}\mathbf{R}^{3}_{2} \cdot \mathbf{R}^{2}_{1} \cdot \mathbf{R}^{1}_{0}. \qquad \text{(B.43)}
\end{aligned}$$

Angular Velocity

The pre-collision relative angular velocities between each successive frame are

$$\begin{aligned}
{}^{-}\boldsymbol{\omega}^{0}_{1/0} &= {}^{-}\dot{\phi} \ {}^{-}\hat{\mathbf{Z}}^{0}_{0}, \\
{}^{-}\boldsymbol{\omega}^{1}_{2/1} &= {}^{-}\dot{\psi} \ {}^{-}\hat{\mathbf{X}}^{1}_{1}, \\
{}^{-}\boldsymbol{\omega}^{2}_{3/2} &= {}^{-}\dot{\theta}_{st} \ {}^{-}\hat{\mathbf{Y}}^{2}_{2}, \text{ and} \\
{}^{-}\boldsymbol{\omega}^{3}_{4/3} &= {}^{-}\dot{\theta}_{st} \ {}^{-}\hat{\mathbf{Y}}^{3}_{3}. \qquad \text{(B.44)}
\end{aligned}$$

The pre-collision absolute angular velocity of the stance and swing legs written in the fixed frame basis are

$$\begin{aligned}
{}^{-}\boldsymbol{\omega}^{0}_{3/0} &= {}^{-}\boldsymbol{\omega}^{0}_{1/0} + {}^{-}\boldsymbol{\omega}^{0}_{2/1} + {}^{-}\boldsymbol{\omega}^{0}_{3/2} \text{ and} \qquad \text{(B.45)} \\
{}^{-}\boldsymbol{\omega}^{0}_{4/0} &= {}^{-}\boldsymbol{\omega}^{0}_{4/3} + {}^{-}\boldsymbol{\omega}^{0}_{3/0} \qquad \text{(B.46)}
\end{aligned}$$

where

$$\begin{aligned} {}^{-}\boldsymbol{\omega}^0_{1/0} &= {}^{-}\boldsymbol{\omega}^0_{1/0}, \\ {}^{-}\boldsymbol{\omega}^0_{2/1} &= [\mathbf{R}^1_0]^T \cdot {}^{-}\boldsymbol{\omega}^1_{2/1}, \\ {}^{-}\boldsymbol{\omega}^0_{3/2} &= [\mathbf{R}^2_0]^T \cdot {}^{-}\boldsymbol{\omega}^2_{3/2}, \text{ and} \\ {}^{-}\boldsymbol{\omega}^0_{4/3} &= [{}^{-}\mathbf{R}^3_0]^T \cdot {}^{-}\boldsymbol{\omega}^3_{4/3}. \end{aligned} \tag{B.47}$$

Center of Mass Position and Absolute Acceleration

The pre-collision stance and swing leg center of mass positions with respect to the pre-collision stance and swing frame origins are

$$\begin{aligned} {}^{-}\mathbf{d}^3_{3/3} &= x\,{}^{-}\hat{\mathbf{X}}^3_3 + y\,{}^{-}\hat{\mathbf{Y}}^3_3 + z\,{}^{-}\hat{\mathbf{Z}}^3_3 \text{ and} \\ {}^{-}\mathbf{d}^4_{4/4} &= -x\,{}^{-}\hat{\mathbf{X}}^4_4 - y\,{}^{-}\hat{\mathbf{Y}}^4_4 + (\ell - z)\,{}^{-}\hat{\mathbf{Z}}^4_4. \end{aligned} \tag{B.48}$$

The pre-collision position of the center of mass of the stance leg relative to the hip joint is

$${}^{-}\mathbf{d}^3_{3/4} = x\ {}^{-}\hat{\mathbf{X}}^3_3 + y\ {}^{-}\hat{\mathbf{Y}}^3_3 - (\ell - z)\ {}^{-}\hat{\mathbf{Z}}^3_3. \tag{B.49}$$

The pre-collision position of the center of mass of the swing leg relative to the swing foot is

$${}^{-}\mathbf{d}^4_{4/5} = x\ {}^{-}\hat{\mathbf{X}}^4_4 - y\ {}^{-}\hat{\mathbf{Y}}^4_4 - z\ {}^{-}\hat{\mathbf{Z}}^3_3. \tag{B.50}$$

The pre-collision positions of the hip relative to the stance foot and swing foot are, respectively

$${}^{-}\mathbf{r}^3_{4/3} = \ell\ {}^{-}\hat{\mathbf{Z}}^3_3 \text{ and} \tag{B.51}$$

$${}^{-}\mathbf{r}^4_{4/5} = -\ell\ {}^{-}\hat{\mathbf{Z}}^4_4. \tag{B.52}$$

The pre-collision stance and swing center of mass positions with respect to the origin of the pre-collision fixed frame written in the fixed frame basis are

$$\begin{aligned} {}^{-}\mathbf{d}^0_{3/0-} &= {}^{-}\mathbf{d}^0_{3/3} \\ &= [{}^{-}\mathbf{R}^3_0]^T \cdot^{-} \mathbf{d}^3_{3/3} \text{ and} \\ \mathbf{d}^0_{4/0-} &= {}^{-}\mathbf{d}^0_{4/4} + {}^{-}\mathbf{r}^0_{4/0-} \\ &= [{}^{-}\mathbf{R}^4_0]^T \cdot^{-} \mathbf{d}^4_{4/4} + [{}^{-}\mathbf{R}^3_0]^T \cdot^{-} \mathbf{r}^3_{4/3}. \end{aligned} \tag{B.53}$$

The pre-collision position of center of mass of the stance leg with respect to the point of collision of the swing foot on the ground (the post-collision origin of the fixed frame,0^+) written in the basis of the fixed frame coordinates is

$${}^{-}\mathbf{d}^0_{3/0^+} = {}^{-}\mathbf{d}^0_{3/4} + {}^{-}\mathbf{r}^0_{4/5}. = [{}^{-}\mathbf{R}^3_0]^T \cdot^{-} \mathbf{d}^3_{3/4} + [{}^{-}\mathbf{R}^4_0]^T \cdot^{-} \mathbf{r}^4_{4/5} = {}^{-}\mathbf{d}^0_{3/5}. \tag{B.54}$$

The pre-collision position of center of mass of the swing leg with respect to the point of collision of the swing foot on the ground, 0^+, written in the fixed frame coordinates is

$${}^{-}\mathbf{d}^0_{4/0^+} = {}^{-}\mathbf{d}^0_{4/5} = [{}^{-}\mathbf{R}^4_0]^T \cdot^{-} \mathbf{d}^4_{4/5} = {}^{-}\mathbf{d}^0_{4/5}. \tag{B.55}$$

The pre-collision velocities of the center of mass of the stance and swing legs written in the fixed frame basis are, respectively,

$$\begin{aligned} {}^{-}\mathbf{v}^0_3 &= \frac{d}{dt}\left({}^{-}\mathbf{d}^0_{3/0-}\right) \text{ and} \\ {}^{-}\mathbf{v}^0_4 &= \frac{d}{dt}\left({}^{-}\mathbf{d}^0_{4/0-}\right). \end{aligned} \tag{B.56}$$

Moment of Inertia Matrices

The pre-collision moment of inertia matrices for the stance and swing legs calculated with respect to the fixed frame are, respectively

$$\begin{aligned} {}^{-}\left[{}^{0}\mathbf{I}^{3}\right] &= \left[{}^{-}\mathbf{R}_{0}^{3}\right]^{T}\cdot\mathbf{I}\cdot\left[{}^{-}\mathbf{R}_{0}^{3}\right] \text{ and} \\ {}^{-}\left[{}^{0}\mathbf{I}^{4}\right] &= \left[{}^{-}\mathbf{R}_{0}^{4}\right]^{T}\cdot\mathbf{I}\cdot\left[{}^{-}\mathbf{R}_{0}^{4}\right]. \end{aligned} \tag{B.57}$$

B.3.4 Angular Momentum

The pre-collision angular momentum for the stance leg about the origin of the post-collision fixed frame, 0^{+} written in the fixed frame basis is

$${}^{-}\left(\mathbf{H}_{/0^{+}}^{3}\right)^{0} = {}^{-}\mathbf{H}_{/3}^{0} + {}^{-}\mathbf{d}_{3/0^{+}}^{0}\times m_{3}\,{}^{-}\mathbf{v}_{3}^{0} \tag{B.58}$$

where

$${}^{-}\mathbf{H}_{/3}^{0} = {}^{-}\left[{}^{0}\mathbf{I}^{3}\right]\cdot\,{}^{-}\boldsymbol{\omega}_{3/0}^{0}. \tag{B.59}$$

The angular momentum for the swing leg about the origin of the post-collision fixed frame written in the fixed frame basis is

$${}^{-}\left(\mathbf{H}_{/0^{+}}^{4}\right)^{0} = {}^{-}\mathbf{H}_{/4}^{0} + \mathbf{d}_{4/0^{+}}^{0}\times m_{4}\,{}^{-}\mathbf{v}_{4}^{0} \tag{B.60}$$

where

$${}^{-}\mathbf{H}_{/4}^{0} = {}^{-}\left[{}^{0}\mathbf{I}^{4}\right]\cdot\,{}^{-}\boldsymbol{\omega}_{4/0}^{0}. \tag{B.61}$$

The component along the hinge axis at the hip, of angular momentum about the origin of the swing frame for the stance leg, written in the fixed frame basis, is

$$\left\{{}^{-}\left(\mathbf{H}_{/4}^{3}\right)^{0} = {}^{-}\mathbf{H}_{/3}^{0} + {}^{-}\mathbf{d}_{3/4}^{0}\times m_{3}\,{}^{-}\mathbf{v}_{3}^{0}\right\}\cdot\hat{\mathbf{Y}}_{4}^{0} \tag{B.62}$$

where

$$\hat{\mathbf{Y}}_{4}^{0} = {}^{-}[\mathbf{R}_{0}^{4}]^{T}\cdot\hat{\mathbf{Y}}_{4}^{4}. \tag{B.63}$$

B.3.5 Post-collision Quantities

Rotation Matrices

Again, the post-collision rotation matrices between frames for the heading and bank frames are the same as those for pre-collision but different for the stance and swing frames as defined below:

$${}^{+}\mathbf{R}_{2}^{3}(\theta_{st}^{+}) = \begin{bmatrix} c\theta_{st}^{+} & 0 & -s\theta_{st+} \\ 0 & 1 & 0 \\ s\theta_{st}^{+} & 0 & c\theta_{st}^{+} \end{bmatrix}, \text{ and} \tag{B.64}$$

$${}^{+}\mathbf{R}_{3}^{4}(\theta_{sw}^{+}) = \begin{bmatrix} c\theta_{sw}^{+} & 0 & -s\theta_{sw}^{+} \\ 0 & 1 & 0 \\ s\theta_{sw}^{+} & 0 & c\theta_{sw}^{+} \end{bmatrix}. \tag{B.65}$$

$$\tag{B.66}$$

Then, the rotation matrices between each intermediate frame and the fixed frame are

$$\mathbf{R}_{0}^{2} = \mathbf{R}_{1}^{2}\cdot\mathbf{R}_{0}^{1}, \tag{B.67}$$

$${}^{+}\mathbf{R}_{0}^{3} = {}^{+}\mathbf{R}_{2}^{3}\cdot\mathbf{R}_{1}^{2}\cdot\mathbf{R}_{0}^{1}, \text{ and} \tag{B.68}$$

$${}^{+}\mathbf{R}_{0}^{4} = {}^{+}\mathbf{R}_{3}^{4}\cdot\;{}^{+}\mathbf{R}_{2}^{3}\cdot\mathbf{R}_{1}^{2}\cdot\mathbf{R}_{0}^{1}. \tag{B.69}$$

Angular Velocity

The post-collision relative angular velocities between each successive frame are

$$\begin{aligned} {}^{+}\boldsymbol{\omega}^0_{1/0} &= {}^{+}\dot{\phi}\ {}^{+}\hat{\mathbf{Z}}^0_0, \\ {}^{+}\boldsymbol{\omega}^1_{2/1} &= {}^{+}\dot{\psi}\ {}^{+}\hat{\mathbf{X}}^1_1, \\ {}^{+}\boldsymbol{\omega}^2_{3/2} &= {}^{+}\dot{\theta_{st}}\ {}^{+}\hat{\mathbf{Y}}^2_2, \text{ and} \\ {}^{+}\boldsymbol{\omega}^3_{4/3} &= {}^{+}\dot{\theta_{st}}\ {}^{+}\hat{\mathbf{Y}}^3_3. \end{aligned} \tag{B.70}$$

The post-collision absolute angular velocity of the stance and swing legs written in the fixed frame basis are

$$ {}^{+}\boldsymbol{\omega}^0_{3/0} = {}^{+}\boldsymbol{\omega}^0_{1/0} + {}^{+}\boldsymbol{\omega}^0_{2/1} + {}^{+}\boldsymbol{\omega}^0_{3/2} \text{ and} \tag{B.71}$$

$$ {}^{+}\boldsymbol{\omega}^0_{4/0} = {}^{+}\boldsymbol{\omega}^0_{4/3} + {}^{+}\boldsymbol{\omega}^0_{3/0} \tag{B.72}$$

where

$$\begin{aligned} {}^{+}\boldsymbol{\omega}^0_{1/0} &= {}^{+}\boldsymbol{\omega}^0_{1/0}, \\ {}^{+}\boldsymbol{\omega}^0_{2/1} &= [\mathbf{R}^1_0]^T \cdot {}^{+}\boldsymbol{\omega}^1_{2/1}, \\ {}^{+}\boldsymbol{\omega}^0_{3/2} &= [\mathbf{R}^2_0]^T \cdot {}^{+}\boldsymbol{\omega}^2_{3/2}, \text{ and} \\ {}^{+}\boldsymbol{\omega}^0_{4/3} &= [{}^{+}\mathbf{R}^3_0]^T \cdot {}^{+}\boldsymbol{\omega}^3_{4/3}. \end{aligned} \tag{B.73}$$

Center of Mass Position and Absolute Acceleration

The post-collision stance and swing leg center of mass positions with respect to the post-collision stance and swing frame origins are

$$\begin{aligned} {}^{+}\mathbf{d}^3_{3/3} &= x\ {}^{+}\hat{\mathbf{X}}^3_3 - y\ {}^{+}\hat{\mathbf{Y}}^3_3 + z\ {}^{+}\hat{\mathbf{Z}}^3_3 \text{ and} \\ {}^{+}\mathbf{d}^4_{4/4} &= -x\ {}^{+}\hat{\mathbf{X}}^4_4 + y\ {}^{+}\hat{\mathbf{Y}}^4_4 + (\ell - z)\ {}^{+}\hat{\mathbf{Z}}^4_4. \end{aligned} \tag{B.74}$$

The post-collision position of the hip relative to the stance foot is

$$ {}^{+}\mathbf{r}^3_{4/3} = \ell\ {}^{+}\hat{\mathbf{Z}}^3_3. \tag{B.75}$$

The post-collision stance and swing center of mass positions with respect to the origin of the post-collision fixed frame written in the fixed frame basis are

$$\begin{aligned} {}^{+}\mathbf{d}^0_{3/0+} &= {}^{+}\mathbf{d}^0_{3/3} \\ &= [{}^{+}\mathbf{R}^3_0]^T \cdot {}^{+}\mathbf{d}^3_{3/3} \text{ and} \\ \mathbf{d}^0_{4/0+} &= {}^{+}\mathbf{d}^0_{4/4} + {}^{+}\mathbf{r}^0_{4/0+} \\ &= [{}^{+}\mathbf{R}^4_0]^T \cdot {}^{+}\mathbf{d}^4_{4/4} + [{}^{+}\mathbf{R}^3_0]^T \cdot {}^{+}\mathbf{r}^3_{4/3}. \end{aligned} \tag{B.76}$$

The post-collision position of the hip relative to the origin of the post-collision fixed frame written in the fixed frame basis is

$$ {}^{+}\mathbf{r}^0_{4/0+} = [{}^{+}\mathbf{R}^3_0]^T \cdot {}^{+}\mathbf{r}^3_{4/3}. \tag{B.77}$$

The post-collision velocities of the center of mass of the stance and swing legs written in the fixed frame basis are, respectively,

$$\begin{aligned} {}^{+}\mathbf{v}^0_3 &= \frac{d}{dt}\left({}^{+}\mathbf{d}^0_{3/0+}\right) \text{ and} \\ {}^{+}\mathbf{v}^0_4 &= \frac{d}{dt}\left({}^{+}\mathbf{d}^0_{4/0+}\right). \end{aligned} \tag{B.78}$$

Moment of Inertia Matrices

The post-collision moment of inertia matrices for the stance and swing legs calculated with respect to the fixed frame are, respectively

$$\begin{aligned} {}^{+}\left[{}^{0}\mathbf{I}^{3}\right] &= \left[{}^{+}\mathbf{R}_{0}^{3}\right]^{T} \cdot {}^{+}\mathbf{I} \cdot \left[{}^{+}\mathbf{R}_{0}^{3}\right] \text{ and} \\ {}^{+}\left[{}^{0}\mathbf{I}^{4}\right] &= \left[{}^{+}\mathbf{R}_{0}^{4}\right]^{T} \cdot {}^{+}\mathbf{I} \cdot \left[{}^{+}\mathbf{R}_{0}^{4}\right]. \end{aligned} \tag{B.79}$$

B.3.6 Angular Momentum

The post-collision angular momentum for the stance leg about the origin of the post-collision fixed frame, 0^{+} written in the fixed frame basis is

$${}^{+}\left(\mathbf{H}_{/0^{+}}^{3}\right)^{0} = {}^{+}\mathbf{H}_{/3}^{0} + {}^{+}\mathbf{d}_{3/0^{+}}^{0} \times m_{3}\, {}^{+}\mathbf{v}_{3}^{0} \tag{B.80}$$

where

$${}^{+}\mathbf{H}_{/3}^{0} = {}^{+}\left[{}^{0}\mathbf{I}_{+}^{3}\right] \cdot {}^{+}\boldsymbol{\omega}_{3/0}^{0}. \tag{B.81}$$

The angular momentum for the swing leg about the origin of the post-collision fixed frame written in the fixed frame basis is

$${}^{+}\left(\mathbf{H}_{/0^{+}}^{4}\right)^{0} = {}^{+}\mathbf{H}_{/4}^{0} + \mathbf{d}_{4/0^{+}}^{0} \times m_{4}\, {}^{+}\mathbf{v}_{4}^{0} \tag{B.82}$$

where

$${}^{+}\mathbf{H}_{/4}^{0} = {}^{+}\left[{}^{0}\mathbf{I}_{+}^{4}\right] \cdot {}^{+}\boldsymbol{\omega}_{4/0}^{0}. \tag{B.83}$$

The component along the hinge axis at the hip, of angular momentum about the origin of the swing frame for the swing leg, written in the fixed frame basis, is

$$\left\{ {}^{+}\left(\mathbf{H}_{/4}^{4}\right)^{0} = {}^{+}\mathbf{H}_{/4}^{0} + {}^{+}\mathbf{d}_{4/4}^{0} \times m_{4}\, {}^{+}\mathbf{v}_{4}^{0} \right\} \cdot \hat{\mathbf{Y}}_{4}^{0} \tag{B.84}$$

where

$$\hat{\mathbf{Y}}_{4}^{0} = {}^{+}[\mathbf{R}_{0}^{4}]^{T} \cdot \hat{\mathbf{Y}}_{4}^{4}. \tag{B.85}$$

B.3.7 The Collision Rule

Once we find the angular momentum quantities for pre- and post- collision we can write the conservation of angular momentum relations as

$${}^{+}\mathbf{A}({}^{+}\phi, {}^{+}\psi, {}^{+}\theta_{st}, {}^{+}\theta_{sw}) \begin{Bmatrix} {}^{+}\dot{\phi} \\ {}^{+}\dot{\psi} \\ {}^{+}\dot{\theta}_{st} \\ {}^{+}\dot{\theta}_{sw} \end{Bmatrix} = {}^{-}\mathbf{A}({}^{-}\phi, {}^{-}\psi, {}^{-}\theta_{st}, {}^{-}\theta_{sw}) \begin{Bmatrix} {}^{-}\dot{\phi} \\ {}^{-}\dot{\psi} \\ {}^{-}\dot{\theta}_{st} \\ {}^{-}\dot{\theta}_{sw} \end{Bmatrix}. \tag{B.86}$$

where ${}^{+}\mathbf{A}$ and ${}^{-}\mathbf{A}$ are 4x4 matrices that are functions of the pre- and post- collision configuration variables.

B.3.8 Assembling the Collision Rule Matrices

The Maple® codes for assembling, ${}^{+}\mathbf{A}$ and ${}^{-}\mathbf{A}$, the pre- and post- collision matrices, are given below.

```
#################################################################
#jump3D_ff_minus

#jump3D_ff_minus generates the pre-collision collision-rule
#matrix.  The output is minus_matrix.

#Invoke linear algebra package
with(linalg):
#Kinematics
#Rotations Matrices

rot_0_1:=matrix([[cos(phi(t)),sin(phi(t)),0],
                 [-sin(phi(t)),cos(phi(t)),0],
                 [0,0,1]]):
rot_1_2:=matrix([[1,0,0],
                 [0,cos(psi(t)),sin(psi(t))],
                 [0,-sin(psi(t)),cos(psi(t))]]):
rot_2_3m:=matrix([[cos(thetastm(t)),0,-sin(thetastm(t))],
                 [0,1,0],
                 [sin(thetastm(t)),0,cos(thetastm(t))]]):
rot_3_4m:=matrix([[cos(thetaswm(t)),0,-sin(thetaswm(t))],
                 [0,1,0],
                 [sin(thetaswm(t)),0,cos(thetaswm(t))]]):
rot_0_2:=multiply(rot_1_2,rot_0_1):
rot_0_3m:=multiply(rot_2_3m,multiply(rot_1_2,rot_0_1)):
rot_0_4m:=multiply(rot_3_4m,
           multiply(rot_2_3m,
             multiply(rot_1_2,rot_0_1))):

#Angular velocity

w3_0_0:=add(array([0,0,diff(phi(t),t)]),
            add(multiply(transpose(rot_0_1),
               array([diff(psi(t),t),0,0])),
                multiply(transpose(rot_0_2),
                 array([0,diff(thetastm(t),t),0])))):
w4_0_0:=add(w3_0_0,multiply(transpose(rot_0_3m),
               array([0,diff(thetaswm(t),t),0]))):

#Position Vectors

d3_0m_0:=    multiply(transpose(rot_0_3m),array([x,y,z])):
d4_0m_0:=add(multiply(transpose(rot_0_3m),array([0,0,1])),
             multiply(transpose(rot_0_4m),array([-x,-y,1-z]))):
d4_4_0:=     multiply(transpose(rot_0_4m),array([-x,-y,1-z])):

d3_0p_0:=add(
           multiply(transpose(rot_0_3m),array([x,y,-(1-z)])),
           multiply(transpose(rot_0_4m),array([0,0,-1]))):
d3_4_0:=   multiply(transpose(rot_0_3m),array([x,y,-(1-z)])):

d4_0p_0:=  multiply(transpose(rot_0_4m),array([-x,-y,-z])):

#Angular momenta
#Moment of Inertia Matrices

#w.r.t d3
Id3_3:=matrix([[I11,I12,I13],
               [I12,I22,I23],
               [I13,I23,I33]]):

#w.r.t d4
Id4_4:=matrix([[I11,I12,I13],
               [I12,I22,I23],
```

```
              [I13,I23,I33]]):

#About point 0_plus...

H0p_0:=add(
          add(
            multiply(
             multiply(transpose(rot_0_3m),
              multiply(Id3_3,rot_0_3m)),
                                    w3_0_0),
            crossprod(d3_0p_0,evalm(m*map(diff,d3_0m_0,t)))),
          add(
           multiply(
                   multiply(transpose(rot_0_4m),
                       multiply(Id4_4,rot_0_4m)),
                                       w4_0_0),
            crossprod(d4_0p_0,evalm(m*map(diff,d4_0m_0,t))))):

#About point 4...

H4_0:=innerprod(
          add(
           multiply(
                     multiply(transpose(rot_0_3m),
                       multiply(Id3_3,rot_0_3m)),
                                       w3_0_0),
           crossprod(d3_4_0,evalm(m*map(diff,d3_0m_0,t)))),
          multiply(transpose(rot_0_3m),array([0,1,0]))):

angdot:= array([diff(phi(t),t),diff(psi(t),t),diff(thetastm(t),t),
                diff(thetaswm(t),t)]):

Angmom:=array([H0p_0[1],H0p_0[2],H0p_0[3],H4_0]):

for i from 1 by 1 to 4 do
 for j from 1 by 1 to 4 do
 mp[i,j]:=coeff(expand(Angmom[i]),angdot[j],1)

od;
od;

g:=(i,j) ->mp[i,j]:
coef_matrix:=matrix(4,4,g):

for r from 1 by 1 to 4 do
for s from 1 by 1 to 4 do
Twocoef_matrix[r,s]:=simplify(subs(phi(t)=x1,psi(t)=x3,
        thetastm(t)=x5m,thetaswm(t)=x7m, coef_matrix[r,s])):
Threecoef_matrix[r,s]:=
         subs(sin(x1)=s1,sin(x3)=s3,sin(x5m)=s5m,sin(x7m)=s7m,
              cos(x1)=c1,cos(x3)=c3,cos(x5m)=c5m,cos(x7m)=c7m,
                                       Twocoef_matrix[r,s]):
od:
od:

gg:=(r,s) ->Threecoef_matrix[r,s]:
temp_matrix:=matrix(4,4,gg):

minus_matrix:=map(collect,map(collect,map(collect,map(collect,

map(collect,
map(collect,map(collect,map(collect,map(collect,map(collect,
map(collect,map(collect,map(collect,map(collect,map(collect,
map(collect,map(collect,map(collect,temp_matrix
```

```
       ,s1),c1),s3),c3),s5m),c5m),c7m),s7m)
       ,x),y),z),m)
       ,I11),I12),I13),I22),I23),I33):

#interface(screenwidth=60);
######################################################################

######################################################################
#jump3D_ff_plus

#jump3D_ff_plus generates the post-collision collision-rule
#matrix.  The output is plus_matrix.

#Invoke linear algebra package
with(linalg):
#Kinematics
#Rotations Matrices

rot_0_1:=matrix([[cos(phi(t)),sin(phi(t)),0],
                 [-sin(phi(t)),cos(phi(t)),0],
                 [0,0,1]]):
rot_1_2:=matrix([[1,0,0],
                 [0,cos(psi(t)),sin(psi(t))],
                 [0,-sin(psi(t)),cos(psi(t))]]):
rot_2_3p:=matrix([[cos(thetastp(t)),0,-sin(thetastp(t))],
                 [0,1,0],
                 [sin(thetastp(t)),0,cos(thetastp(t))]]):
rot_3_4p:=matrix([[cos(thetaswp(t)),0,-sin(thetaswp(t))],
                 [0,1,0],
                 [sin(thetaswp(t)),0,cos(thetaswp(t))]]):
rot_0_2:=multiply(rot_1_2,rot_0_1):
rot_0_3p:=multiply(rot_2_3p,multiply(rot_1_2,rot_0_1)):
rot_0_4p:=multiply(rot_3_4p,multiply(rot_2_3p,
                           multiply(rot_1_2,rot_0_1))):

#Angular velocity

w3_0_0:=add(array([0,0,diff(phi(t),t)]),
            add(multiply(transpose(rot_0_1),
              array([diff(psi(t),t),0,0])),
               multiply(transpose(rot_0_2),
                 array([0,diff(thetastp(t),t),0])))):
w4_0_0:=add(w3_0_0,multiply(transpose(rot_0_3p),
               array([0,diff(thetaswp(t),t),0]))):

#Position Vectors

d3_0p_0:=    multiply(transpose(rot_0_3p),array([x,-y,z])):
d4_0p_0:=add(multiply(transpose(rot_0_3p),array([0,0,1])),
             multiply(transpose(rot_0_4p),array([-x,y,1-z]))):
d4_4_0:=     multiply(transpose(rot_0_4p),array([-x,y,1-z])):

#Angular momenta
#Moment of Inertia Matrices

#w.r.t d3
Id3_3:=matrix([[I11,I12,I13],
               [I12,I22,I23],
               [I13,I23,I33]]):

#w.r.t d4
Id4_4:=matrix([[I11,I12,I13],
               [I12,I22,I23],
               [I13,I23,I33]]):
```

```
#About point 0_plus...

H0p_0:=add(
          add(
         multiply(
                  multiply(transpose(rot_0_3p),
                      multiply(Id3_3,rot_0_3p)),
                                       w3_0_0),
           crossprod(d3_0p_0,evalm(m*map(diff,d3_0p_0,t)))),

          add(
          multiply(
                  multiply(transpose(rot_0_4p),
                      multiply(Id4_4,rot_0_4p)),
                                       w4_0_0),
           crossprod(d4_0p_0,evalm(m*map(diff,d4_0p_0,t))))):

#About point 4...

H4_0:=innerprod(
           add(
            multiply(
                     multiply(transpose(rot_0_4p),
                       multiply(Id4_4,rot_0_4p)),
                                       w4_0_0),
           crossprod(d4_4_0,evalm(m*map(diff,d4_0p_0,t)))),
          multiply(transpose(rot_0_4p),array([0,1,0]))):

angdot:= array([diff(phi(t),t),diff(psi(t),t),diff(thetastp(t),t),
                diff(thetaswp(t),t)]):

Angmom:=array([H0p_0[1],H0p_0[2],H0p_0[3],H4_0]):

for i from 1 by 1 to 4 do
 for j from 1 by 1 to 4 do
 mp[i,j]:=coeff(expand(Angmom[i]),angdot[j],1)

od;
od;

g:=(i,j) ->mp[i,j]:
coef_matrix:=matrix(4,4,g):

for r from 1 by 1 to 4 do
for s from 1 by 1 to 4 do
Twocoef_matrix[r,s]:=
      simplify(subs(phi(t)=x1,psi(t)=x3,thetastp(t)=x5p,
                    thetaswp(t)=x7p, coef_matrix[r,s])):
Threecoef_matrix[r,s]:=
      subs(sin(x1)=s1,sin(x3)=s3,sin(x5p)=s5p,sin(x7p)=s7p,
           cos(x1)=c1,cos(x3)=c3,cos(x5p)=c5p,cos(x7p)=c7p,
                          Twocoef_matrix[r,s]):
od:
od:

gg:=(r,s) ->Threecoef_matrix[r,s]:
temp_matrix:=matrix(4,4,gg):

plus_matrix:=
    map(collect,map(collect,map(collect,map(collect,map(collect,
    map(collect,map(collect,map(collect,map(collect,map(collect,
    map(collect,map(collect,map(collect,map(collect,map(collect,
    map(collect,map(collect,map(collect,temp_matrix
       ,s1),c1),s3),c3),s5p),c5p),c7p),s7p)
```

```
        ,x),y),z),m)
        ,I11),I12),I13),I22),I23),I33):

#interface(screenwidth=60);
```

Appendix C

Derivation of the Infinite Sequences of The Measure of Angular Rate of the 2D Rimless Wheel

Here, we derive the three very special infinite sequences of the after-collision angular rate that leave the 2D rimless wheel eventually in the vertical position. Each of the sequences is constructed as follows. First, we find the first point in the sequence as the measure of angular velocity after one collision such that, after the next collision, the wheel reaches the vertical in infinite time. Then, we find the second point as the measure of angular velocity such that the after a collision the wheel emerges with the measure of angular velocity that is the first point in the sequence and so on up to the m_{th} measure of angular velocity in the sequence.

For example, consider the first sequence, ${}^{dn}z_m > {}^{dn}z$. In terms of the map P, the first point in the sequence, ${}^{dn}z_1$, the point that gets mapped to ${}^{dn}z$ after one collision, is found by solving

$$\begin{aligned} {}^{dn}z &= P({}^{dn}z_1) \quad \text{or} && \text{(C.1)} \\ {}^{dn}z_1 &= \frac{{}^{dn}z}{\mu^2} - 4\lambda^2 \sin\alpha \sin\frac{\pi}{n}. && \text{(C.2)} \end{aligned}$$

Then, similarly,

$$\begin{aligned} {}^{dn}z_1 &= P({}^{dn}z_2) \quad \text{or} && \text{(C.3)} \\ {}^{dn}z_2 &= \frac{{}^{dn}z_1}{\mu^2} - 4\lambda^2 \sin\alpha \sin\frac{\pi}{n}(1+\frac{1}{\mu^2}) \\ &= \frac{{}^{dn}z}{(\mu^2)^2} - 4\lambda^2 \sin\alpha \sin\frac{\pi}{n}(1+\frac{1}{\mu^2}). && \text{(C.4)} \end{aligned}$$

Next,

$${}^{dn}z_3 = \frac{{}^{dn}z}{(\mu^2)^3} - 4\lambda^2 \sin\alpha \sin\frac{\pi}{n}(1+\frac{1}{\mu^2}+\frac{1}{(\mu^2)^2}) \qquad \text{(C.5)}$$

and so on until

$${}^{dn}z_m = \frac{{}^{dn}z}{\mu^{2m}} - 4\lambda^2 \sin\alpha \sin\frac{\pi}{n}(1+\frac{1}{\mu^2}+\frac{1}{(\mu^2)^2}+\cdots+\frac{1}{\mu^{2(m-1)}})$$

$$= \frac{{}^{dn}z}{\mu^{2m}} - 4\lambda^2 \sin\alpha \sin\frac{\pi}{n} \sum_{k=1}^{m} \frac{1}{\mu^{2(k-1)}}. \tag{C.6}$$

The other two infinite sequences are derived similarly. All three sequences and their conditions for existence are summarized in detail below. For each of the sequences to exist, the necessary condition is that $\alpha \leq \frac{\pi}{n}$; otherwise, the vertical position does not exist.

- 1. There exists a monotonically increasing infinite sequence of angular velocities after collision, ${}^{dn}\dot{\theta}_m > {}^{dn}\dot{\theta} > 0$, such that if the wheel starts with any angular velocity in the sequence, the wheel will eventually stop in the vertical position in the downhill direction after a finite number of collisions; i.e., each measure of angular velocity $z({}^{dn}\dot{\theta}_m) = {}^{dn}z_m > {}^{dn}z > 0$ gets mapped eventually by the map P to ${}^{dn}z$ in m iterations, $P^m({}^{dn}z_m) = {}^{dn}z$. The sequence ${}^{dn}z_m$ is

$${}^{dn}z_m = \frac{{}^{dn}z}{\mu^{2m}} - 4\lambda^2 \sin\alpha \sin\frac{\pi}{n} \sum_{k=1}^{m} \frac{1}{\mu^{2(k-1)}}. \tag{C.7}$$

  Summing the series yields

$${}^{dn}z_m = \frac{{}^{dn}z}{\mu^{2m}} - 4\lambda^2 \sin\alpha \sin\frac{\pi}{n} \frac{\mu^{2m}-1}{\mu^2-1} \frac{\mu^2}{\mu^{2m}}. \tag{C.8}$$

  The existence of this sequence requires that each angular velocity after collision in the sequence be greater than the angular velocity after collision that is necessary for the wheel to eventually stop in the vertical position; i.e., the inequality ${}^{dn}z_m > {}^{dn}z > 0$ holds. This requirement yields a necessary and sufficient condition for the existence of the sequence,

$$\begin{aligned} g(\alpha, \lambda^2, n) &> 0 \quad \text{or} \\ \alpha &< \alpha_c \end{aligned} \tag{C.9}$$

  where the function g and critical angle α_c are defined in Equations (2.29) and (2.30).

- 2. There exists a monotonically decreasing sequence of angular velocities after collision, ${}^{up}\dot{\theta}_m < {}^{up}\dot{\theta} < 0$, such that if the wheel starts with any angular velocity in the sequence, the wheel will eventually stop in the vertical position in the uphill direction after a finite number of collisions; i.e., each measure of angular velocity $z({}^{up}\dot{\theta}_m) = {}^{up}z_m < {}^{up}z < 0$ gets mapped eventually by the map P to ${}^{up}z$ in m iterations, $P^m({}^{up}z_m) = {}^{up}z$. The sequence ${}^{up}z_m$ is

$${}^{up}z_m = \frac{{}^{up}z}{\mu^{2m}} - 4\lambda^2 \sin\alpha \sin\frac{\pi}{n} \frac{\mu^{2m}-1}{\mu^2-1} \frac{\mu^2}{\mu^{2m}}. \tag{C.10}$$

  The existence of this sequence requires that each angular velocity after collision in the sequence be greater in magnitude than the angular velocity after collision necessary for the wheel to eventually stop in the vertical position; i.e., the inequality ${}^{up}z_m < {}^{up}z < 0$ holds. This requirement leads to a necessary condition for the existence of the sequence,

$$1 - \cos\frac{\pi}{n}\cos\alpha + \frac{1+\mu^2}{1-\mu^2}\sin\frac{\pi}{n}\sin\alpha > 0. \tag{C.11}$$

  This equality holds for any slope angle, $0 \leq \alpha \leq \frac{\pi}{2}$. But, we already have the more restrictive condition for the sequence to exist, $0 \leq \alpha \leq \frac{\pi}{n}$, so that the vertical position is attainable. This condition is necessary and sufficient.

- 3. First, there exists an angular velocity after collision, ${}^{up}\dot{\theta} < {}^{up}\bar{\dot{\theta}} < 0$, where ${}^{up}\bar{\dot{\theta}} = -(\frac{{}^{dn}\dot{\theta}}{\mu})$, such that the wheel fails to make it past the vertical position in the uphill direction, reverses

direction, makes one collision in the downhill direction and eventually stops in the vertical position ; i.e., $z(^{up}\bar{\dot{\theta}}) = {}^{up}\bar{z} = -(\frac{^{dn}z}{\mu^2})$, ${}^{up}z < {}^{up}\bar{z} < 0$, gets mapped by P in one iteration to ${}^{dn}z$. If $^{up}\bar{\dot{\theta}}$ exists, then there exists a monotonically decreasing sequence of angular velocities after collision, ${}^{up}\dot{\theta}_m < {}^{up}\dot{\theta} < 0$, such that if the wheel starts with any angular velocity in the sequence, the wheel will eventually stop in the vertical position in the downhill direction; i.e., each measure of velocity $z(^{up}\bar{\dot{\theta}}_m) = {}^{up}\bar{z}_m$, ${}^{up}\bar{z}_m < {}^{up}z < 0$ gets mapped eventually by P to ${}^{up}\bar{z}$ in m iterations and then to ${}^{dn}z$ in one iteration, $P^{m+1}({}^{up}\bar{z}_m) = {}^{dn}z$. The sequence ${}^{up}\bar{z}_m$ is

$$ {}^{up}\bar{z}_m = -\frac{^{dn}z}{\mu^{2(m+1)}} - 4\lambda^2 \sin\alpha \sin\frac{\pi}{n}\frac{\mu^{2m}-1}{\mu^2-1}\frac{\mu^2}{\mu^{2m}}. \tag{C.12} $$

The existence of this sequence requires that the inequalities ${}^{up}z < {}^{up}\bar{z} < 0$ and ${}^{up}\bar{z}_m < {}^{up}z < 0$ hold. Both of these inequalities yield the condition

$$ \begin{aligned} g(\alpha, \lambda^2, n) &< 0 \quad \text{or} \\ \alpha &> \alpha_c. \end{aligned} \tag{C.13} $$

Thus, a necessary and sufficient condition for the sequence to exist is that the slope be intermediate in size; i.e., $\alpha_c < \alpha < \frac{\pi}{n}$.

Appendix D

3-1-2 Euler Angles

The rotating frames and their associated bases, coordinates, and angles of rotation used to define the 3-1-2 Euler angles are summarized in Table D.1. The frames and Euler angles are illustrated in

Table D.1: Description of the Rotating Frames and the 3-1-2 Euler angles.

Reference Frames: Bases, Coordinates, and Rotation Angles			
Frame	Basis	Coordinates	Euler Angle
$\mathcal{F} \equiv$ Fixed Frame	$\mathbf{e}_f = (\hat{\mathbf{i}}_f, \hat{\mathbf{j}}_f, \hat{\mathbf{k}}_f)$	(x_f, y_f, z_f)	NA
$\mathcal{H} \equiv$ Heading Frame	$\mathbf{e}_h = (\hat{\mathbf{i}}_h, \hat{\mathbf{j}}_h, \hat{\mathbf{k}}_h)$	(x_h, y_h, z_h)	Heading Angle, ϕ
$\mathcal{B} \equiv$ Bank Frame	$\mathbf{e}_b = (\hat{\mathbf{i}}_b, \hat{\mathbf{j}}_b, \hat{\mathbf{k}}_b)$	(x_b, y_b, z_b)	Bank Angle, ψ
$\mathcal{W} \equiv$ Body Frame	$\mathbf{e}_w = (\hat{\mathbf{i}}_w, \hat{\mathbf{j}}_w, \hat{\mathbf{k}}_w)$	(x_w, y_w, z_w)	Pitch Angle, θ

figure D.1. The heading angle ϕ is a rotation of the heading frame $\mathcal{H}$ with respect to the fixed frame $\mathcal{F}$ about the z_f axis; the bank angle ψ is a rotation of the bank frame $\mathcal{B}$ with respect to the heading frame about the x_h axis; and the pitch angle is a rotation of the body frame $\mathcal{W}$ with respect to the bank frame about the y_b axis.

The general angular orientation described so far may be represented by a product of three principal rotation matrices:

$$\mathbf{R}(\phi, \psi, \theta) \equiv \mathbf{R}_2(\theta)\mathbf{R}_1(\psi)\mathbf{R}_3(\phi) \tag{D.1}$$

where

$$\begin{aligned}
\mathbf{R}_3(\phi) &= \begin{bmatrix} c\phi & s\phi & 0 \\ -s\phi & c\phi & 0 \\ 0 & 0 & 1 \end{bmatrix}, \\
\mathbf{R}_1(\psi) &= \begin{bmatrix} 1 & 0 & 0 \\ 0 & c\psi & s\psi \\ 0 & -s\phi & c\phi \end{bmatrix}, \text{ and} \\
\mathbf{R}_2(\theta) &= \begin{bmatrix} c\theta & -s\theta & 0 \\ 0 & 1 & 0 \\ s\theta & 0 & c\theta \end{bmatrix}. \qquad \text{(D.2)}
\end{aligned}$$

(D.3)

The letters 'c' and 's' are shorthand for cosine and sine. So, multiplying the three matrices together,

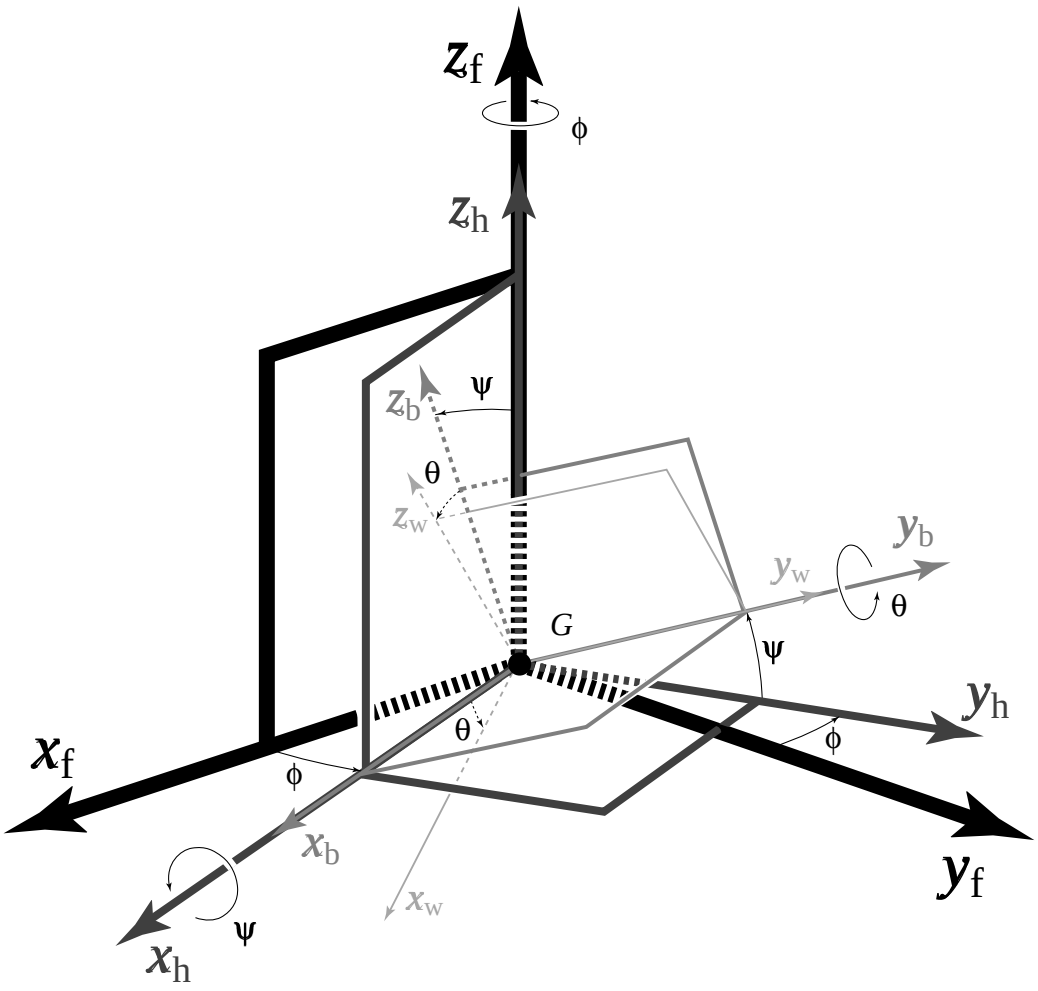

Figure D.1: The 3-1-2 Euler angles and associated rotating frames.

we get

$$\mathbf{R}(\phi,\psi,\theta) = \begin{bmatrix} c\theta\ c\phi - s\theta\ s\phi s\psi & c\theta\ s\phi + s\theta\ s\phi\ c\psi & s\theta\ c\psi \\ -c\psi\ s\phi & c\phi\ c\psi & s\psi \\ s\theta\ c\phi & s\phi\ s\theta - c\phi\ s\psi\ c\theta & c\psi\ c\theta \end{bmatrix}. \tag{D.4}$$

Thus, the relationship between the reference frame bases are:

$$\begin{aligned} \mathbf{e}_h &= \mathbf{R}_3(\phi)\mathbf{e}_f \\ \mathbf{e}_b &= \mathbf{R}_1(\psi)\mathbf{e}_h = \mathbf{R}_1(\psi)\mathbf{R}_3(\phi)\mathbf{e}_f \\ \mathbf{e}_w &= \mathbf{R}_2(\theta)\mathbf{e}_b = \mathbf{R}_2(\theta)\mathbf{R}_1(\psi)\mathbf{e}_h = \mathbf{R}(\phi,\psi,\theta)\mathbf{e}_f. \end{aligned} \tag{D.5}$$

There are 12 independent Euler angle sets which is due to the possible combinations of three different numbers. That is, there are 12 different sequences of rotations about each of the coordinate axes to describe the same spatial orientation. We have chosen 3-1-2 Euler angles because the heading and bank angles do not change through a collision. That this so can be shown as follows. Consider the case of the 3D rimless spoked wheel. (The results are the same for the planar 3D walking mechanism.)

We move the origins of each of the frames instantaneously with each collision, from the tip of spoke i to the tip of spoke $i+1$ currently in contact with the ground at collision $i+1$. After a collision, then, we redefine the wheel orientation with the respect to the newly positioned frames.

As the origins of the various frames i are moved to the tip of the colliding spoke $i+1$, however, we not only translate the wheel frame but also rotate it by $-\frac{2\pi}{n}$ about the y_b-axis with respect to the bank frame so that the z_w-axis of the new wheel frame is aligned with spoke $i+1$. The spoke presently on the ground in some sense characterizes the orientation of the wheel frame with respect to the bank frame. Thus, the pitch angle changes from $\frac{\pi}{n}$ to $-\frac{\pi}{n}$ through a downhill collision.

The orientation of the wheel basis with respect to the fixed frame basis just before collision $i+1$ is given by Equation (D.5)

$${}^{i+1}\mathbf{e}_w^- = \left[\mathbf{R}({}^{i+1}\phi^-,\ {}^{i+1}\psi^-,\ {}^{i+1}\theta^- = -\frac{2\pi}{n})\right]\mathbf{e}_f. \tag{D.6}$$

The relationships between the wheel frame and its associated basis from before to after collision $i+1$ are

$${}^{i+1}\mathcal{W}^+ \neq {}^{i+1}\mathcal{W}^-,\ {}^{i+1}\mathbf{e}_w^+ = \left[\mathbf{R}_2(\theta = -\frac{2\pi}{n})\right]\ {}^{i+1}\mathbf{e}_w^-. \tag{D.7}$$

The question now is whether the bank or heading frames change their orientation with respect to the fixed frame through a collision. The answer can be seen as follows.

For each of the 12 Euler angle sets where sequential rotations are around new axes, there are equivalent sequences of rotations about the fixed frame axes that result in the same final orientation of a rigid body (e.g., see Craig [87]). For instance, 3-1-2 Euler angles defined with respect to intermediate moving frames are equivalent to 2-1-3 Euler angles about the fixed frame axes. So, to answer the above question, we can look at rotations of the wheel in reverse order about the fixed frame axes. If we rotate the wheel frame by $\theta = -\frac{2\pi}{n}$ about the fixed frame y_f-axis, as we would to rotate the wheel frame through a collision about the intermediate bank frame $y_b - axis$, obviously no rotations ψ and ϕ are required about the x_f or z_f axes, respectively. Thus, if we make a rotation of the wheel frame about the final y_b-axis through a collision, there is no change in the orientation of the bank and heading frames with respect to the fixed frame.

The relationships of the bank and heading frames and their associated bases from before to after a collision $i+1$ are, thus,

$$\begin{aligned} {}^{i+1}\mathcal{H}^+ &= {}^{i+1}\mathcal{H}^-,\ {}^{i+1}\mathbf{e}_h^+ = {}^{i+1}\mathbf{e}_h^- \\ {}^{i+1}\mathcal{B}^+ &= {}^{i+1}\mathcal{B}^-,\ {}^{i+1}\mathbf{e}_b^+ = {}^{i+1}\mathbf{e}_b^- \end{aligned} \tag{D.8}$$

D.1 Equivalent Finite Rotations

Here, we show how, for each of the twelve independent Euler angle sets, there exists an equivalent rotation sequences about the fixed frame axes. To see that this is true, consider a sequence of two rotations about two axes in the same basis and compare the result to a sequence of rotations about two axes in different frames that are rotated from each other. Let $\mathbf{R}^1$ be a rotation about an *axis* 1 and $\mathbf{R}^2$ a rotation about an *axis* 2, $\mathbf{R}^1 : \mathbb{R}^3 \to \mathbb{R}$ and $\mathbf{R}^2 : \mathbb{R}^3 \to \mathbb{R}$.

D.1.1 Rotations about Fixed Frame Axes

Consider *rotation* 1 followed by *rotation* 2, both with respect to the same basis $\mathcal{A} = \mathbf{e}_i$. Let $\mathbf{v} = \mathbf{R}^1 \cdot \mathbf{u}$ and $\mathbf{w} = \mathbf{R}^2 \cdot \mathbf{R}^1 \cdot \mathbf{u}$ where $\mathbf{R}^1 = R^1_{ij}\mathbf{e}_i\mathbf{e}_j$, $\mathbf{R}^2 = R^2_{ij}\mathbf{e}_i\mathbf{e}_j$, and $\mathbf{u}$, $\mathbf{v}$, $\mathbf{w} \in \mathbb{R}^3$. Also, $\mathbf{R}^2 \cdot \mathbf{R}^1 = R^2_{ij}\mathbf{e}_i\mathbf{e}_j \cdot R^1_{\ell k}\mathbf{e}_\ell\mathbf{e}_k = R^2_{ij} \cdot R^2_{jk}\mathbf{e}_i\mathbf{e}_k$. Finally,

$$\begin{aligned} \mathbf{w} &= R^2_{ij}R^1_{jk}\mathbf{e}_i\mathbf{e}_k \cdot \mathbf{u}_\ell \\ &= R^2_{ij}R^1_{j\ell}\mathbf{e}_i. \end{aligned} \tag{D.9}$$

D.1.2 Rotations about Moving Frame Axes

Next, consider *rotation* 2 followed by *rotation* 1 about a *new axis* in basis $\mathcal{B} = \hat{\mathbf{e}}_i$ rotated by $\mathbf{R}^2$ from the basis $\mathcal{A} = \mathbf{e}_i$. Note that *new axis* 1 has the same orientation with respect to $\mathcal{B}$ as *axis* 1 has with respect to $\mathcal{A}$.

Define $\hat{\mathbf{R}}^1$ to be a rotation about axis 1 with respect to the basis $\mathcal{B} = \hat{\mathbf{e}}_i$

$$\hat{\mathbf{R}}^1 = R^1_{ij}\hat{\mathbf{e}}_i\hat{\mathbf{e}}_i \tag{D.10}$$

where

$$\begin{aligned} \hat{\mathbf{e}}_1 &= \mathbf{R}^2 \cdot \mathbf{e}_1 \\ \hat{\mathbf{e}}_2 &= \mathbf{R}^2 \cdot \mathbf{e}_2 \\ \hat{\mathbf{e}}_3 &= \mathbf{R}^2 \cdot \mathbf{e}_3 \end{aligned} \tag{D.11}$$

or

$$\begin{aligned} \hat{\mathbf{e}}_k &= R^2_{ij}\mathbf{e}_i\mathbf{e}_j \cdot \mathbf{e}_k \\ &= R^2_{ik}\mathbf{e}_i. \end{aligned} \tag{D.12}$$

So, in terms of the basis $\mathcal{A} = \mathbf{e}_i$,

$$\begin{aligned} \hat{\mathbf{R}}^1 &= R^1_{ij}\ R^2_{ki}\mathbf{e}_k\ R^2_{\ell j}\mathbf{e}_\ell \\ &= \underbrace{R^1_{ij}R^2_{ki}R^2_{\ell j}}_{\hat{R}_{k\ell}}\mathbf{e}_k\mathbf{e}_\ell. \end{aligned} \tag{D.13}$$

Let $\mathbf{v}' = \mathbf{R}^2 \cdot \mathbf{u}$ and $\mathbf{w}' = \hat{\mathbf{R}}^1 \cdot \mathbf{R}^2 \cdot \mathbf{u}$ where $\mathbf{u}$, $\mathbf{v}'$, $\mathbf{w}' \in \mathbb{R}^3$ and

$$\begin{aligned} \hat{\mathbf{R}}^1 \cdot \mathbf{R}^2 &= R^1_{ij}R^2_{ki}R^2_{\ell j}\mathbf{e}_k\mathbf{e}_\ell \cdot R^2_{rs}\mathbf{e}_r\mathbf{e}_s \\ &= R^1_{ij}R^2_{ki}R^2_{\ell j}R^2_{\ell s}\mathbf{e}_k\mathbf{e}_s \\ &= R^1_{ij}R^2_{ki}\delta_{js}\mathbf{e}_k\mathbf{e}_s \\ &= R^2_{ki}R^1_{ij}\delta_{js}\mathbf{e}_k\mathbf{e}_s \\ &= R^2_{ki}R^1_{is}\mathbf{e}_k\mathbf{e}_s. \end{aligned} \tag{D.14}$$

Finally, then,

$$\begin{aligned} \mathbf{w}' = w_k \mathbf{e}_k &= R^2_{ki} R^1_{is} \mathbf{e}_k \mathbf{e}_s \cdot u_r \mathbf{e}_r \\ &= R^2_{ki} R^1_{ir} u_r \mathbf{e}_k. \end{aligned} \tag{D.15}$$

Equation (D.9) is equivalent to Equation (D.15). Thus, if we rotate a rigid body through some angle θ_1 about *axis* 1 and then about *axis* 2 through an angle θ_2 (axes 1 and 2 fixed with respect to each other in a basis $\mathcal{A}$), then that sequence of rotations is equivalent to rotating the rigid body first about the same *axis* 2 in $\mathcal{A}$ through an angle θ_2 followed by rotating it about a *new axis* 1 fixed in a basis $\mathcal{B}$ through an angle θ_1. $\mathcal{B}$ is rotated from $\mathcal{A}$ about *axis* 2 by an angle θ_2. The orientation of the *new axis* 1 with respect to $\mathcal{B}$ is the same as the orientation of *axis* 1 with respect to $\mathcal{A}$.

D.2 Absolute Angular Velocity and Acceleration

Written in the body frame coordinates, the absolute angular velocity of a rigid body $\mathcal{W}$ in terms of the 3-1-2 Euler angles and their rates is,

$$\boldsymbol{\omega}_{\mathcal{W}/\mathcal{F}} = \boldsymbol{\omega}_{\mathcal{H}/\mathcal{F}} + \boldsymbol{\omega}_{\mathcal{B}/\mathcal{H}} + \boldsymbol{\omega}_{\mathcal{W}/\mathcal{B}} \tag{D.16}$$

$$= \dot{\phi}\hat{\mathbf{k}}_f + \dot{\psi}\hat{\mathbf{i}}_h + \dot{\theta}\hat{\mathbf{j}}_b \tag{D.17}$$

$$= \left(c\theta\ \dot{\psi} - s\theta\ c\psi\ \dot{\phi}+\right)\hat{\mathbf{i}}_w + \left(s\psi\ \dot{\phi} + \dot{\theta}\right)\hat{\mathbf{j}}_w + \tag{D.18}$$

$$\left(c\theta\ c\psi\ \dot{\phi} + s\theta\ \dot{\psi}\right)\hat{\mathbf{k}}_w. \tag{D.19}$$

Again, in body frame coordinates, the absolute angular acceleration of a rigid body $\mathcal{W}$ in terms of the 3-1-2 Euler angles and their rates is,

$${}^{\mathcal{F}}\dot{\boldsymbol{\omega}}_{\mathcal{W}/\mathcal{F}} = {}^{\mathcal{W}}\dot{\boldsymbol{\omega}}_{\mathcal{W}/\mathcal{F}} \tag{D.20}$$

$$\begin{aligned} &= \left[c\theta\left(\ddot{\psi} - c\psi\ \dot{\theta}\dot{\phi}\right) + s\theta\ \left(\dot{\psi}\left(s\psi\ \dot{\phi} - \dot{\theta}\right) - c\psi\ \ddot{\phi}\right) i\right]\hat{\mathbf{i}}_w + \\ &\left[c\psi\ \dot{\psi}\dot{\phi} + s\psi\ \ddot{\phi} + \ddot{\theta}\right]\hat{\mathbf{j}}_w + \\ &\left[c\theta\left(\dot{\psi}\left(\dot{\theta} - s\psi\ \dot{\phi}\right) + c\psi\ \ddot{\phi}\right) + s\theta\left(\ddot{\psi} - c\psi\ \dot{\theta}\dot{\phi}\right)\right]\hat{\mathbf{k}}_w. \end{aligned} \tag{D.21}$$

Equation (D.20) says that the absolute rate of change of the absolute angular velocity of body $\mathcal{W}$ (i. e., with respect to fixed frame $\mathcal{F}$) is equal to the rate of change of the angular velocity of body $\mathcal{W}$ with respect to itself.

Appendix E

Maple® Code for the Perturbation Analysis of the Stability of the 3D Rimless Wheel

Presented here are the Maple® codes used to find the analytical approximations to the return map eigenvalues evaluated at the limit cycle fixed point. There are three files:

1. nonlineqns_rimless3D_for_approx (generates the full nonlinear equations of motion of the rimless wheel between spoke collisions;
2. approx1 (finds the approximate limit cycle pitch angle $\Theta(T)$ and period T^*);
3. approx2 (finds the matrix that takes the state of the wheel just after a collision to just before the next (matrix $\mathbf{E}$);
4. approx3 (finds the total collision rule matrix and its approximation, matrix ($\mathbf{B}$));
5. construct_stride (finds the matrix that represents the correction the perturbation map to account for the perturbed limit cycle period (matrix $\mathbf{D}$), constructs the approximation to the Jacobian $\mathbf{A} = \mathbf{BDE}$, AND finds the approximate eigenvalues.)

```
#################################################################
#nonlineqns_rimless3D_for_approx
#################################################################
#This file generates the nonlineqns of motion of the 3D wheel
#in between collision for use in the approximation scheme in
#file approx1. The equation for angular momentum balance about
#the contact point (A) of the spoke currently on the ground is
#saved in `nonlinear_rimless3D_eqnset.m` The applied moment
#is save as the vector applmom and the rate of change of angular
# momentum is saved as HadotF.

# Now, we proceed with the equations of motion between collisions.
#Load linear algebra package.

with(linalg);

#Define the 3-1-2 Euler angles phi,psi, and theta as
#functions of time.

PSI:=psi(t);
PHI:=phi(t);
```

```
THETA:=theta(t);

#Define the angular velocity in terms of the heading, bank,
#and pitch rates

wh:=array([0,0,diff(phi(t),t)]); #in fixed frame basis
wb:=array([diff(psi(t),t),0,0]); #in heading frame basis
wp:=array([0,diff(theta(t),t),0]); #in bank frame basis

#Define the rotation matrices

rot1:=matrix([[1,0,0],[0,cos(PSI),sin(PSI)],
                                    [0,-sin(PSI),cos(PSI)]]);
rot2:=matrix([[cos(THETA),0,-sin(THETA)],[0,1,0],
                                  [sin(THETA),0,cos(THETA)]]);
rot3:=matrix([[cos(PHI),sin(PHI),0],[-sin(PHI),cos(PHI),0],
                                                    [0,0,1]]);
rot:=multiply(rot2,multiply(rot1,rot3));

#Define the angular velocity vector in the wheel frame basis

whwheel:=multiply(rot2,multiply(multiply(rot1,rot3),wh));
wpwheel:=multiply(rot2,wp);
wbwheel:=multiply(rot2,multiply(rot1,wb));

w:= add(whwheel,add(wpwheel,wbwheel));

#Define the angular acceleration vector wrto wheel frame
#expressed in wheel frame basis.

wprime:=map(diff,w,t); #;i.e., (wdotW/F)/W.

#Define the moment of inertia matrix with respect to the
#wheel frame at A.

inertia:=matrix([[J+m*l^2,0,0],[0,2*J+m*l^2,0],[0,0,J]]);

#Compute the angular momentum about A in wheel frame.

HA:=multiply(inertia,w);
#                  (1)      (2)
#Now use Hdot/F = (HA)dot/W + wW/F x HA =
#I*(wdotW/F)/W + wW/F x HA.

#(1)...Compute the rate of change of angular momentum w.r.t.
#the wheel frame.

HdotW:=multiply(inertia,wprime);

# (2)...Compute w cross angular momentum about A.
wcrossHA:=crossprod(w,HA);

#Compute the absolute rate of change of angular momentum
#about A with respect to fixed frame, all in terms of wheel
#frame basis vectors. i.e. just add (1) and (2) from above
#to get (Ha)dot/F.

HadotF:=add(HdotW,wcrossHA);

#Define the gravity unit vector in terms of the fixed frame
#F unit vectors. Remember, the fixed frame is tilted an angle
#alpha!!!

gravity:=array([sin(alpha),0,-cos(alpha)]);
```

```
gravity:=evalm(grav*gravity);

#Compute the gravity vector in the the wheel frame coordinates
gravprime:=multiply(rot,gravity);

#Define the vector from A to pt. CM in terms of wheel frame unit
#vectors. Note: disk has sopke-length l.

rca:=array([0,0,l]);

#This is not part of wheel, it is part of spoked wheel!
#Compute the applied moment due to gravity about pt. A

appliedforce:=evalm(m*gravprime);
applmom:=crossprod(rca,appliedforce);

#Form the equations of motion:  M=Hdot.

eqnset:={applmom[1]=HadotF[1],applmom[2]=HadotF[2],
                                    applmom[3]=HadotF[3]};

eqn1:=simplify(subs(grav=1,m=1,l=1,applmom[1]=HadotF[1]));
eqn2:=simplify(subs(grav=1,m=1,l=1,applmom[2]=HadotF[2]));
eqn3:=simplify(subs(grav=1,m=1,l=1,applmom[3]=HadotF[3]));

varset:={diff(phi(t),t$2),diff(psi(t),t$2),diff(theta(t),t$2)};
eqnset:={eqn1, eqn2, eqn3};
SolutionSet:=solve(eqnset,varset);


save SolutionSet, HadotF, applmom,
                              `nonlinear_rimless3D_eqnset.m`;
#####################################################################

#####################################################################
#approx1
#####################################################################
#Aproximation of the the Map representing the motion of the
#Rimless 3D Wheel
#####################################################################

#We pursue a perturbation expansion of the map representing
#the motion of the wheel about the limit cycle motion in order
#to determine its stability.  We use two smallness parameters:
#DELTA for the the limit cycle motion between #collisions and
#EPSILON for the perturbations from the limit cycle.  In this
#way we can distinguish between the size of the perturbations
#and the #size of the small but finite motion between collision.
#DELTA is O(1/n), where n is the number of spokes
#between #collisions.
#####################################################################
#The approximation to the pitch angle is saved as the variable
#final_x and the approximation to the limit cycle period as
#final_T in a file final_x_T.m The second derivatives from the
#equations of motion are saved in the

#We start with the nonlinear equations of motion for the 3D
#rimless wheel between spoke collisions.  These equations were
#generated using the MAPLE batch file
#nonlineqns_rimless3D_for_approx and stored in
#nonlinear_rimless3D_eqnset.m
#####################################################################

#Read in equations of motion.
```

```
read `nonlinear_rimless3D_eqnset.m`;
#Non-dimensionalization:
#     non_dim. time: tau= t*(sqrt(grav/length)
#     non_dim. inertia: J=I1/m*l^2 2J=I2/m*l^2
#NOTE: From here on, tau is `t'.

eqn1:=simplify(subs(grav=1,m=1,l=1,applmom[1]=HadotF[1]));
eqn2:=simplify(subs(grav=1,m=1,l=1,applmom[2]=HadotF[2]));
eqn3:=simplify(subs(grav=1,m=1,l=1,applmom[3]=HadotF[3]));

#We aproximate the equations of motion near the fixed point
#to first order in EPSILON by substituting p
#hi=phi0+epsilon*phi_hat,
#psi=psi_0+epsilon*psi_hat,
#and theta=theta_0+epsilon*theta_hat.

#First, we define the perturbations as functions of time.

PHI_h:=phi_h(t);
PSI_h:=psi_h(t);
THETA_h:=theta_h(t);
THETA_0:=theta_0(t);

eqn1a:=simplify(subs(phi(t)=phi_0+epsilon*phi_h(t),
                     psi(t)=psi_0+epsilon*psi_h(t),
                    theta(t)=THETA_0+epsilon*theta_h(t),
                    eqn1));

eqn2a:=simplify(subs(phi(t)=phi_0+epsilon*phi_h(t),
                    psi(t)=psi_0+epsilon*psi_h(t),
                    theta(t)=THETA_0+epsilon*theta_h(t),
                    eqn2));

eqn3a:=simplify(subs(phi(t)=phi_0+epsilon*phi_h(t),
                    psi(t)=psi_0+epsilon*psi_h(t),
                    theta(t)=THETA_0+epsilon*theta_h(t),
                    eqn3));

#Keeping with our strategy, we taylor expand the three
#equations of motion up to O(EPSILON).

lineqnset11:=
  convert(taylor(op(2,eqn1a)-op(1,eqn1a),epsilon=0,2),polynom);
lineqnset22:=
  convert(taylor(op(2,eqn2a)-op(1,eqn2a),epsilon=0,2),polynom);
lineqnset33:=
  convert(taylor(op(2,eqn3a)-op(1,eqn3a),epsilon=0,2),polynom);

#These equations above are the perturbed equations of motion
#up to order EPSILON.

#################################################################
#Now, we proceed to further approximate these three perturbed
#equations  by using a second small parameter to expand THETA_0,
#the limit cycle pitch angle as a function of time between
#collisions.  To begin, we rescale time in the EPSILON perturbed
#equations.

#First, we rescale nondim. time tau in the perturbed eqns.
#tau=DELTA*tau1. tau is O(1/n)  between collisions.  Thus, tau1
#is O(1).  NOTE: Again, as above, we let `t' be tau1.

lin1:=simplify(subs(diff(phi_h(t),t$2)=tempphi/delta^2,
              diff(psi_h(t),t$2)=temppsi/delta^2,
```

```
              diff(theta_h(t),t$2)=temptheta/delta^2,
              diff(THETA_0,t$2)=temptheta0/delta^2,lineqnset11));

lin2:=simplify(subs(diff(phi_h(t),t$2)=tempphi/delta^2,
              diff(psi_h(t),t$2)=temppsi/delta^2,
              diff(theta_h(t),t$2)=temptheta/delta^2,
              diff(THETA_0,t$2)=temptheta0/delta^2,lineqnset22));

lin3:=simplify(subs(diff(phi_h(t),t$2)=tempphi/delta^2,
              diff(psi_h(t),t$2)=temppsi/delta^2,
              diff(theta_h(t),t$2)=temptheta/delta^2,
              diff(THETA_0,t$2)=temptheta0/delta^2,lineqnset33));

lin11:=simplify(subs(diff(phi_h(t),t)=diff(phi_h(t),t)/delta,
                     diff(psi_h(t),t)=diff(psi_h(t),t)/delta,
                     diff(theta_h(t),t)=diff(theta_h(t),t)/delta,
                     diff(THETA_0,t)=diff(THETA_0,t)/delta,
                     lin1));

lin22:=simplify(subs(diff(phi_h(t),t)=diff(phi_h(t),t)/delta,
                     diff(psi_h(t),t)=diff(psi_h(t),t)/delta,
                     diff(theta_h(t),t)=diff(theta_h(t),t)/delta,
                     diff(THETA_0,t)=diff(THETA_0,t)/delta,
                     lin2));

lin33:=simplify(subs(diff(phi_h(t),t)=diff(phi_h(t),t)/delta,
                     diff(psi_h(t),t)=diff(psi_h(t),t)/delta,
                     diff(theta_h(t),t)=diff(theta_h(t),t)/delta,
                     diff(THETA_0,t)=diff(THETA_0,t)/delta,
                     lin3));

#We now rescale the  limit cycle pitch angle between collision,
#theta_0(t)=DELTA*x(t) since theta_0(t) is 0(1/n);thus,
#x(t) is 0(1).

#Rescale slope angle alpha=alphabar*DELTA. alpha is 0(1/n).
#Thus, alphabar is 0(1).

lineqn11:=subs( tempphi=diff(phi_h(t),t$2),
              temppsi=diff(psi_h(t),t$2),
              temptheta=diff(theta_h(t),t$2),
              temptheta0=diff(THETA_0,t$2),lin11);

lineqn22:=subs( tempphi=diff(phi_h(t),t$2),
              temppsi=diff(psi_h(t),t$2),
              temptheta=diff(theta_h(t),t$2),
              temptheta0=diff(THETA_0,t$2),lin22);

lineqn33:=subs( tempphi=diff(phi_h(t),t$2),
              temppsi=diff(psi_h(t),t$2),
              temptheta=diff(theta_h(t),t$2),
              temptheta0=diff(THETA_0,t$2),lin33);

lineqn1:=
 subs(THETA_0=delta*x(t),alpha=delta*alphabar,lineqn11);

lineqn2:=
 subs(THETA_0=delta*x(t),alpha=delta*alphabar,lineqn22);

lineqn3:=
 subs(THETA_0=delta*x(t),alpha=delta*alphabar,lineqn33);


#For our limit cycle motion, we have a functional relationship
```

```
#between phi and psi:psi_0=arctan(-sin(phi_0)*tan(DELTA*alphabar)
#So, here we expand psi_0 up to O(DELTA^3) to be consistent with
#our approximation strategy.

psi_0_tay:=convert(
             taylor(
               arctan(-sin(phi_0)*tan(delta*alphabar)),
                                        delta=0,4),polynom);

#From this we get psi_0_tay=-alphabar*sin(phi_0)*delta and
#substitute below.

# Now, we isolate the zeroth and  first order terms in
#EPSILON AND expand our equations up to O(DELTA^2).

lin1a:=subs(psi_0=psi_0_tay,
          expand(delta^2*coeff(collect(lineqn1,epsilon),epsilon,0)));

lin1b:=subs(psi_0=psi_0_tay,expand(delta^2*coeff(collect(lineqn1,epsilon),
                                                 epsilon,1)));

lin2a:=subs(psi_0=psi_0_tay,expand(delta^2*coeff(collect(lineqn2,epsilon),
                                                 epsilon,0)));

lin2b:=subs(psi_0=psi_0_tay,expand(delta^2*coeff(collect(lineqn2,epsilon),
                                                 epsilon,1)));
lin3a:=subs(psi_0=psi_0_tay,expand(delta^2*coeff(collect(lineqn3,epsilon),
                                                 epsilon,0)));

lin3b:=subs(psi_0=psi_0_tay,expand(delta^2*coeff(collect(lineqn3,epsilon),
                                                 epsilon,1)));

lin1a_taylor:=convert(taylor(lin1a,delta=0,4),polynom);
lin1b_taylor:=convert(taylor(lin1b,delta=0,4),polynom);
lin2a_taylor:=convert(taylor(lin2a,delta=0,6),polynom);
lin2b_taylor:=convert(taylor(lin2b,delta=0,4),polynom);
lin3a_taylor:=convert(taylor(lin3a,delta=0,4),polynom);
lin3b_taylor:=convert(taylor(lin3b,delta=0,4),polynom);

#NOTE: We expand Lin2a, an  equation which is the zeroth
# order term in the second rescaled EPSILON expansion
#equation lineqn2, up to O(DELTA^6).  We will need this
#order of approximation in order to solve for the
#expansion coefficients in x(t) up to O(DELTA^2).
##########################################################
#Now, we solve for x(t), the aproximation to the angle
#between collisions up to order delta^2.  We start with
eqn. lin2a_taylor from above.
##########################################################
# Part one: order DELTA
##########################################################
#We get the equation for x(t) by picking off the
#coefficient of the DELTA^2 term in lin2a_taylor;

eqn_for_x:=simplify((lambda^2)*
           subs((2*J+1)=1/lambda^2,
                factor(coeff(lin2a_taylor,delta))+
                   coeff(lin2a_taylor,delta^3)*delta^2));
#Now, we seek a second order approximation to x(t).

expand_x(t):=x0(t)+delta^2*x1(t)+delta^4*x2(t);

#Next, we substitue this approximation into the
#equation for x.
```

```
expand_eqn_x:=
   collect(expand(subs(x(t)=expand_x(t),eqn_for_x=0)),delta);

#We begin to  solve for x0(t) and x1(t) by applying the
#initial condition that x(0)=-Pi;

order_0:=op(4,op(1,expand_eqn_x));
order_2:=coeff(op(3,op(1,expand_eqn_x)),delta,2);
x0_solns:=dsolve(order_0=0,x0(t));
x0_solnss:=subs(_C1=A0, _C2=A1, x0_solns);
x0_soln:=subs(A0=-Pi,op(2,x0_solnss));

order_2s:=subs(x0(t)=x0_soln,order_2);
x1_solns:=dsolve(order_2s=0,x1(t));
x1_soln:=subs(_C2=A2,op(2,x1_solns)-_C1);

#With x0 and x1 thus far, we can now rewrite our approximation
#to x(t);

expand_x(t):=x0_soln+delta^2*x1_soln;

#But, to finish,  we need to apply the end_of_cycle condition
#and collision condition for the limit cycle to exist:
#(1)x(T)=Pi and (2) mu*xdot(T)=xdot(0). T is the time between
#collisions in the lmit cycle motion.  We will
#name T 'T_coll' here and approximate it up to O(DELTA^2).

#(1)Enforce end_of_cycle angle, x=Pi.

T_coll:=T0+delta^2*T1;
x_colls:=collect(expand(subs(t=T_coll,expand_x(t))),delta);
ord_0:=-Pi+A1*T0;
T0_soln:=solve(ord_0=Pi,T0);
# no use yet: ord_2:=coeff(x_colls,delta^2)

#(2)enforce limit cycle condition


mu_1:=1-((delta^2)*(2*lambda^2*(Pi^2)));
xprime(t):=diff(expand_x(t),t);
xprime0:=subs(t=0,xprime(t));
xprimeT_colls:=collect(expand(subs(t=T_coll,xprime(t))),delta);
xprimeT_coll:=op(3,xprimeT_colls)+op(4,xprimeT_colls);


limcycle_cond:=collect(expand(
                subs(A2=0,mu_1*
                  subs(T0=T0_soln,xprimeT_coll)=xprime0)),delta);

#Finally, we solve for remaining coefficients of integration.

const1:=solve(coeff(op(2,op(1,limcycle_cond)),delta^2)=0,A1);
constant_1:=
      subs(abs(alphabar)=alphabar,abs(cos(phi_0))=cos(phi_0),
               abs(const1[2]));

#And, here are x0(t), x1(t) and T0.

x0last(t):=subs(A1=constant_1,x0_soln);
x1last(t):=subs(A1=constant_1,x1_soln);
T0last:=subs(A1=constant_1,T0_soln);

#But, we still need T1 and one more constant of integration
```

```
#to completely determine x1(t).
############################################################
# Part two: order DELTA^2
############################################################
#The procedure is the same as above except that we keep higher
#order terms to find T1 and the remaining constant of
#integration _C3.

neweqn_for_x:=collect(simplify((lambda^2)*
              subs((2*J+1)=1/lambda^2,
                factor(coeff(lin2a_taylor,delta))+
                 coeff(lin2a_taylor,delta^3)*delta^2+
                  coeff(lin2a_taylor,delta^5)*delta^4)),delta);
newexpand_x(t):=x0(t)+delta^2*x1(t)+delta^4*x2(t);
newexpand_eqn_x:=convert(taylor(op(1,collect(expand(subs(
          x(t)=newexpand_x(t),neweqn_for_x=0)),delta)),delta=0,6),
                                                        polynom);

order_4s:=subs(x0(t)=x0last(t),x1(t)=x1last(t),
                coeff(newexpand_eqn_x,delta^4));
x2_solns:=dsolve(order_4s=0,x2(t));
x2_soln:=collect(subs(_C2=A3,_C1=0,op(2,x2_solns)),t);
newest_expandx(t):=
            x0last(t)+(delta^2)*x1last(t)+(delta^4)*x2_soln;
newT_coll:=T0+delta^2*T1+delta^4*T2;
newx_colls:=
   collect(expand(subs(t=newT_coll,newest_expandx(t))),delta);
newestx_colls:=subs(T0=T0last,
               convert(taylor(newx_colls,delta=0,6),polynom));
neword_2:=coeff(newestx_colls,delta^2);
T1_soln:=solve(neword_2=0,T1);

newmu_1:=1-((delta^2)*(2*lambda^2*(Pi^2)))+
                             (delta^4*(2/3)*lambda^2*(Pi^4));
newxprime(t):=diff(newest_expandx(t),t);
newxprime0:=subs(t=0,newxprime(t));

newxprimeT_collss:=
   convert(taylor(collect(expand(
     subs(t=newT_coll,newxprime(t))),delta),delta=0,6),polynom);

newxprimeT_collsss:=subs(T0=T0last,newxprimeT_collss);

newlimcycle_cond:=
     collect(expand(
      subs(A3=0,newmu_1*(newxprimeT_collsss)=newxprime0)),
                                                   delta);

const2_eqn:=
   subs(T1=T1_soln,
     coeff(taylor(op(1,newlimcycle_cond),delta=0,6),delta^4)=0);

const2aa:=solve(const2_eqn,A2);
constant_2:=const2aa;

x0final(t):=x0last(t);
x1final(t):=collect(subs(A2=constant_2,x1last(t)),t);
T0final:=T0last;
T1final:=subs(A2=constant_2,T1_soln);

#This is the approximation to theta_0(t) up to O(DELTA^2).

final_x:=simplify(collect(x0final(t)+(delta^2)*x1final(t),t));
```

```
#This is the approximation to the time between collision in
#the limit cycle up to O(DELTA^2).

final_T:=simplify(T0final+delta^2*T1final);

save final_x, final_T, `final_x_T.m`;


#####################################################################
#Now, we return to our three perturbed equations of motion and
insert our approximation to x(t).  We will work with equations
linia_taylor and linib_taylor, where i=1,2,3.  We have already
used lin2a_taylor to get x(t) leaving five equations.  Recall,
these six equations linia_taylor and linib_taylor are the
zeroth and first order coefficients,respectively, from our
three perturbed equations of motion( up to O(EPSILON)), lineqni,
i=1,2,3..
#####################################################################

#First, lin1a_taylor shows that the zeroth order term in lineqn1
#has only O(DELTA^3) terms and higher.

#Second, lin2a_taylor gave us x(t) up to O(delta^2).

#Third, lin3a_taylor gives us that the zeroth order term in
#lineqn3 is identically zero.

#Now, we shall move on to linib_taylor, i=1,2,3, to get
#approximations to the perturbations to the limit cycle motion,
#phi_h(t), psi_h(t), and theta_h(t).  To do this, we substitute
#our approximation to x(t), expand, and  ......

newlin1b:=convert(lin1b_taylor,polynom);
newlin2b:=convert(lin2b_taylor,polynom);
newlin3b:=convert(lin3b_taylor,polynom);

newerlin1b:=convert(taylor(
               subs(x(t)=final_x,newlin1b),delta=0,4),polynom);
newerlin2b:=convert(taylor(newlin2b,delta=0,4),polynom);
newerlin3b:=convert(taylor(
               subs(x(t)=final_x,newlin3b),delta=0,4),polynom);

varset:={diff(phi_h(t),t$2),diff(psi_h(t),t$2),
                                        diff(theta_h(t),t$2)};
eqnset:={newerlin1b=0,newerlin2b=0,newerlin3b=0};
Solution:=solve(eqnset,varset);
#Then, by hand, we pick off the second derivative solutions and
#save them as phiddot, psiddot, and thetaddot.

save phiddot, psiddot, thetaddot, `double_derivs.m`;

#Second derivatives solved for and stored in double_derivs.m
#We will solve these equations in a file called approx2.
#####################################################################

#####################################################################
#approx2
#####################################################################
#This batch file finds the matrix that maps the perturbation to
#a limit cycle just after a collision to just before the next
#collision (matrix E), calls it stride3, and saves it in
#finalstride3.m This matrix is loaded into construct_stride.


#First, we read in the second derivatives, final_x, and final_T
```

```
with(linalg);

read `double_derivs.m`;
read `final_x_T.m`;

#Then, we simplify the equations .

phi_h_ddot:=
  factor(collect(convert(
      taylor(phiddot,delta=0,4),polynom),diff(psi_h(t),t)));
psi_h_ddot:=collect(collect(collect(factor(convert(
            taylor(psiddot,delta=0,4),polynom)),psi_h(t)),
           diff(phi_h(t),t)),phi_h(t));
theta_h_ddot:=convert(taylor(thetaddot,delta=0,5),polynom);
temp_thetahddot:=
     collect(collect(collect(theta_h_ddot,diff(psi_h(t),t)),
                     theta_h(t)),phi_h(t));

######################################################################
phihddot:=subs(J=((1/lambda^2)-1)/2,phi_h_ddot);

psihddot1:=collect(subs(J=((1/lambda^2)-1)/2,
   simplify(coeff(psi_h_ddot,diff(phi_h(t),t)))*diff(phi_h(t),t)+
   simplify(coeff(psi_h_ddot,psi_h(t)))*psi_h(t)+
   simplify(coeff(op(3,psi_h_ddot),phi_h(t)))*phi_h(t)),
                diff(phi_h(t),t));

psihddot:=op(1,psihddot1)+simplify(op(2,psihddot1))+
                                        simplify(op(3,psihddot1));

thetahddot:=subs(J=((1/lambda^2)-1)/2,simplify(
        coeff(temp_thetahddot,diff(psi_h(t),t)))*diff(psi_h(t),t)+
        simplify(coeff(temp_thetahddot,theta_h(t)))*theta_h(t)+
        simplify(coeff(temp_thetahddot,phi_h(t)))*phi_h(t));

#Now, we expand the  perturbations up to O(DELTA^3)

new_phi_h(t):=phi_h0(t)+delta*phi_h1(t)+delta^2*phi_h2(t)+
                                              delta^3*phi_h3(t);
new_psi_h(t):=psi_h0(t)+delta*psi_h1(t)+delta^2*psi_h2(t)+
                                              delta^3*psi_h3(t);
new_theta_h(t):=theta_h0(t)+delta*theta_h1(t)+delta^2*theta_h2(t)
                +delta^3*theta_h3(t);

new_phihddot:={expand(diff(new_phi_h(t),t$2))=
               convert(taylor(expand(subs(
               phi_h(t)=new_phi_h(t),psi_h(t)=new_psi_h(t),
                   theta_h(t)=new_theta_h(t),phihddot)),
                                         delta=0,4),polynom)};
new_psihddot:={expand(diff(new_psi_h(t),t$2))=
               convert(taylor(expand(subs(
               phi_h(t)=new_phi_h(t),psi_h(t)=new_psi_h(t),
                   theta_h(t)=new_theta_h(t),psihddot)),
                                        delta=0,4),polynom)};
new_thetahddot:={expand(diff(new_theta_h(t),t$2))=
                 convert(taylor(expand(subs(
                 phi_h(t)=new_phi_h(t),psi_h(t)=new_psi_h(t),
                   theta_h(t)=new_theta_h(t),thetahddot)),
                                        delta=0,6),polynom)};

#Then, we solve for the zeroth-order terms and substitute them
#back into the equations.
```

```
phih0(t):=phihp_i+phihdotp_i*t;
psih0(t):=psihp_i+psihdotp_i*t;
thetah0(t):=thetahp_i+thetahdotp_i*t;

newer_phihddot:=expand(subs(
        theta_h1(t)=0,phi_h0(t)=phih0(t),psi_h0(t)=psih0(t),
                       theta_h0(t)=thetah0(t),new_phihddot));
newer_psihddot:=expand(subs(
        theta_h1(t)=0,phi_h0(t)=phih0(t),psi_h0(t)=psih0(t),
                       theta_h0(t)=thetah0(t),new_psihddot));
newer_thetahddot:=expand(subs(
          theta_h1(t)=0,phi_h0(t)=phih0(t),psi_h0(t)=psih0(t),
                       theta_h0(t)=thetah0(t),new_thetahddot));
#Next, we solve for the first order terms and substitute them
#into the equations.

soln_phih1(t):=op(2,subs(_C1=0,_C2=0,dsolve(coeff(
                op(1,op(1,newer_phihddot)),delta)=
                coeff(op(2,op(1,newer_phihddot)),delta),
                phi_h1(t))));
soln_psih1(t):=op(2,subs(_C1=0,_C2=0,dsolve(coeff(
                op(1,op(1,newer_psihddot)),delta)=
                coeff(op(2,op(1,newer_psihddot)),delta),
                psi_h1(t))));
#soln_thetah1(t)=0;

newest_phihddot:=
   expand(subs(phi_h1(t)=soln_phih1(t),psi_h1(t)=soln_psih1(t),
                        newer_phihddot));
newest_psihddot:=
   expand(subs(phi_h1(t)=soln_phih1(t),psi_h1(t)=soln_psih1(t),
                        newer_psihddot));
newest_thetahddot:=
   expand(subs(phi_h1(t)=soln_phih1(t),psi_h1(t)=soln_psih1(t),
                       newer_thetahddot));


#And, we solve for the second order terms.

soln_phih2(t):=op(2,subs(_C1=0,_C2=0,dsolve(
                  coeff(op(1,op(1,newest_phihddot)),delta^2)=
                  coeff(op(2,op(1,newest_phihddot)),delta^2),
                  phi_h2(t))));

soln_psih2(t):=op(2,subs(_C1=0,_C2=0,dsolve(
                  coeff(op(1,op(1,newest_psihddot)),delta^2)=
                  coeff(op(2,op(1,newest_psihddot)),delta^2),
                  psi_h2(t))));
soln_thetah2(t):=op(2,subs(_C1=0,_C2=0,dsolve(
                  coeff(op(1,op(1,newest_thetahddot)),delta^2)=
                  coeff(op(2,op(1,newest_thetahddot)),delta^2),
                  theta_h2(t))));

final_phihddot:=
  expand(subs(phi_h2(t)=soln_phih2(t),psi_h2(t)=soln_psih2(t),
              theta_h2(t)=soln_thetah2(t),newest_phihddot));
final_psihddot:=
  expand(subs(phi_h2(t)=soln_phih2(t),psi_h2(t)=soln_psih2(t),
              theta_h2(t)=soln_thetah2(t),newest_psihddot));
final_thetahddot:=
  expand(subs(phi_h2(t)=soln_phih2(t),psi_h2(t)=soln_psih2(t),
              theta_h2(t)=soln_thetah2(t),newest_thetahddot));
```

```
soln_phih3(t):=op(2,subs(_C1=0,_C2=0,dsolve(
                  coeff(op(1,op(1,final_phihddot)),delta^3)=
                  coeff(op(2,op(1,final_phihddot)),delta^3),
                  phi_h3(t))));

soln_psih3(t):=op(2,subs(_C1=0,_C2=0,dsolve(
                  coeff(op(1,op(1,final_psihddot)),delta^3)=
                  coeff(op(2,op(1,final_psihddot)),delta^3),
                  psi_h3(t))));

soln_thetah3(t):=op(2,subs(_C1=0,_C2=0,dsolve(
                  coeff(op(1,op(1,final_thetahddot)),delta^3)=
                  coeff(op(2,op(1,final_thetahddot)),delta^3),
                  theta_h3(t))));

#Finally, we put together our approximations to phi_h, psi_h,
#and theta_h, up to O(DELTA^2).

soln_phih(t):=phih0(t)+delta*soln_phih1(t)+delta^2*soln_phih2(t)
               +delta^3*soln_phih3(t);
soln_psih(t):=psih0(t)+delta*soln_psih1(t)+delta^2*soln_psih2(t)
               +delta^3*soln_psih3(t);
soln_thetah(t):=
  thetah0(t)+0+delta^2*soln_thetah2(t)+delta^3*soln_thetah3(t);

diff_phih(t):=diff(soln_phih(t),t);
diff_psih(t):=diff(soln_psih(t),t);
diff_thetah(t):=diff(soln_thetah(t),t);

phihm_iplus1:=convert(taylor(collect(expand(subs(
            t=final_T,soln_phih(t))),delta),delta=0,4),polynom);
psihm_iplus1:=convert(taylor(collect(expand(subs(
            t=final_T,soln_psih(t))),delta),delta=0,4),polynom);
thetahm_iplus1:=convert(taylor(collect(expand(subs(
          t=final_T,soln_thetah(t))),delta),delta=0,4),polynom);
phihdotm_iplus1:=convert(taylor(collect(expand(subs(
          t=final_T,diff_phih(t))),delta),delta=0,4),polynom);
psihdotm_iplus1:=convert(taylor(collect(expand(subs(
          t=final_T,diff_psih(t))),delta),delta=0,4),polynom);
thetahdotm_iplus1:=convert(taylor(collect(expand(subs(
          t=final_T,diff_thetah(t))),delta),delta=0,5),polynom);
statep_i:=array([phihp_i,phihdotp_i,psihp_i,
                 psihdotp_i,thetahp_i,thetahdotp_i]);
statem_iplus1:= array([phihm_iplus1,phihdotm_iplus1,
                       psihm_iplus1,psihdotm_iplus1,
                       thetahm_iplus1,thetahdotm_iplus1]);
for r from 1 by 1 to 6 do
for s from 1 by 1 to 6 do
mm[r,s]:=factor(coeff(expand(statem_iplus1[r]),statep_i[s],1));
od;
od;
f:=(r,s) ->mm[r,s];
stride3:=matrix(6,6,f);
#save stride3, `finalstride3.m`;
#####################################################################

#####################################################################
#construct_stride
#####################################################################
#This batch file contructs the approximation to the Jacobian
#matrix (J approx. equal B*D*E) at a limit cycle and finds the
#approximate eigenvalues.

with(linalg);
read `finalstride3.m`;
```

```
read `jump_mats.m`;

#First, we unscale the stride3 matrix.  aa is the unscaling
#matrix.

aa:=diag(1,delta,1,delta,1,delta);

stride3_new:=multiply(inverse(aa),multiply(stride3,(aa)));

#Below, we construct the map matrix representation that takes
#an epsilon perturbation from the limit cycle motion just after
#a collision to just after the next collision.  That is, given
#a disturbance  to the limit cycle motion after a collision
#multiplied by the matrix, we find what happens to the
#disturbance after the next collision. Then, consistent with
#our approximation scheme, we expand each element of the matrix
#to O(delta^2).

stride_map:=multiply(jacob_at_limcycle,
                          multiply(third_matrix,stride3_new));
taylor_map:=map(taylor,stride_map,delta=0,3);
new_stride_map:=map(convert,taylor_map,polynom);

#Now, we find the characteristic polynomial of the matrix and
# then proceed to find its eigenvalues.

char_poly:=factor(charpoly(new_stride_map,sigma));

#Happily, we find that the characteristic polynomial factors
#into two roots and a fourth order polynomial.  One root is
#sigma0 = 0, and the other is
#sigma1 = 1 - 4*delta^2*lambda^2*Pi^2.

#Sigma0 = 0 corresponds to the constraint in the map on the
#`pitch angle' theta ALWAYS being fixed just before and after
#each collision, theta = pi/n, whether the wheel is in a limit
#cycle or not.  The eigenvalue of zero tells us that if we
#disturb the pitch angle just after a collision, the pitch
#angle returns to theta = pi/n just after the next collision;
#that is, in one iteration of the stride map.

#Sigma1 = 1 - 4*delta^2*lambda^2*pi^2 corresponds to the
#two-dimensional limit cycle motion of the wheel; i. e., the
#wheel attaining the same velocity after each collision when
#rolling straight downhill(or at any heading downhill as long
#as the gravity vector lies in the plane of the wheel.) Sigma1
#is an O(delta^2) approximation to the eigenvalue we obtain
#from the exact 2D nonlinear analysis, sigma = mu^2 =
#(2J+cos(2*pi)/(2J+1))^2 < 1. Clearly, Sigma1 < 1, also.
#An eigenvalue less than one tells us that, given a disturbance
#only to the limit cycle pitch angle rate, the wheel will
#asymptotically return to the limit cycle pitch angle rate
#after each collision.So, with our approximation scheme, we
#have found an eigenvalue that corresponds to the 2D limit
#cycle motion.

sigma0:=0;
sigma1:=1- 4*delta^2*lambda^2*Pi^2;

#Now, we obtain the fourth order polynomial left form the
#characteristic polynomial and then proceed to obtain the
#remaining four roots.

newchar_poly0:=factor(char_poly/
```

```
                ((sigma-1+(4*delta^2*Pi^2*lambda^2))*sigma));

#First, we make a substitution to ease the future calculations.

newchar_poly:=
         expand(subs(alphabar=gamma/cos(phi_0),newchar_poly0));

#Now, first let delta=0, which corresponds to n going to infinity.
#This should give four eigenvalues equal to one - coreesponding
#to the rolling disk.

sigma_roots:=solve(subs(delta=0,newchar_poly)=0,sigma);

#This, in fact, gives us sigma = 1, 1, 1, 1.
#This tells us that for delta not equal to zero, the eigenvalues
#should be 'near' one for small delta. So, to proceed let's look
#for eigenvalues of the form sigma = 1 + delta*beta_0 +
#delta^2*beta_1 and see what we get.  Of course we could have
#chosen sigma = beta_0+delta*beta_1+delta^2*beta_2 but
#we would have found beta_0 = 1 anyway.

sigma_approx:=1+delta*beta_0+delta^2*beta_1;

newerchar_poly:=
               expand(subs(sigma=sigma_approx,newchar_poly));

root0:=solve(coeff(collect(
                     newerchar_poly,delta),delta,4)=0,beta_0);
root0a:=root0[1];
root0b:=simplify(root0[3]);
root0c:=factor(root0[4]);

#Note:  root0b=-root0c.

root1a:= simplify(
         solve(
         subs(beta_0=root0a,coeff(collect(newerchar_poly,delta),
                       delta,6)=0),beta_1)[2]);

root1b:=simplify(subs(beta_0=root0b,
        simplify(solve(
         coeff(
          collect(newerchar_poly,delta),delta,5)
                                       =0,beta_1))));
root1c:=simplify(subs(beta_0=root0c,
        simplify(solve(
         coeff(
          collect(newerchar_poly,delta),delta,5)
                                       =0,beta_1))));

#Note: root1b=root1c.

#Finally, we get the four remaining eigenvalues .

#First, we have the eigenvalue for delta = 0:

sigma2:=1;

#Next, we have the eigenvalue for beta_0=0 and beta_1=root1a;

sigma3:=1+root0a*delta+delta^2*root1a;

#Third, we have the eigenvalue for beta_0=root0a and
#beta_1=root1b=root1c.
```

```
sigma4:=1+root0b*delta+delta^2*root1b;

#And, last, we have the eigenvalue for beta_0=root0b and
#beta_1=root1b=root1c.

sigma5:=1+delta*root0c+delta^2*root1c;

#Put the six eigenvalues into a vector.

eigen_roots:=vector([sigma0,sigma1,sigma2,sigma3,sigma4,sigma5]);

#A numerical evaluation using the original polynomial and our
#final e-values for comparision.

solve(
 evalf(
  subs(
   delta=0.01,alphabar=2,lambda=sqrt(2/3),
                                phi_0=Pi/10,char_poly))=0,sigma);

evalf(
  subs(
   delta=0.01,lambda=sqrt(2/3),gamma=2*cos(Pi/10),
                                           op(1,eigen_roots)));


#For stability, need pi*lambda^2-2*gamma < 0. This gives that
#root1b=root1c < 0. This implies that the numerator of
#root1b=root1c must be > 0.

#Now, say that for pi*lambda^2-2*gamma<0, that
#root0b = i*|root0b| and root0c = -i*|root0c|=-root0c.

#Then, for stability, we want |sigma4|=|sigma5| < 1.  (sigma4
#and sigma5 are complex conjugates. This gives the stability
#condition that |root0b|^2<-2*root1b, to O(delta^2).

abs_root0b:=2*Pi*sqrt(2)*sqrt((2*gamma)-
               (Pi*lambda^2))/(sqrt(gamma)*sqrt(1+(lambda^2)));
stab_cond:=factor(-abs_root0b^2-2*root1b);

#For stab_cond=gamma*lambda^2*(1-lambda^2)>0, we have stability.
#This condition always satisfied if pi*lambda^2 -
#2*gamma < 0, gamma >0, and lambda^2 < 1.

#Now, lets turn to sigma3.  For stability, we need root1a < 0.
#This gives a stability criterion for the minimum effective
#slope gamma =alphabar*cos(phi_0).

stab_crit_eqn:=collect(numer(
              subs(gamma=alphabar*cos(phi_0),root1a)),alphabar);

stab_crit:=s
     implify(factor(solve(stab_crit_eqn=0,alphabar))*cos(phi_0));

#Thus, our stability criterion is
#gamma > stab_crit=pi*lambda^2/(1 + lambda^2).

#FINAL NOTE: Our approximation blows up when 2*gamma=pi*lambda^2!
#####################################################################
```

Bibliography

[1] D. A. Winter. *The Biomechanics and Motor Control of Human Gait: Normal, Elderly, and Pathological.* University of Waterloo Press, Waterloo, Ontario, second edition, 1991.

[2] M. Garcia and A. Ruina. Passive kneed walking: Mechanics and efficiency. To be submitted to Journal of Theoretical Biology, 1997.

[3] M. Garcia. *Stability, Chaos, and Scaling Laws: Passive–Dynamic Gait Models.* PhD thesis, Cornell University, Ithaca, NY, 1998. In preparation.

[4] T. McGeer. Passive dynamic biped catalogue. In R. Chatila and G. Hirzinger, editors, *Proc., Experimental Robotics II: The 2nd International Symposium*, pages 465–90, Berlin, 1992. Springer–Verlag.

[5] Giovanni Alfonso Borelli. *On the Movement of Animals.* Springer-Verlag, Berlin, 1989. The first edition of the work was published under the title *De Motu Animalium* in two parts after Borelli's death in 1679, the first part in 1680, the second in 1681. The current text was translated by Dr. Paul Maquet from the translated edition published in 1743 by Peter Gosse in The Hague. The Proposition XXXII and its proof is on p. 38 of the translation.

[6] D. T. Greenwood. *Principles of Dynamics.* Prentice Hall, Englewood Cliffs, New Jersey, 1965.

[7] S. Goyal. private communication, 1992.

[8] R. S. Hand. Comparisons and stability analysis of linearized equations of motion for a basic bicycle model. Master's thesis, Cornell University, Ithaca, NY, 1988.

[9] M. Hubbard. Lateral dynamics and stability of the skateboard. *J. Appl. Mech.*, 46:931–936, 1979.

[10] J. V. Fowble and A. D. Kuo. Stability and control of passive locomotion in 3-D. In *Biomechanics and Neural Control of Movement*, pages 28–9, Mount Sterling, OH, 1996. Engineering Foundation Conferences, EFC.

[11] T. McGeer. Powered flight, child's play, silly wheels, and walking machines. In *Proc., IEEE International Conference on Robotics and Automation*, pages 1592–7, Piscataway, NJ, 1989. IEEE, IEEE.

[12] S. Mochon and T. A. McMahon. Ballistic walking. *J. Biomechanics*, 13:49–57, 1980.

[13] S. Mochon and T. McMahon. Ballistic walking: An improved model. *Math. Biosci.*, 52:241–260, 1980.

[14] M. J. Coleman and A. Ruina. An uncontrolled walking toy that cannot stand still. *Physical Review Letters*, 80(16):3658–3661, April 20 1998.

[15] Walk this way. *The Economist*, 345(8048):124–5, December 20, 1997 – January 2, 1998 1998.

[16] M. Garcia, A. Chatterjee, A. Ruina, and M. J. Coleman. The simplest walking model: Stability, complexity, and scaling. In press, 1998.

[17] D. A. Winter. *Biomechanics and Motor Control of Human Movement*. Wiley, second edition, 1990.

[18] F. Zajac and J. M. Winters. Modeling musculoskeletal movement systems: Joint and body-segment dynamics, musculotendinous actuation and neuromuscular control. In J. M. Winters and S. L-Y. Woo, editors, *Multiple Muscle Systems: Biomechanics and Movement Organization*, chapter 8, pages 121–148. Springer-Verlag, New York, 1990.

[19] G. T. Yamaguchi. Performing whole-body simulations of gait with 3-D, dynamic musculoskeletal models. In J. M. Winters and S. L-Y. Woo, editors, *Multiple Muscle Systems: Biomechanics and Movement Organization*, chapter 43, pages 663–679. Springer-Verlag, New York, 1990.

[20] G. T. Yamaguchi and F. E. Zajac. Restoring natural gait to paraplegics through neuromuscular stimulation: A feasibility study. In J.L. Stein, J.A. Ashton-Miller, and M.G. Pandy, editors, *Issues in Modeling and Control of Biomechanical Systems: presented at the Winter Annual Meeting of the American Society of Mechanical Engineers, San Francisco, California, December 10-15, 1989*, pages 41–48, New York, 1989. the Biomechanical Systems Technical Panel of the Dynamic Systems and Control Division, ASME, American Society of Mechanical Engineers.

[21] Gary T. Yamaguchi and Felix E. Zajac. Restoring unassisted natural gait to paraplegics via functional neuro muscular stimulation: A computer simulation study. *IEEE Transactions on Biomedical Engineering*, 37:886–902, 1990.

[22] J. M. Hausdorff and W. K. Durfee. Open-loop position control of the knee joint using electrical stimulation of the quadriceps and hamstrings. *Medical and Biological Engineering and Computing*, 29(3):269–280, May 1991.

[23] I. Anderson, E. Parkinson, B. Scroggins, and J. B. Walker. FES for joint stabilization during stance phase of locomotion in spinal cord injured. In G. Harris and C. Walker, editors, *Proc. of the Annual International Conference of the IEEE Engineering in Medicine and Biology Society*, pages 1581–1572, New York, 1988. IEEE, IEEE.

[24] R. Kobetic, E. B. Marsolais, and H. J. Chizeck. Control of kinematics in paraplegic gait by functional electrical stimulation. In G. Harris and C. Walker, editors, *Proc. of the Annual International Conference of the IEEE Engineering in Medicine and Biology Society*, page 1579, New York, 1988. IEEE, IEEE.

[25] G. Taga, Y. Yamaguchi, and H. Shimizu. Self-organized control of bipedal locomotion by neural oscillators in an unstable environment. *Biological Cybernetics*, 65(3):147–159, 1991.

[26] M. G. Pandy and N. Berme. Synthesis of human walking: A three-dimensional model for single support. part one: Normal gait. In J.L. Stein, editor, *Biomechanics of Normal and Prosthetic Gait : presented at the Winter Annual Meeting of the American Society of Mechanical Engineers, Boston, Massachusetts, December 13-18, 1987*, pages 1–8, New York, 1987. the Bioengineering Division, ASME, ASME.

[27] M. G. Pandy and N. Berme. Synthesis of human walking: A three-dimensional model for single support. part two: Pathological gait. In J.L. Stein, editor, *Biomechanics of Normal and Prosthetic Gait : presented at the Winter Annual Meeting of the American Society of Mechanical Engineers, Boston, Massachusetts, December 13-18, 1987*, pages 9–16, New York, 1987. the Bioengineering Division, ASME, ASME.

[28] R. Beckett and K. Chang. An evaluation of the kinematics of gai t by minimum energy. *Journal of Biomechanics*, pages 147–59, 1973.

[29] J. J. Collins. The redundant nature of locomotor optimization laws. *Journal of Biomechanics*, 28:251–267, 1995.

[30] W. L. Nelson. Physical principles for economics of skilled movements. *Biological Cybernetics*, 46:135–147, 1983.

[31] Yildirim Hurmuzlu and Gordon Moskowitz. The role of impact in the stability of bipedal locomotion. *Dynamics and Stability of Systems*, 1:217–234, 1986.

[32] Yildirim Hurmuzlu and Gordon Moskowitz. Bipedal locomotion stabilized by impact and switching: I. two- and three- dimensional models. *Dynamics and Stability of Systems*, 2:73–96, 1987.

[33] T. Mita, T. Kashiwase, and T. Kawase. Realisation of a high speed biped using modern control theory. *International Journal of Control*, 40(1):107–119, 1984.

[34] M. Yamada, J. Furusho, and A. Sano. Dynamic control of a walking robot with kick action. In *Proc. of the International Conference on Advanced Robotics*, pages 405–412, Tokyo, 1985. Robotics Society of Japan.

[35] A. Takanishi, M. Ishida, Y. Yamazaki, and I. Kato. The realization of dynamic walking by the biped walking robot WL-10RD. In *Proc. of the International Conference on Advanced Robotics*, pages 459–466, Tokyo, 1985. Robotics Society of Japan.

[36] T-T. Lee and J-H. Liao. Trajectory planning and control of a 3-link biped robot. In *Proc. 1988 IEEE International Conference on Robotics and Automation*, pages 820–823, New York, 1988. IEEE.

[37] Y-F. Zheng, J. Shen, and F. Sias. A motion control scheme for a biped robot to climb sloping surfaces. In *Proc. 1988 IEEE International Conference on Robotics and Automation*, pages 814–816, New York, 1988. IEEE, IEEE.

[38] H. Miura and I. Shimoyama. Dynamic walk of a biped. *International Journal of Robotics Research*, 3(2):60–74, 1984.

[39] G. F. Phillips, B. J. Andrews, H. Chizeck, and K. Barnacle. Finite state control of paraplegic gait using a hybrid FNS orthosis. In G. Harris and C. Walker, editors, *Proc. of the Annual International Conference of the IEEE Engineering in Medicine and Biology Society*, page 1671, New York, 1988. IEEE, IEEE.

[40] C. A. Phillips. Electrical muscle stimulation in combination in combination with a reciprocating gait orthosis for ambulation by paraplegics. *Journal of Biomedical Engineering*, 11(4):338–344, July 1989.

[41] W. K. Durfee and J. M. Hausdorff. Regulating knee joint position by combining electrical stimulation with a controllable friction brake. *Annals of Biomedical Engineering*, 18(6):575–596, 1990.

[42] J. V. Basmajian and R. Tuttle. EMG of locomotion in gorilla and man. In R.B. Stein, K.G. Pearson, R.S. Smith, and J.B Redford, editors, *Control of Posture and Locomotion*, pages 599–609. Plenum Press, New York, 1973. Proc. of an International Symposium at the University of Alberta, August 20-22, 1973.

[43] T. McGeer. Passive dynamic walking. *Intern. J. Robot. Res.*, 9(2):62–82, April 1990.

[44] T. McGeer. Passive walking with knees. In *Proc., 1990 IEEE International Conference on Robotics and Automation*, pages 1640–5, Los Alamitos, CA, 1990. IEEE, IEEE.

[45] A. Goswami, B. Thuilot, and B. Espiau. Compass-like biped robot, part I: Stability and bifurcation of passive gaits. Rapport de recherche 2996, Unité de recherche INRIA Rhône-Alpes, St. Martin, France, October 1996.

[46] J. I. Neimark and N. A. Fufaev. *Dynamics of Nonholonomic Systems*, volume 33 of *Translations of Mathematical Monographs*. American Mathematical Society, Providence, Rhode Island, 1972.

[47] H. Ziegler. *Principles of Structural Stability*. A Blaisdell Book in Solid Mechanics. Blaisdell, Waltham, MA, 1968.

[48] D. Zenkov, A. Bloch, and J. Marsden. The energy-momentum method for the stability of nonholonomic systems. Technical report, University of Michigan, 1997.

[49] A. Ruina. Nonholonomic stability aspects of piecewise holonomic systems. *Reports on Mathematical Physics*, 1998.

[50] M. Bühler and D. E. Koditschek. From stable to chaotic juggling: Theory, simulation, and experiments. In *1990 IEEE International Conference on Robotics and Automation*, pages 1976–1981. IEEE Robotics and Automation Society, IEEE, 1990. The Proc. are from a conference held during May 13-18, 1990 in Cincinnati, Ohio.

[51] J. Guckenheimer and P. Holmes. *Nonlinear Oscillations, Dynamical Systems, and Bifurcations of Vector Fields*. Springer-Verlag, New York, 1983.

[52] R. Pratap, S. Mukherjee, and F. C. Moon. Dynamic behavior of a bilinear hysteretic elasto-plastic oscillator, part I: Free oscillations. *Journal of Sound and Vibration*, 172(3):321–337, 1994.

[53] R. Pratap, S. Mukherjee, and F. C. Moon. Dynamic behavior of a bilinear hysteretic elasto-plastic oscillator, part II: Oscillations under periodic impulse forcing. *Journal of Sound and Vibration*, 172(3):339–358, 1994.

[54] S. W. Shaw and P. J. Holmes. A periodically forced piecewise linear oscillator. *Journal of Sound and Vibration*, 90(1):129–155, 1983.

[55] S. W. Shaw and R. H. Rand. The transition to chaos in a simple mechanical system. *International Journal of Non-Linear Mechanics*, 24(1):41–56, 1989.

[56] A. A. Andronov, A. A. Vitt, and S. E. Khaikin. *Theory of Oscillators*. Dover, 1966.

[57] Y. Hurmuzlu. Dynamics of bipedal gait: Part I — objective functions and the contact event of planar five-link biped. *Journal of Applied Mechanics*, 60:331–337, June 1993.

[58] Y. Hurmuzlu. Dynamics of bipedal gait: Part II — stability analysis of a planar five-link biped. *Journal of Applied Mechanics*, 60:337–343, June 1993.

[59] Bernard Brogliato. *Nonsmooth Impact Mechanics: Models, Dynamics and Control*. Springer, London, UK, 1996.

[60] D. E. Koditschek and M. Bühler. Analysis of a simplified hopping robot. *The International Journal of Robotics Research*, 10:587–605, December 1991.

[61] M. Raibert. *Legged Robots that Balance*. MIT Press, Cambridge, Mass., 1986.

[62] M. Henon. On the numerical computation of Poincaré maps. *Physica 5D*, pages 412–414, 1982.

[63] Rodolfo Margaria. *Biomechanics and Energetics of Muscular Excercise.* Clarendon Press, Oxford, 1976.

[64] T. McGeer and L. H. Palmer. Wobbling, toppling, and forces of contact. *American Journal of Physics*, 57:1089–96, December 1989.

[65] A. Back, J. Guckenheimer, and M. Myers. A dynamical simulation facility for hybrid systems. Technical Report 92-6, Mathematical Sciences Institute, Cornell University, Ithaca, NY, April 1992.

[66] T. McGeer. Dynamics and control of bipedal locomotion. *Progress in Robotics and Intelligent Systems*, 1990.

[67] M. E. Carvallo. Théorie du movement du monocycle et de bicyclette. premiére partie. cerceau et monocycle. *Journal de L'École Polytechnique, Series 2*, 5:119–188, 1900.

[68] J. Papadopoulos. private communication, 1988.

[69] Y. Rocard. *General Dynamics of Vibrations.* Frederick Ungar Publishing Co., New York, third edition, 1960.

[70] R. S. Sharp. The stability and control of pivot-framed tricycles. In J. K. Hedrick, editor, *Proc., 8th IAVSD–Symposium; The Dynamics of Vehicles on Roads and Tracks*, pages 564–77, Lisse, 1983. IAVSD–IUTAM, Swets and Zeitlinger B. V.

[71] H. Bondi. The rigid body dynamics of unidirectional spin. *Proc. of the Royal Society of London*, 405:265–274, 1986.

[72] O. M. O'reilly. The dynamics of rolling disks and sliding disks. *Nonlinear Dynamics*, 10:287–305, 1996.

[73] R. Cushman, J. Hermans, and D. Kemppainen. *The Rolling Disc*, volume 19 of *Progress in Nonlinear Differential Equations and Their Applications*, pages 21–60. Birkhäuser Verlag, Basel, Switzerland, 1996.

[74] M. Coleman, A. Chatterjee, and A. Ruina. Motions of a rimless spoked wheel: A simple 3D system with impacts. *Dynamics and Stability of Systems*, 12(3):139–69, September 1997.

[75] T. McMahon. Mechanics of locomotion. *International Journal of Robotics Research*, 3(2):4–28, 1984.

[76] H. Hemami and B. Chen. Stability analysis and input design of a two-link planar biped. *The International Journal of Robotics Research*, 3(2):93–101, Summer 1984.

[77] J. Furusho and A. Sano. Sensor-based control of a nine-link biped. *The International Journal of Robotics Research*, 9(2):83–98, April 1990.

[78] V. V. Beletskii. Nonlinear effects in dynamics of controlled two-legged walking. In *Nonlinear Dynamics in Engineering Systems*, pages 17–26, Berlin, 1990. IUTAM, Springer-Verlag. The Proc. are from an IUTAM symposium held in 1989 in Stuttgart, Germany.

[79] M. G. Pandy and N. Berme. Synthesis of human walking: a planar model for single support. *Journal of Biomechanics*, 21(12):1053–1060, 1988.

[80] M. Vukobratovic, B. Borovac, D. Surla, and D. Stokic. *Scientific Fundamentals of Robotics 7—Biped Locomotion: Dynamics, Stability, Control, and Application.* Communications and Control Engineering Series. Springer-Verlag, Berlin, 1990.

[81] A. Goswami, B. Espiau, and A. Keramane. Limit cycles in a passive compass gait biped and passivity-mimicking control laws. *Autonomous Robots*, 4(3):273–86, 1997.

[82] B. Thuillot, A. Goswami, and B. Espiau. Bifurcation and chaos in a simple passive bipedal gait. In *Proc., 1997 IEEE International Conference on Robotics and Automation*, pages 792–8, New York, NY, 1997. IEEE, IEEE.

[83] A. Chatterjee. private communication, 1988.

[84] J. Hale and H. Kocak. *Dynamics and Bifurcations*, volume 3 of *Texts in Applied Mathematics*. Springer-Verlag, New York, 1991.

[85] P. G. Drazin. *Nonlinear Systems*. Cambridge texts in applied mathematics. Cambridge University Press, Cambridge, 1992.

[86] R. L. Devaney. *An Introduction to Chaotic Dynamical Systems*. Addison-Wesley, Reading, MA, 1989.

[87] John Craig, editor. *Introduction to Robotics*. Addison Wesley, 1989.